Evaluating the Impact of Land Cover Composition on Water, Energy, and Carbon Fluxes in Urban and Rangeland Ecosystems of the Southwestern United States

by

Nicole Pierini Templeton

A Dissertation Presented in Partial Fulfillment
of the Requirements for the Degree
Doctor of Philosophy

Approved June 2017 by the
Graduate Supervisory Committee:

Enrique R. Vivoni, Chair
Steven R. Archer
Giuseppe Mascaro
Russell L. Scott
Zhi-Hua Wang

ARIZONA STATE UNIVERSITY

August 2017

ABSTRACT

Urbanization and woody plant encroachment, with subsequent brush management, are two significant land cover changes that are represented in the southwestern United States. Urban areas continue to grow, and rangelands are undergoing vegetation conversions, either purposely through various rangeland management techniques, or by accident, through inadvertent effects of climate and management. This thesis investigates how areas undergoing land cover conversions in a semiarid region, through urbanization or rangeland management, influences energy, water and carbon fluxes. Specifically, the following scientific questions are addressed: (1) what is the impact of different urban land cover types in Phoenix, AZ on energy and water fluxes?, (2) how does the land cover heterogeneity influence energy, water, and carbon fluxes in a semiarid rangeland undergoing woody plant encroachment?, and (3) what is the impact of brush management on energy, water, and carbon fluxes?

The eddy covariance technique is well established to measure energy, water, and carbon fluxes and is used to quantify and compare flux measurements over different land surfaces. Results reveal that in an urban setting, paved surfaces exhibit the largest sensible and lowest latent heat fluxes in an urban environment, while a mesic landscape exhibits the largest latent heat fluxes, due to heavy irrigation. Irrigation impacts flux sensitivity to precipitation input, where latent heat fluxes increase with precipitation in xeric and parking lot landscapes, but do not impact the mesic system. In a semiarid managed rangeland, past management strategies and disturbance histories impact vegetation distribution, particularly the distribution of mesquite trees. At the site with less mesquite coverage, evapotranspiration (ET) is greater, due to greater grass cover. Both

sites are generally net sinks of CO_2, which is largely dependent on moisture availability, while the site with greater mesquite coverage has more respiration and generally greater gross ecosystem production (GEP). Initial impacts of brush management reveal ET and GEP decrease, due to the absence of mesquite trees. However the impact appears to be minimal by fall. Overall, this dissertation advances the understanding of land cover change impacts on surface energy, water, and carbon fluxes in semiarid ecosystems.

DEDICATION

I would like to dedicate this dissertation to my husband Ryan for his unrelenting support, encouragement, and love. He's always provided an ear to listen to ideas and frustrations, a hand to pull me up, and a smile to celebrate the little victories along the way. His encouragement and inspiration over the years has been unparalleled, and I'll never be able to thank him enough. I would also like to dedicate this dissertation to my family (Lou, Paula, Sam, Forrest and Rita) for their endless encouragement and guidance.

ACKNOWLEDGMENTS

First, I would like to thank my advisor, Dr. Enrique R. Vivoni. I appreciate the immense support, patience, and encouragement provided to make my Ph.D. a positive and productive experience. I am grateful for the hydrology group established at ASU, led by Dr. Vivoni, which provided advice and comedic or active relief when necessary. The people I've met through our group at ASU (too many to list) are all thoughtful, caring individuals, and that is a reflection of our advisor.

I would like to thank each of my committee members for providing valuable insight and encouragement. Dr. Russell Scott gave great advice and insight to my research objectives. His patience is extremely appreciated, from helping with eddy covariance setups and data processing to explaining carbon fluxes to a water person, which took several times until I understood. I am grateful to Dr. Zhi-hua Wang, who was always very encouraging and is a great professor, helping with my understanding of land-atmosphere interactions. I would like to thank Dr. Steven Archer for offering support in my research, and perhaps the most eloquently told history of woody plant encroachment I will ever hear. And I would like to thank Dr. Giuseppe Mascaro for providing an outlet to think ideas through and always offering perspective.

Funding throughout my Ph.D. was provided by the U.S. Army Research Office (Grant 65962-EVII and Grant 56059-EV-PCS), the National Science Foundation (Grant EF1049251 and Grant DEB-1026865), the U.S. Department of Agriculture (Grant 2015-67019-23314) and the Ira A. Fulton Schools of Engineering Dean's Fellowship through Arizona State University. I am thankful for the financial support from the above-mentioned funding sources.

TABLE OF CONTENTS

CHAPTER Page

APPENDIX Page

LIST OF TABLES

Table Page

LIST OF FIGURES

Figure Page

Figure Page

Figure Page

CHAPTER 1

INTRODUCTION

MOTIVATION

Land cover change directly and indirectly affects surface energy, water, and carbon fluxes, which impacts the local, regional and global cycles and surface-atmosphere interactions. For this dissertation, particular energy fluxes of interest include net radiation, which consists of incoming and outgoing shortwave and longwave radiation, sensible heat flux, latent heat flux, and ground heat flux. Together, these components comprise the surface energy balance (SEB). Water fluxes are focused on precipitation and evapotranspiration. Carbon fluxes are evaluated at an ecosystem scale, thus components of interest include net ecosystem exchange, gross ecosystem production, and ecosystem respiration. Each of these fluxes describe an exchange (energy, water or carbon) between the land surface and the atmosphere. Therefore, land surface composition has a large impact (e.g. Sala et al., 2000; Bounoua et al., 2002; Betts, 2001; Pielke et al., 1998). Land cover change is the alteration of the Earth's land surface and is constantly occurring across the world due to human influence. Two major types of land cover change are urbanization and rangeland modifications, which are highly dynamic (Lambin et al., 2001). Urbanization is the transformation of rural areas to cities. Rangelands include landscapes that are used by grazers and are composed of various fractions of grasses and tree cover with modifications resulting from particular rangeland management to control livestock grazing. As land cover change continues, it is vital to understand land cover impacts on the surface energy, water, and carbon fluxes.

Two significant types of land cover change that are representative of the southwestern United States will be studied in this dissertation: urbanization and woody plant encroachment (with subsequent brush management). As cities continue to grow worldwide, the transformation of natural environments into urban land covers will accelerate (United Nations, 2015). Urban land use typically exemplifies a shift to impervious land cover, including concrete, asphalt, gravel cover and buildings, as well as landscaping that involves native and non-native plants (e.g., Grimm et al., 2008; Wu et al., 2011; Cook et al., 2012). Semiarid rangelands (grasslands, shrublands, and savannas) are important ecosystems, as they account for roughly 50% of the Earth's land surface (Bailey, 1996) and approximately 30% of the world's population, that are distinctive of the southwestern United States. These environments are sensitive to landscape changes due to various factors, both natural and anthropogenic, such as overgrazing, increasing agricultural pressure, climate change, increases in CO_2 and N deposition, and wildfires (Archer, 1994; Scholes and Archer, 1997; Van Auken, 2009; Eldridge et al., 2011).

In the Phoenix, Arizona, metropolitan area, rapid urbanization during the second half of the 20th century led to the conversion of agriculture and desert lands into urban and suburban developments (e.g., Hirt et al., 2008; Jenerette et al., 2011). Urbanization was accompanied by outdoor water use in residential, commercial and recreational areas based upon different strategies, including mesic (sprinkler irrigated turf grass) and xeric (drip irrigated shrubs or trees with gravel cover) landscaping (e.g., Volo et al., 2014; Song and Wang, 2015; Yang and Wang, 2015). The outdoor water used for urban vegetation in arid regions promotes a higher degree of plant biodiversity (Hope et al., 2003; Buyantuyev and Wu, 2012), impacts the local thermal comfort (Gober et al., 2010;

Song and Wang, 2015) and affects the soil water balance (Volo et al., 2014, 2015). Modeling studies have also shown that the material, thermal and hydrologic properties of urban surfaces, such as roofs, green spaces and buildings, impact energy and water exchanges with the atmosphere (e.g., Grimmond and Oke, 2002; Arnfield, 2003; Georgescu et al., 2009; Grimmond et al., 2010; Lee et al., 2012; Schaffer et al., 2015; Benson-Lira et al., 2016; Yang et al., 2016).

Woody plant encroachment is a worldwide phenomenon that has been observed in semiarid rangelands as they undergo a conversion from grasslands to savannas. This phenomenon has been well studied and documented in North America (e.g., Archer et al., 2001; Van Auken, 2000; Huxman et al., 2005; Browning et al., 2008), Australia (e.g., Burrows et al., 1990; Fensham, 1998), southern Africa (e.g., Moore et al., 1970; Burgess, 1995; Hudak and Wessman, 1998; Roques et al., 2001), and South America (e.g., Soriano, 1979; Silva et al., 2001). Woody plant encroachment can be defined as the increase in density, cover, and biomass of indigenous woody or shrub plants (Van Auken, 2009), and can be due to indigenous or invasive woody plants. Several hypotheses have emerged as the driver to encroachment. Grazing, for example, can lead to woody plant encroachment directly by reducing perennial grasses and so reducing competition or by spreading seeds (Brown and Archer, 1990; Harrington, 1991) or indirectly by reducing fire frequency and intensity (Savage and Swetnam, 1990; Archer, 1995; Oba et al., 2000). The effect of woody plant encroachment in semiarid areas on the landscape properties has been widely researched as this shift may significantly alter the structure and function of these ecosystems (e.g., Archer et al., 2001; Van Auken, 2000, 2009). Dryland management has traditionally focused on reducing woody plant cover (brush

management) to increase forage production, steamflow, and groundwater recharge (Huxman et al., 2005; Archer and Predick, 2014). However, there is less known about the impact of brush management on other ecosystem services, such as ecosystem primary production, and land surface-atmosphere interactions (Archer, 2009). There is a tight coupling between vegetation and water in semiarid ecosystems, and implications of woody plant encroachment and brush management on energy, water and carbon cycles are not well understood (Huxman et al., 2005).

Meteorological flux measurements using the eddy covariance (EC) technique provide a detailed quantification of surface processes and their interactions with atmospheric and land surface conditions (e.g., Baldocchi et al., 1988; Wilson et al., 2002; Baldocchi et al., 2003). The EC method provides a direct way to measure energy, water and carbon exchanges from the surface to the atmosphere over a particular scale of interest, typically a type of ecosystem. The EC technique is used to measure urban fluxes (Grimmond and Christen, 2012), however, EC measurement in urban systems can be challenging due to the inherent heterogeneity of the urban surface (Grimmond, 2006; Kotthaus and Grimmond, 2012). As semiarid rangelands have evolved from grasslands to savannas with an increase in woody cover, their surfaces have also become more heterogeneous. Woody plants influence stream flow, soil moisture, soil nutrients, among other components, that impact vegetation distribution, particularly grass and bare soil cover (Scholes and Archer, 1997). Spatial heterogeneity in woody savannas is further complicated by temporal dynamics of tree and grass interactions, and brush management techniques (Archer and Predick, 2014). Thus it is vital to understand the influence of land cover spatial heterogeneity on flux measurements using the EC technique.

The EC source area is a time-variable land surface area that directly contributes to the flux measurements and is a function of atmospheric conditions, the measurement height and roughness properties (Schmid, 1994; Grimmond, 2006). Over spatially heterogeneous surfaces, it is necessary to understand land cover variability with respect to wind direction at an EC tower to accurately interpret flux measurements (Aubinet et al., 2000; Baldocchi, 2003). The spatial variability of surface conditions is temporally dynamic and particularly complicated in urban systems and woody savannas, therefore it is necessary to characterize land cover in these systems.

The overarching goals of this dissertation are as follows:

(1) Measure meteorological variables and fluxes over different land covers in a semiarid urban system and in a semiarid rangeland.

(2) Characterize land cover distribution in urban and managed rangeland environments to fully understand meteorological and flux measurements.

(3) Evaluate water and energy flux differences among common semiarid urban land cover types and their sensitivity to precipitation.

(4) Determine impact of land cover distribution on water, energy and carbon fluxes among two towers within a managed semiarid rangeland, and how variability links to seasonal phenology.

(5) Assess the initial impact of brush management (woody plant treatment) on water, energy and carbon fluxes within a managed semiarid rangeland.

CHAPTER OUTLINE

The work presented in this dissertation intends to advance the understanding of how dynamic land cover composition in semiarid ecosystems, specifically an urban area and a rangeland, impacts energy, water, and carbon fluxes.

In Chapter 2, the link between different urban land cover types in a semiarid ecosystem, Phoenix, AZ, to energy and water land-atmosphere exchanges is evaluated. While model applications have indicated that the built environment impacts energy and water exchanges (e.g., Song and Wang, 2015; Wang *et al.*, 2016), few studies have directly observed the effects of different urban land cover types on the surface energy balance or the partitioning of turbulent fluxes. In this study, we conducted meteorological flux measurements using the eddy covariance technique to obtain a detailed quantification of SEB processes and relate them to the urban land cover distributions within the sampled footprints of three short-term deployments and a stationary reference site in Phoenix. Comparisons of standard weather variables, meteorological fluxes and normalized SEB quantities between the mobile and reference sites were carried out to account for the effect of time-varying (seasonal) conditions during the short-term deployments. A particular focus of the analysis was placed on the comparative role of precipitation events and outdoor water use on modifying the turbulent flux partitioning given the strong natural water limitations in the arid urban area.

In Chapter 3, we explore a different type of land cover change observed in semiarid ecosystems, woody plant encroachment, and analyze its impact on energy, water, and carbon land-atmosphere interactions. Grasslands and savannas are particularly susceptible to woody plant encroachment. These semiarid systems can represent different

scales of heterogeneity, due to vegetation changes such as woody plant encroachment, or other disturbances that impact vegetation distribution. Woody plant encroached landscapes and subsequent brush management lead to changes in ecosystem services that are not well understood. The EC method is a well-established technique to measure fluxes between the surface and the atmosphere, and can be used over nearby landscapes to reveal how disturbance and vegetation distribution differences impact water and carbon fluxes. In this study, observations are compared from two eddy covariance towers in the Sonoran Desert which represent landscapes that have undergone the encroachment of velvet mesquite (*Prosopis velutina* Woot.). While the sites are nearby, they have experienced different disturbance histories, which is well documented through the SRER data archives (McClaran, 2003). Current landscape conditions are characterized using terrain and vegetation classification from orthoimagery and data from the EC towers.

Based upon the work from Chapter 3, Chapter 4 explores the initial impact of a specific type of brush management, aerially applied herbicide to treat mesquite trees, which is a technique used across southwest U.S. rangelands. The impact of brush management (BM) on water and carbon fluxes is not well understood, and influences the management of rangelands. In this study, two eddy covariance towers are compared to evaluate the initial impacts of an aerially applied mesquite treatment. Water and carbon fluxes, specifically evapotranspiration, net ecosystem exchange, ecosystem respiration, and gross ecosystem production, are evaluated between the two sites to determine if and what differences are caused from mesquite treatment in the energy, water, and carbon cycles. Comparing flux measurements allows for greater insight into the initial impact of mesquite treatment.

Finally, Chapter 5 summarizes the general conclusions and reflects on future research from the preceding chapters. Chapters 2 to 4 correspond to three journal articles that are submitted or in preparations:

Chapter 2: Templeton, N.P., E.R. Vivoni, Z-H. Wang, and A.P Schreiner-McGraw (2017) Quantifying Water and Energy Fluxes over Different Urban Land Covers in Phoenix, Arizona. (Under review, *International Journal of Climatology*).

Chapter 3: Templeton, N.P., E.R. Vivoni, R.L. Scott, S.R. Archer, J.A. Biederman, and A.T. Naito (2017) Degree of Woody Plant Encroachment Influences Seasonality of Water, Energy, and Carbon Dioxide Exchanges. (In preparation, *Agricultural and Forest Meteorology*).

Chapter 4: Templeton, N.P., E.R.Vivoni, R.L. Scott, and S.R. Archer (2017) Initial Impacts of Brush Management on Water and Carbon Fluxes in a Southwestern U.S. Rangeland. (In preparation, *Ecosphere*).

CHAPTER 2

QUANTIFYING WATER AND ENERGY FLUXES OVER DIFFERENT URBAN LAND COVERS IN PHOENIX, AZ

INTRODUCTION

As cities continue to grow worldwide, the transformation of natural environments into urban land covers will accelerate (United Nations, 2015). Urban land use typically exemplifies a shift to impervious land cover, including concrete, asphalt, gravel cover and buildings, as well as landscaping that involves native and non-native plants (e.g., Grimm et al., 2008; Wu et al., 2011; Cook et al., 2012). The outdoor water used for urban vegetation in arid regions, for instance, promotes a higher degree of plant biodiversity (Hope et al., 2003; Buyantuyev and Wu, 2012), impacts the local thermal comfort (Gober et al., 2010; Song and Wang, 2015) and affects the soil water balance (Volo et al., 2014, 2015). Modeling studies have also shown that the material, thermal and hydrologic properties of urban surfaces, such as roofs, green spaces and buildings, impact energy and water exchanges with the atmosphere (e.g., Grimmond and Oke, 2002; Arnfield, 2003; Georgescu et al., 2009; Grimmond et al., 2010; Lee et al., 2012; Schaffer et al., 2015; Benson-Lira et al., 2016; Yang et al., 2016). Intra-urban studies have been conducted in European cities (Christen and Vogt, 2004; Offerle et al., 2006) to explore energy partitioning and the surface energy balance (SEB), with an emphasis on comparing across different urban land covers and to nearby rural areas. Nevertheless, few studies have observed the effects of different types of urban land covers on the SEB in arid and

semiarid environments and the partitioning of turbulent fluxes in a comparative manner (Coutts et al., 2007; Best and Grimmond, 2016).

Understanding the links between urban land cover and the SEB processes that mediate microclimatic conditions is critical for planning and design purposes (Mitchell et al., 2008; Middel et al., 2012; Georgescu et al., 2015; Wang et al., 2016), in particular for cities facing an urban heat island (UHI). In the Phoenix, Arizona, metropolitan area, rapid urbanization during the second half of the 20th century led to the conversion of agriculture and desert lands into urban and suburban developments (e.g., Hirt et al., 2008; Jenerette et al., 2011). Urbanization was accompanied by outdoor water use in residential, commercial and recreational areas based upon different strategies, including mesic (sprinkler irrigated turf grass) and xeric (drip irrigated trees with gravel cover) landscaping (e.g., Volo et al., 2014; Song and Wang, 2015; Yang and Wang, 2015). The use of outdoor water for vegetated landscaping also ameliorates, to some extent, the UHI effect (Gober et al., 2010; Buyantuyev and Wu, 2010; Norton et al., 2015), whereby the SEB processes are modified by buildings, urban materials and anthropogenic heat emissions (e.g., Landsberg, 1981; Oke, 1982; Grimmond et al., 2010; Wang et al., 2013; Salamanca et al., 2014). While the cooling properties of urban green spaces are recognized, quantitative studies on the effect of residential landscaping on surface energy fluxes, including evapotranspiration, are relatively rare (c.f., Coutts et al., 2007; Goldbach and Kuttler, 2013; Litvak and Pataki, 2016) with most prior work relying on empirical relations between urban temperature and measures of the cooling potential of different land covers (see Jenerette et al., 2011; Middel et al., 2015).

Meteorological flux measurements using the eddy covariance (EC) technique provide a detailed quantification of SEB processes and their interactions with atmospheric and land surface conditions (e.g., Baldocchi et al., 1988; Wilson et al., 2002; Anderson and Vivoni, 2016). Urban flux measurements, however, are challenging due to deployment logistics, security concerns and the ability to take measurements without disrupting typical activity (Grimmond, 2006; Kotthaus and Grimmond, 2012). Nevertheless, there is a need for urban flux observations in arid and semiarid climates (Grimmond and Christen, 2012), in particular for different types of urban land cover patches captured in the footprint of EC measurements (Grimmond et al., 2010; Loridan and Grimmond, 2012). The EC footprint, or source area, is a time-variable land surface area that directly contributes to the flux measurements and is a function of atmospheric conditions, the measurement height and urban roughness properties (Schmid, 1994; Grimmond, 2006). Recent studies using EC footprint measurements in different urban areas, for example, have identified the role of irrigated vegetation on evapotranspiration (Chow et al., 2014a), the effect of urban density on heat storage (Christen and Vogt, 2004; Offerle et al., 2006; Coutts et al., 2007) and the increase in anthropogenic heat emissions after urbanization (Hong and Hong, 2016).

In this study, I use a trailer-mounted (mobile) EC tower to measure meteorological fluxes and the surface energy balance in three urban settings within Arizona State University (ASU) in the Phoenix metropolitan area. These short-term deployments (average duration of 57 days each) in the winter, early summer and North American monsoon (NAM, July-September) seasons are compared to a stationary (reference) EC tower located in a suburban neighborhood and spanning the entire

sampling period of 273 days (1 January to 30 September 2015). The three mobile sites represent different urban land cover types or patches (i.e., xeric landscaping, parking lot and mesic landscaping) that are expected to vary in terms of the SEB and the partitioning of turbulent fluxes due to variations in urban materials, outdoor water use and the morphology of the built environment. In all deployments, the EC measurements were designed to capture turbulent fluxes for the characteristic urban patch inside the EC footprint without extending to the neighborhood scale which consists of a heterogeneous mosaic of different types of urban land cover. Thus, the objectives of this effort are to: (1) quantify and compare the SEB processes over different urban land cover types in relation to a reference location in an arid environment, and (2) relate the differences in the observed SEB metrics to the observed land cover characteristics of the urban source areas of the flux measurements. A focus is placed on the role of precipitation events and outdoor water use on modifying the partitioning of the turbulent fluxes to capture how the linkage of the energy and water balances varies across the sites.

METHODS

Study sites and their characteristics

The study sites are in the Phoenix metropolitan area which has a population of approximately 4.1 million as of 2010 (US Census Bureau, 2010). Due to its location in the Sonoran Desert, Phoenix has a hot, arid climate (Koppen classification BWh) that has been underrepresented with respect to urban flux measurements (Chow et al., 2014a). Average annual temperature is 24 °C at the Phoenix Sky Harbor International Airport (PHX), with seasonal average temperatures of 14.1, 22.9, 33.9 and 24.8 °C, for winter,

spring, summer and fall. The precipitation regime is bimodal with winter frontal storms and summer thunderstorms during the North American Monsoon (Adams and Comrie, 1997; Vivoni et al., 2008; Mascaro, 2017). Mean annual precipitation is 204 mm/yr based on observations from 1981 to 2010 at PHX, with winter (December, January and February, DJF) and summer (July, August and September, JAS) amounts of 68.3 mm and 67.8 mm, respectively. Spring and early summer (March, April, May and June, MAMJ) are typically dry accounting for only 17% of the mean annual precipitation.

Each deployment site represents a common type of urban land cover in Phoenix. Table 2.1 summarizes site characteristics, while Figure 2.1 indicates their location and provides a photograph of each EC tower. The xeric landscaping (XL) site, placed during the winter months on the ASU Tempe campus (Figure 2.1d), was composed of palo verde (*Parkinsonia florida*) trees with gravel and bare soil cover (undeveloped). Trees were irrigated using a drip system and ranged in height from 3 to 4 meters. In contrast, the parking lot (PL) site on the ASU Tempe campus was a large pavement area with a small proportion of gravel cover (undeveloped) and minimal trees (Figure 2.1c), deployed during the early summer. The parking lot is near an intersection with high traffic and frequently contained vehicles. The mesic landscaping (ML) site was installed at the ASU Polytechnic campus (Figure 2.1e) during the summer and consisted of a regularly irrigated turf grass area using a sprinkler system (approximately 2-3 days per week, 3 times per day, for 20 to 30 minutes each time), with undeveloped land cover nearby. The large grassy area is located among a series of low-rise, single-family homes with undeveloped landscaping, previously used to investigate microclimatic and soil moisture conditions in residential yards (Martin et al., 2007; Volo et al., 2014). All of the

Table 2.1. General characteristics for the four study sites.

Site	Land Cover	UTM Easting (m)	UTM Northing (m)	Latitude	Longitude	Elevation (m)
XL	Palo Verde - Xeric	413797	3698213	33.420°	-111.927°	354
PL	Pavement	412725	3698373	33.421°	-111.939°	356
ML	Turf Grass - Mesic	436646	3686041	33.312°	-111.681°	411
REF	Residential	393794	3705539	33.484°	-112.143°	337

deployment sites are in the built environment such that bare soil conditions are disturbed, generally consist of light-colored, coarse-grained (sandy to sandy loam) textures and have partial gravel cover from landscaping activities. The reference (REF) site represents a suburban residential area in Phoenix consisting of single-family homes, streets, open spaces and other buildings (Figure 2.1b). The EC deployment at the REF site is described by Chow et al. (2014a). In this study, the REF site is a reference location that encompasses the entire period and allows comparisons to the shorter deployments at each mobile EC site, as described next.

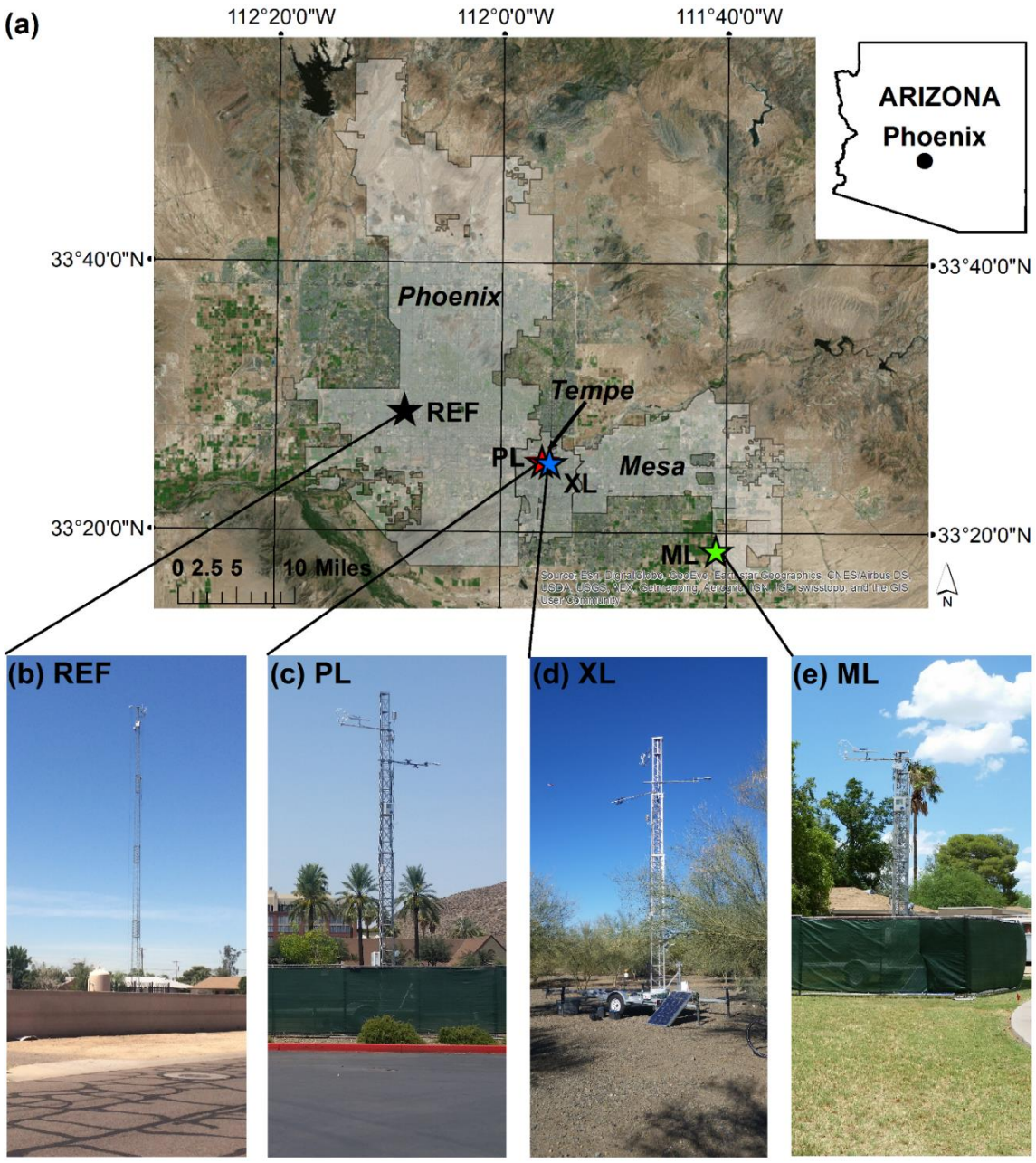

Figure 2.1. Four study sites located in Phoenix: (a), including photographs of the EC deployments at: (b) suburban (REF) site in low-rise, single-family residential area in Phoenix (c) parking lot (PL) site at ASU Tempe campus, Tempe on an impervious surface near a high traffic intersection, (d) palo verde (XL) site at ASU Tempe campus in a landscaping consisting of drip irrigated trees with gravel surface and (e) turf grass (ML) site near residential housing at ASU Polytechnic campus in Mesa in a landscape consisting of regularly irrigated turf grass.

Table 2.2. Instrumentation at mobile EC tower, including number of sensors in parentheses.

Instrument/model	Manufacturer	Variable measured
Tower		
3D sonic anemometer/CSAT3 (1)	Campbell Scientific	Three-dimensional wind velocities, virtual sonic temperature
Infrared gas analyzer/LI-7500A (1)	Li-Cor Biosciences	Water vapor and carbon dioxide concentrations
Temperature and relative humidity sensor/HMP155A (3)	Vaisala	Air temperature and relative humidity
Four component net radiometer/CNR4 (1)	Kipp & Zonen	Incoming and outgoing shortwave and longwave radiation
Pyranometer/SP-110 (1)	Apogee Instruments	Total shortwave radiation
Barometer/CS100 (1)	Setra Systems	Barometric pressure
Near ground level		
Rain gauge/TE525MM (1)	Texas Electronics	Precipitation
Infrared radiometer/SI-111 (1)	Apogee Instruments	Surface temperature
Below ground level		
Soil heat flux plate/HFP01SC (1)	Hukseflux	Ground heat flux
Soil averaging thermocouple/TCAV (2)	Campbell Scientific	Soil temperature
Water content reflectometer/CS616 (3)	Campbell Scientific	Soil volumetric water content

Eddy covariance measurements and data processing

The mobile EC platform consists of a telescoping tower that extends to a maximum height of 15 m. In this study, EC measurements were carried out at a height of 7.0 (XL), 9.0 (PL) and 8.0 m (ML) to ensure that fluxes were observed within the surface layer and above the zero plane displacement heights. High-frequency turbulent fluxes were measured using an open-path infrared gas analyzer and a three-dimensional sonic anemometer (Table 2.2) and aligned to the dominant wind direction for each deployment. Dominant wind directions were determined from wind rose diagrams from meteorological stations on the ASU Tempe campus for the XL and PL sites and from a

Table 2.3. EC deployment specifications, including orientation, height and frequency of turbulent instruments and duration of each deployment.

Site	Orientation (deg)	Height (m)	Freq. (Hz)	Start Day and Time	End Day and Time	Total Days
XL	21	7.0	20	1/20/2015 12:00	3/13/2015 8:30	53
PL	227	9.0	10	5/19/2015 15:00	6/30/2015 6:00	43
ML	230	8.0	10	7/9/2015 13:00	9/18/2015 8:30	74
REF	270	22.1	10	1/1/2015 0:00	9/30/2015 23:30	273

nearby airport (~1 km) for the ML site. Site conditions were inspected to select the measurement height for each case to obtain sensible and latent heat fluxes above the average height of the urban land cover of interest, while maintaining a relatively small EC footprint. The REF site, however, had a taller height of 22.1 m intended to sample fluxes from a broader area (Chow et al., 2014a). Measurements were sampled at frequencies of 10 or 20 Hz (Table 2.3), recorded with a datalogger (CR5000, Campbell Scientific) and processed at 30 min intervals using the EdiRE software program (Clement, 1999). EC processing was performed consistently for all sites and included correcting for fluctuations in stability (Foken et al., 2006) and density (Webb et al., 1980), using the sonic temperature to calculate sensible heat flux (Paw U et al., 2000), rotating the coordinate frame to set the mean vertical wind speed to zero during each 30 min interval (Wilczak et al., 2001) and removing signal lags in the gas concentrations (Massman, 2001). Flux data were also filtered to exclude periods with precipitation (> 0.2 mm/30 min), when the wind direction was 180˚ ± 10˚ from the direction at which instruments were mounted and for outliers greater than 3 standard deviations. Additional sensors recorded radiation, meteorological and soil conditions as 30 min averages (Table 2.2). For all mobile deployments, a four component net radiometer was installed at the

same 5 m height to measure incoming and outgoing shortwave and longwave radiation. Soil moisture was measured at 5 and 50 cm depths at XL, and 5, 15 and 50 cm depths at ML to quantify soil responses to precipitation and urban irrigation. Ground heat flux was measured using a heat flux plate at 5 cm depth and two thermocouples at 2 and 4 cm depths at all sites except the pavement surface at PL. Due to limitations in available equipment or access to soil for measuring ground heat flux at many sites, we only installed one sensor per deployment. Average soil temperature (T_{soil}) for the 0 to 5 cm depth was determined by averaging the thermocouple measurements and the rate of change of T_{soil} was used with the soil water content to determine energy stored in the layer above the plate. Further details on the setup and instruments at the REF site are found in Chow *et al.* (2014a).

Urban surface energy balance and meteorological comparisons

The urban surface energy balance (SEB) is described as:

$$Q^* + Q_F = Q_H + Q_E + \Delta Q_S + \Delta Q_A \quad (2.1)$$

where Q^* is the net radiation, Q_F is the anthropogenic heat flux, Q_H is sensible heat flux, Q_E is latent heat flux, and ΔQ_S and ΔQ_A are the net changes of heat storage and advection, all in W/m^2 (Oke, 1988). The processed turbulent fluxes and radiation, meteorological and soil measurements were used to quantify the SEB for a simple plane facet (Arnfield, 2003) as:

$$Q^* - Q_G = Q_H + Q_E \quad (2.2)$$

where Q_G is ground heat flux. This equation assumes that anthropogenic heat and advection are negligible and only considers the conductive heat flux from the surface

(Q_G), whereas ΔQ_S represents all energy storage in the control volume. While this is not the case in urban areas (e.g., Oke, 1988; Sailor, 2011; Chow *et al.*, 2014a), we use energy balance closure (ε) as a measure of the residual quantity ($1 - \varepsilon$) not captured by the measured fluxes, as in Chow *et al.* (2014b):

$$\varepsilon = \frac{\sum(Q_H + Q_E)}{\sum(Q^* - Q_G)} \tag{2.3}$$

We also compute a separate residual term (RES) to approximate an upper limit of ΔQ_S that includes Q_G (Christen and Vogt, 2004; Chow *et al.*, 2014b) as follows:

$$RES = Q^* - Q_H - Q_E \tag{2.4}$$

For the EC systems deployed, net radiation (Q*) is obtained from measurements of the incoming and outgoing components of shortwave ($K_\downarrow$ and $K_\uparrow$) and longwave ($L_\downarrow$ and $L_\uparrow$) radiation as:

$$Q^* = Q_\downarrow - Q_\uparrow = (K_\downarrow + L_\downarrow) - (K_\uparrow + L_\uparrow) \tag{2.5}$$

where $Q_\downarrow$ is the total incoming radiation and $Q_\uparrow$ is the total outgoing radiation. To compare observations at the sites (Loridan and Grimmond, 2012), we estimated ratios of sensible heat flux to total incoming radiation ($Q_H/Q_\downarrow$), latent heat flux to total incoming radiation ($Q_E/Q_\downarrow$) and the sum of sensible and latent heat fluxes to total incoming radiation ($(Q_H+Q_E)/Q_\downarrow$). All normalized quantities are computed after aggregation to the daily scale such that differences among sites at a higher temporal resolution are not captured. We also compared standard weather observations of air temperature (*TA*), precipitation (*P*) and vapor pressure deficit (*VPD*, obtained from relative humidity and air temperature) from each deployment to the REF site. Averaged diurnal cycles of Q^*, Q_G,

Q_H and Q_E were obtained over all sampled days at each site. Furthermore, we estimated the evaporative fraction (*EF*) at local noon time of each day and as a daily average as:

$$EF = \frac{Q_E}{Q_H + Q_E} \tag{2.6}$$

to provide further insight into the partitioning of turbulent fluxes in different urban land covers. Additional analyses, such as evaluating the temporal dynamics of Q^*, soil moisture and *EF*, were performed for subsets of days classified as 'wet' or 'dry' based on the occurrence of precipitation (P > 0.2 mm/day) taken to be the day of and two days after a storm event.

Urban land cover characterization and footprint analysis

To characterize the source areas of the flux measurements, a consistent land cover classification was performed for each mobile EC site using high-resolution (0.30 m cell size) color orthoimagery from the U.S. Geological Survey (http://lta.cr.usgs.gov/high_res_ortho). Classifications were based on the Red, Green and Blue (RGB) signatures using a maximum likelihood method in ArcGIS 10.4 (Image Classification Tool) and utilized training samples that were verified with site visits. Following prior efforts in Phoenix (e.g., Myint *et al*., 2011; Zhao *et al*., 2015), land cover was classified into five general types: (1) trees, (2) grass, (3) undeveloped (gravel or bare soil), (4) pavement and (5) buildings or cement. For comparison, we employed the classification of Chow *et al.* (2014a) based on a 2.4 m resolution Quickbird image (Myint *et al.*, 2011) for a circular region of 1 km^2 around the REF site. This analysis is well suited for the REF site where the source area is larger and more difficult to classify

Table 2.4. Urban land cover percentages within 80% source area and radiometer footprint. The percentage of flux originating from a 500 m radius fetch centered at each EC site is shown. REF site information is as reported in Chow *et al.* (2014a).

Urban Land Cover	80% Source Area			Radiation Footprint			
	XL	PL	ML	XL	PL	ML	REF
Trees	38.2%	5.9%	16.2%	34.4%	2.2%	6.8%	4.6%
Grass	0.4%	0.7%	28.1%	0.0%	0.7%	43.6%	10.0%
Undeveloped	29.7%	13.9%	34.6%	65.6%	29.6%	34.5%	36.8%
Pavement	8.3%	57.4%	12.8%	0.0%	67.5%	4.1%	22.0%
Buildings or Cement	23.4%	22.1%	8.3%	0.0%	0.0%	11.0%	26.4%
% in 500 m fetch	97.1%	94.5%	96.4%				

accurately. Table 2.4 reports on urban land cover percentages for each site, with REF indicating low-rise buildings (26.4%), undeveloped (36.8%) surface cover and a proportion of non-vegetated urban cover of 85.2%. For the mobile EC sites, we computed the percentage of each land cover class within the EC footprint and within the radiometer footprint (Table 2.4). The EC footprint was obtained using the analytical model of Kormann and Meixner (2001) for an area of 500 m by 500 m centered at each site and a horizontal pixel resolution of 5 m selected to be less than the measurement height (Van de Boer *et al.*, 2013). The model is applied in the surface layer at the EC measurement height for each deployment which is above the average tree and building heights. The surface layer consists of roughly the bottom 10% of the boundary layer which represents a physical layer with “constant flux” arising from the land surface and can be mathematically formulated using the Monin-Obukhov Similarity Theory (MOST) adopted in the model (Stull, 1988). For its operation, the model requires the measurement height, fetch radius, wind speed and direction, friction velocity and a stability criterion. Since measurement heights were above the zero plane displacements (2.5, 2.0 and 5.0 m

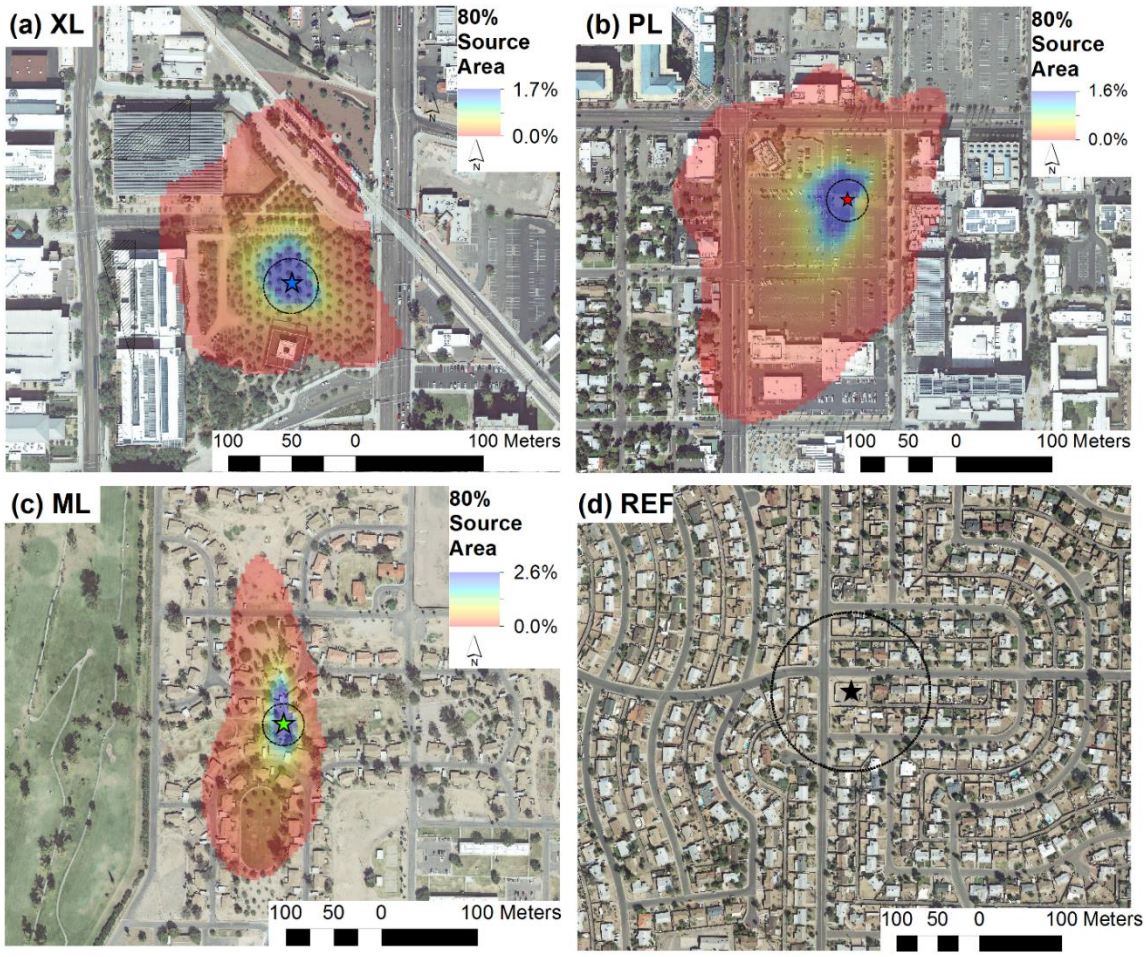

Figure 2.2. Study site orthoimagery with the 80% source areas (colored 5 m by 5 m pixels with percent contribution for each) and radiometer source areas (black circles) at: (a) XL, (b) PL, (c) ML and (d) REF sites.

at the XL, PL and ML sites), the application of MOST and the concept of stability are valid (Foken et al., 2006). Following Anderson and Vivoni (2016), the EC footprint was calculated for each 30 min interval of turbulent daytime conditions, averaged over each daytime period and aggregated to derive a unique footprint for each deployment. We selected the 80% threshold as the source area to define the EC footprint (Schmid, 1994), as shown in Figure 2.2 (the percent contribution of each 5 m by 5 m pixel indicated by color). While the 80% source areas appear large (red areas), most of the flux

contributions are from regions near the EC towers (blue areas) and a 500 m radius contains >94% of the footprint (Table 2.4). In addition, we used the radiometer height to obtain an approximate circular (fixed) footprint for these measurements (Schmid et al., 1991) based on the 95% source area (or 1492 m^2 for a 5 m height) that overlap well with the higher EC contributions. While this estimate does not account for elements of the urban environment, it is a first approximation based on flat, homogeneous terrain that is suitable for our analyses. As shown in Table 2.4, urban land cover distributions have similar patterns between the EC and radiometer footprints. For instance, at the XL site, the dominant land covers are undeveloped land in the form of gravel cover (29.7% for 80% source area and 65.6% for radiometer footprint) and trees (38.2% and 34.4%, respectively). As at other sites, this indicates that as proximity to the EC tower increases (blue areas overlapping with radiometer circle), the distribution of urban land cover types reflect the intended sampling plan.

RESULTS AND DISCUSSION

Meteorological conditions and comparison to long-term averages

The mobile EC deployments measured meteorological variables across a variety of urban land covers during different seasons, while the REF site spanned the entire study period. Figure 2.3 shows the variation of precipitation, air temperature, vapor pressure deficit and net radiation. Each deployment recorded several storm events of varying intensity with observed differences between the mobile EC and reference sites (Table 2.5). For instance, the NAM season at ML exhibited a lower precipitation (5.4 mm) as

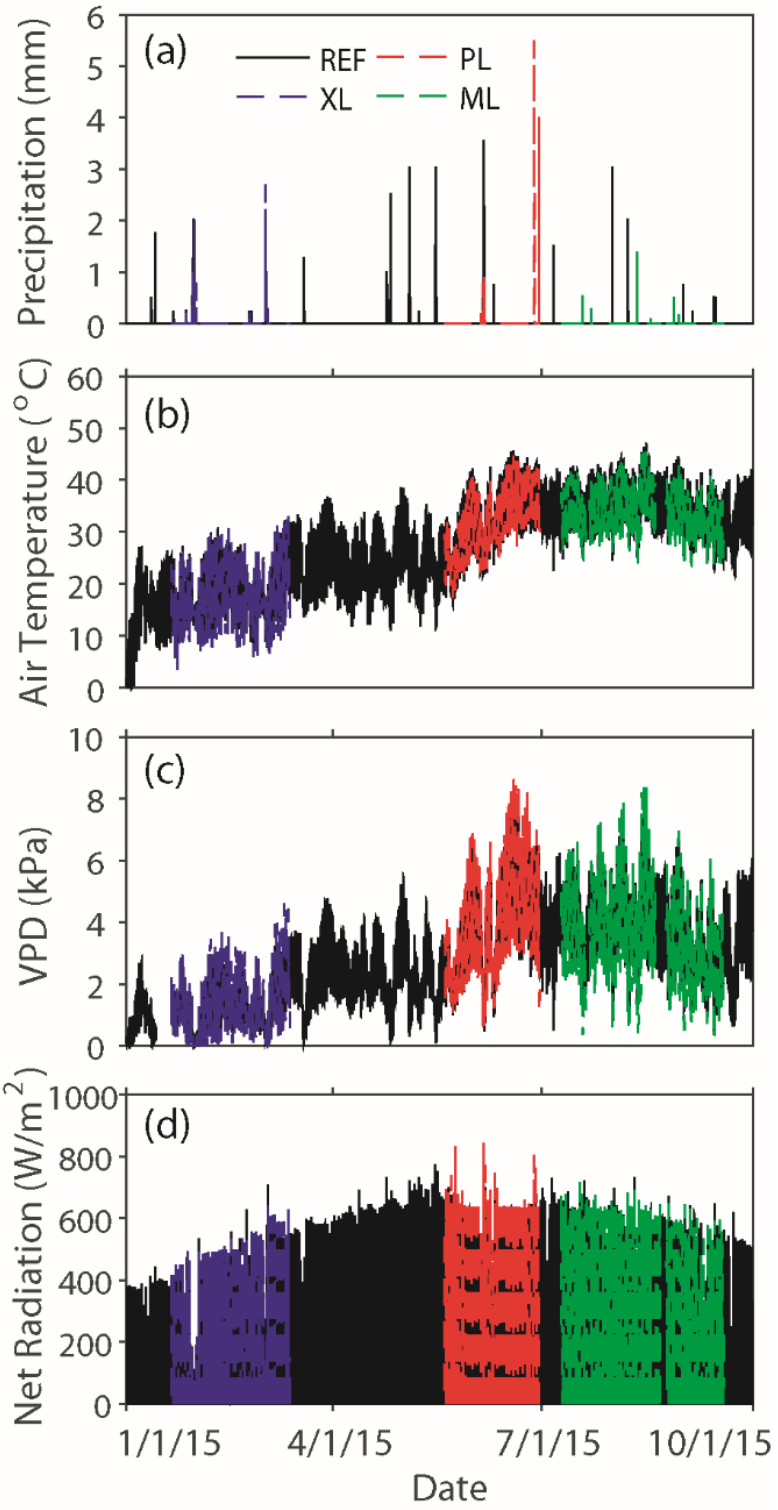

Figure 2.3. Comparison of meteorological measurements during entire study period (1 January to 30 September, 2015) including: (a) precipitation, (b) air temperature, (c) vapor pressure deficit (*VPD*) and (d) net radiation, shown as 30 min averages.

Table 2.5. Time-averaged meteorological conditions including measured (Meas.), reference (Ref. at REF) and long-term average (PHX) for precipitation (*P*), air temperature (*TA*), vapor pressure deficit (*VPD*) and net radiation (Q^*) during each deployment. Long-term average Q^* is not available at PHX.

Site	*P* (mm)			*TA* (ºC)			*VPD* (kPa)			Q^* (W/m^2)		
	Meas.	**Ref.**	**Long-term**	**Meas.**	**Ref.**	**Long-term**	**Meas.**	**Ref.**	**Long-term**	**Meas.**	**Ref.**	**Long-term**
XL	38.6	27.4	43.4	16.8	18	15.6	1.18	1.31	0.84	68.1	61.5	-
PL	15.2	8.6	1.5	32.5	32.6	31.7	4.05	3.93	3.08	152	141	-
ML	5.4	13.7	57.9	33.6	34.5	34	3.46	3.73	2.82	149.2	107	-

compared to the REF site (13.7 mm) due to the spatial variation in timing and magnitude of individual precipitation pulses in Phoenix (Mascaro, 2017). Furthermore, the 2015 NAM season was exceptionally dry at both sites, as compared to the long-term average at PHX (57.9 mm). In general, precipitation at all sites was lower than the long-term (1981-2010) average, except for two localized storm events on 27 and 29 June 2015 measured at the PL site (5.7 mm and 4 mm) during a typically dry period of the early summer.

The temporal variations in *TA, VPD* and Q^* reflect the seasonal progression from winter to summer as well as the effects of storm events which tend to lower all quantities. The winter deployment at XL was characterized by low values of *TA* and *VPD* that are fairly similar to long-term averages and the REF site (Table 2.5). As expected, increases in *TA* and *VPD* occur in the early summer deployment at PL (red lines in Figure 2.3) and reach a maximum during the NAM season at ML (green lines in Figure 2.3). While temporal changes in *TA* and *VPD* are consistent between each site and the reference location, small biases can be noted that are likely related to the urban land cover. For instance, the REF site is 1 to 2 °C warmer than the XL and ML sites, which is consistent with the higher fraction of non-vegetated urban cover (85.2% at REF versus 61.4% and 55.7% at XL and ML, respectively). In addition, smaller differences in *TA* and *VPD* are noted between the PL (93.4% non-vegetated) and REF sites since the non-vegetated urban cover fractions are more similar. Net radiation exhibits more notable differences between each site and the reference location, ranging from 7 to 43 W/m^2 lower Q^* at REF when averaged over each period (Table 2.5), though Pearson's correlation coefficients are high (0.97, 0.98 and 0.95 for XL, PL and ML, respectively). Minimal differences in Q^* are observed between the XL and REF sites during the winter months

when Q^* is relatively low. Larger differences among sites are observed as the year progresses in the early summer and NAM season corresponding with larger Q^* values. The lower Q^* at the REF site is linked to the urban land cover differences within the larger radiometer footprint (29,153 m^2 at REF as compared to 1492 m^2 at mobile EC sites). Notably, the largest differences in Q^* are between the REF and ML sites where the latter is characterized by a much higher fraction of vegetation (14.6% at REF, 50.4% at ML).

Net radiation components and their link to urban land cover

We inspected the outgoing components of shortwave ($K_\uparrow$) and longwave ($L_\uparrow$) radiation to diagnose differences in net radiation among sites. Figure 2.4 presents daily-averaged comparisons of $K_\uparrow$(lines) and $L_\uparrow$ (dots) over each deployment (winter, early summer and NAM). $K_\uparrow$ is generally higher at the REF site, consistent with a lower Q^*, due to a higher albedo (a) over the urban materials in the larger radiometer footprint, as compared to the mobile EC sites. Noon-time albedo measurements ($a = K_\uparrow/K_\downarrow$) averaged over each period yielded values of 0.109 (XL), 0.094 (PL), 0.167 (ML) and 0.169 (REF). Albedo computed from daily-averaged values show similar trends among the sites: 0.115 (XL), 0.100 (PL), 0.171 (ML) and 0.173 (REF), consistent with Offerle *et al*. (2006). Albedo estimates also match well with the dominant urban land cover in each radiometer footprint and with values reported for the REF site by Chow *et al.* (2014a), where residential and more vegetated areas have relatively higher values. While some trends are observed within each season (i.e., increasing $K_\uparrow$ during winter and decreasing $K_\uparrow$ during

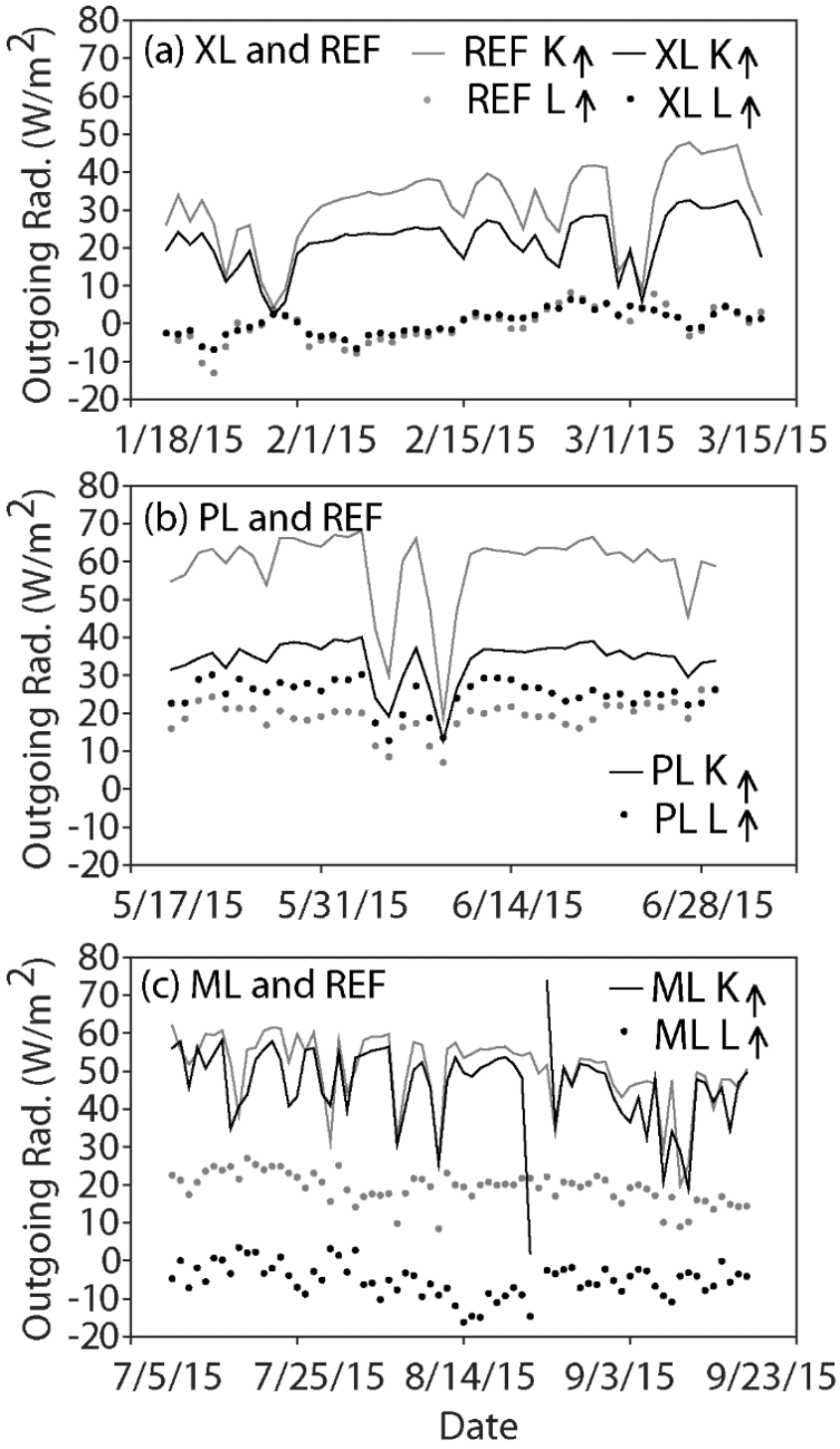

Figure 2.4. Comparison of daily-averaged outgoing shortwave radiation ($K_{\uparrow}$, lines) and outgoing longwave radiation ($L_{\uparrow}$, dots) at: (a) XL and REF sites, (b) PL and REF sites and (c) ML and REF sites. Gray colors correspond to REF site, while black colors represent mobile EC sites.

the NAM), the largest daily changes in $K\uparrow$ correspond to the effects of storm events that moistened urban land covers and changed albedo for short periods of time (1 to 3 days). In addition, larger differences in $K\uparrow$ occur between the PL (dark-colored pavement) and REF (light-colored cement and undeveloped surfaces) sites that have large albedo differences, while the most similar $K\uparrow$ occurs for the ML and REF sites which have the most similar albedo. This is consistent with urban measurements by Santillán-Soto et al. (2015) who reported much lower values of $K\uparrow$ for pavement surfaces as compared to other urban land covers, including cement, grass and clay surfaces. It also indicates that the large differences in Q^* between the ML site and the REF site during the NAM season are not due to variations of shortwave components or albedo differences.

Site comparisons of Q^* are also aided by inspecting $L\uparrow$ and its link to measured shallow soil temperature averaged from 2 and 4 cm depths (T_{soil}) at the XL, ML and REF sites. As with $K\uparrow$, the outgoing longwave radiation exhibits trends within each season (i.e., increasing $L\uparrow$ during winter and decreasing $L\uparrow$ during the NAM) and decreases in response to storm events (Figure 2.4). Similar winter $L\uparrow$ values at the XL and REF sites are consistent with a similar time-averaged T_{soil} during the period (18.3 and 18.7 °C, respectively), whereas large differences in $L\uparrow$ during the NAM season at the ML and REF sites are due to large differences in time-averaged T_{soil} (29.7 and 41.2 °C). As a result, observed differences in Q^* between the ML and REF sites are due primarily to $L\uparrow$ and T_{soil} which are moderated by the urban land cover, specifically the turf grass at ML which cools significantly under the influence of outdoor water use, in particular near the end of summer. Interestingly, the early summer period at PL and REF sites showed

simultaneous differences in both $K\uparrow$ and $L\uparrow$ that were not apparent in the other comparisons. This suggests that pavement surfaces at the PL site are distinct from suburban land cover at the REF site, which consists of undeveloped and impervious surfaces, in terms of both albedo and surface temperatures, despite having similar non-vegetated fractions (97.1% and 85.3%, respectively). While there is a higher $L\uparrow$ at PL, the control of albedo on absorbing radiation is stronger (lower a and $K\uparrow$), thus leading to a higher Q^* as compared to the REF site.

Surface energy balance and partitioning of turbulent fluxes

We inspected the energy balance closure (ε) for each site (Table 2.6), finding that 64-90% of the available energy (Q^*-Q_G) was measured as turbulent fluxes (Q_H+Q_E). Higher residuals ($1-\varepsilon$) at the PL site are reduced slightly when considering Q_G from the REF site as a surrogate quantity, suggesting higher anthropogenic inputs (e.g., Salamanca *et al*., 2014) or other factors such as heat advection or storage (e.g., Bassett *et al*., 2016), as compared to the other sites. It is important to note that only one heat flux plate is installed at each site and does not represent the same spatial scale of the turbulent fluxes. Nevertheless, the estimated energy balance closure is within the range of other EC studies across different ecosystems (e.g., Wilson *et al*., 2002). Figure 2.5 presents the averaged diurnal cycle of Q^*, Q_H, Q_E and Q_G at 30 min intervals for each deployment, with the dashed lines representing simultaneous conditions at the REF site. Q^* follows anticipated seasonal patterns, with increasing noon-time values from winter to early summer followed by a reduction during the NAM. At all mobile EC sites, the diurnal rise and peak of Q^* occurs slightly earlier due to the longitudinal distance to the reference site,

Table 2.6. Energy balance closure using two techniques: (1) Linear fit ($Q_H + Q_E = m(Q^* - Q_G) + b$) with slope ($m$), intercept ($b$) and coefficient of determination (R^2) and (2) ε or the ratio of the sum of ($Q_H + Q_E$) to the sum of ($Q^* - Q_G$). PL site is reported with no Q_G measurement and with a surrogate Q_G from the REF site. Sample size of 30 min intervals provided for each period.

Site	Sample Size	Slope (m)	Intercept (b)	R^2	ε
XL	2299	0.52	26.72	0.91	0.84
PL - no Q_G	1739	0.35	50.58	0.83	0.64
PL - with Q_G	1739	0.44	41.71	0.81	0.69
ML	2873	0.72	33.4	0.89	0.84
REF	12412	0.59	35.17	0.78	0.9

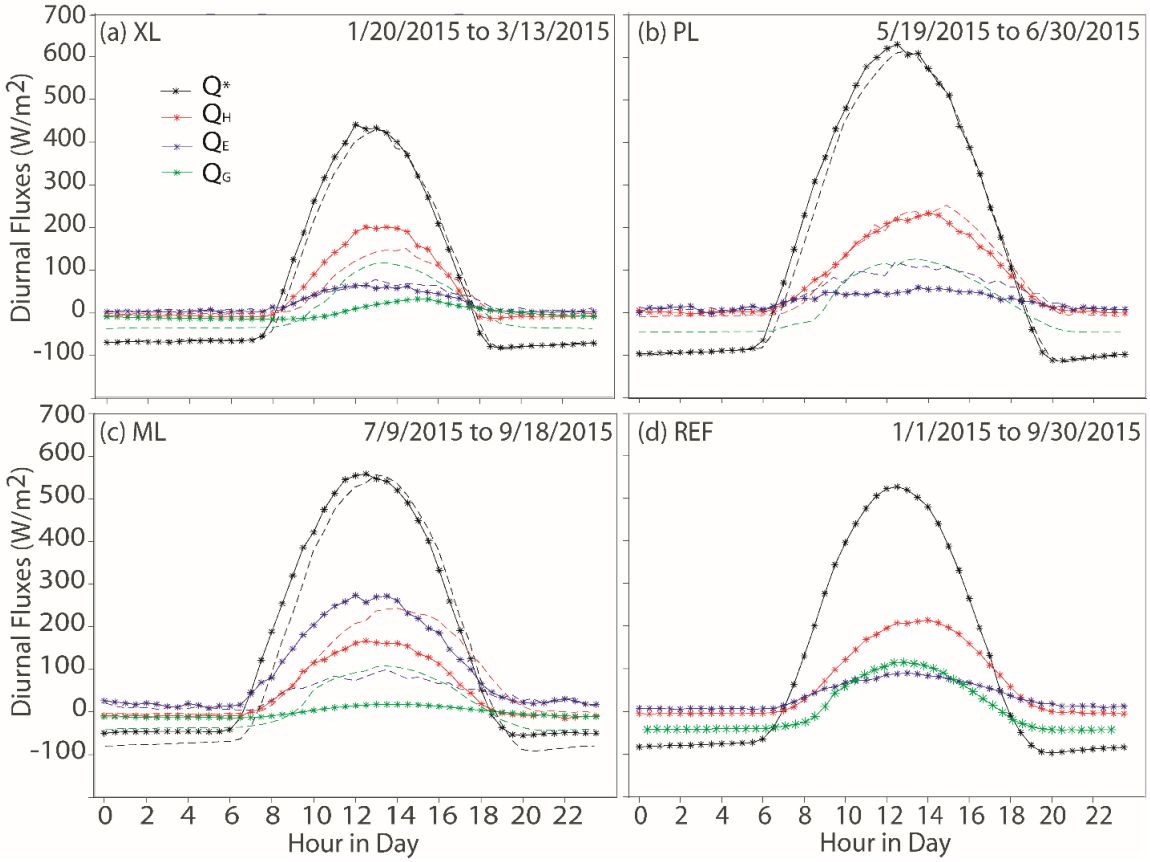

Figure 2.5. Averaged diurnal cycle of surface energy fluxes at 30 min intervals for the: (a) XL, (b) PL, (c) ML and (d) REF sites. For reference, dashed lines in (a-c) represent the corresponding measurements at the REF site. The PL site does not have Q_G measurements.

located 42.8 km west of ML. The partitioning of Q^* is dominated by Q_H at all sites, except ML, with Q_H exhibiting a diurnal peak that is delayed by 1.1 hours with respect to Q^* when averaged over all sites. The smaller Q_G peak exhibits a larger delay, averaging 1.7 hours after Q^* over all sites, though it tends to be earlier and of greater magnitude at REF where the sensor is placed in an unshaded bare area. While the delayed Q_G peaks may be biased by the placement of the ground heat flux sensors, other studies have noted a peak in Q_G after Q^* (e.g., Wang and Mitsuta, 1992; Ma et al., 2005; Templeton et al., 2014). Interestingly, the frequent outdoor water use and mesic landscaping at ML substantially increases Q_E relative to the REF site (i.e., by 174.2 W/m^2 for peak values), leading to a substantial reduction in Q_H and Q_G during the NAM. Comparisons of Q_E at the other sites indicate that winter water input (irrigation and precipitation) has a similar impact at XL and REF. The XL site received more precipitation (11.2 mm) and was regularly irrigated, while the REF site was dependent on outdoor water use in residences and open spaces. In contrast, the early summer has a higher Q_E at the REF site as compared to the PL site, which had higher precipitation but low to negligible outdoor water use.

To further investigate the energy balance components, a daily residual (RES) term was compared across sites (Figure 2.6). The RES term represents an upper limit of ΔQ_S since it includes any underestimations of Q_H and Q_E (i.e., the energy balance closure problem) as well as other terms of the urban energy balance (Q_F, Q_G, ΔQ_S and ΔQ_A).

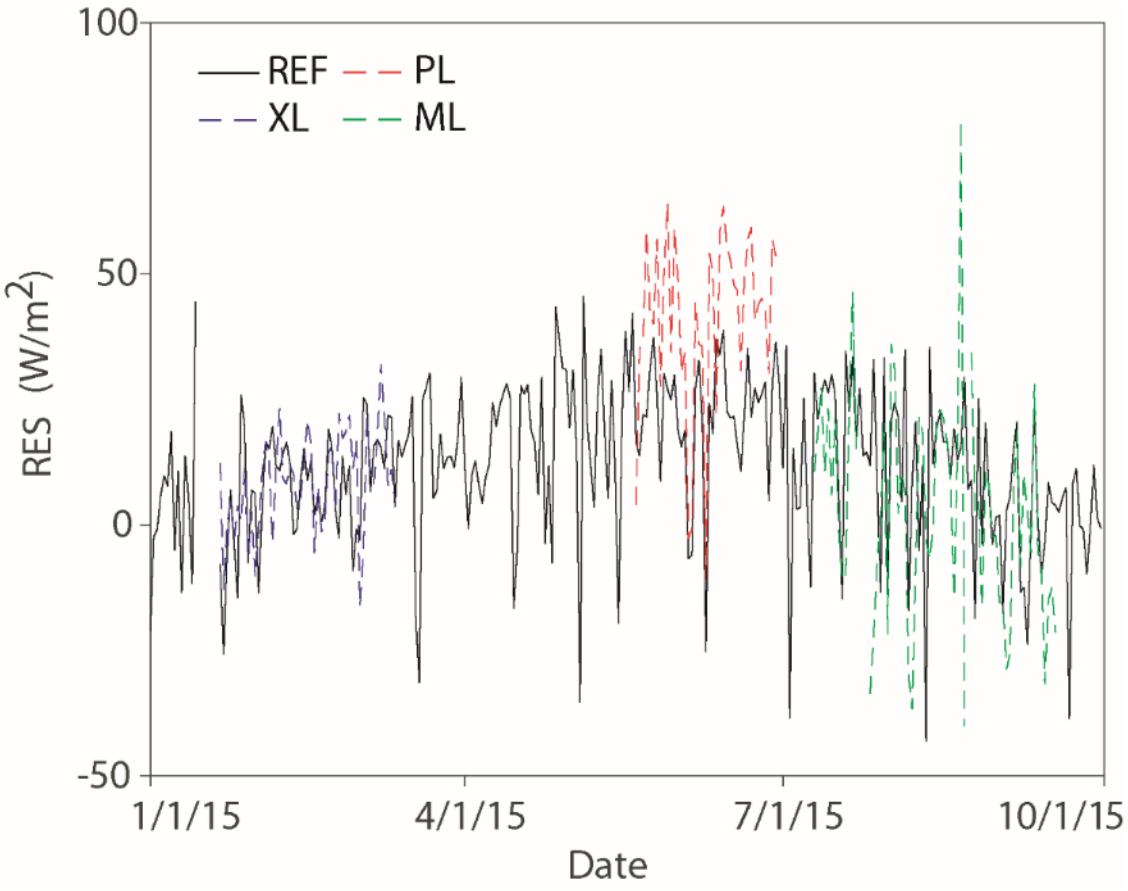

Figure 2.6. Daily residual (RES) computed at the XL, PL, ML and REF sites.

RES increases at the REF site from the winter months into the early summer, but starts to decrease during the NAM until relatively low values are obtained in September. This seasonal variation is consistent with changes in ground heat flux (Q_G) included in ΔQ_S as well as heat storage in other elements of the urban environment (e.g., buildings, trees and impervious surfaces). At the XL site, the RES term matches very well with estimates at the REF site, with similar averages of 8.4 and 7.6 W/m^2 during the deployment period, respectively, indicating a similar amount of ΔQ_S. In contrast, RES at the PL site is twice as large as compared to the REF site (average values of 41.1 and 22.2 W/m^2), suggesting a higher ΔQ_S is likely at the PL site due to the large percentage of pavement cover.

Similarly, the differences in RES between the ML and REF sites are appreciable, with a lower time-averaged RES term at ML as compared to the REF site (4.5 and 8.7 W/m^2), which is linked to the lower capacity for heat storage in frequently irrigated mesic landscaping.

As a measure of turbulent flux partitioning, the evaporative fraction (EF_{noon}) was evaluated at noon-time and averaged for all days of each deployment period. Figure 2.7 shows the daily EF_{noon} as a function of wind direction which can be related to the urban land cover around each site. We also computed averaged daytime (10:00 a.m. to 2:00 p.m.) *EF* (EF_{day}) for each site and then averaged these values over the deployment periods. Consistent with prior analyses, EF_{noon} and EF_{day} vary from low values over the pavement surface (PL) to high values in the turf grass (ML), as shown in Table 2.7 for averaged conditions. In addition, the EF_{noon} at each site is similar for all sampled wind directions, indicating that EF_{noon} is homogeneous with respect to the land cover in each EC footprint. Note that some wind directions were not sampled at the mobile EC sites (e.g., north at ML), but the longer period at the REF site could capture contributions from all directions. This also explains the larger variability in EF_{noon} at the REF site where the observations spanned several seasons, resulting in an average EF_{day} of 0.32, which is higher than at XL and PL (Table 2.7). A comparison across the sites at the daily scale also reveals that ML has a consistently higher EF_{day}, and XL and PL have a lower EF_{day}, with respect to the REF site.

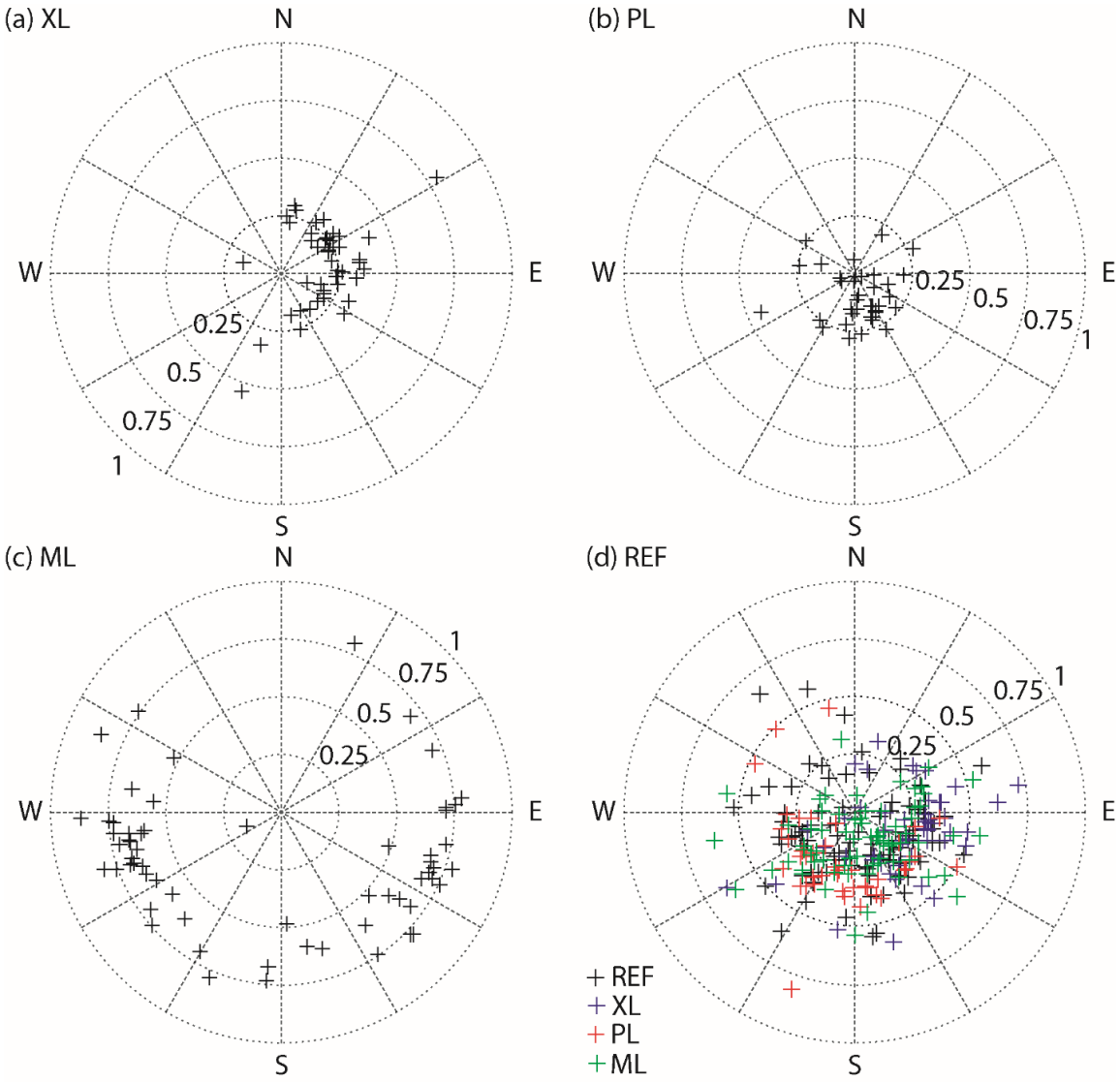

Figure 2.7. Radial diagrams of daily *EF* at noon-time with respect to wind direction for the: (a) XL, (b) PL, (c) ML and (d) REF sites. Color-coding in (d) depicts overlapping observations during deployments at the other sites or intervening periods (black, labeled REF).

Table 2.7. Comparison of normalized surface fluxes averaged over each deployment period, including evaporative fraction determined at noon time (EF_{noon}) and evaporative fraction averaged over day time periods (EF_{day}).

Site	$Q_H/Q_\downarrow$	$Q_E/Q_\downarrow$	$(Q_H+Q_E)/Q_\downarrow$	EF_{noon}	Ef_{day}
XL	0.145	0.097	0.242	0.27	0.27
PL	0.206	0.073	0.279	0.16	0.22
ML	0.132	0.302	0.434	0.61	0.64
REF	0.172	0.108	0.28	0.29	0.32

Average daily turbulent heat flux ratios were evaluated for the duration of the REF period (Figure 2.8). Although Q^* increases substantially as the year progresses, the sensible heat ratio has a small increase, with average values of $Q_H/Q_\downarrow$ = 0.11 (winter), 0.17 (early summer) and 0.21 (NAM). There is higher variability in the latent heat flux ratio due to precipitation, but seasonal averages are nearly identical at $Q_E/Q_\downarrow$ = 0.10 (winter), 0.11 (early summer) and 0.12 (NAM). Similar seasonal values of $Q_E/Q_\downarrow$ above zero in an arid climate are a strong indicator of the contribution of outdoor water use on turbulent heat fluxes. The response of $Q_E/Q_\downarrow$ to storm events at the REF site further shows that water limitations to evapotranspiration are still present. Table 2.7 complements this comparison with $Q_H/Q_\downarrow$, $Q_E/Q_\downarrow$ and $(Q_H+Q_E)/Q_\downarrow$ averaged over each deployment period. Consistent with the prior analysis, the PL site has the lowest $Q_E/Q_\downarrow$ and the highest $Q_H/Q_\downarrow$, indicating that the pavement surface primarily channels available energy into sensible heat flux (low *EF*). The sprinkler irrigated turf grass (ML) exhibits the opposite trends (e.g., lowest $Q_H/Q_\downarrow$ and highest $Q_E/Q_\downarrow$) with a dominance of latent heat flux (high *EF*). In addition, ML had the highest $(Q_H+Q_E)/Q_\downarrow$, indicating that available energy was more efficiently converted into turbulent fluxes, as opposed to Q_G, $K_\uparrow$ or $L_\uparrow$, for the mesic landscaping.

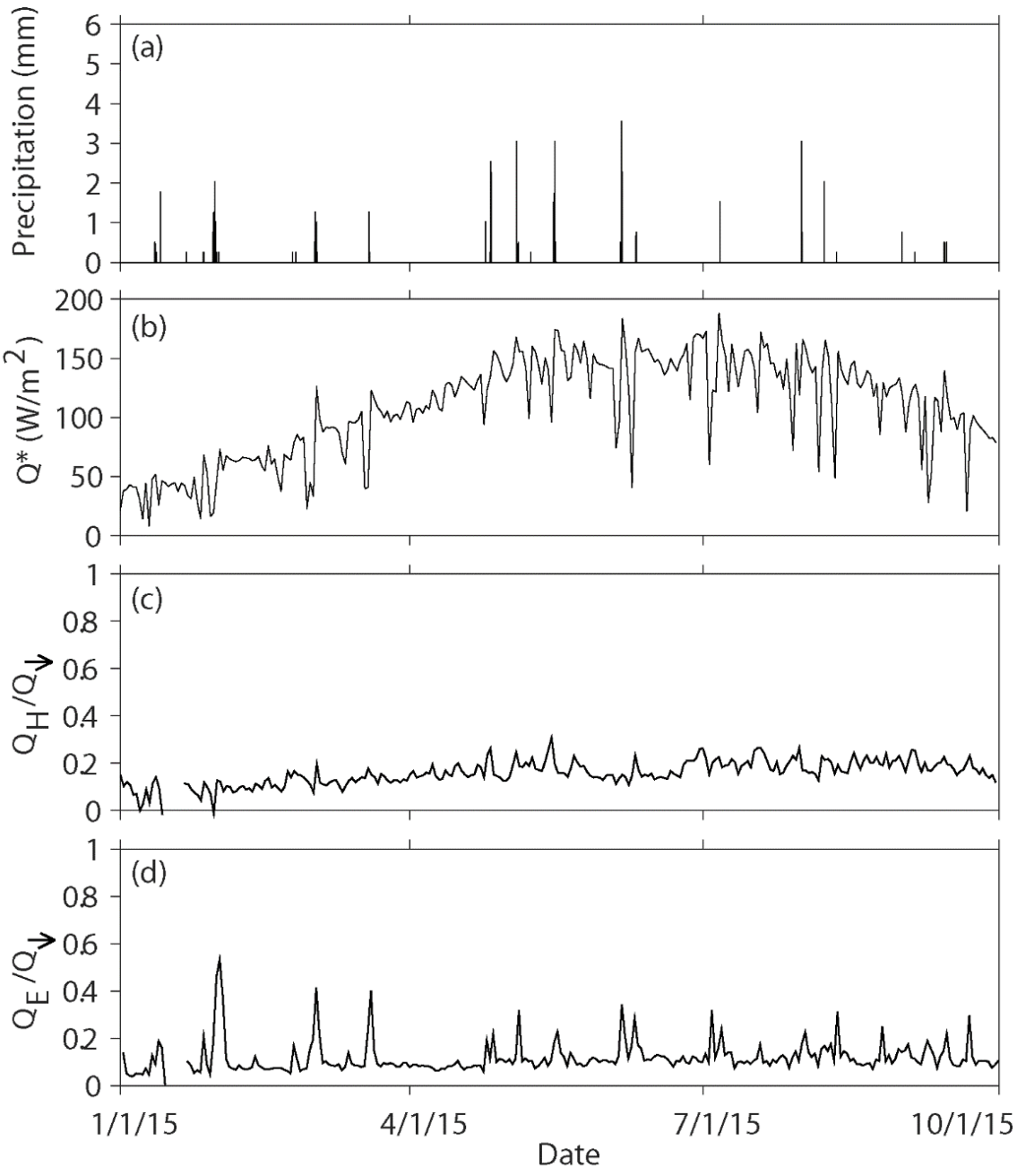

Figure 2.8. Meteorological variables and fluxes at the REF site: (a) precipitation and averaged daily (b) net radiation (Q*) and turbulent heat flux ratios of (c) $Q_H/Q_\downarrow$ and (d) $Q_E/Q_\downarrow$.

Sensitivity of turbulent fluxes to precipitation and outdoor water use

To evaluate the sensitivity of turbulent fluxes to wetness conditions, we classified each day as either 'wet' or 'dry' depending on precipitation occurrence ($P > 0.2$ mm/day). Figure 2.9 presents the variation of $Q_H/Q_{\downarrow}$, $Q_E/Q_{\downarrow}$ and EF for wet and dry days during each season in comparison to REF. Notably, precipitation increases $Q_E/Q_{\downarrow}$ for most sites and seasons, leading to a higher EF, without a considerable change in $Q_H/Q_{\downarrow}$. This suggests urban land covers support similar sensible heat flux under different weather conditions. The increase in latent heat flux, however, is limited to those sites and seasons with low water availability. For instance, the winter $Q_E/Q_{\downarrow}$ and EF increase at both the XL (by 0.10 and 0.18) and REF (by 0.12 and 0.15) sites due to a sequence of storm events, indicating that water-limited conditions exist despite the various types of outdoor water use at the sites. In contrast, differences are observed between the ML and REF sites with respect to their response to storm events during the NAM season. No changes in $Q_E/Q_{\downarrow}$ and EF are noted at ML (by <0.01 and 0.01) between dry and wet days, while increases of $Q_E/Q_{\downarrow}$ and EF occur at the REF site due to the additional water (by 0.04 and 0.06). In effect, more frequent irrigation at the ML site during the NAM season renders the partitioning of turbulent fluxes insensitive to storm events indicating that water is not limiting.

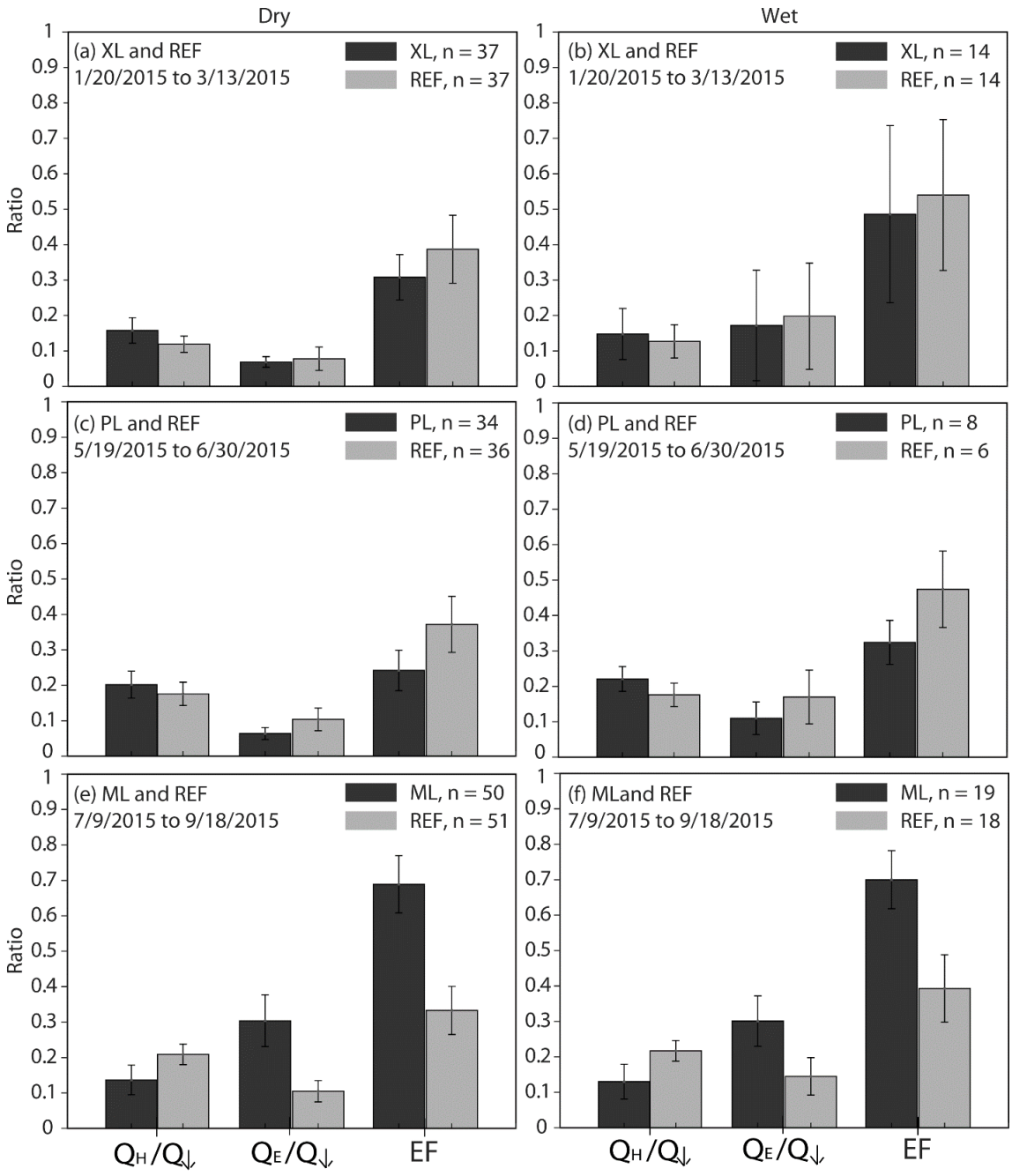

Figure 2.9. Comparison of averaged daily $Q_H/Q_{\downarrow}$, $Q_E/Q_{\downarrow}$ and *EF* for dry (left) and wet (right) days during overlapping periods for the: (a, b) XL and REF site, (c, d) PL and REF site and (e, f) ML and REF site. *n* is the number of days and the error bars represent ±1 standard deviation.

We inspected the SEB and soil moisture responses to storm events to further discern the impact of outdoor water use on the sensitivity to precipitation. Fig. 10 presents storms at the XL and REF sites (2 – 3 March) and the ML and REF sites (18 July and 31 August, respectively). For each case, precipitation, net radiation and shallow soil moisture are shown at 30-min intervals, while the daily *EF* is obtained as the averaged from 10:00 a.m. to 2:00 p.m. Q^* exhibits larger variations in response to cloud cover during the winter (XL and REF sites) since the storm event occurred during daylight hours, whereas the summer storms (ML and REF sites) were both nocturnal in nature, though small variations in Q^* also occur during subsequent days. Shallow soil moisture increases a small amount in response to the storm events across the varying levels of soil water content (i.e., similar wetness at XL and REF, but wetter conditions at ML than REF due to outdoor water use). More importantly, *EF* clearly shows a differential response among sites and seasons. For the water-limited winter conditions, the storm event led to an increase in *EF* at both sites of 0.13 and 0.16 (difference between *EF* prior to and after the storm), or 36% and 80% relative increases, lasting about 1 and 3 days at the REF and XL sites, respectively. Consistent with prior analysis, the REF site exhibited a higher *EF* than the XL site, though the differences are reduced during wet days. The more sensitive *EF* response at XL is likely due to its higher percentage (68.3%) of land cover that can absorb precipitation (e.g., grass, trees and undeveloped land) as compared to REF (51.5%). In contrast, the summer storm events lead to an increase in *EF* of 0.26 at the REF site, but a small decrease of 0.01 in *EF* at the ML site, or relative differences of 124% and -2%, respectively. This occurs despite the higher percentage at ML (78.9%) of permeable urban land cover in the EC footprint and is closely linked to

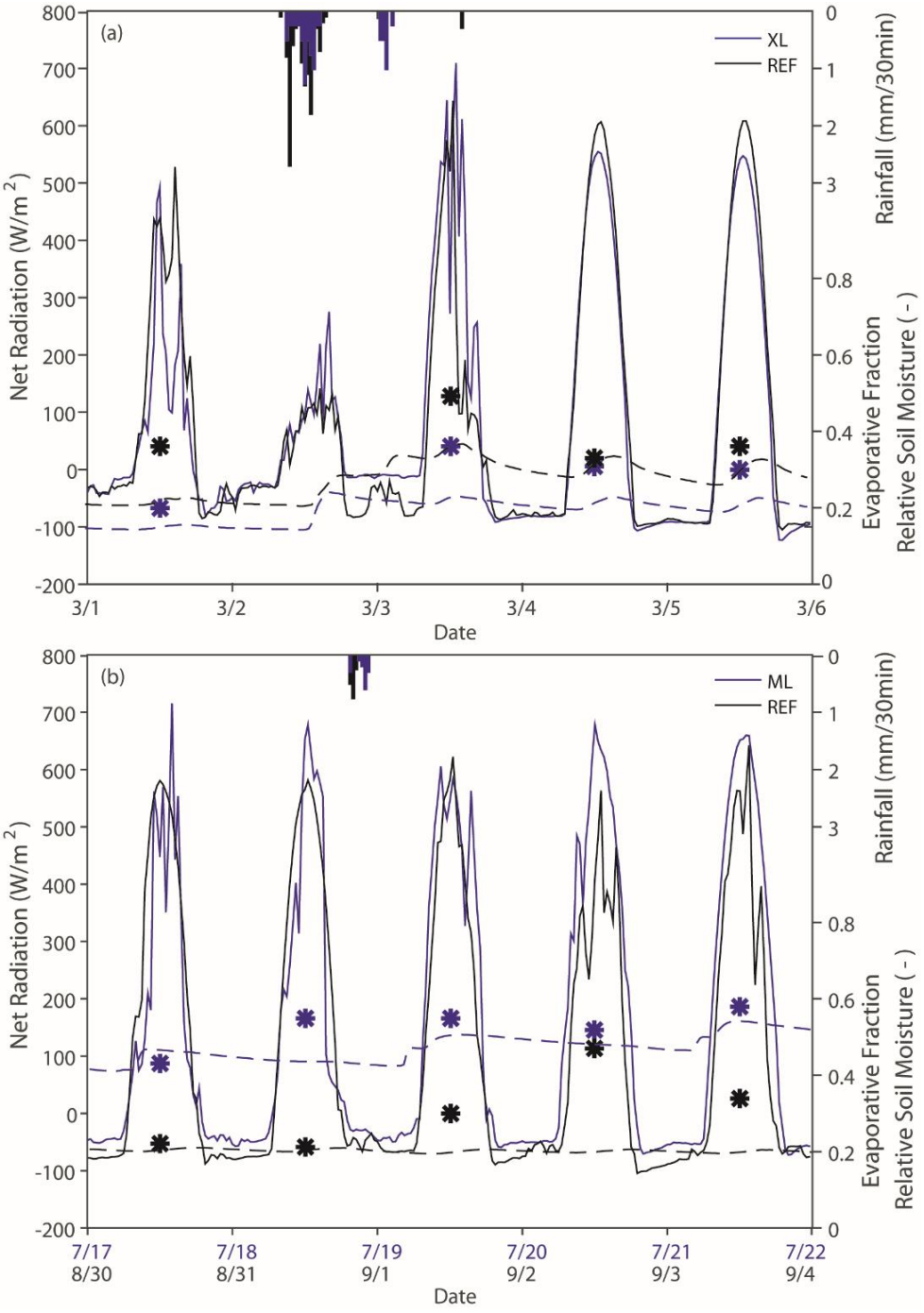

Figure 2.10. Comparison of precipitation (bars), net radiation (solid lines), shallow relative soil moisture (with an assumed porosity value of 0.4 strictly for presentation purposes) at 5 cm depth (dashed lines) and noon-time evaporative fraction (symbol) between: (a) XL and REF sites during the winter deployment and (b) ML and REF sites during the NAM season. Note that two similar events of 1.5 mm precipitation accumulation (18 July at XL and 31 August at REF) are compared in (b) since simultaneous localized storms did not occur during the NAM season.

responses to storm events and to outdoor water use in its larger footprint.
the high soil moisture conditions. Thus, the frequent outdoor water use at ML sustains a high *EF* that is insensitive to additional water, while the more water-limited conditions at REF allow for both responses to storm events and to outdoor water use in its larger footprint. Note that while the large increase in *EF* at REF on 2 September cannot be attributed to precipitation, the net radiation measurements suggest the occurrence of cloud cover. Thus, the large increase in *EF* is likely due to a delayed reaction to nighttime precipitation on 31 August or possibly to some other outdoor water use increase at the REF site (e.g., additional irrigation input).

SUMMARY AND CONCLUSIONS

While model applications have indicated that the built environment impacts energy and water exchanges (e.g., Song and Wang, 2015; Wang et al., 2016), few studies have directly observed the effects of different urban land cover types on the surface energy balance or the partitioning of turbulent fluxes. In this study, we conducted meteorological flux measurements using the eddy covariance technique to obtain a detailed quantification of SEB processes and relate them to the urban land cover distributions within the sampled footprints of three short-term deployments and a stationary reference site in Phoenix. Comparisons of standard weather variables, meteorological fluxes and normalized SEB quantities between the mobile and reference sites were carried out to account for the effect of time-varying (seasonal) conditions during the short-term deployments. A particular focus of the analysis was placed on the comparative role of precipitation events and outdoor water use on modifying the

turbulent flux partitioning given the strong natural water limitations in the arid urban area. Results from the observational comparisons across sites, seasons and urban land cover types indicated:

(1) Meteorological conditions were similar between the sites, but had small biases attributed to variations in vegetated land cover, with a higher *TA* at the REF site as compared to the XL and ML sites. Despite these similarities, large biases were noted in the time-averaged Q^*, with the REF site having values of 7 to 43 W/m^2 less than the other sites, attributed to the larger radiometer footprint and its differences in impervious surfaces and undeveloped land cover.

(2) Individual radiation components and ancillary measurements provided insight into the large differences in Q^* among sites by isolating the effects of albedo on $K_{\uparrow}$ and of shallow soil temperature on $L_{\uparrow}$. Lower Q^* at the REF site was found to be either due to a higher albedo (relative to xeric landscaping at XL), a higher soil temperature (relative to mesic landscaping at ML) or a combination of both factors (relative to the parking lot at PL).

(3) The surface energy balance revealed sharp differences in the partitioning between sensible and latent heat flux among the sites based upon normalized quantities. For instance, *EF* was found to be much larger in the irrigated turf grass at ML, where a higher $(Q_H+Q_E)/Q_{\downarrow}$ was also measured. Sensible heat flux, on the other hand, was the dominant flux and exhibited lower variations among the other sites, suggesting less frequent or extensive outdoor water use.

(4) The sensitivity of SEB processes to precipitation events varied considerably among the sites in accordance with the soil moisture conditions established through

outdoor water use. While different urban land covers support similar sensible heat flux under different weather conditions, the latent heat flux varies significantly at those locations that are water-limited, whereas frequent sprinkler irrigation at ML renders the *EF* insensitive to additional water input.

Based upon these comparisons, key differences in the surface energy balance among the sites can be attributed to the urban land cover contained in the measurement footprints, including the frequency and amount of outdoor water use. While the mobile deployments only sampled individual seasons, comparisons to the reference site provided an opportunity to draw the important conclusions listed above. Nevertheless, it would be desirable to conduct cross-site comparisons over a full year and to improve the correspondence in the footprint dimensions among deployments. Longer comparisons, for instance, could be used to evaluate if frequent or high outdoor water use effectively decouples turbulent flux partitioning from precipitation during other seasons. Furthermore, additional studies are needed to verify if the application of urban irrigation can be an effective proxy for quantifying the spatiotemporal variability of the surface energy balance in arid urban areas. A fruitful avenue would be the validation of a numerical model that simulates urban energy and water fluxes (e.g., Grimmond and Oke, 1991; Järvi et al., 2011; Wang et al., 2013) and its subsequent application to quantify the link between urban irrigation and SEB processes. Based on this approach, considerable improvements could be made in estimating the spatiotemporal variability of the urban surface energy budget in desert cities.

CHAPTER 3

DEGREE OF WOODY PLANT ENCROACHMENT INFLUENCES THE SEASONALITY OF WATER, ENERGY, AND CARBON DIOXIDE EXCHANGES

INTRODUCTION

Arid and semiarid ecosystems, or drylands, are of global importance as grasslands, shrublands and savannas occupy nearly 50% of the Earth's land surface (Bailey, 1996). Woody plant encroachment in drylands has been documented in North America (e.g., Archer et al., 2001; Van Auken, 2000; Huxman et al., 2005; Browning et al., 2008), Australia (e.g., Burrows et al., 1990; Fensham, 1998), southern Africa (e.g., Roques et al., 2001) and South America (e.g., Silva et al., 2001). Encroachment is a critical issue for rangelands, particularly where the primary land use is livestock grazing (Browning and Archer, 2011; Archer and Predick, 2014). The management of rangelands has historically focused on increasing forage availability by reducing woody plants (i.e., brush management) to maximize livestock production (Archer, 2010). However, woody plant encroachment in arid and semiarid ecosystems does not necessarily equate to degradation or desertification (Eldridge et al., 2011). Woody plants introduce and influence different ecosystem services and biodiversity within rangelands, and the effects of brush management on these services are not well understood to date (Archer and Predick, 2014).

Woody plant encroachment has transformed arid and semiarid landscapes over the past century, affecting ecosystem services and hydrologic processes (e.g., Breshears et al., 1998; Kurc and Small, 2004; Huxman et al., 2005; Pierini et al., 2014). For instance,

shrub encroachment may promote primary production, nutrient cycling, carbon sequestration and accumulation of soil organic matter, but reduce groundwater recharge (Archer, 2010; Archer et al., 2001). Since landscapes undergoing woody plant encroachment represent ~30% of global net primary productivity (Field et al., 1998), it is vital to quantify the spatial and temporal exchanges of water, energy and carbon with the atmosphere in these ecosystems (e.g., Breshears et al., 1998; Abrahams et al., 2003; Gutiérrez-Jurado et al., 2006; Mueller et al., 2007; Van Auken, 2009; Eldridge et al., 2011; Templeton et al., 2014). When woody plant encroachment occurs in the form of trees into desert grasslands, a savanna ecosystem results, with decreased grass cover and increased above- and below-ground carbon storage (Eldridge et al, 2011). Woody savannas are typically characterized by low annual and highly variable precipitation with soil water resources playing an important role in tree-grass competition (e.g., Scholes and Archer, 1997; Browning et al., 2008; Archer, 2010), among other factors including grazing activity, rangeland management and fire disturbances (Van Auken, 2000; Van Auken, 2009; Eldridge et al., 2011).

While water, energy and carbon fluxes have been quantified in woody savannas (e.g., Williams and Albertson, 2004; Scott et al., 2009; Pierini et al., 2014), the role of the spatial heterogeneity in vegetation, such as the relative amount of tree and grass cover, has not been identified due to difficulties inherent in observational methods. The eddy covariance (EC) method is widely used to quantify land-atmosphere exchanges over homogeneous landscapes (e.g., Baldocchi et al., 1998). However, EC measurements over heterogeneous ecosystems need to be carefully inspected to link the measured meteorological fluxes to spatial distribution of land surface states and vegetation cover

(Detto et al., 2006; Alfieri and Blanken, 2012; Anderson and Vivoni, 2016). This is particularly important in encroached landscapes where the presence of woody plants can alter the distribution of soil properties, accumulate water and nutrients under canopies and change the resource flow between woody plants and interspace areas that can be populated by grass species or bare soil (D'Odorico et al., 2012). The spatial heterogeneity of woody savannas is further compounded by the temporal dynamics of tree and grass cover in response to establishment legacies and brush management efforts (Archer and Predick, 2014).

In this study, I compare long-term meteorological flux measurements from two eddy covariance towers (ECT) in a woody plant encroached savanna of the Santa Rita Experimental Range (SRER) in southern Arizona. The two towers are relatively close in proximity (~1.5 km), however their landscapes present different amounts of grass cover and woody plants, specifically *Prosopis velutina* Woot., or velvet mesquite trees (McClaran, 2003; Polyakov et al., 2010). These differences are due to legacies of prior brush management and variations in the underlying soil conditions that are linked to topographic position. The purpose of this comparison is to quantify and explain differences in measured water, energy and carbon fluxes in relation to observed variations in the spatial pattern of vegetation species. I utilize high-resolution aerial imagery and landscape characterizations to capture differences in elevation, soil and vegetation type, including an analysis of the effect of measured wind directions at each ECT. In so doing, we attempt to answer the following questions: "How does spatial heterogeneity within a woody savanna affect water, energy and carbon exchanges?" and "Are there detectable differences with wind direction that can be attributed to variation of

vegetation in the sampled areas?" These are important considerations for assessing the representativeness of EC measurements in arid and semiarid ecosystems. Furthermore, to my knowledge, this is the first attempt at systematically comparing an AmeriFlux site (ARS ECT) to a nearby installation (ASU ECT) over a long period.

SITE DESCRIPTIONS

The two ECT sites are located in the SRER, which lies in the Sonoran Desert, about 45 km south of Tucson, Arizona, on alluvial fans emanating from the Santa Rita Mountains (Figure 3.1). Established in 1903, SRER is the oldest continuously-operating rangeland research facility in the United States (McClaran, 2003). Its rich history provides an opportunity to understand vegetation changes and disturbances over the past century. Recent efforts have focused on quantifying water, energy and carbon fluxes in the woody savanna: the Agricultural Research Service ECT (ARS ECT, 31.82 °N and 110.86 °W, 1116 m) established in 2004 (Scott et al., 2009) and the Arizona State University ECT (ASU ECT, 31.82 °N and 110.85 °W, 1168 m) installed in May 2011 (Pierini et al., 2014). In this study, meteorological flux measurements collected from the ECTs are directly compared for an overlapping period from July 1, 2011 to June 15, 2016, prior to an aerial herbicide application to the mesquite trees at the ASU ECT site on June 19, 2016 (Naito et al., 2017). The primary land use in the study area is cattle grazing and since both ECT sites are located within the same pasture (pasture 2N), these are exposed to an identical grazing schedule of once per year for 1 to 3 months (Santa Rita Experimental Range Digital Database).

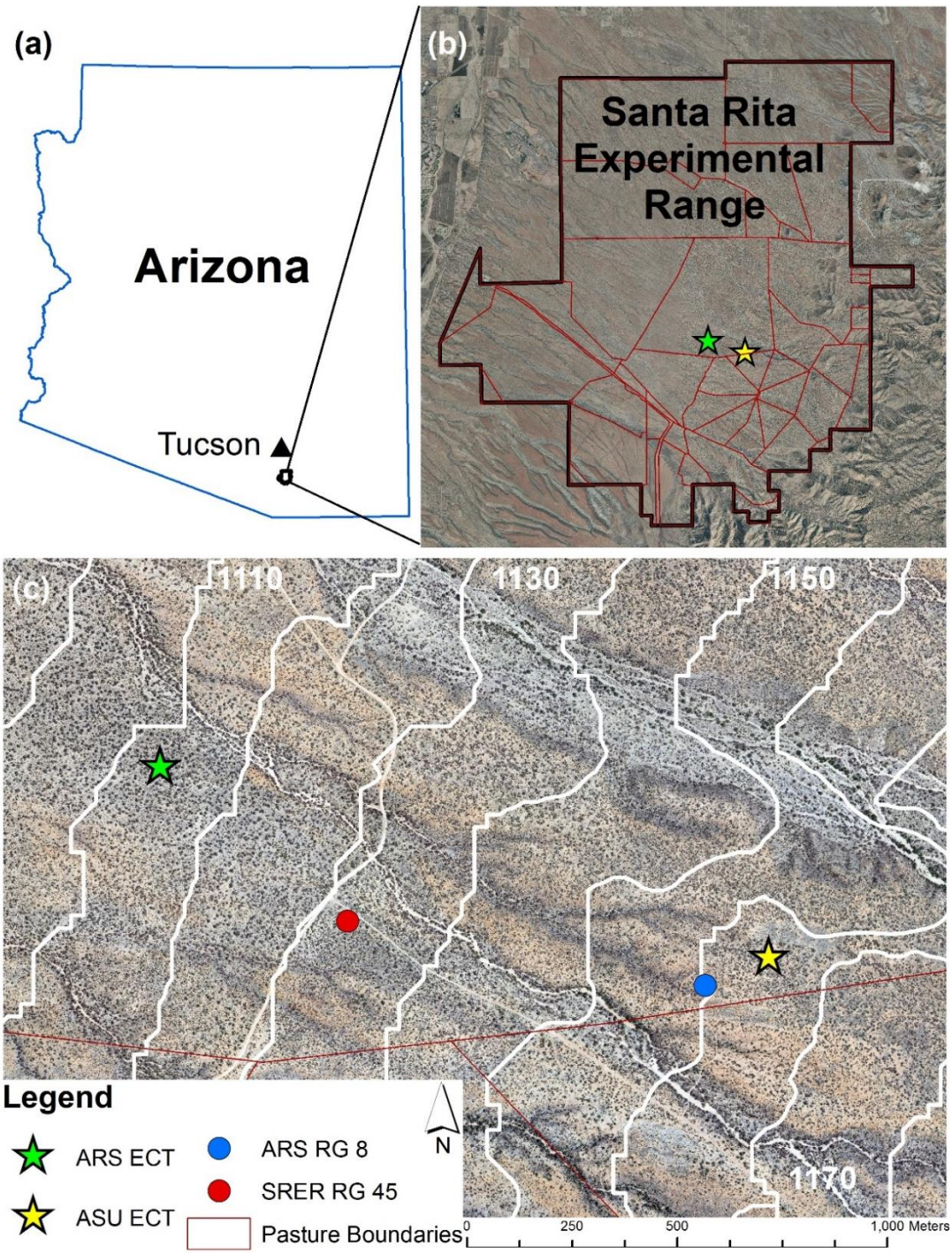

Figure 3.1. (a) Location of the study sites, south of Tucson, Arizona, and (b) in the Santa Rita Experimental Range, with pasture boundaries (red lines). The 1 m aerial photographs in (b) are from the Arizona Regional Image Archive. (c) Instrument locations, including the SRER RG 45 and ARS RG 8 rain gauges. The 0.30 m aerial photographs in (c) are from a LiDAR flight taken in April 2011, which also provided the elevation contour lines (m).

Although the sites are close, their disturbance histories differ since the 1970s: the area where the ASU ECT is located underwent mesquite treatment in 1974 via the basal application of diesel oil, with reapplication as needed (Martin and Morton, 1993) and was affected by a fire on June 2, 1994 that burned 4000 ha in SRER (Huang et al., 2007). In contrast, the woody savanna in the location of the ARS ECT has remained undisturbed by brush management or fire.

A detailed soil survey conducted at SRER by the Natural Resources Conservation Service (Breckenfeld and Robinett, 2003) indicate the two sites lie on different soil types (Figure 3.2a). Soils at ARS ECT are in the Combate-Diaspar complex (CdB), characterized by excellent drainage and sandy loam textures on alluvial channel deposits, while ASU ECT is located in the Sasabe-Baboquivari complex (SbC) with less well-drained sandy clay and sandy clay loam subsoils that are characteristic of an alluvial fan terrace. Soil differences are consistent with the topographic position of each site (i.e., alluvial channel versus fan terrace) that explain the small elevation difference (52 m). In addition, the soil and landform characteristics underlie spatial variations in vegetation cover. Current vegetation at both sites consists of velvet mesquite trees, grass species [nonnative Lehmann lovegrass (*Eragrostis lehmanniana* Nees), black grama (*Bouteloua eriopoda* Torr.), Arizona cottontop (*Digitaria californica* Benth) and Santa Rita threeawn (*Aristida glabrata* Vasey)], shrubs [hackberry (*Celtis pallida* Torr.) and catclaw acacia (*Acacia greggii* Gray)], and various succulents [cholla (*Opuntia spinisior* Englem), prickly pear (*Opuntia engelmannii* Salm-Dyck) and fishhook barrel (*Ferocactus wislizeni* Britt. & Rose)]. High-resolution imagery acquired during a Light Detection And Ranging

(LiDAR) flight (Pima Association of Governments, 2011; Figure 3.1c) show that alluvial deposits have more mesquite trees that are distributed in a uniform fashion around the ARS ECT, while the fan terrace has sparser tree cover with a higher spatial variability around the ASU ECT. Climate of SRER is semiarid (Koppen classification BWh) with a bimodal precipitation regime and average annual temperatures of 19 °C. April through June are relatively warm, with average temperatures of 23 °C, while temperatures slightly increase during the summer period (July through September) to 26 °C, typical of the Sonoran Desert. Summer rainfall (July to September) occurs during the North American monsoon (NAM) (Adams and Comrie, 1997) with lower precipitation amounts during the winter months (December to March). Rainfall measurements at four sites (Figure 3.1c) include long-term monthly data (1936 to 2016) from SRER RG 45, a weighing rain gauge (1976 to 2016) at ARS RG8 and tipping bucket rain gauges at the ASU ECT and ARS ECT sites. Based on the ARS RG8 site, Polyakov et al. (2010) report a mean annual precipitation of 458 mm/yr with about 54% occurring during the NAM. Small differences across the rain gauges are anticipated due to the varying designs and the localized nature of storm events, in particular during the summer season (Goodrich et al., 2008). With the bimodal precipitation in this system, there are generally two green up periods. The first occurs during the spring time, when mesquite trees produce leaves (late March to late April), drawing water from deeper soil depths (Cable, 1977). The second is larger and occurs during the monsoon (July), where perennial grasses increase canopy cover with a smaller increase in mesquite cover (Cable, 1975).

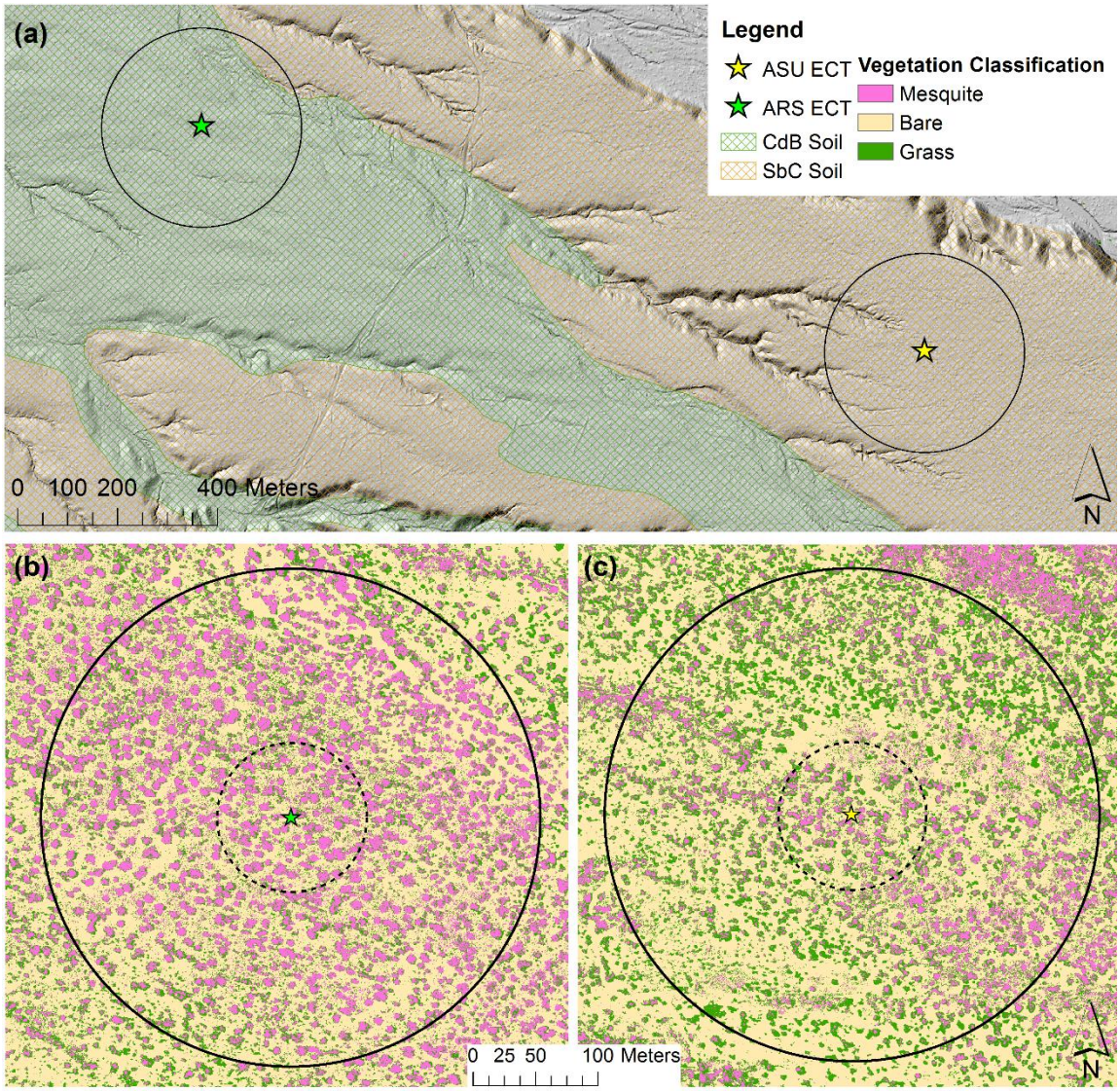

Figure 3.2. (a) Soil types at ARS and ASU ECT sites on a hillshaded relief map, with 200 m radius circles. Vegetation classification from a 0.30 m orthoimage product from a LiDAR flight in April 2011 at (b) ARS ECT site and (c) ASU ECT site, with the black solid circles indicating a 200 m radius and the black dashed lines indicating a 60 m radius centered at each tower.

METHODS

Environmental measurements and data processing

While the two eddy covariance sites are managed by independent groups (ARS and ASU), a long-term collaboration has ensured similar sampling protocols, data processing and instrument cross-calibration efforts. The ARS ECT site is part of the AmeriFlux network (http://dx.doi.org/10.17190/AMF/1246104) as described by Scott et al. (2009; 2015). The ASU ECT site includes the instrumentation listed in Table 3.1 and has been documented by Pierini et al. (2014), Schreiner-McGraw et al. (2016) and Anderson and Vivoni (2016). ARS ECT sampled EC data at 10 Hz frequency and at ASU ECT, EC data were sampled at a 20 Hz frequency. EC instruments at ARS ECT are mounted at 8 m and an orientation of 225°, similar to ASU ECT where EC instruments are mounted at 7 m, oriented at 240°. Processing of the raw flux measurements included removal of time periods when: (1) rainfall occurred, (2) wind direction could be obstructed by the tower, (3) friction velocity was less than 0.15 m/s, and (4) for outliers greater than 3 standard deviations. Standard corrections were also applied using protocols described in Scott et al. (2009) and a detailed comparison of the processing steps was conducted. This included processing the ASU ECT data with the same gap-filling procedure for ARS ECT (Scott et al., 2009) to obtain net ecosystem exchange (NEE) and evapotranspiration (ET). At both sites, NEE is partitioned into ecosystem respiration (R_{eco}) and gross ecosystem production (GEP) following Reichstein et al. (2005) such that $NEE = R_{eco} - GEP$, with $NEE < 0$ indicating CO_2 uptake by the ecosystem.

Table 3.1. Instrumentation at the ASU ECT site.

Instrument/model (Quantity)	Manufacturer	Variable measured	Height or Depths (m)
Above ground level			
3D sonic anemometer/CSAT3 (1)	Campbell Scientific	Three-dimensional wind velocities, virtual sonic temperature	7.0
Infrared gas analyzer/LI-7500A (1)	LI-COR Biosciences	Water vapor and carbon dioxide concentrations	7.0
Temperature and relative humidity sensor/HMP45C (1)	Vaisala	Air temperature and relative humidity	1.5
Two component net radiometer/CNR2 (1)	Kipp & Zonen	Net shortwave and longwave radiation	5.0
Pyranometer/CMP3 (1)	Kipp & Zonen	Incoming solar radiation	5.0
Quantum sensor/SQ-110 (2)	Apogee Instruments	Photosynthetically active radiation	9.0
Pyranometer/SP-110 (2)	Apogee Instruments	Total shortwave radiation	9.0
Barometer/CS100 (1)	Setra	Barometric pressure	
Near ground level			
Rain gauge/TE525MM (1)	Texas Electronics	Precipitation	1.1
Infrared radiometer/SI-111 (1)	Apogee Instruments	Surface temperature	1.4
Below ground level			
Soil heat flux plate/HFP01SC (2)	Hukseflux	Ground heat flux	0.05
Soil averaging thermocouple/TCAV (4)	Campbell Scientific	Soil temperature	0.02, 0.04
Water content reflectometer/CS616 (6)	Campbell Scientific	Soil volumetric water content	0.05, 0.15, 0.30, 0.50, 0.75, 1.0

Remote sensing and vegetation transects

The LiDAR flight provided a 1 m digital elevation model (DEM), a 1 m canopy height model, and a 0.3 m color orthoimage for both EC sites. The image was classified based on the Red, Green and Blue (RGB) signatures using a maximum likelihood method in ArcGIS 10.4 (Image Classification Tool) into three general types: mesquite, grass, or bare (soil). To guide the classification, results were compared with vegetation transects at the ARS ECT site conducted in June and July, 2014, and subsequently verified at the ASU ECT site using mesquite cover data from November 2015 (no grass or bare cover available at ASU ECT). Vegetation transects at the two sites followed similar procedures, where cover measurements were taken from line transects extending 60 m from each tower along the eight cardinal directions. Based on the image analysis, the circular (60 m) regions around each tower are composed of: (1) 34% mesquite, 17% grass and 49% bare (as compared to 35%, 15% and 50% from line transects at ARS ECT), and (2) 20% mesquite, 23% grass and 57% bare (as compared to 21% mesquite cover at ASU ECT).

To quantify vegetation response and seasonality at each site, Moderate resolution Imaging Spectroradiometer (MODIS) products, specifically enhanced vegetation index (EVI, Huete et al., 2002) and albedo, were used. Products obtained were 16 day composites of EVI (MOD13Q1, 250 m spatial resolution) and 8 day composites of albedo (MYD43A, 500 m spatial resolution) from June 26, 2011 to June 17, 2016 (ORNL DAAC, 2008).

Comparison approaches and statistical metrics

EC observations were compared at 30-min, daily, monthly and annual resolutions for meteorological variables and fluxes during periods of available data at both sites. Comparisons at 30-min and daily resolutions were performed using the correlation coefficient (CC), standard error of estimates (SEE), root mean squared error (RMSE) and bias (B). CC was obtained as:

$$CC = \frac{\sum_{i=1}^{N}(ASU_i - \overline{ASU})(ARS_i - \overline{ARS})}{\left[\sum_{i=1}^{N}(ASU_i - \overline{ASU}\right]^{0.5}\left[\sum_{i=1}^{N}(ARS_i - \overline{ARS}\right]^{0.5}} \quad (3.1)$$

where the overbar denotes a temporal mean for the ASU and ARS ECT sites during N time periods. SEE measures the deviations between the datasets from the 1:1 line (perfect fit), while RMSE measures the differences relative to the linear regression between the two series as:

$$SEE = \sqrt{\frac{\sum_{i=1}^{N}(ASU_i - ARS_i)^2}{N}} \quad \text{and} \quad (3.2)$$

$$RMSE = \sqrt{\frac{\sum_{i=1}^{N}(ASU_i - ASU_i')^2}{N}} \quad (3.3)$$

where ASU_i' is the predicted value based on a linear regression between the ASU and ARS time series. Bias (B) reveals the mean temporal differences between the two sites as:

$$B = \frac{\overline{ARS}}{\overline{ASU}} \quad (3.4)$$

Given the differences noted in the amount and distribution of mesquite trees between the two ECT sites, we conducted analyses to quantify the variation of meteorological fluxes as a function of the wind direction for the time period of the measurement. For this purpose, wind directions at each ECT were classified into 10 degree bins (36 total bins). Comparisons were then carried out of water, energy and carbon flux differences (ARS minus ASU) for each wind direction to detect whether a relationship was obtained with the vegetation cover. Values were aggregated for the entire sampling period as well as for specific phenological periods.

RESULTS AND DISCUSSION

Vegetation characteristics and patterns

Figure 3.2 presents the vegetation classification around each ECT tower, while Table 3.2 summarizes the cover percentage (mesquite, grass and bare) over 60 and 200 m radius areas. Clear differences are noted in the distribution of mesquite trees, with a higher cover and more homogeneous distribution around the ARS ECT site. In addition, there are more trees at ARS ECT for at all heights, in particular for heights greater than 1 m (Table 3.3). We hypothesize that these differences are due to variations in the soil and landform conditions discussed previously as well as differences in site history, where the ASU ECT site has experienced more disturbances (fire and brush management) affecting mesquite trees. Bare (soil) cover is similar among the classifications. It is expected that bare soil at both sites fills in with perennial grasses during the NAM and annuals, depending on winter precipitation. In particular, a large bare patch to the north of the ASU ECT generally has grasses after the wet season (Anderson and Vivoni, 2016), but

are not detected in the classified image from the dry season (April). Seasonal transitions between grass and bare cover and lower numbers of mesquite trees contribute to an

Table 3.2. Vegetation cover percentage [mesquite, grass and bare (soil)] for 60 and 200 m radius circles around ASU and ARS ECT sites.

	ARS ECT	ASU ECT	ARS ECT	ASU ECT
	60 m	60 m	200 m	200 m
Mesquite	34	20	30	15
Grass	17	23	18	25
Bare (Soil)	49	57	52	60

increased heterogeneity of vegetation around the ASU ECT.

To further quantify the spatial variability around each ECT site, vegetation cover for each classification was quantified as a function of direction based on 10 degree bins (36 bins) using 0° to specify north (Figure 3.3). ARS ECT has a higher mesquite cover in all directions except for the range of 140 to 150° (S-SE). Furthermore, there is less variability in mesquite coverage with direction at ARS ECT (CV = 15.2%, where CV is the coefficient of variation of mesquite cover in a radial direction) as compared to ASU ECT (CV = 40.2%), indicating more homogeneous conditions. The lower amounts of mesquite cover at ASU ECT lead to higher grass and bare soil cover along most directions (one exception of bare cover for 140 to 150° bin). Nevertheless, the variation of grass and bare soil cover with direction is similar for both sites, with nearly identical CV values (Grass CV of 12.4% and 12.9% and Bare CV of 10.4% and 10.8% at the ARS and ASU ECT sites, respectively), indicating that the spatial heterogeneity of vegetation cover in the radial direction is dominated by the spatial patterns of mesquite trees.

Table 3.3. Distribution of mesquite canopy heights (% of 1 m by 1 m pixels per class) for 200 m radius circles around ASU and ARS ECT sites.

Frequency Distribution	ARS ECT	ASU ECT
0 to 0.5 m	47	60
0.5 to 1.0 m	9	11
1.0 to 2.0 m	21	19
2.0 to 4.0 m	30	9
4.0 to 6.0 m	3	1

Vegetation response following rainfall is apparent in the MODIS data (Figure 3.4). EVI increases with precipitation, indicating greater leaf area index and changes in canopy architecture and plant physiognomy, and albedo decreases, as the canopies become more dense and grasses fill in bare soil areas. Generally, EVI is greater at ARS ECT (average of 0.1607±0.0485) compared to ASU ECT (average of 0.1528±0.0367), however average albedo is also greater at ARS ECT (ARS: 0.1007±0.0114, ASU: 0.0968±0.0117), which may indicate a difference in the amount of grass coverage at ASU that fills in the bare soil area. Monthly average EVI and albedo values are shown in Table 3.4. On average, ARS ECT has particularly larger EVI values compared to ASU ECT in March, and during the monsoon season (July, August and September). ASU ECT has higher values for one month (November), which may be a result of increased grass coverage. Differences in average monthly albedo values are less prominent, however the largest differences occur in May, June, and August through November. Albedo values at both sites decrease with the onset of the NAM (July), and gradually increase in each subsequent month.

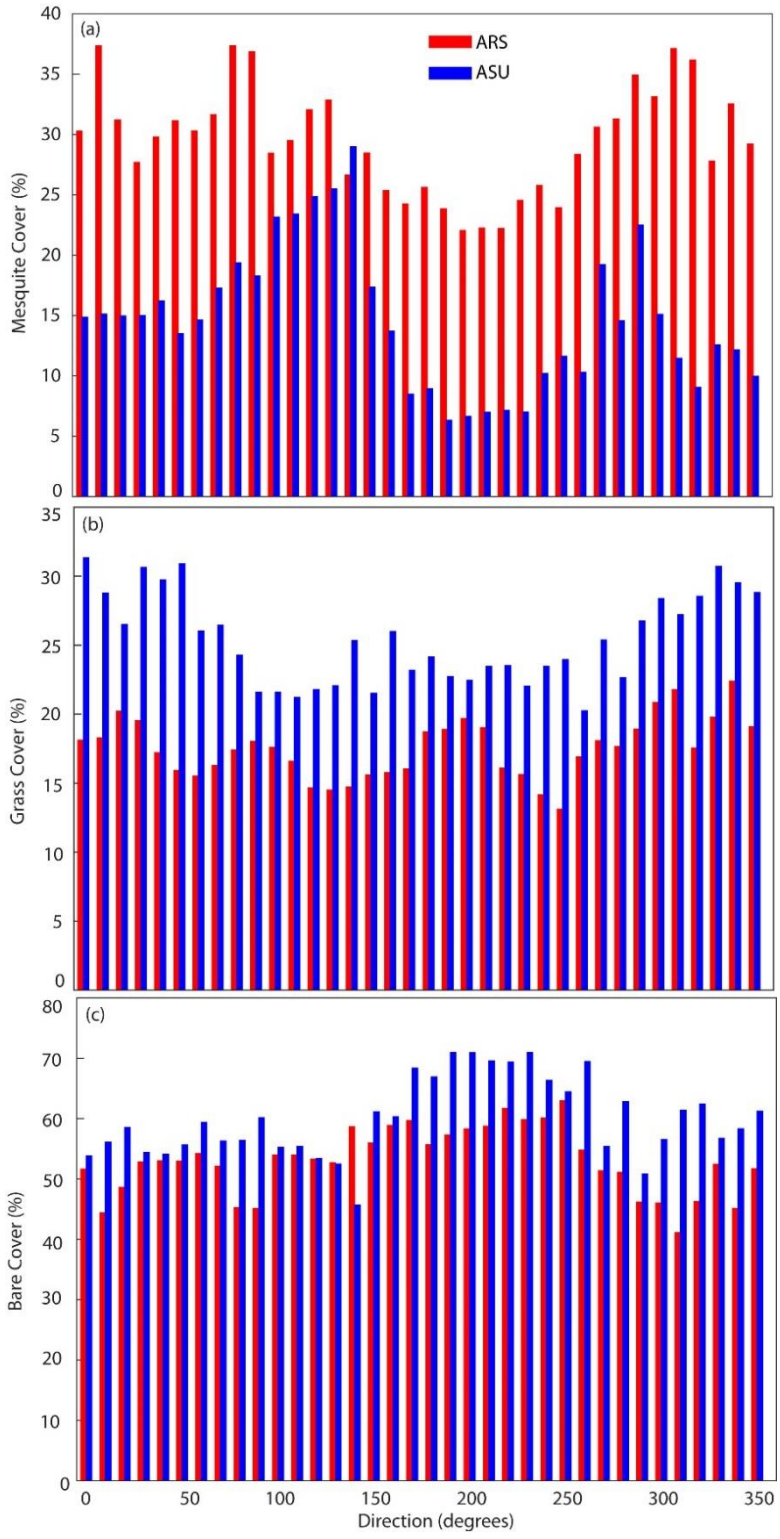

Figure 3.3. Vegetation cover (%) within 200 m radius for each 10 degree bin (36 total) at ARS and ASU ECT sites: (a) mesquite tree, (b) grass and (c) bare (soil) covers.

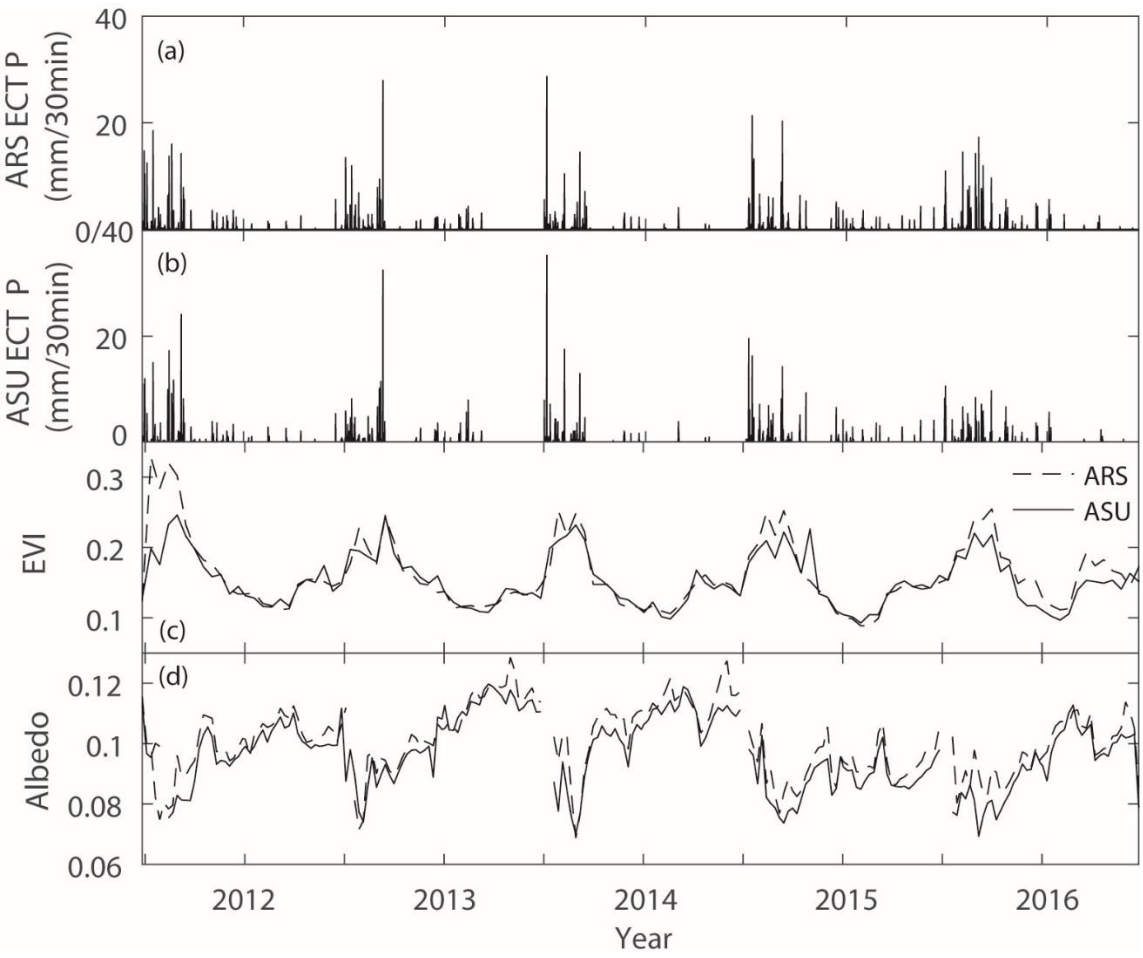

Figure 3.4. Measurements and data from July 1, 2011 to June 15, 2016, including (a) precipitation (mm/30min) measured at ARS ECT, (b) precipitation (mm/30min) measured at ASU ECT, (c) MODIS enhanced vegetation index (EVI), and (d) MODIS albedo.

Table 3.4. Monthly average EVI and albedo values obtained from MODIS products at ARS and ASU sites, with standard deviation in parentheses.

	EVI		Albedo	
	ARS ECT	ASU ECT	ARS ECT	ASU ECT
January	0.1194 (0.0133)	0.1167 (0.0122)	0.1023 (0.0064)	0.1002 (0.0081)
February	0.1089 (0.0108)	0.1060 (0.0082)	0.1073 (0.0090)	0.1047 (0.0090)
March	0.1294 (0.0264)	0.1227 (0.0149)	0.1098 (0.0078)	0.1079 (0.0091)
April	0.1508 (0.0177)	0.1480 (0.0109)	0.1044 (0.0115)	0.1014 (0.0103)
May	0.1496 (0.0097)	0.1466 (0.0109)	0.1074 (0.0115)	0.1024 (0.0099)
June	0.1438 (0.0125)	0.1425 (0.0116)	0.1086 (0.0094)	0.1033 (0.0091)
July	0.2180 (0.0524)	0.1892 (0.0152)	0.0927 (0.0119)	0.0896 (0.0086)
August	0.2368 (0.0435)	0.2093 (0.0228)	0.0889 (0.0099)	0.0830 (0.0077)
September	0.2210 (0.0305)	0.2060 (0.0210)	0.0894 (0.0067)	0.0833 (0.0079)
October	0.1678 (0.0133)	0.1664 (0.0069)	0.0972 (0.0103)	0.0922 (0.0106)
November	0.1527 (0.0177)	0.1571 (0.0288)	0.0996 (0.0064)	0.0950 (0.0056)
December	0.1333 (0.0159)	0.1303 (0.0156)	0.0993 (0.0067)	0.0962 (0.0070)

Comparisons of meteorological variables and fluxes

Meteorological and flux variables were compared at three different temporal resolutions: 30-min, daily and monthly averages. Table 3.5 summarizes the 30-min and daily statistical metrics for air temperature (T_a), vapor pressure deficit (VPD), net radiation (R_n), sensible heat flux (H) and latent heat flux (LE), among others. Generally, the correlation coefficient (CC) between the ARS and ASU ECT sites is high for all variables and the bias (B) is close to one, indicating that temporal means are similar at both sites. Similarities in the meteorological variables can be noted in Figure 3.5 where monthly averages and ±1 standard deviations are presented for T_a, VPD and R_n. Overall, ARS ECT is slightly warmer than ASU ECT due to its lower elevation, with an average temperature of 19.6 °C as compared to 19.0 °C, consistent with Table 3.4. Air temperature at both sites peaks in June (29.3 and 28.7 °C at ARS and ASU ECT,

Table 3.5. Statistical metrics between ARS and ASU ECT sites at different temporal resolutions (30 min and daily). Correlation Coefficient (CC) and BIAS are dimensionless, Standard Error of Estimates (SEE) and Root Mean Squared Error (RMSE) have dimensions of variable indicated. Percent data indicates available, valid data amount for both sites.

30 Minute Comparison	CC	SEE	RMSE	BIAS	% Data
Air Temperature [°C]	0.9551	2.62	2.65	1.02	86.53%
Vapor Pressure Deficit [kPa]	0.9469	0.41	0.41	1.03	86.53%
Net Radiation [W/m^2]	0.9839	43.21	43.15	1.00	74.27%
Sensible Heat Flux [W/m^2]	0.9076	50.14	51.82	1.06	74.23%
Latent Heat Flux [W/m^2]	0.7886	29.56	31.13	1.01	69.56%
LE+H [W/m^2]	0.9050	62.80	64.69	1.05	69.53%
Carbon Flux [mg CO_2/m^2*s]	0.7357	0.06	0.06	0.88	71.93%
Daily Comparison	**CC**	**SEE**	**RMSE**	**BIAS**	**% Data**
Air Temperature [°C]	0.9439	2.36	2.43	0.98	97.18%
Vapor Pressure Deficit [kPa]	0.8764	0.42	0.45	0.97	77.72%
Net Radiation [W/m^2]	0.6670	33.49	40.43	1.03	88.11%
Sensible Heat Flux [W/m^2]	0.8310	12.65	21.65	1.03	82.20%
Latent Heat Flux [W/m^2]	0.8235	11.73	15.11	0.93	82.48%
LE + H [W/m^2]	0.7611	16.41	29.19	1.00	81.54%
ET [mm/day]	0.7870	0.59	0.61	1.04	90.11%

respectively), prior to the NAM season, and is lowest in December. VPD is also slightly higher at the ARS ECT as compared to the ASU ECT (averages of 1.77 and 1.72 kPa, respectively) and peak in June prior to the NAM. Interesting differences are noted in R_n among the sites at daily and monthly resolutions. Net radiation is generally larger at ARS ECT (daily B = 1.03), with a seasonal signature related to the vegetation distribution around each tower. In the warm season (April to August), site differences in R_n (Δ = ARS minus ASU) are positive with a peak in May (Δ = +9.95 W/m^2 at ARS), and corresponds to greater EVI values and larger differences in albedo from the MODIS datasets. This is also attributed to the higher mesquite cover at the ARS ECT site whose greenness period

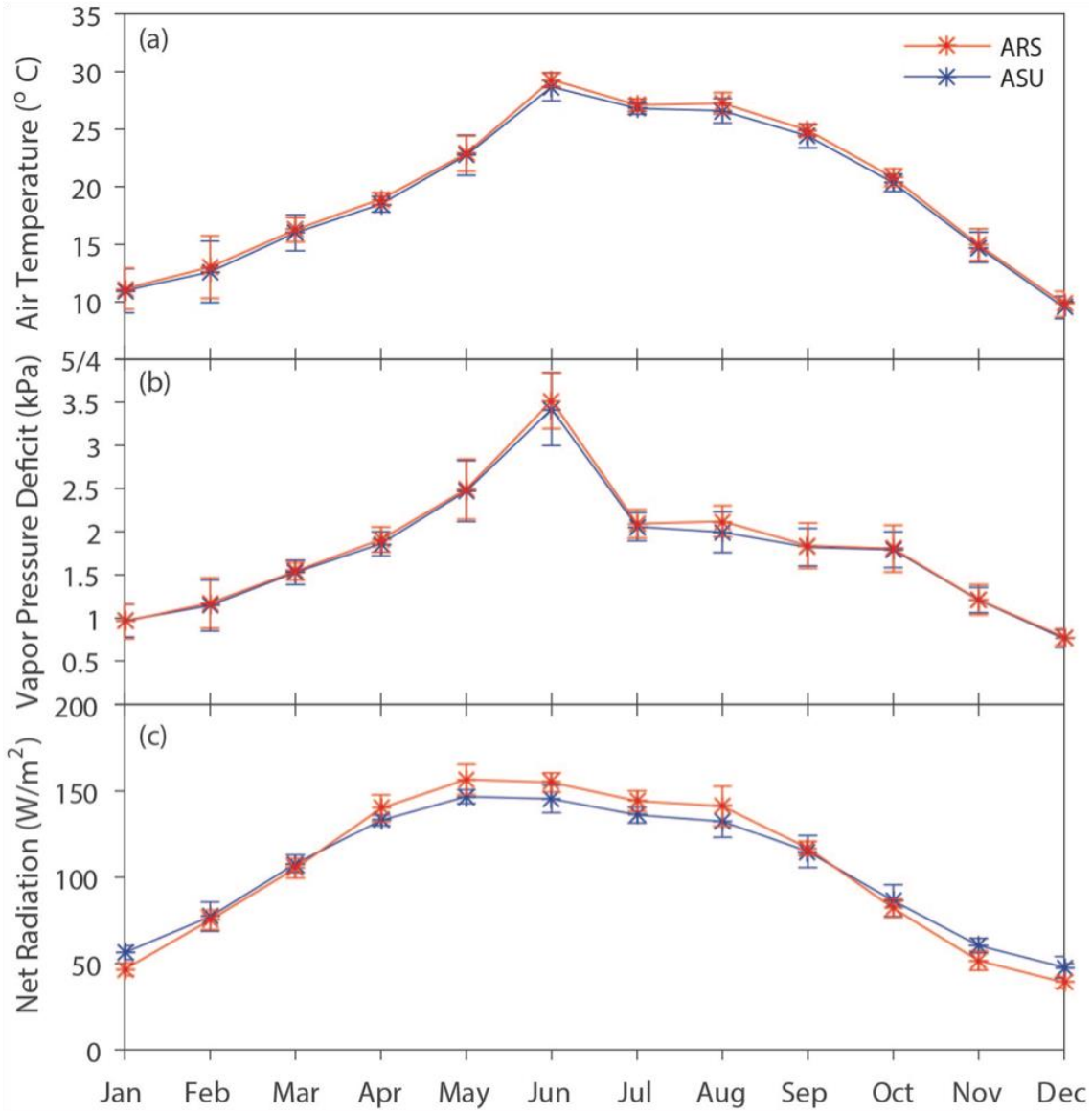

Figure 3.5. Monthly average meteorological variables: (a) air temperature (°C), (b) vapor pressure deficit (kPa) and (c) net radiation (W/m^2). Bars represent ±1 monthly standard deviation.

from April to September shades the surface (Scholes and Archer, 1997), which would increase R_n relative to the ASU ECT site with less mesquite cover. In contrast, the winter period (October to March) exhibits negative site differences, with a peak in January (Δ = -9.61 W/m^2 at ARS). During this time period, grasses have filled in bare soil areas after

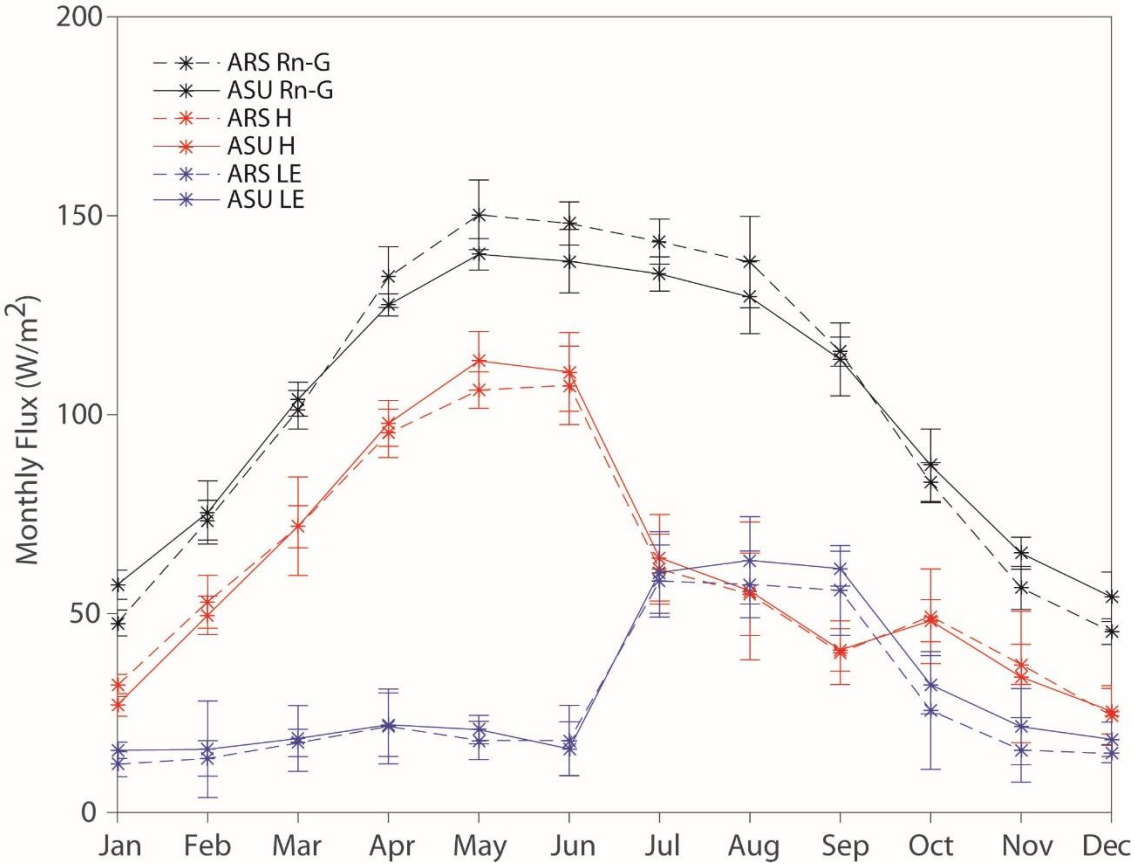

Figure 3.6. Monthly average and standard deviation of net radiation minus ground heat flux ($R_n - G$), sensible heat flux (H) and latent heat flux (LE) for ARS (dashed) and ASU (solid) ECT sites.

the NAM season, with EVI greater at ASU in October, which is more common at the ASU ECT site and leads to slightly larger amounts of R_n relative to the ARS ECT site. The increased grass cover at ASU ECT would provide reduced albedo and surface shading. Meanwhile, the mesquite leaves begin to yellow and dry in late fall, and drop by December (Cable, 1977), therefore the ARS ECT site is expected to have lower canopy cover.

To further evaluate differences among the ECT sites, average monthly fluxes are presented in Figure 3.6 in the form of available energy ($R_n - G$, where G is ground heat

flux), sensible (H) and latent (LE) heat fluxes (also see comparisons in Table 3.5). As noted for R_n, the ARS ECT has higher available energy from April to August, while ASU ECT exhibits larger values from October to March. At both sites, $R_n - G$ peaks in May and remains relatively high during the summer. Due to the low amounts of soil water prior to the NAM, sensible heat flux peaks in June at the ARS ECT (107.4 W/m^2) and in May at ASU ECT (113.5 W/m^2), accounting for a large percentage of the available energy (71% and 81%, respectively). The larger values of H at the ASU ECT site from April to June are likely related to its higher fraction of bare soil cover in the dry season (Table 3.2). As expected from prior studies in the woody savanna (Scott et al., 2009; Pierini et al., 2014), sensible heat flux decreases abruptly with the onset of the NAM, with negligible differences among the ECT sites throughout the rest of the year. With the arrival of summer storms, latent heat flux peaks in July at both sites, remains high during the NAM and consumes a larger percentage of available energy (48% and 54% at ARS and ASU ECT sites for September). Generally, LE is slightly greater at ASU ECT with large differences observed between August and November (Δ = -5.48 W/m^2 to -6.47 W/m^2), an indication of the effect of higher grass cover at the ASU ECT site in the NAM and winter periods.

Precipitation, evapotranspiration and carbon flux differences

Cumulative precipitation (P) and evapotranspiration (ET) are compared for each year in the study period in Figure 3.7, with partial accumulations shown for 2011 and 2016. Cumulative P exhibits two distinct wet seasons (winter and summer), with horizontal dotted lines indicating a dry period, while cumulative ET increases more

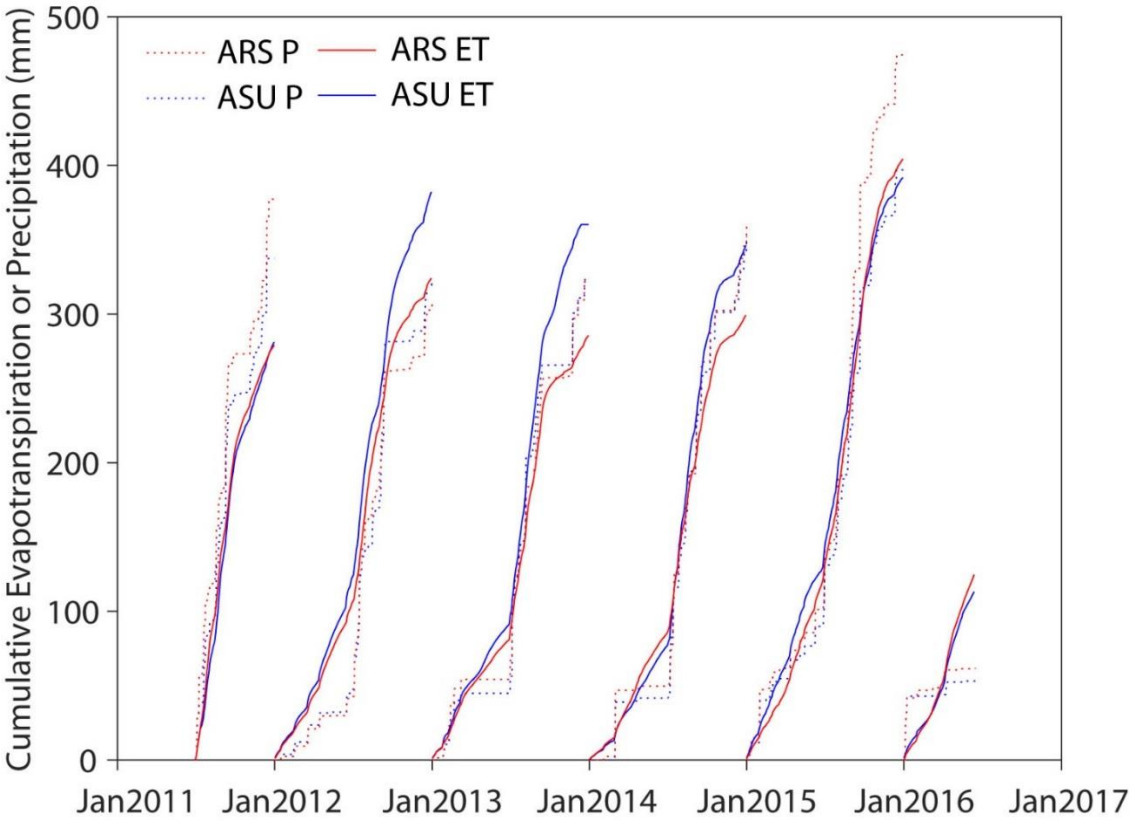

Figure 3.7. Cumulative evapotranspiration (solid) and precipitation (dotted) at ARS and ASU ECT sites. Partial accumulations are shown for 2011 (begins July 1) and 2016 (ends June 15).

Table 3.6. Cumulative precipitation at ASU ECT, ARS ECT, ARS RG 8 and SRER RG 45. [a]Data only include partial years (July 1 to December 30, 2011, and January 1 to June 15, 2016).

	Cumulative Precipitation (mm)			
	ARS ECT	ASU ECT	ARS RG 8	SRER RG 45
2011[a]	377.44	337.57	348.87	373.38
2012	307.08	322.28	337.32	316.23
2013	323.34	321.95	336.43	314.2
2014	359.42	352.04	369.19	376.17
2015	474.47	397.14	414.27	453.64
2016[a]	54.36[a]	53.21[a]	61.72[a]	61.98[a]

Table 3.7. Cumulative evapotranspiration (ET), net ecosystem exchange (NEE), respiration (R_{eco}) and gross ecosystem production (GEP). [a]Data only include partial years (July 1 to December 30, 2011, and January 1 to June 15, 2016).

	ET (mm)		NEE (g C/m^2)		R_{eco} (g C/m^2)		GEP (g C/m^2)	
	ARS	ASU	ARS	ASU	ARS	ASU	ARS	ASU
2011[a]	279.17	281.25	-80.24	-45.01	218.86	191.03	299.10	236.07
2012	324.10	382.25	-54.48	-93.15	299.37	258.62	353.85	351.77
2013	285.67	360.34	-3.23	-57.31	285.46	279.67	288.70	336.98
2014	299.35	346.44	-43.27	1.03	315.38	302.61	358.66	301.59
2015	404.26	391.85	-51.27	-60.25	387.83	278.21	439.10	338.46
2016[a]	125.30	113.92	-51.02	7.90	105.23	48.16	48.16	40.26

gradually starting with mesquite greening in April, with a steeper slope during the NAM season in response to precipitation, and continuing as perennial grasses fill in bare areas during the fall season. Overall, the differences in total ET (Table 3.7) depend on variation of total precipitation (Table 3.6) among the sites and on the effects of the vegetation distribution. For most years (2012-2014) when the precipitation distribution is sufficiently similar (within 20 mm/yr), the ASU ECT site exhibits a higher ET with most of the noted differences occurring after the NAM season in response to perennial grass cover. For 2015, when the ARS ECT had a significantly larger P (+77 mm), due to a series of fall storms, the total amount of ET slightly exceeded the ARS ECT site (Table 3.7). Furthermore, the ratio of ET/P is generally greater at the ASU ECT site (Table 3.8), even with considering different rainfall estimates. For ARS ET measurements, ratios were calculated using rainfall measurements from ARS ECT and SRER RG 45. Ratios for ASU were calculated using ASU ET measruements and P from ASU ECT and ARS RG 8. Average ARS ratios are 0.91±0.09 and 0.91±0.08 using ARS ECT and SRER RG 45 P estimates, respectively, while the average ASU ratios are larger at 1.07±0.09 and

Table 3.8. ET/P ratios calculated for complete study years (2012 to 2015). Ratios are calculated between ARS ET and ARS ECT P, ARS ET and SRER RG 45 P, ASU ET, and ASU ECT P, and ASU ET and ARS RG 8, based on rain gauge proximity to ET measurements.

	ARS ECT	ARS-SRER RG 45	ASU ECT	ASU-ARS RG 8
2012	1.06	1.02	1.19	1.13
2013	0.90	0.91	1.12	1.07
2014	0.83	0.80	0.98	0.94
2015	0.85	0.89	0.99	0.95

1.02±0.08, using ASU ECT and ARS RG 8 estimates, respectively. This suggests that higher amounts of grass cover at ASU ECT allow for a larger variation in cumulative ET between years, in particular after the NAM season, as compared to the less dynamic mesquite-dominated ET at the ARS ECT site. Figure 3.8 presents a comparison of cumulative ET, NEE, R_{eco} and GEP for each study year (including partial periods) at the two ECT sites, with total amounts shown in Table 3.6. In general, both sites are net sinks for CO_2 with annual values of NEE < 0 across most periods. Cumulative NEE typically exhibits two positive peaks each year, in early April and early July, related to a respiratory pulse (R_{eco}) prior to the greening of mesquite trees and the establishment of grass cover. These are followed by periods of negative NEE values associated with photosynthetic activity of mesquite trees and perennial grasses during periods of higher rates of GEP than R_{eco}. Differences in NEE among the ECT sites for the various years are difficult to diagnose. It is clear that the ARS ECT site has larger R_{eco} for all periods, driven by the increased air temperatures that underlie the estimation method (Reichstein et al., 2005). Site differences in GEP, however, are mainly due to varying amounts of evapotranspiration (GEP = 1.08ET + 5.69, R^2 = 0.86 at ARS and GEP = 0.82ET + 27.04, R^2 = 0.63 at ASU, respectively), which was found to be a stronger predictor of GEP than

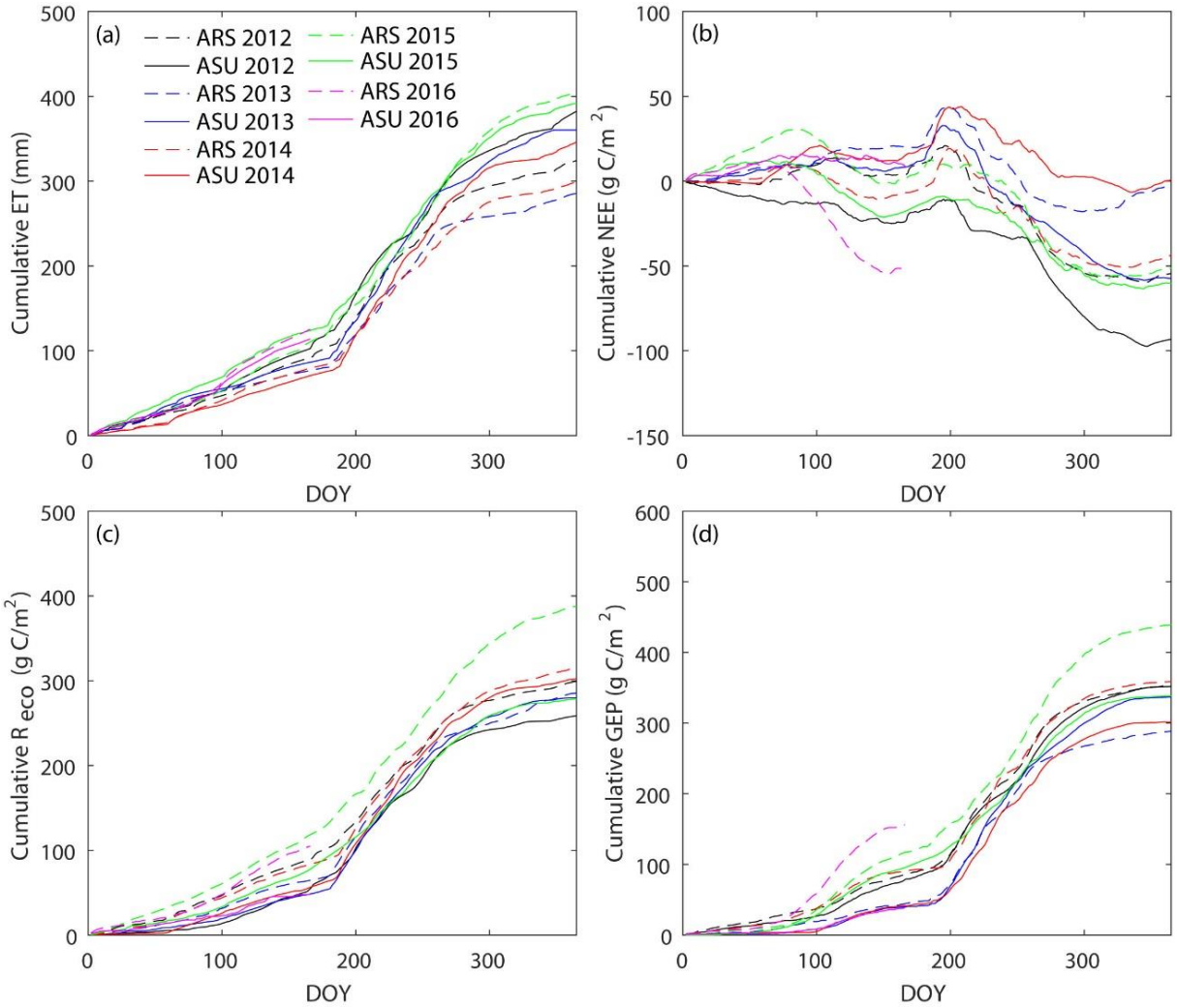

Figure 3.8. Comparison of cumulative annual (a) evapotranspiration (ET), (b) net ecosystem exchange (NEE), (c) respiration (R_{eco}) and (d) gross ecosystem production (GEP) for ARS (dashed) and ASU (solid) ECT sites. Partial year data shown for 2016 and 2011 is excluded.

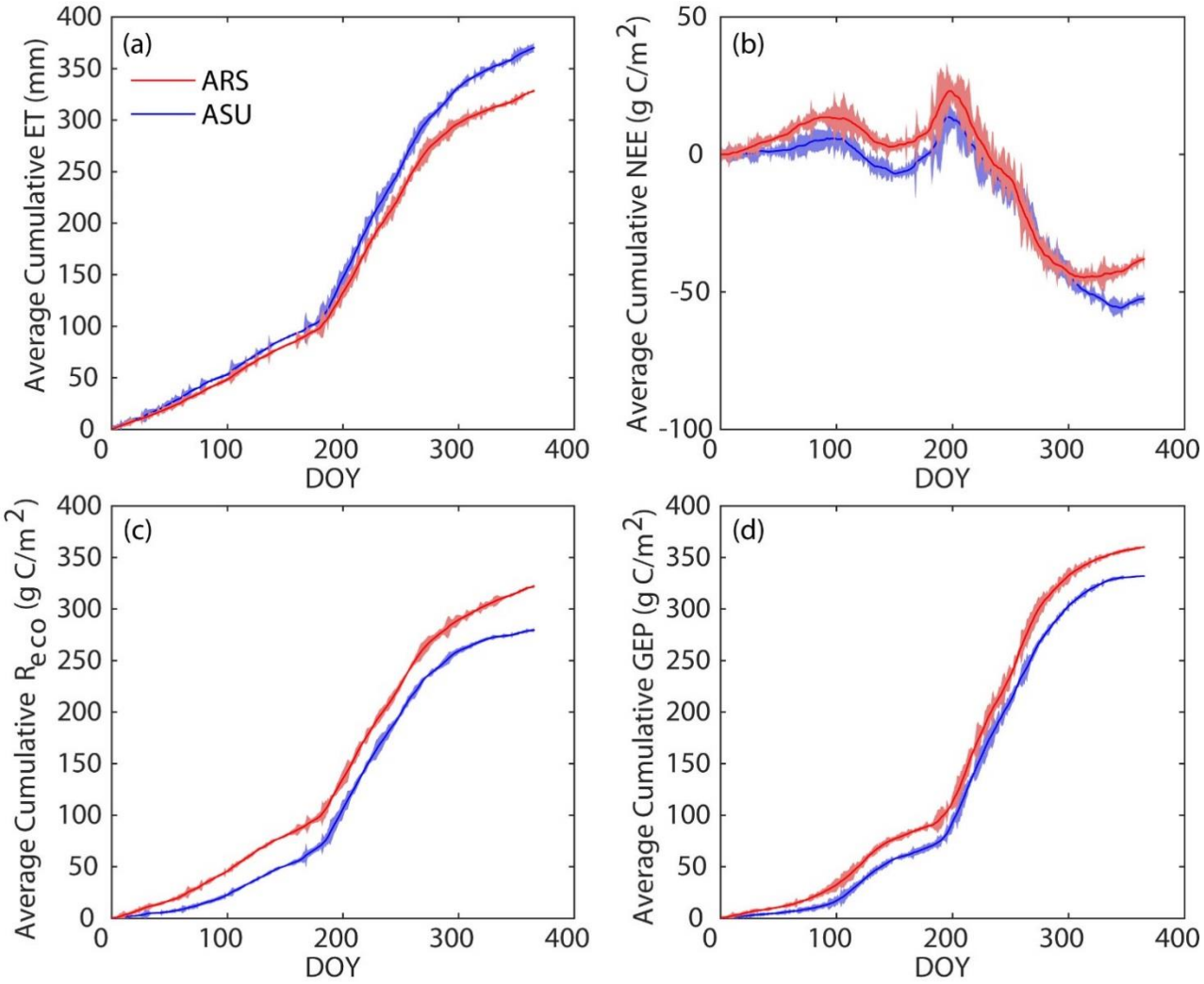

Figure 3.9. Average annual (2012 to 2015) cumulative (a) evapotranspiration (ET), (b) net ecosystem exchange (NEE), (c) respiration (R_{eco}) and (d) gross ecosystem production (GEP) for ARS (red) and ASU (blue) ECT sites. Standard deviation is multiplied by 10, and shown with red/blue shaded areas.

cumulative precipitation. Note that annual ET is composed of differing proportions of mesquite and grass transpiration, as well as bare soil evaporation, at each ECT site that vary in time in response to soil water availability. As a result, cumulative NEE can be similar across sites for a particular year, for instance in 2015, when high precipitation amounts lead to large ET and GEP, likely driven by uniformly productive conditions across all plant types. In contrast, for a year with lower precipitation, such as 2013, cumulative NEE can be several times more negative at the ASU ECT site due to the effects of annual grass ET on higher GEP during the fall season.

Figure 3.9 futher illustrates differences in cumulative ET, NEE, R_{eco} and GEP for full study years (2012 to 2015) at the two ECT sites by comparing the average cumulative values and standard deviations (which are multiplied by a factor of 10 for presentation purposes). The largest disparity in ET generally occurs during the late monsoon and fall periods. NEE has the largest variability at both sites, whereas R_{eco} has the smallest. GEP is fairly similar between the two sites during the early NAM season, however larger differences are observed in spring, associated with mesquite coverage differences, and the late NAM season.

Wind direction impact on fluxes

Given the variation of vegetation composition around each ECT, we computed daytime (8:00 to 17:00, local time) fluxes as a function of wind direction (10 degree bins or 36 bins). Wind directions from the backside of the ECT setup were omitted (35 to 55° and 50 to 70° at ARS and ASU ECT, respectively). Figure 3.10 presents wind rose diagrams at each site, indicating that the most dominant wind directions are 240-250° at

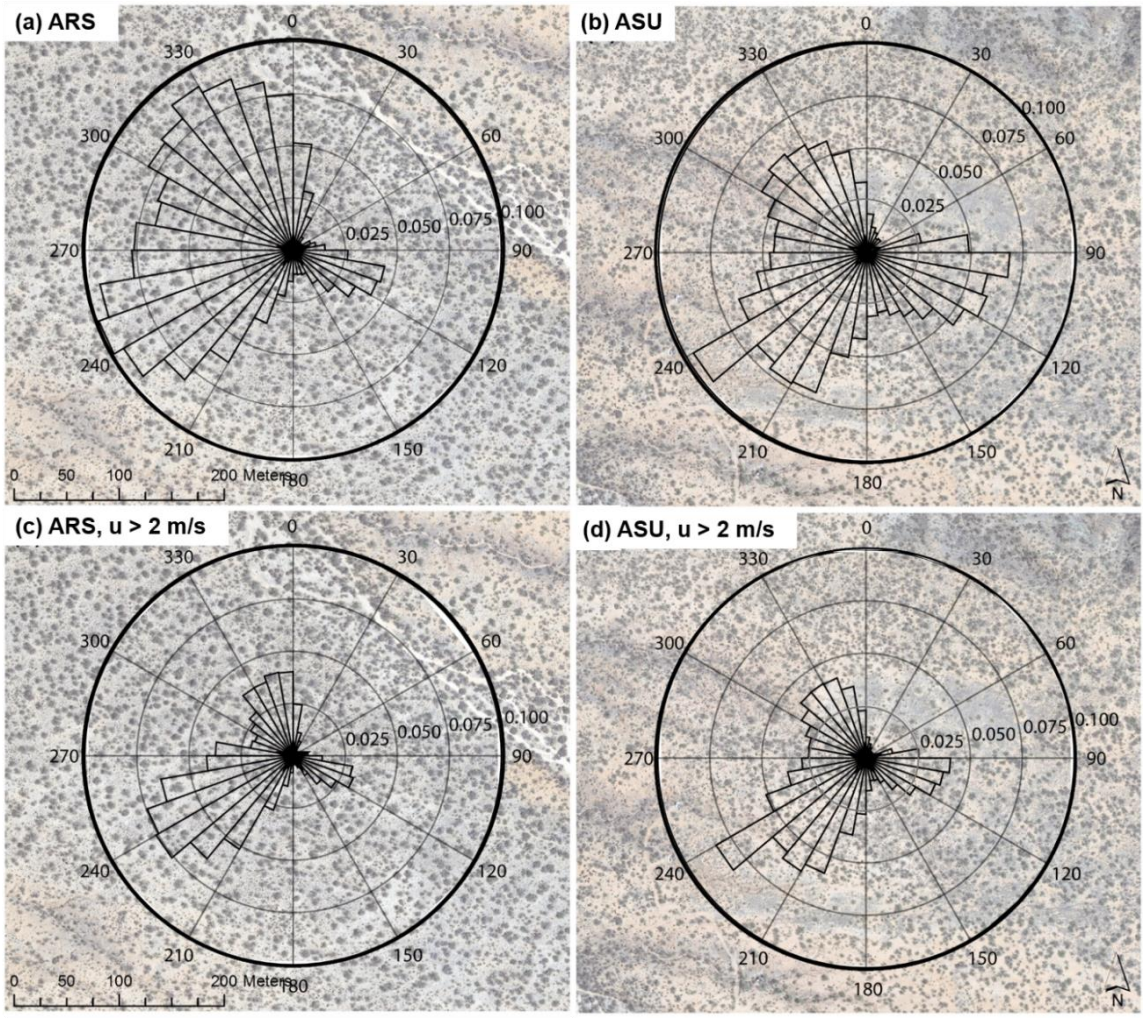

Figure 3.10. Histogram of daytime wind direction for each 10 degree bin (36 total) at ARS and ASU ECT sites: (a, b) no minimum wind speed (u) threshold and (c, d) for u > 2 m/s.

ARS ECT and 230-240° at ASU ECT, consistent with the southwest direction during the NAM season. Both sites have additional wind from the east-southeast (~90 to 120°) as a result of winds from the Santa Rita Mountains to the east. Wind direction patterns are next analyzed with a minimum wind speed (u) threshold set to 2 m/s to filter out less significant winds. General patterns hold, where the most dominant wind direction at both sites is from the southwest (230 to 250° at ARS and 230 to 240° at ASU). Both sites also

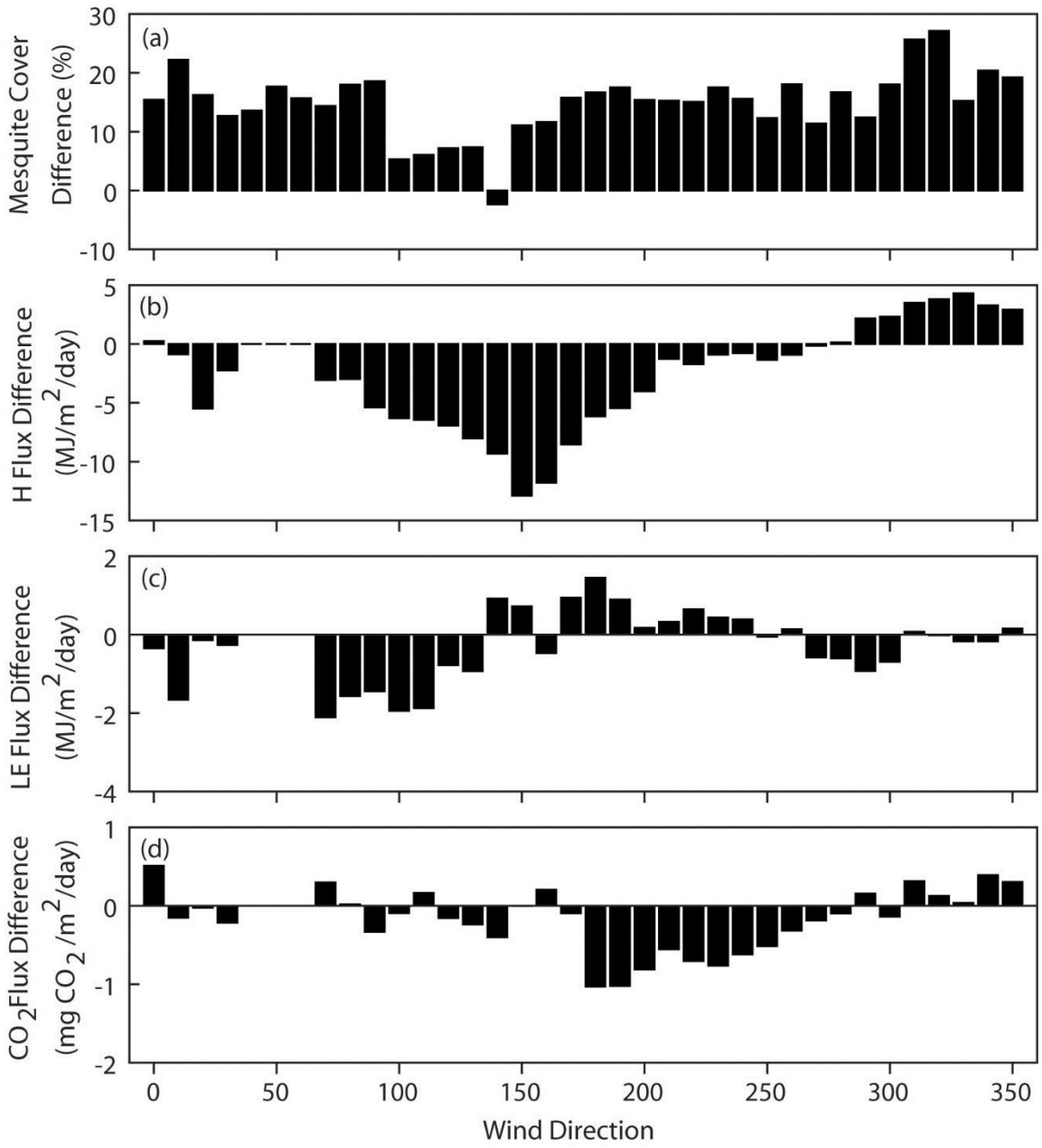

Figure 3.11. Daytime differences (ARS minus ASU) as a function of wind direction (10 degree bins) for u > 2 m/s of (a) mesquite cover (%), (b) sensible heat flux (MJ m^{-2} day^{-1}), (c) latent heat flux (MJ m^{-2} day^{-1}) and (d) carbon flux (g CO_2 m^{-2} day^{-1}).

have a high frequency of winds from the north-northwest direction. This is significant because of the large patch of bare soil and perennial grass cover north of the ASU ECT.

Figure 3.11 presents differences (ARS minus ASU) of daytime (30-min average) sensible heat, latent heat and carbon flux measurements for each wind direction (10 degree bins) over the entire study period. These flux differences are presented in reference to the difference (ARS minus ASU) in mesquite cover for each wind direction. A clear difference is noted in sensible heat flux with wind direction, where ASU ECT exhibits a higher H primarily from 70 to 210° (east to south-southeast), coinciding with relatively low differences in mesquite cover (also see Figure 3.10). Where the mesquite cover differences are highest from 300 to 20° (northwest to north), the ARS ECT has greater sensible heat flux indicating the role of vegetation spatial heterogeneity. In terms of the latent heat flux, less prominent differences are noted (±2 W/m^2 for LE as compared to -13 to +4 W/m^2 for H). The ARS ECT has higher LE from the east-southeast direction (70 to 140°), even though mesquite cover is most similar over this range, and a transition is noted in which the ARS ECT (170 to 250°) has slightly higher LE. Carbon flux differences are largest for the southwest wind directions (180 to 280°) and of small magnitude for the other directions. This is explained in Figure 3.12 through a comparison of daytime values for each ECT site for periods of time when $u > 2$ m/s. Negative values at both sites indicate carbon uptake (photosynthesis), in particular for the range of wind directions from 180° to 270° (south to west) where ARS ECT has a significantly higher carbon uptake. Over this dominant wind direction, higher photosynthesis is observed from the larger mesquite cover at the ARS ECT site.

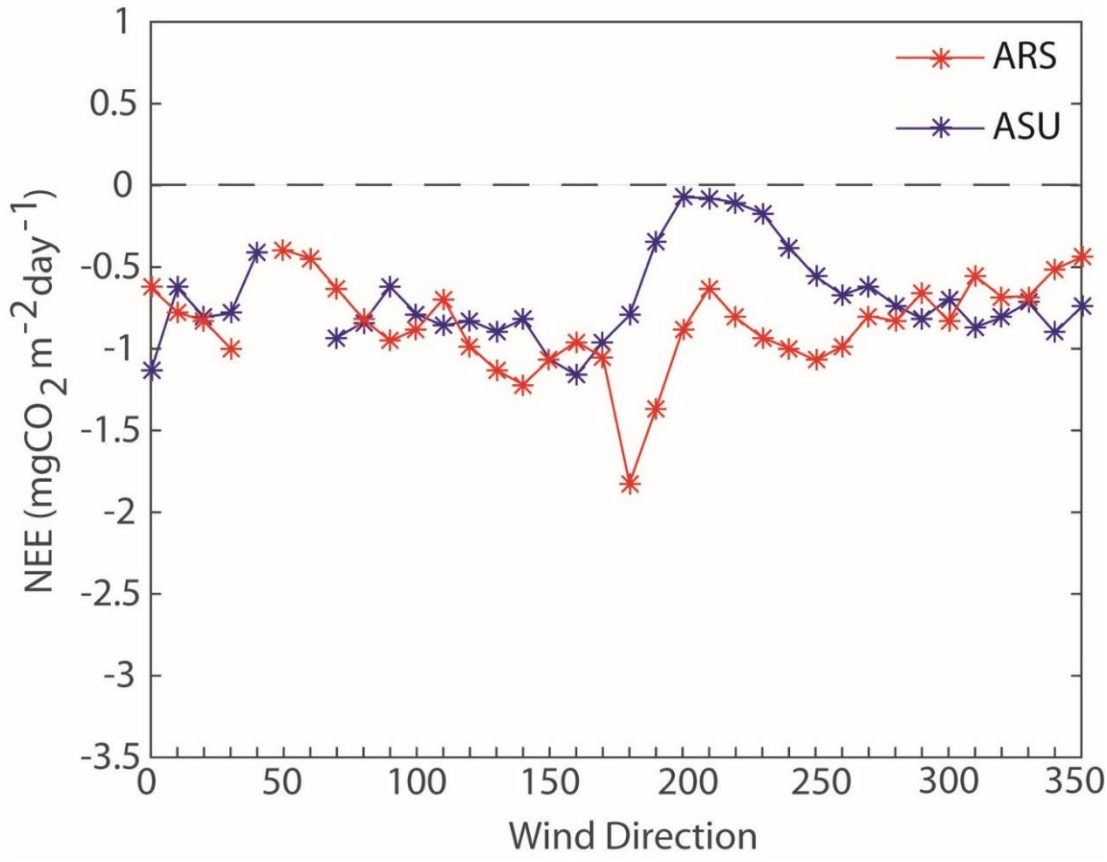

Figure 3.12. Daytime carbon flux as a function of wind direction (10 degree bins) for u > 2 m/s.

Seasonal influences on wind direction impact

Given the different vegetation compositions and their distinctive phenology at each site, the effect of wind direction on the meteorological fluxes is expected to change with seasonality. Mesquite trees produce leaves in spring (Cable, 1977), while perennial grasses green and occupy bare soil areas after the NAM onset. Figure 3.13 describes the flux differences (ARS minus ASU) for each season: winter (January to March), spring (April to June), summer (July to September) and fall (October to December). Similar patterns are noted for sensible heat flux for all seasons, though the summer presents an increase in H at the ARS ECT from the north to northwest (290 to 10°). The consistently

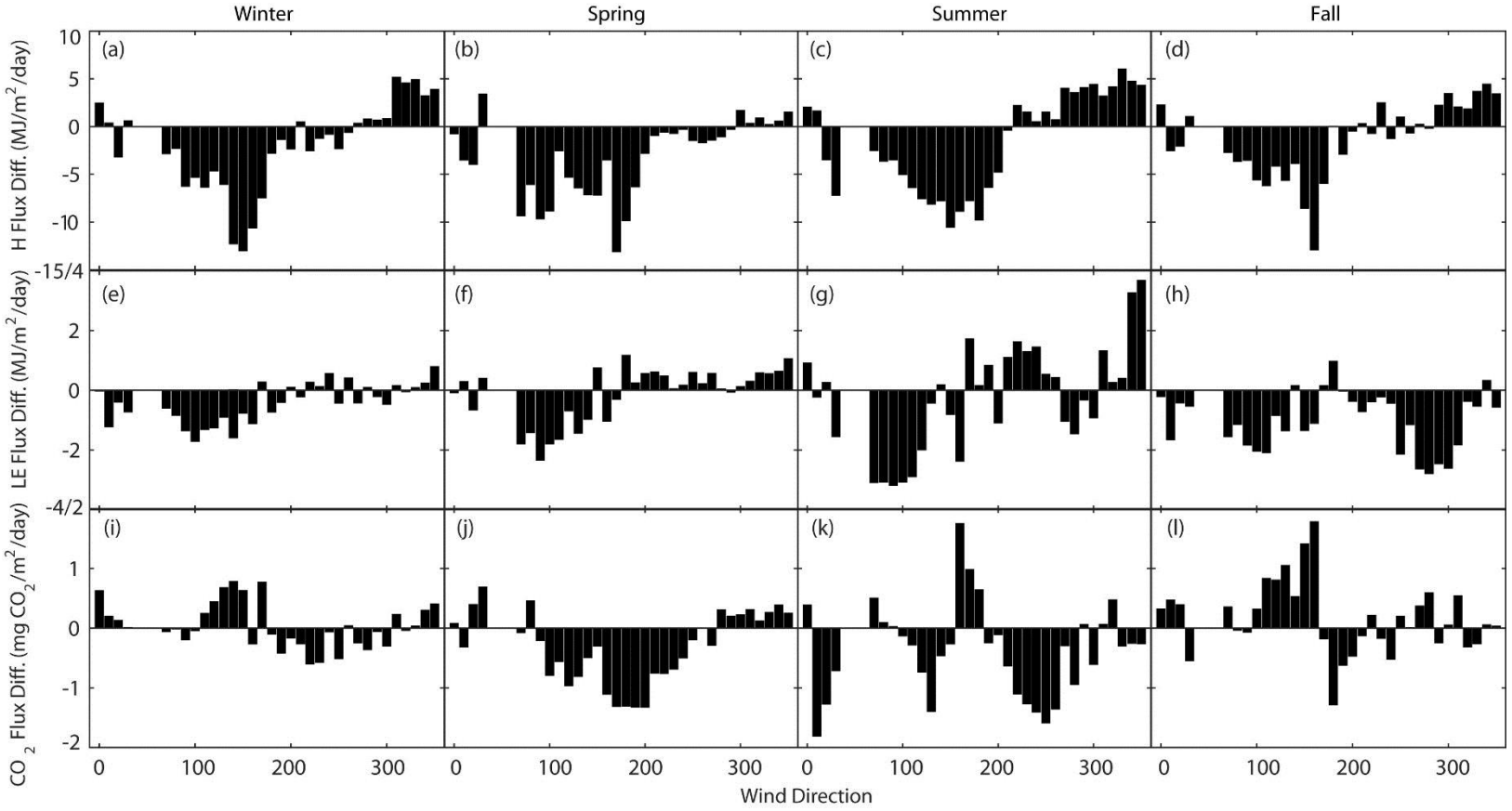

Figure 3.13. Daytime differences (ARS minus ASU) as a function of wind direction (10 degree bins) for u > 2 m/s of (a,b,c,d) sensible heat flux (MJ m^{-2} day^{-1}), (e,f,g,h) latent heat flux (MJ m^{-2} day^{-1}) and (i,j,k,l) carbon flux (g CO_2 m^{-2} day^{-1}), averaged winter, spring, summer and fall

higher H at the ASU ECT site from the east to south-southeast direction for all season indicates that the vegetation phenology plays a minor role in this spatial heteorogeneity. More notable seasonal differences are present in latent heat flux. Generally, there is larger LE for most wind directions at the ASU ECT site during winter and fall due to the active grass cover when mesquite trees are dormant. In the summer, ARS ECT has a greater LE in two directions (210 to 270° and 310 to 10°) that coincide with high mesquite differences. While this LE pattern amplifies similar differences observed in spring, it is reversed during the fall, indicating that a transition in phenological controls on ET occurs from mesquite to grass-dominant contributions.

There is also significant directional variability in carbon fluxes across the seasons, as detailed in Figure 3.14 as daytime values at each ECT site for periods when $u > 2$ m/s. As expected during the winter, carbon fluxes are near zero or slightly positive due to a dominance of R_{eco}, with only minor directional differences among sites. During the spring, the ARS ECT site has more negative carbon flux, in particular between 80 and 260°, due to the leafing out of mesquite trees. The two sites behave similarly during the summer when large amounts of carbon uptake ($GEP > R_{eco}$, $NEE < 0$) occur, with differences in the southwest (180 to 270°) and northeast (10 to 50°) directions where ARS ECT has higher LE due to a higher mesquite cover. In the fall period, on the other hand, the ASU ECT site has greater carbon uptake as compared to the ARS ECT site, in particular when winds are from the southeast (100 to 170°), due to an active grass cover. Overall, the variations of the measured fluxes with wind direction at the two sites indicates that seasonal phenology plays an important role in structuring the spatial heterogeneity in the woody savanna.

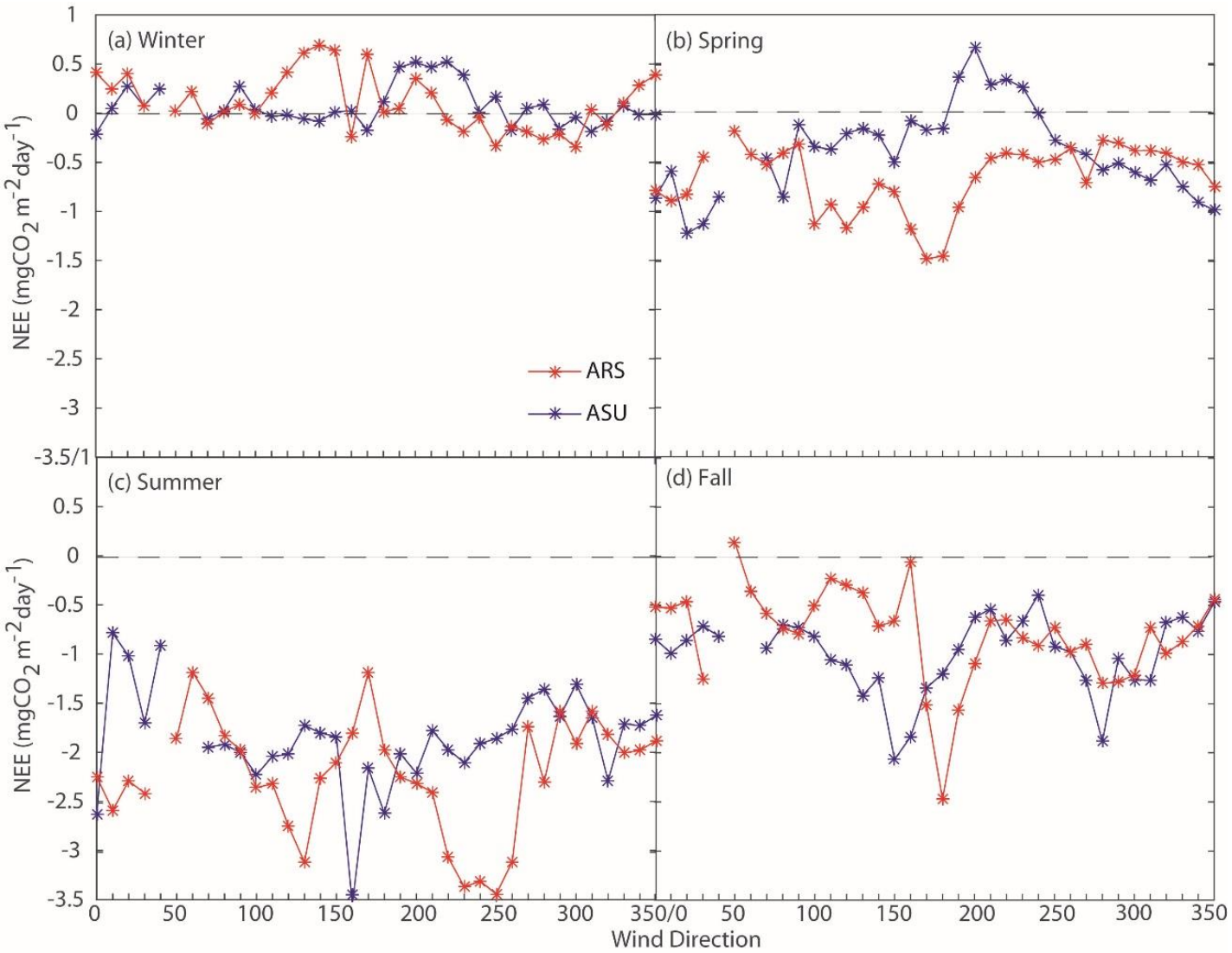

Figure 3.14. Daytime carbon flux as a function of wind direction (10 degree bins) for u > 2 m/s for (a) winter, (b) spring, (c) summer and (d) fall.

SUMMARY AND CONCLUSIONS

Grasslands and savannas are important ecosystems that can represent different scales of vegetation heterogeneity, such as woody plant encroachment, or other disturbances that impact vegetation distribution. Woody plant encroached landscapes and subsequent brush management lead to changes in ecosystem services that are not well understood. The effect of spatial heterogeneity on energy, water and carbon fluxes is difficult to discern. The eddy covariance method is a well-established technique to measure fluxes between the surface and the atmosphere, however it is necessary to understand how the spatial heterogeneity impacts flux measurements. In this study, long-term meteorological flux measurements are compared between two eddy covariance towers in the Sonoran Desert, which represent landscapes that have undergone the encroachment of velvet mesquite. The purpose of the comparison is to explore how spatial heterogeneity of vegetation distribution in this woody savanna landscape affects energy, water, and carbon fluxes.

Comparisons between the two sites reveal mesquite, grass, and bare cover vary between the two sites, where the ARS ECT has a greater amount of mesquite (30% vs. 15%) and the ARS ECT has a greater amount of grass (25% vs. 18%), based on an April 2011 orthoimage. Mesquite canopies are taller at the ARS ECT compared to the ASU ECT. Differences in vegetation cover are likely due to historical disturbance differences (past mesquite treatment and wildfire) and soil differences. Mesquite coverage varies radially around each tower, with greater variability around ASU ECT, indicating greater heterogeneity. Grass and bare (soil) coverage also varies radially, and is greater at ASU ECT, however the differences between the two sites are more uniform. As a result of

mesquite cover differences, net radiation is greater at the ARS ECT site from April to September, and lower from October to March. The mesquite begins to leaf in April, which could lower surface temperature, due to shading effects and albedo differences, and increase net radiation at ARS ECT. Net radiation is higher at the ASU ECT site from October to March, possibly because perennial grasses fill in bare areas, reducing albedo and surface temperature. More grass cover is observed at ASU ECT, expected because of less mesquite cover at the site.

Sensible heat flux (H) is greater at ARS ECT from October to February, likely due to less grass cover. ASU ECT has higher H values from March to September, which may be a result of less mesquite cover. Latent heat flux (LE) peaks in July at both sites, expected with the increase in precipitation, and remains high during the NAM. LE is greater at ASU ECT for all months with the exception of June. The difference in LE between the two sites may be indicative of the grass cover differences and the relatively strong influence of grass to latent heat. Generally, ASU ECT has higher annual cumulative evapotranspiration (ET), with the exception of the particularly wet year at ARS ECT in 2015. Greater ET measured at ASU ECT may be indicative of fewer, smaller mesquite trees, thus less canopy cover and shading. ET/P ratios are greater at ASU ECT every year, indicating that vegetation difference play a role in the ET differences. Cumulative net ecosystem exchange (NEE) differences vary from year to year, however ASU ECT generally has greater carbon uptake during full year analysis, with the exception of 2014. Cumulative gross ecosystem production (GEP) follows trends similar to cumulative ET and precipitation, and is general greater at ARS ECT, except for

2013, likely due to greater mesquite coverage. Cumulative respiration (R_{eco}) is greater at the ARS ECT for all study year periods.

Fluxes are evaluated radially, where there is a clear difference in sensible heat with respect to wind direction, coinciding with relatively low differences in mesquite cover. There is less variability in latent heat flux. CO_2 flux differences are largest in the southwest wind direction. Seasonal analysis indicates more substantial latent heat and CO_2 flux directional variability. LE is higher at ASU ECT during the fall and winter, corresponding to a greater amount of active grass cover and dormant mesquite trees. ARS ECT has greater LE in the spring and summer in specific directions with greater mesquite differences. CO_2 fluxes follow similar trends, with greater uptake during the spring at ARS vs. greater uptake in the fall at ASU, due to shifts between active mesquite and active grass cover, and the cover differences between the two sites. Both sites behave similarly during the summer, however the largest differences occur in the directions where ARS has relatively higher mesquite cover.

By evaluating these two datasets, the effect of spatially heterogeneous vegetation cover on energy, water, and carbon fluxes is examined. Particularly, the variations of measured fluxes directionally indicate that heterogeneous vegetation cover affects fluxes, and the impact shifts seasonally. Further insight into differences between the two sites could be obtained by inspecting event-scale responses to fluxes. It would also be fruitful to expand the comparison analysis over a longer time period, where differences can be established during wetter and drier years, or wetter and drier NAM periods. However, quantifying these differences provides knowledge to how the woody-plant encroached landscapes and their disturbance histories impact their current states.

CHAPTER 4

INITIAL IMPACTS OF BRUSH MANAGEMENT ON WATER AND CARBON FLUXES IN A SOUTHWESTERN U.S. RANGELAND

INTRODUCTION

Grasslands, shrublands, and savannas represent approximately 50% of the Earth's land surface (Bailey, 1996) and are inhabited by more than 30% of the world's population. These landscapes also represent approximately 30% of terrestrial net primary productivity (Field et al., 1998), thus are significant in global water and carbon cycles (Campbell and Stafford Smith, 2000). These landscapes are particularly susceptible to woody plant encroachment, which has transformed arid and semiarid landscapes over the past century, affecting ecosystems services (e.g., Breshears et al., 1998; Kurc and Small, 2004; Huxman et al., 2005).

Woody plants may have unintended consequences or benefits, depending on management goals, that need to be better understood (Archer, 2010; Archer et al., 2011). Brush management (BM) has been a popular technique to reduce woody plant cover on rangelands, usually with a goal to enhance livestock production (Archer, 2009; Browning and Archer, 2011; Archer and Predick, 2014). Research regarding brush management impact has focused on forage production and water yield (Martin and Morton, 1993; Lemberg et al., 2002; Huxman et al., 2005; Newman et al., 2006). There is less known about brush management impact on other ecosystem services however, including ecosystem primary production, carbon sequestration, sediment yield, land surface-atmosphere interactions, biodiversity, among others, especially at long time scales

(Archer, 2009). Evaluating brush management impacts on ecosystem services may lead to a non-traditional approach to manage woody plants.

Vital supporting services in semiarid systems are evapotranspiration (ET) and net ecosystem exchange (NEE), which describe water vapor and CO_2 fluxes between the land and atmosphere. Gross carbon uptake (gross ecosystem production, GEP) and release (ecosystem respiration, R_{eco}) describe the carbon fluxes based on NEE measurements for an ecosystem. Typically, rangelands release CO_2 during dry periods and uptake CO_2 during wet periods (Scott et al., 2009). Woody plant encroachment shifts landscape composition, thus impacting water and carbon fluxes, which has been studied in southern Arizona rangelands (Yepez et al., 2003; Scott et al., 2006; Browning et al., 2008; Scott et al., 2009; Pierini et al, 2014). Subsequent brush management (BM) would further impact water and carbon fluxes, and has been far less examined (Archer, 2009). After BM, or treatment, it is expected that ET will not significantly change, since ET/PPT is close to unity (Scott, 2010), however water availability shift from trees to grass and bare soil will likely impact NEE. There is an unknown effect on R_{eco} and GEP, especially over a long time period (years to decades). Initially after treatment, GEP would be expected to decrease, due to the loss of mesquite uptake. However, as grass cover increases without competing mesquite trees, GEP would be expected to recover, but it is unknown if it will meet or exceed pre-treatment GEP. Evaluating impacts of BM immediately after treatment will help with understanding the influences on water and carbon fluxes.

In this study, an aerially applied mesquite treatment, a BM technique, was conducted as part of a USDA-NIFA and USDA-ARS project entitled, "Brush management and ecosystem services: a quantification of trade-offs," in June 2016. The

impact of the mesquite treatment on water fluxes, particularly ET, and carbon fluxes [NEE, R_{eco}, and GEP] are evaluated. The treatment consisted of 45 acres surrounding the Arizona State University eddy covariance tower (ASU ECT), located in the Santa Rita Experimental Range (SRER). The USDA-Agricultural Research Service operates an eddy covariance tower (ARS ECT) that lies approximately 1.5 km to the west of ASU ECT and serves as a control tower for this study. Although the two sites have different characteristics (disturbance histories, vegetation distribution, soil type), as summarized in Chapter 3, approximately 5 years of pre-treatment data help discern existing disparities from flux differences due to mesquite treatment. By comparing and contrasting flux measurements, greater insight is obtained as to how mesquite treatment initially impacts water and carbon fluxes in a semiarid rangeland ecosystem.

METHODS

Characterization of study sites

The study sites represent a semiarid, managed rangeland landscape, located in the Santa Rita Experimental Range (SRER), approximately 45 km south of Tucson, Arizona. SRER is along the western alluvial fans of the Santa Rita Mountains, and both sites are in mid elevations of the range. The ARS ECT was established in 2004 (Scott et al., 2009) and the ASU ECT was established in May 2011 (Pierini et al., 2014), approximately 1.5 km east (Figure 4.1a). In this study, datasets collected from the two towers are compared for two different time periods: pre-treatment (July 1, 2011 to June 15, 2015) and post-treatment (July 1, 2016 to December 31, 2016). Primary land use is cattle grazing, and

both towers are within the same pasture, which is grazed approximately once per year for 1 to 3 months.

The climate of SRER is semiarid with bimodal precipitation. Summer rainfall (July to September) is representative of the North American monsoon (NAM) (Adams and Comrie, 1997) with a second, milder precipitation observed during the winter months (December to March). Long-term (1936 to 2016) monthly rainfall observations are obtained from a rain gauge (SRER RG 45) that lies between the two study sites, which reports an annual average of 377 mm. USDA-ARS has operated a weighing rain gauge (ARS RG8) since 1976, which is relatively close to the ASU ECT site. At ARS RG 8, annual average rainfall is 458 mm, with approximately 54% occurring during the NAM season (Polyakov et al., 2010). Generally, there are two green up periods, with the first occurring during the spring (late March to late April), when mesquite trees produce leaves (Cable, 1977). The second, larger period occurs with the onset of the NAM (early July), when grasses become active (Cable, 1975). By fall, mesquite leaves begin to yellow and dry, and will drop by December (Cable, 1977), however depending on winter precipitation, grasses may still be active.

Although the sites are near, their disturbance histories differ significantly since the 1970s, as described in Chapter 3. As part of a study on rainfall, runoff and erosion response to manipulative mesquite treatments, the U.S. Department of Agriculture-Agricultural Research Service (USDA-ARS) established 8 small watersheds in SRER. ASU ECT is located near watershed 7 (WS 7) and watershed 8 (WS 8). WS 8 underwent mesquite treatment in 1974, where diesel oil was applied basally to kill the trees, with reapplication as needed (Martin and Morton, 1993). The treatment area was small (~1.1

ha), however it lies within the ASU ECT footprint. The area surrounding the ASU ECT was also affected by a fire on June 2, 1994 that ultimately burned 4000 ha in SRER (Huang et al., 2007), including both watersheds. The area around ARS ECT was unaffected by the fire.

Over the last century, the rangeland has undergone a shift from a semiarid grassland to a savanna due to the encroachment of the woody tree, *Prosopis velutina* Woot., or velvet mesquite. Vegetation at both sites consists of velvet mesquite, nonnative Lehmann lovegrass (*Eragrostis lehmanniana*), perennial bunchgrasses [black grama (*Bouteloua eriopoda*), Arizona cottontop (*Digitaria californica*), and Santa Rita threeawn (*Aristida glabrata*)], and various succulents [cholla (*Opuntia spinisior*), prickly pear (*Opuntia engelmannii*) and fishhook barrel (*Ferocactus wislizeni*)]. A detailed soil survey was conducted at SRER by the Natural Resources Conservation Service staff in 1997 (Breckenfeld and Robinett, 2003), and the two sites lie on different soil types. The ARS ECT soil is classified as Combate-Diaspar complex (CdB), and the ASU ECT soil is classified as Sasabe-Baboquivari complex (Breckenfeld and Robinett, 2003).

Vegetation classification analysis was performed at each ECT, and is further described in Chapter 3. Land cover was classified into three types (grass, mesquite, bare (soil)). The ARS ECT site is composed of 30% mesquite, 18% grass and 52% bare, while the ASU ECT site is composed of 15% mesquite, 25% grass and 60% bare. Vegetation classification within the treatment area is shown in Figure 4.1b. Key differences between the sites include more mesquite trees at ARS ECT and more grass cover at ASU ECT, which is likely due to differences in site history.

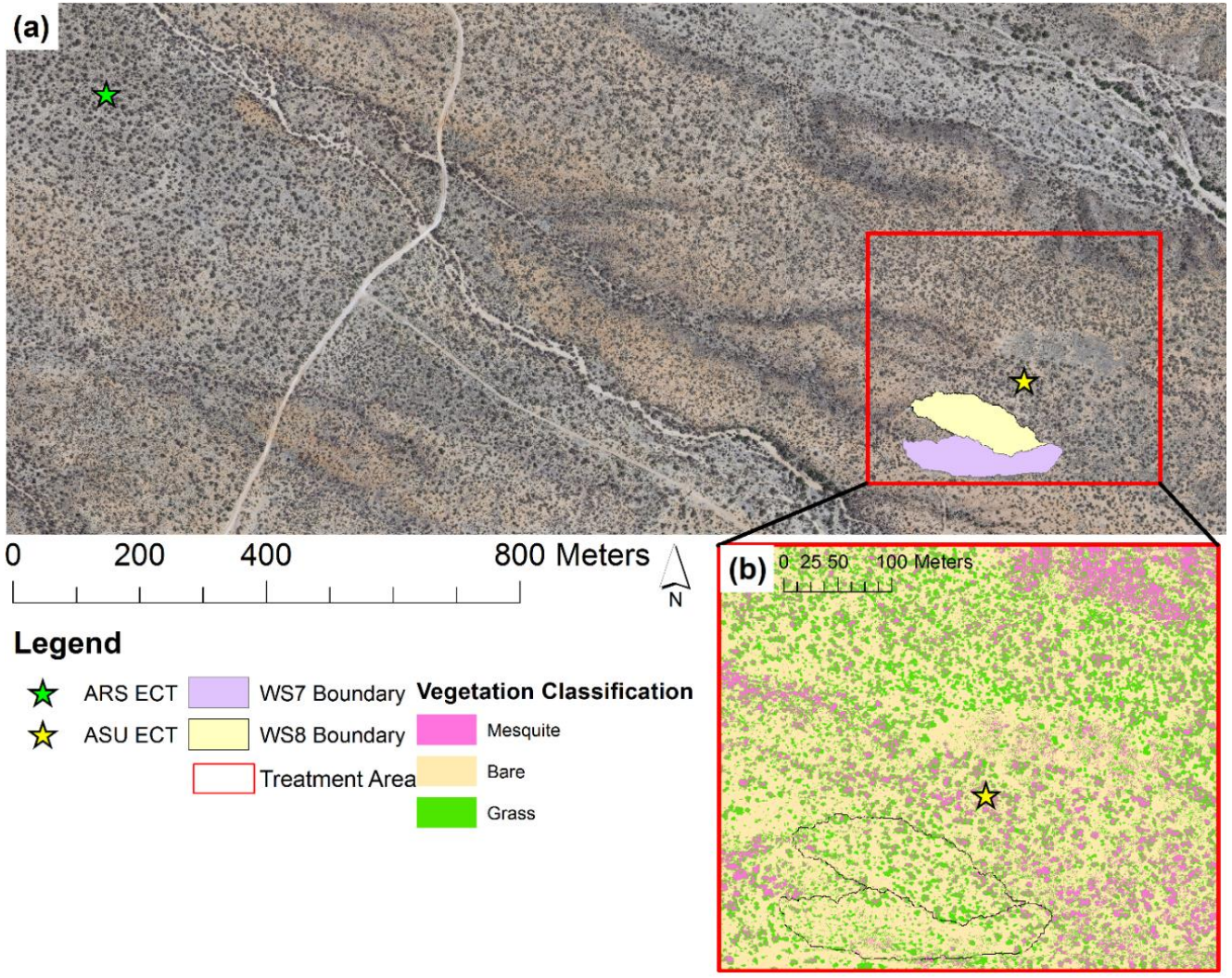

Figure 4.1. (a) ARS ECT, ASU ECT, WS 7 and WS 8 within the Santa Rita Experimental Range (SRER), including treatment area (red box) and (b) vegetation classification within the treatment area, including ASU ECT, WS 7 and WS 8 (black outlines).

To quantify vegetation response and seasonality at each site post-treatment, Moderate resolution Imaging Spectroradiometer (MODIS) products, specifically enhanced vegetation index (EVI, Huete et al., 2002) and albedo, were used. Products obtained were 16 day composites of EVI (MOD13Q1, 250 m spatial resolution) and 8 day composites of albedo (MYD43A, 500 m spatial resolution) from January 1, 2016 to December 31, 2016 (ORNL DAAC, 2008).

The ASU ECT site has had more disturbances, i.e. mesquite treatment and wildfire, particularly with respect to mesquite cover. Therefore, it is anticipated that mesquite cover would be greater at ARS ECT, and with the absence of competing mesquite trees, grass cover would be greater at ASU ECT. Bare cover is similar between the two sites. It is expected that the bare soil at both sites would typically fill in with perennial grasses during and after the monsoon season, however the classification is based on an April image.

Environmental measurements and data processing

Instruments included in the ASU ECT setup measure meteorological variables, soil conditions, and fluxes, and are summarized in Table 3.1 (with further details in Pierini et al., 2014 and Chapter 3). Eddy covariance data were sampled at a 20 Hz frequency and recorded by a datalogger (CR5000, Campbell Sci.). Data was filtered to exclude time periods when there was precipitation, the wind direction was between 37° and 57° due to possible interference from the tower setup, when friction velocity was less than 0.15 m/s, and for outliers greater than 3 standard deviations. Fluxes were then processed using EdiRE (University of Edinburgh), which includes corrections for

fluctuations in stability (Foken et al., 2006) and density (Webb et al., 1980), sonic temperature use to calculate sensible heat flux, rotating the coordinate frame to set the mean vertical wind speed to zero (Wilczak et al., 2001), and removing signal lag in gas concentrations (Massman, 2011). Other measurements were recorded by a datalogger (CR5000, Campbell Sci.) as averages over 30 minute periods. The ARS ECT data collection and processing methods are summarized by Scott et al. (2009) and the ARS ECT site is part of the Ameriflux network.

To accurately compare net ecosystem exchange (NEE) and evapotranspiration (ET) measurements between the two towers, ASU ECT data was processed to follow the same gap-filling procedure established at ARS ECT (Scott et al., 2009). NEE at ASU ECT is partitioned into ecosystem respiration (R_{eco}) and gross ecosystem production (GEP) following ARS ECT procedures (Reichstein et al, 2005; Scott et al, 2009), where, $NEE = R_{eco} - GEP$. Standard sign convention for NEE is used where $NEE < 0$ indicates CO_2 uptake by the ecosystem.

Herbicide treatment

The mesquite treatment, hereafter referred to as BM, was applied to 45 acres surrounding ASU ECT (Figure 4.1a) on June 19, 2016. Treatment was aerially applied by private contractors (Crop Production Services from Chandler, AZ and TriRotor Ag, LLC from Yuma, AZ) and consisted of an herbicide cocktail of clopyralid + aminopyralid + triclopyr + surfactant-adjuvant. The treatment area encompasses ASU ECT, WS 7 and WS 8. Figure 4.2 shows photos of the surrounding area pre-treatment (May 2011), initial

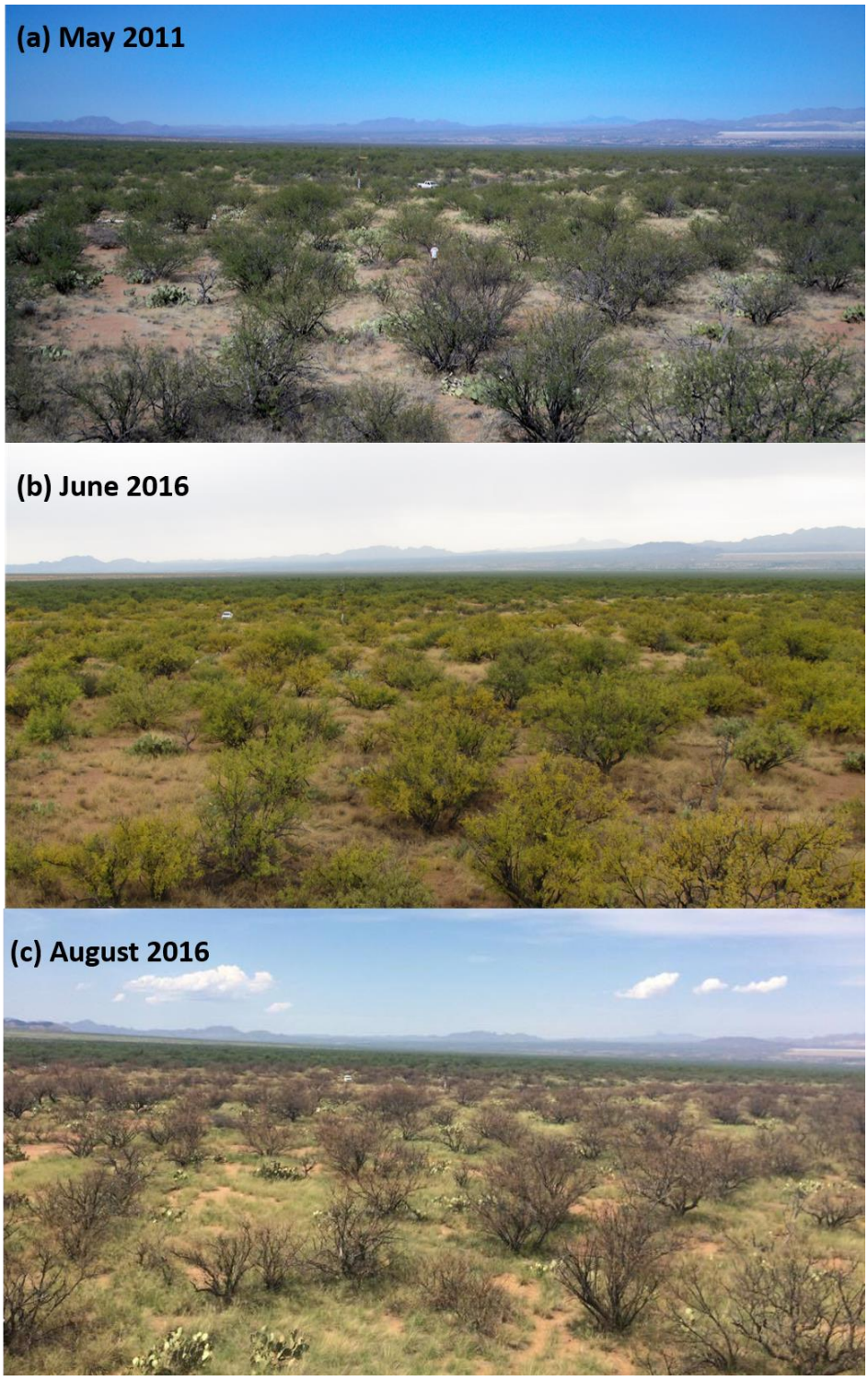

Figure 4.2. View from ASU ECT towards the southeast in (a) May 2011, pre-treatment, (b) June 2016, initial post-treatment, and (c) August 2016, post-treatment.

post-treatment (June 2016), and post-treatment (August 2016). It is important to note that the mesquite treatment initially appeared to work, as leaves fell off trees during the NAM season (by August). However, follow up data (morphologic measurements, accounting for number of basal shoots and new canopy branches) indicate that the treatment was not as effective by the end of the year. Therefore, BM impacts are expected to influence the summer period after treatment (July-August-September 2016), and lessen thereafter.

RESULTS AND DISCUSSION

Annual P, ET and carbon flux comparisons

Annual precipitation (P) comparisons between ARS ECT and ASU ECT reveal important differences (Table 4.1). It is important to note that 2015 and 2016 were relatively wet years at both sites, compared to 2011 to 2014, which averaged 340 mm and 333 mm at ARS ECT and ASU ECT, respectively. Precipitation differences are significant between ARS ECT and ASU ECT sites for 2015 as ARS ECT measured >77 mm of precipitation compared to ASU ECT, with the largest differences occurring during the fall months. This precipitation difference is also apparent when considering two additional rain gauges described in Chapter 3 (Table 3.6). Thus, the late season rainfall influences water and carbon fluxes in the following year, particularly in January through June, before the onset of the next NAM.

To evaluate the impacts of BM on fluxes, annual cumulative plots of ET, NEE, R and GEP are compared between full pre-treatment years (2012 to 2015) and the pre-treatment/post-treatment year (2016) in Figure 4.3 and Table 4.2. Generally, ET is high at both sites in 2015 and 2016, expected due to the high precipitation measurements. ARS

Table 4.1. Cumulative precipitation at ARS ECT and ASU ECT. [a]Data only include partial year (July 1 to December 31, 2011).

	Cumulative Precipitation (mm)	
	ARS ECT	ASU ECT
2011[a]	377.44	337.57
2012	304.79	322.28
2013	318.26	321.95
2014	359.42	352.04
2015	474.47	397.14
2016	404.71	402.21

Table 4.2. Cumulative ET, NEE, R_{eco}, and GEP at ARS ECT and ASU ECT. [a]Data only include partial year (July 1 to December 31, 2011).

	ET (mm)		NEE (g C/m^2)		R_{eco} (g C/m^2)		GEP (g C/m^2)	
	ARS	ASU	ARS	ASU	ARS	ASU	ARS	ASU
2011[a]	279.17	281.25	-80.24	-45.01	218.86	191.03	299.10	236.07
2012	324.10	382.25	-54.48	-93.15	299.37	258.62	353.85	351.77
2013	285.67	360.34	-3.23	-57.31	285.46	279.67	288.70	336.98
2014	299.35	346.44	-43.27	1.03	315.38	302.61	358.66	301.59
2015	404.26	391.85	-51.27	-60.25	387.83	278.21	439.10	338.46
2016	423.44	395.57	-114.67	-116.85	419.97	266.95	534.64	383.79

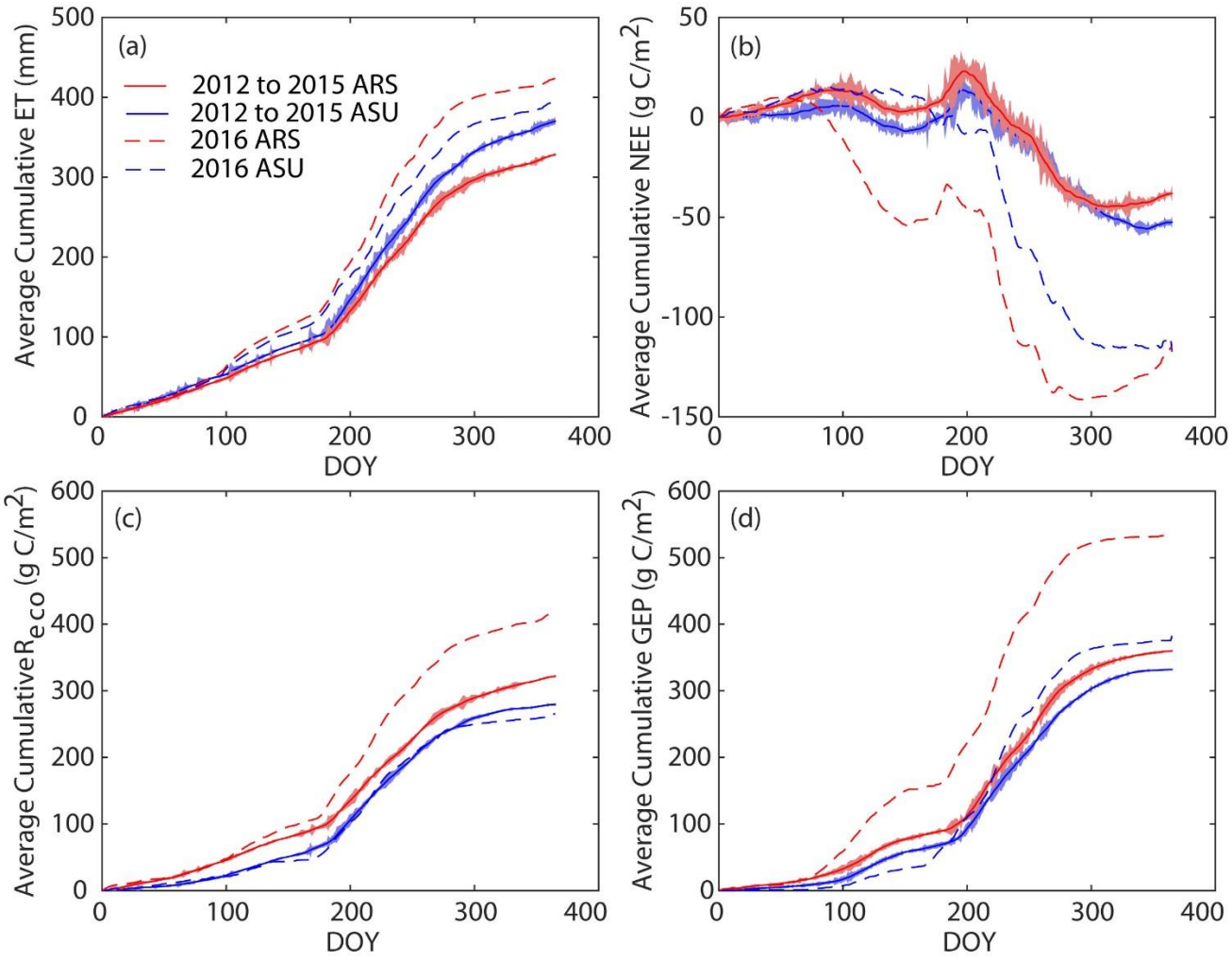

Figure 4.3. Average annual cumulative ET, NEE, Reco and GEP for each study year pre-treatment (solid line, 2012 to 2015) and pre/post-treatment (dashed line, 2016). Shaded areas represent standard deviation multiplied by a factor of 10, for presentation purposes.

ECT has higher ET in 2016, and the differences between the two sites increases post-treatment, which occurred on DOY 171. This would be due to minimal ET rates from mesquite trees post-treatment at ASU ECT, as the leaves were yellowing and falling off. Both sites also have high NEE release in 2016, due to the high precipitation input. For all years, R_{eco} is higher at ARS ECT compared to ASU ECT. The two highest R_{eco} years measured at ARS ECT is 2015 and 2016, while 2013 and 2014 had the highest measured R_{eco} years at ASU ECT. The slightly reduced R_{eco} value measured at ASU ECT in 2016 may be a consequence of BM. Similar patterns for the ARS ECT are shown with GEP estimates, where 2015 and 2016 have the highest values. This is likely due to the high precipitation measurements for both years, and evidence of the influence of water input on carbon fluxes (Scott et al., 2009). ASU ECT also had its highest GEP values in 2016, however 2015 was average.

ET, R_{eco}, and GEP show gradual inclines from DOY 0 to approximately DOY 180, at which point the inclines increase. The increase is due to the onset of the NAM and increased water availability. NEE shows more carbon release in the earlier part of the years (January to March), followed by carbon uptake until ~ DOY 180, due to the springtime growing season, which is dominated by the leafing of mesquite trees. The carbon release is likely a result of winter precipitation. After the onset of the NAM, there is a sharp increase in NEE (carbon release) observed at both sites for all years, associated with ecosystem respiration (Huxman et al., 2004), followed by high carbon uptake through summer and fall, with the curves leveling out by the end of the year as the vegetation and soil activity declined.

BM impacts on flux seasonality

Seasonal patterns of ET, NEE, R_{eco}, and GEP fluxes are further investigated to differentiate the impact of BM vs. precipitation between the two sites. Cumulative measurements were averaged over all pre-treatment full years (2012 to 2015) and then compared to the 2016 cumulative measurements. The measurements were then split into four different seasons, with winter representing January, February and March, spring representing April, May and June, summer is classified as July, August and September, and lastly, fall as October, November and December. Therefore, winter and spring periods represent differences caused by late season and high precipitation in 2015 (pre-treatment), while summer and fall differences are more likely caused by BM.

Cumulative ET (Figure 4.4) is generally greater at ASU ECT for winter, summer and fall for the 2012 to 2015 average, and is about the same between the two sites for spring. In 2016, the opposite trend was observed, where ARS ECT had higher ET measurements. Spring 2016 also had higher ET values at both sites compared to previous years. The higher ET estimates at ARS are likely due to the increased precipitation input from the previous year. There is a larger difference in ET measurements in summer time, which is likely a direct effect of the BM. With the mesquite trees dying back at ASU ECT, it is expected that a lot less ET would occur. However by fall, the difference is less substantial, due to the ineffectiveness of the mesquite treatment or the decreased activity of mesquite post NAM.

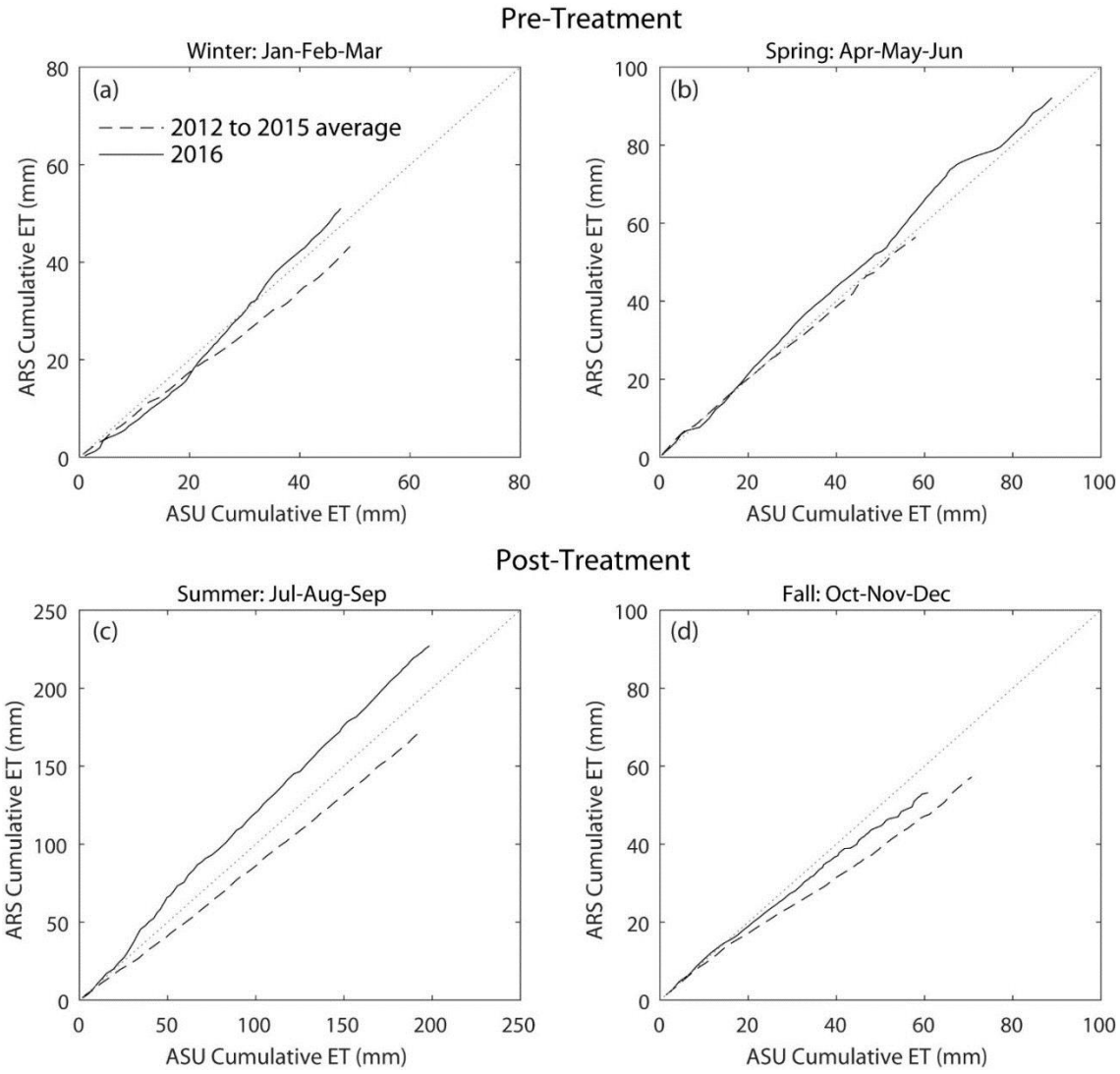

Figure 4.4. Cumulative ET for (a) winter, (b) spring, (c) summer, and (d) fall at ARS and ASU ECT sites for 2012 to 2015 average, and 2016.

Ecosystem respiration rates are greater at ARS ECT for all seasons and all years, with the exception of summer 2012-2015 average, where R_{eco} is about the same between the two sites (Figure 4.5). Cumulative R_{eco} is similar for winter, but there is a large difference observed at ARS ECT in early spring 2016. The time frame is when the mesquite trees are beginning to put on leaves (Cable, 1977). In the summer and fall

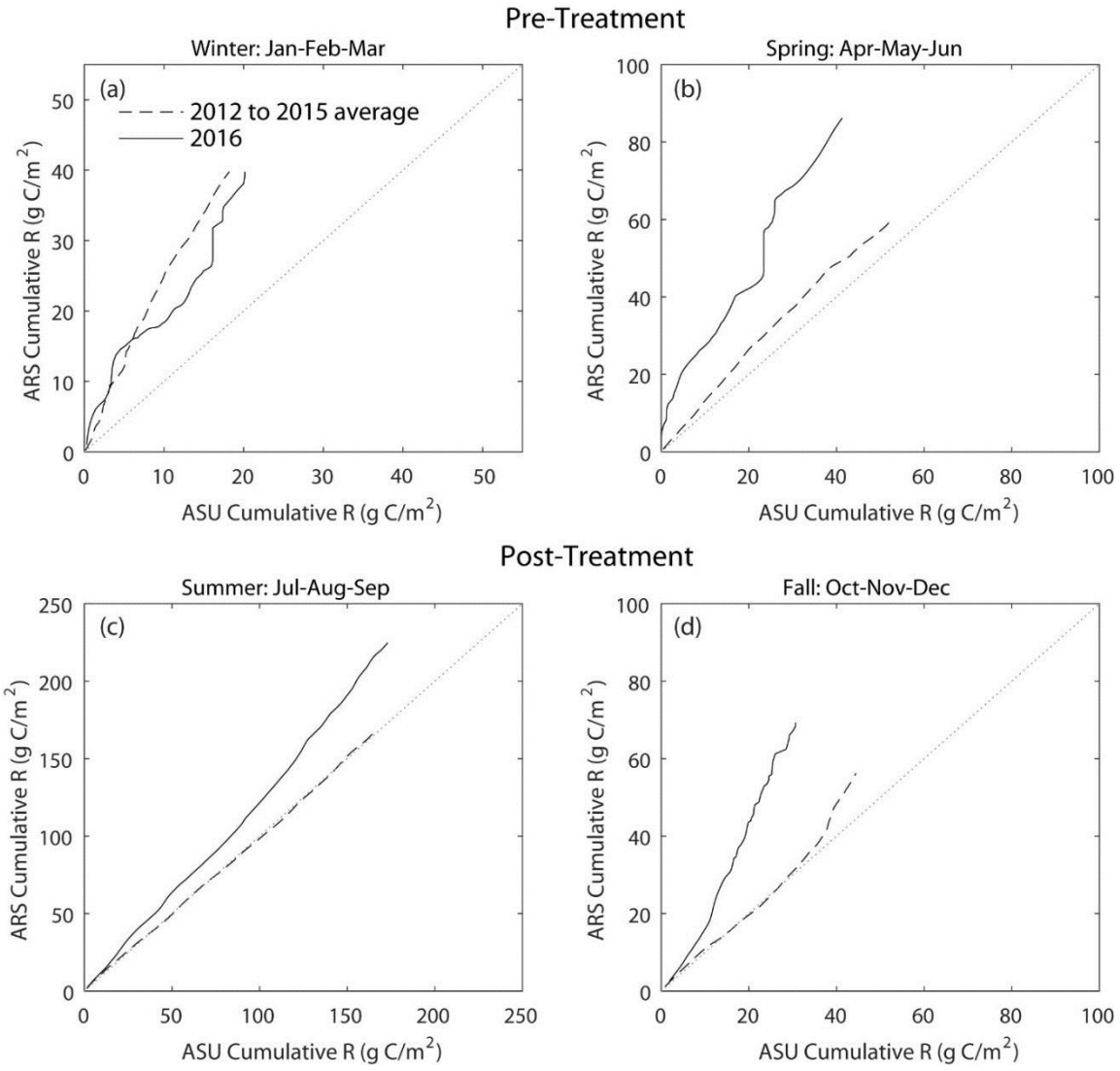

Figure 4.5. Cumulative R_{eco} for (a) winter, (b) spring, (c) summer, and (d) fall at ARS and ASU ECT sites for 2012 to 2015 average, and 2016.

periods, there is a lag in the difference between respiration curves, however as the seasons progress, ARS ECT measures greater R_{eco}. This may be a consequence of BM or a lasting effect of the preceding year's rainfall. Cumulative GEP has very different patterns in winter and spring 2016 compared to previous years (Figure 4.6), which is a direct consequence of preceding rainfall. GEP is substantially greater from winter

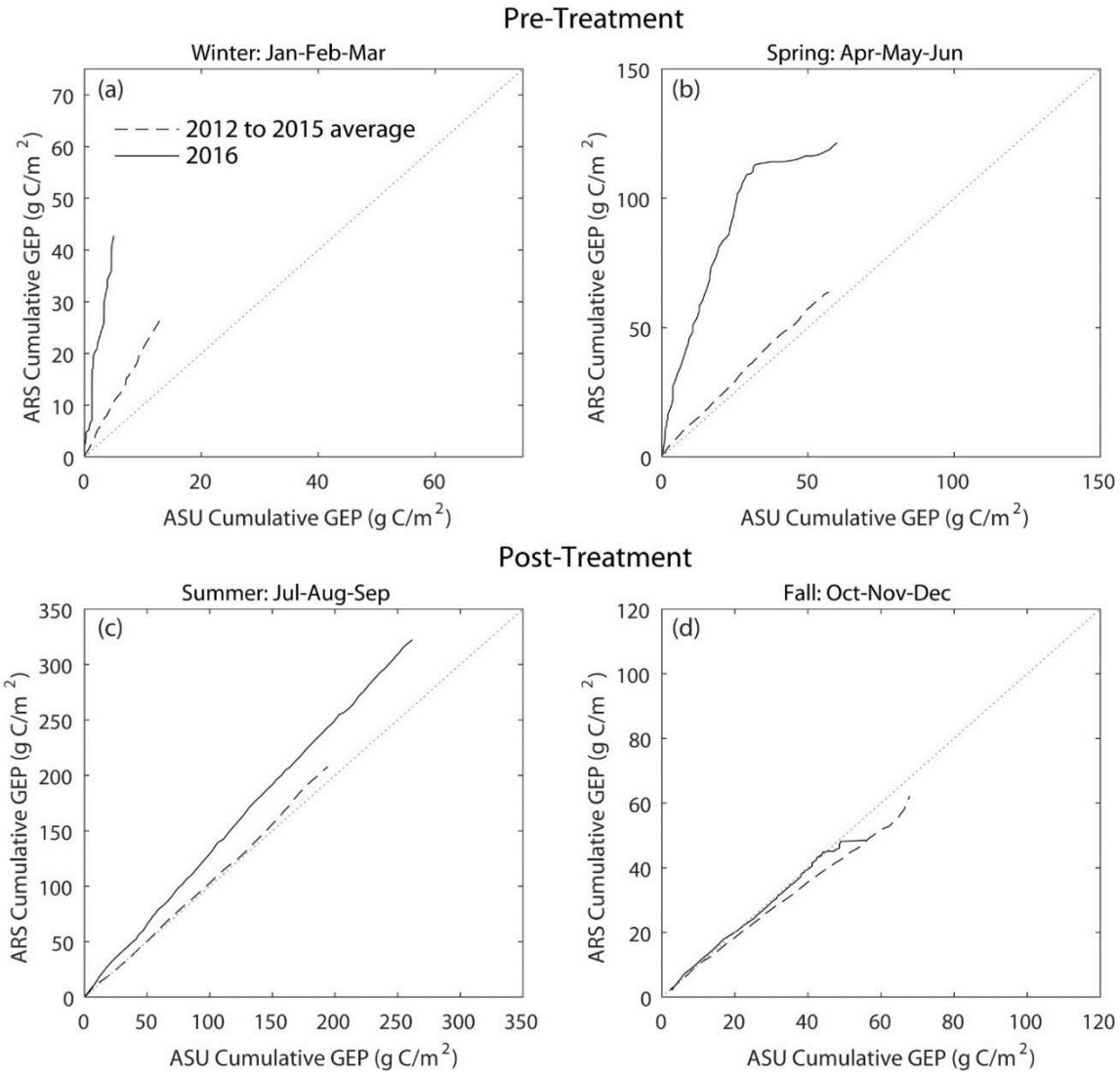

Figure 4.6. Cumulative GEP for (a) winter, (b) spring, (c) summer, and (d) fall at ARS and ASU ECT sites for 2012 to 2015 average, and 2016.

through mid-spring at ARS ECT, but begins to level off and ASU ECT site has a GEP increase during the late spring 2016 period. During the summer, GEP is higher at ARS ECT compared to ASU ECT. This is likely due to BM, but may also be a consequence of the late 2015 precipitation. The ASU ECT site has greater GEP for all years during the fall period, which is likely indicative of a larger amount of active grass cover.

Seasonal influence of ET on GEP pre and post-treatment

Summer and fall time periods were further analyzed to explore differences in P, ET, ET/P, GEP, and water use efficiency primarily due to BM. Cumulative P, ET, ET/P, and GEP summer and fall values are summarized for each year in Table 4.3 and Table 4.4, respectively. The ratios of ET/P and GEP/ET are computed to estimate water use efficiency at each site. In 2016, both sites have a higher than average rainfall during summer, and lower than average during fall, especially at ARS ECT. ET follows a similar trend, where ARS and ASU are slightly greater than average during the summer, and lower during the fall. ET/P is greater at ARS ECT during summer 2016, however, the low P amount results in a very high ET/P ratio for fall 2016 at ARS ECT, whereas ET/P is approximately average at ASU ECT for both time periods. Cumulative GEP is highest at ARS ECT and ASU ECT for summer 2016, compared to previous years. Typically, ARS ECT has a GEP/ET ratio >1 during the summer time, while the ASU ECT GEP ratio is ~1. The average summer GEP/ET ratio for 2011 to 2015 is 1.20 and 0.99 at ARS ECT and ASU ECT sites, respectively. The GEP/ET ratio for 2016 is higher at both sites, although the increase at ARS ECT is 0.22 compared to an increase of 0.33 at ASU ECT. Although summer 2016 ET is more or less consistent with previous years at ASU ECT, the increased GEP values indicate that the ecosystem became more water use efficient post BM, or that ET was less affected by the treatment than GEP. During the fall period, ET and GEP values in 2016 were smaller than the averaged 2011 to 2015 values. However, GEP/ET ratios are relatively similar to previous years, with the average difference at ARS ECT of -0.14, and the average difference at ASU ECT of only 0.01.

Thus, it does not appear BM has a lasting effect on water use efficiency through the fall period, likely due to the lack of effectiveness with the mesquite treatment after the summer period.

Comparing EVI and albedo observations from MODIS reveals differences post-treatment (Figure 4.7). EVI differneces are greatest in July, where the two sites differ by 0.0614 (ARS value – ASU value), compared to an average difference of 0.0288 in July pre-treatment (2012 to 2015). The two sites behave similarly to past conditions in August, however there is another large difference in EVI in September, where the difference in 2016 is greater than the average difference of previous years (2016: 0.0415, 2012 to 2015: 0.0149). October, November and December are similar to pre-treatment averages, with 2016 differences of 0.0008, -0.0070, and -0.0023, compared to 2012 to 2015 values of 0.0014, -0.0044, and 0.0029, respectively. Generally, albedo values are less at ARS ECT and ASU ECT for July, August, and September compared to pre-treatment years, and greater for October, November, and Decmeber. The differences are likely a reflection of the larger than average rainfall measured during the summer 2016 period, and the less than average rainfall during fall 2016 measured at both sites, which impacts vegetation response. Pre-treatment years show a larger difference between the two sites in albedo measurements from July to December, with an average difference of 0.0046 compared to 0.0026 for 2016. The reduction in albedo values at ASU ECT is a direct consequence of the mesquite treatment.

Table 4.3. Summer cumulative ET, GEP for 2011 to 2016, and ET/P and GEP/ET, including an average value computed from 2011 to 2015 data.

Summer	P (mm)		ET (mm)		ET/P		GEP (g C/m$^{2)}$		GEP/ET	
	ARS	ASU	ARS	ASU	ARS	ASU	ARS	ASU	ARS	ASU
2011	273.30	245.36	207.57	201.17	0.76	0.82	235.42	180.49	1.13	0.90
2012	218.94	233.89	170.09	185.73	0.78	0.79	209.15	194.63	1.23	1.05
2013	191.51	211.07	168.65	202.52	0.88	0.96	201.88	218.71	1.20	1.08
2014	218.19	219.20	159.25	204.43	0.73	0.93	205.80	200.23	1.29	0.98
2015	248.67	186.56	188.28	177.31	0.76	0.95	214.67	163.27	1.14	0.92
Average	230.12	219.22	178.77	194.23	0.78	0.89	213.38	191.47	1.20	0.99
2016	240.28	242.06	227.11	198.48	0.95	0.82	322.03	261.58	1.42	1.32

Table 4.4. Fall cumulative ET, GEP for 2011 to 2016, and ET/P and GEP/ET, including an average value computed from 2011 to 2015 data.

Fall	P (mm)		ET (mm)		ET/P		GEP (g C/m$^{2)}$		GEP/ET	
	ARS	ASU	ARS	ASU	ARS	ASU	ARS	ASU	ARS	ASU
2011	104.14	92.20	71.59	80.09	0.69	0.87	63.68	55.58	0.89	0.69
2012	45.21	40.64	48.00	73.58	1.06	1.81	51.91	69.57	1.08	0.95
2013	66.04	56.27	35.32	65.52	0.53	1.16	38.53	76.43	1.09	1.17
2014	91.44	91.06	55.15	65.50	0.60	0.72	58.86	56.90	1.07	0.87
2015	85.85	79.38	90.18	78.13	1.05	0.98	99.30	68.23	1.10	0.87
Average	78.54	71.91	60.05	72.56	0.79	1.11	62.46	65.34	1.05	0.91
2016	25.50	57.15	53.16	60.80	2.09	1.06	48.51	55.92	0.91	0.92

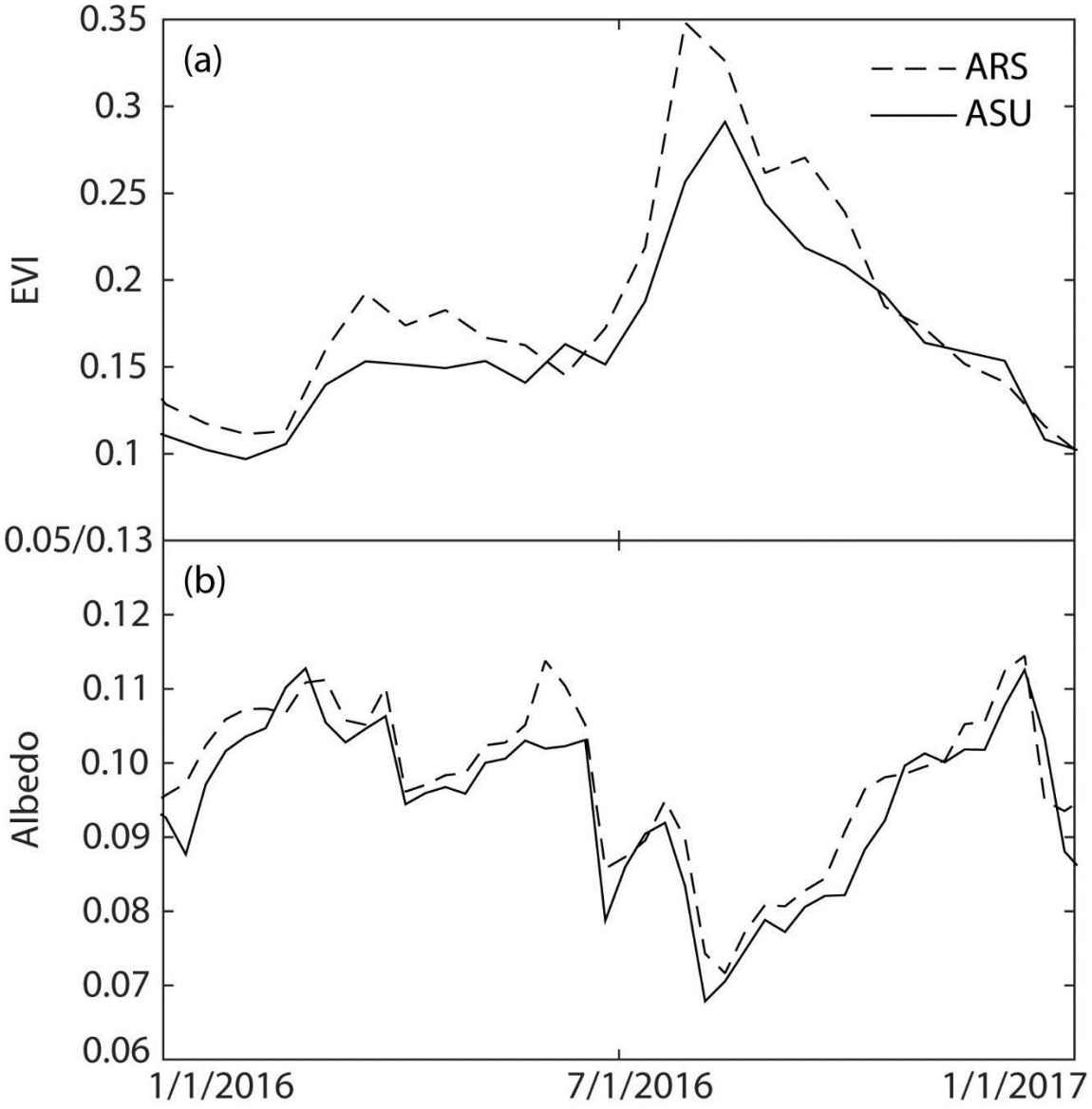

Figure 4.7. Measurements and data from January 1, 2016 to December 31, 2016, including (a) MODIS enhanced vegetation index (EVI), and (b) MODIS albedo.

Table 4.5. Linear regressions and correlation coefficients for annual R_{eco} vs. ET data and GEP vs ET data at ARS ECT and ASU ECT, including pre-treatment years, and pre and post-treatment years.

	ARS ECT		ASU ECT	
	Regression	R^2	Regression	R^2
2012-2015 R_{eco}	y=1.1x-33.3	0.78	y=0.7x+18.6	0.53
2012-2016 R_{eco}	y=1.1x-44.4	0.88	y=0.6x+46.1	0.47
2012-2015 GEP	y=1.1x-5.4	0.89	y=1.0x-37.9	0.91
2012-2016 GEP	y=1.4x-99.4	0.91	y=1.1x-71.5	0.89

R_{eco} and GEP relationship to ET pre and post-treatment

Annual totals of R_{eco} and GEP were plotted against ET to evaluate the relationship between water availability and carbon fluxes over different years at the two sites. A linear regression was applied to the data points and is reported in Table 4.5, along with the correlation coefficient (R^2). Data was evaluated for two distinct time periods: only pre-treamtent years (2012 to 2015), and all years (2012 to 2016), where 2016 serves as a pre/post-treatment year (with BM occurring half way through the year). Both R_{eco} and GEP trends have positive slopes, indicating that as ET (and water availability increases), R_{eco} and GEP increase. ARS ECT has a stronger relationship between R_{eco} and ET compared to ASU ECT. The slope of R_{eco} vs. ET is greater at ARS ECT compared to ASU ECT. Similar trends are observed with GEP and ET, where the slopes are greater at ARS ECT. Including the pre/post-treatment year of 2016 increases the slope of GEP and ET at both sites, therefore greater water availability leads to greater GEP. When evaluating R_{eco}, the slopes do not change at ARS ECT and slightly decrease at ASU ECT, indicating that the increased ET value in 2016 does not impact the relationship between ET and R_{eco}, however the relationship at ASU ECT is relatively weak.

Diurnal Flux Variability Post-Treatment

Average diurnal fluxes for ET were computed to inspect monthly differences post-treatment, specifically July to October 2016 (Figure 4.8). Initially, ARS ECT has higher ET fluxes, particularly mid-day. BM reduces ET at ASU ECT. The ARS ET values are fairly similar between July and August, however, ASU ECT ET rates increase and are slightly higher compared to ARS ECT in August. It is possible the grasses that become active with the NAM overcome the missing mesquite fluxes. MODIS EVI data shows similar values between the two sites in August as well. Interestingly, in September the ET fluxes between the two sites are very similar, regardless of the time of day. ET continues to decrease at both sites into October, however, ASU ECT has greater values, which is likely due to the larger grass cover, whereas the mesquite trees at ARS ECT would become less active.

Mean monthly diurnal NEE fluxes are also evaluated from July to October 2016 (Figure 4.9). At nighttime, positive NEE fluxes in July, August, and September indicate respiration due to increased soil moisture and warm temperatures (Scott et al., 2009). By October, positive nighttime NEE fluxes are minimal. Large negative NEE values indicate photosynthesis, which typically occurs around midday, or slightly earlier. July has relatively large NEE uptake, and ARS ECT is larger compared to ASU ECT. This is likely a consequence of BM. Both sites have larger NEE uptake fluxes in August, however, similarly to ET, ASU ECT is larger. The similar patterns reinforce the coupling between ET and NEE. The NEE fluxes behave very similarly between the two sites in September, and are slightly smaller (magnitude) than the previous months. In October,

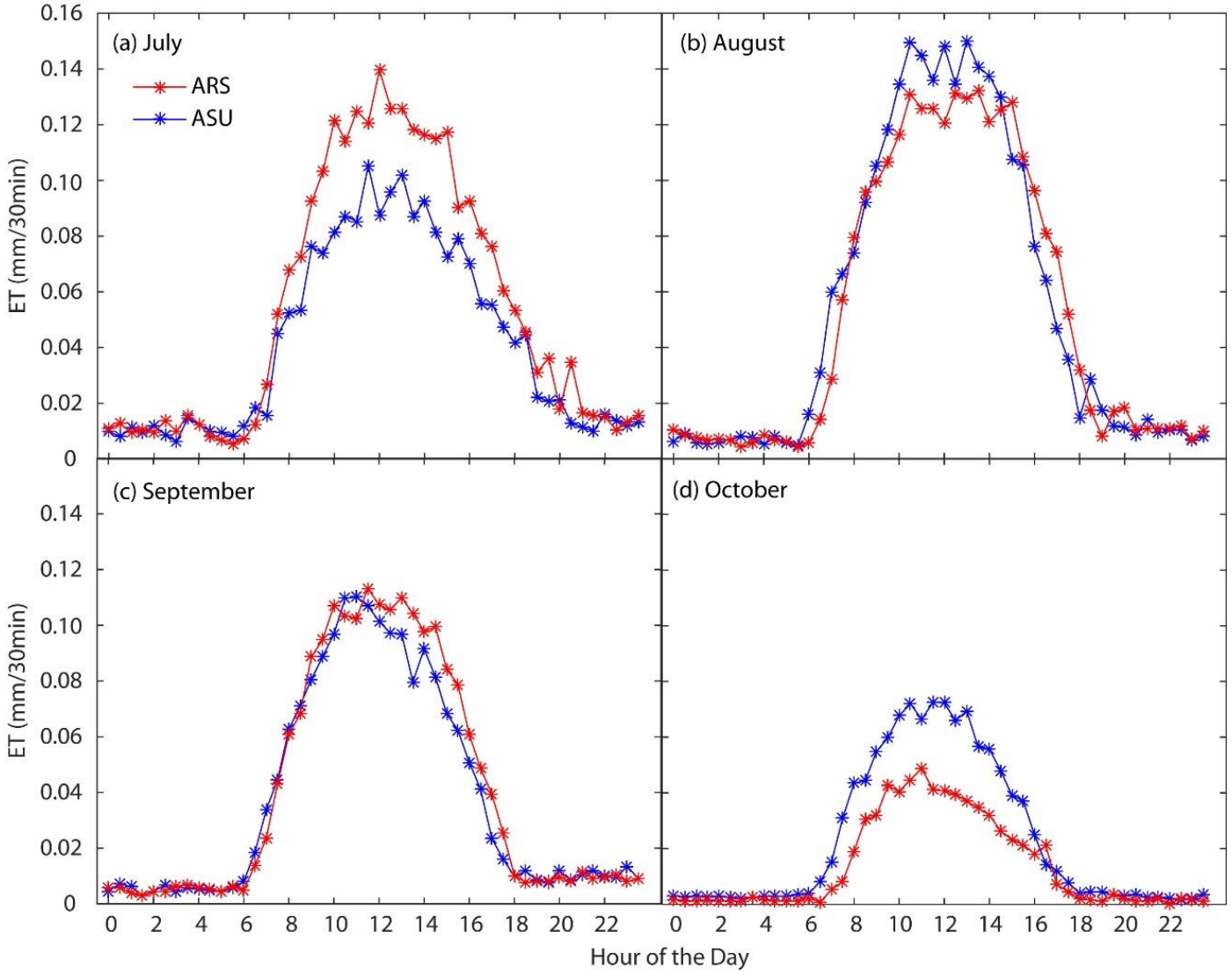

Figure 4.8. Mean monthly diurnal ET in 2016 for (a) July, (b) August, (c) September, and (d) October.

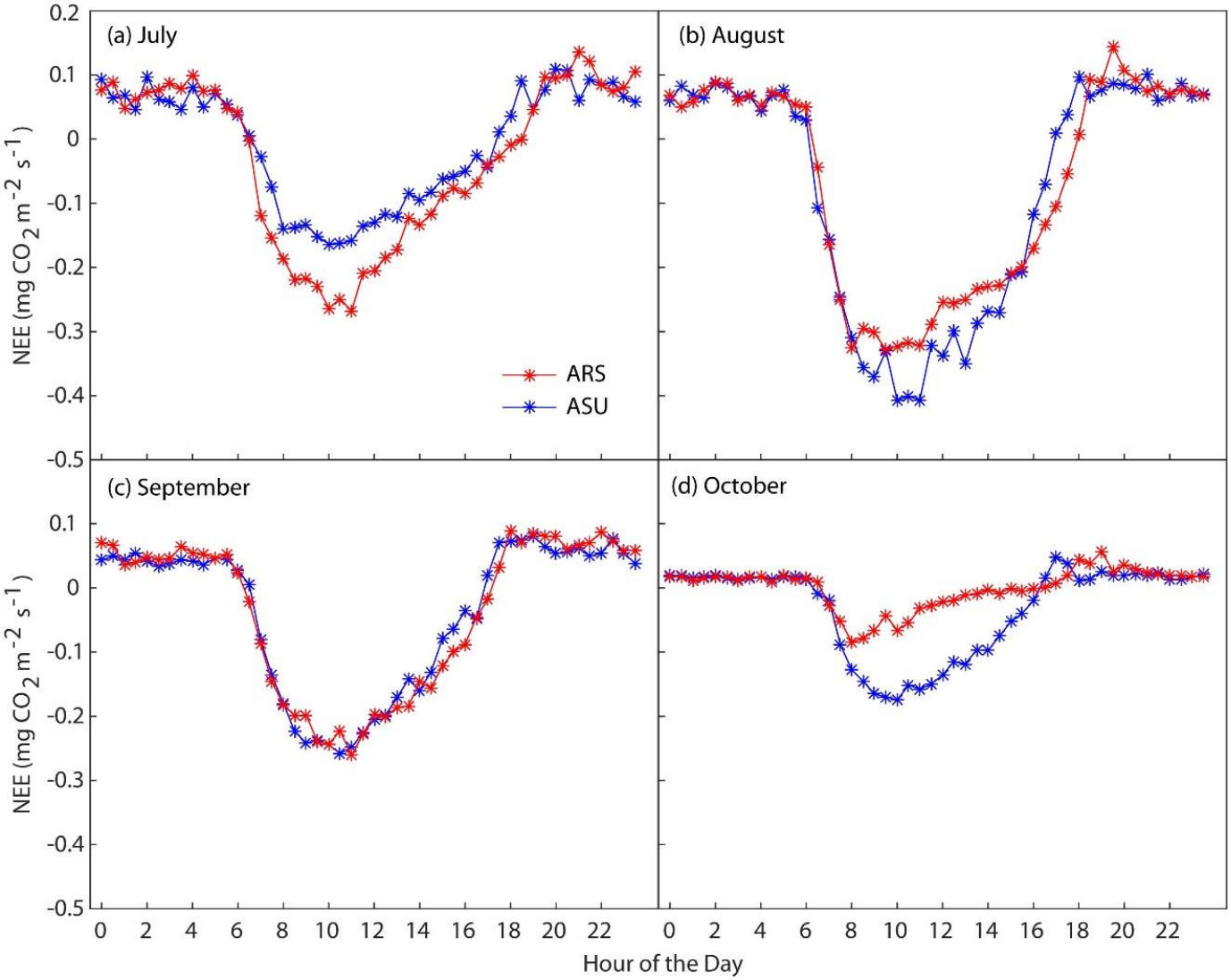

Figure 4.9. Mean monthly diurnal NEE in 2016 for (a) July, (b) August, (c) September, and (d) October.

NEE uptake is much smaller, particularly at the ARS ECT. The ASU site tends to peak NEE uptake around 10:00-11:00 for all months, while the ARS site has an abnormal peak in October, around 8:00. NEE fluxes becoming less negative in October is reflective of the drier and cooler conditions, as vegetation and soil activity is expected to decrease (Scott et al., 2009). It is possible that the impact of BM treatment was minimal by October.

SUMMARY AND CONCLUSIONS

The impact of brush management (BM) on ecosystem services, particularly water and carbon fluxes is not well understood. In this study, two eddy covariance towers are compared to evaluate the initial impacts of an aerially applied mesquite treatment. Water and carbon fluxes, specifically ET, NEE, R_{eco}, and GEP, are evaluated between the two sites to determine if and what differences are caused from mesquite treatment in the water and carbon cycles. Comparing flux measurements allows for greater insight into the initial impact of mesquite treatment, including:

Although 2015 and 2016 were relatively wet years at both sites, ARS ECT received substantially more rainfall in 2015, which strongly influences the water and carbon fluxes measured in early 2016. ET values increased at both sites for 2016, indicative of increased precipitation, however the difference in ET between ARS ECT and ASU ECT increases post-treatment. This is likely due to the lack of mesquite trees to transpire water with the onset of the NAM. R_{eco} is greater at ARS ECT, regardless of the year, and is highest during 2016. R_{eco} observed at ASU ECT for 2016 is average compared to the record of study years, thus its low value may be due to BM, but could

also be influenced by less rainfall from 2015 compared to ARS ECT. GEP in 2016 is strongly influenced by the high rainfall during the previous year at ARS ECT. Winter and spring 2016 periods show the greatest difference between ARS ECT and ASU ECT in GEP.

Water use efficiency, determined by GEP/ET ratio, is higher in summer 2016 for both sites compared to previous years, with the increase greater at ASU ECT compared to ARS ECT. No changes are detected during fall 2016, possibly indicating that BM was no longer impacting the ecosystem. Mean monthly diurnal flux analysis reinforces the coupling between ET and NEE. In July 2016, ARS has greater ET fluxes and more NEE uptake. The pattern shifts in August, where ARS has greater ET fluxes and more negative NEE fluxes. In September, the sites behave very similarly, and by October, the fluxes are smaller, but ASU ECT has greater ET and more negative NEE. Evidence from GEP/ET ratios and diurnal analysis indicate that BM impact was likely minimal by fall 2016.

This study relies on paired eddy covariance towers, which allowed for the differentiation between climate related differences and differences related to BM on post-treatment fluxes. Due to the ineffectiveness of the first mesquite treatment beyond the summer period, a future aerial herbicide application will likely take place and the comparisons presented in this study can guide future comparisons. From evaluating initial impacts to water and carbon fluxes, it is evident that BM impacts several ecosystem services, and the extent of that impact is unknown, especially at long time scales.

CHAPTER 5

CONCLUSIONS AND FUTURE WORK

GENERAL CONCLUSIONS

Urbanization, woody plant encroachment and brush management are land cover changes that are representative of the southwestern United States. Land cover change directly and indirectly affects surface energy, water, and carbon fluxes, which impacts the local, regional and global cycles and surface-atmosphere interactions. Thus, it is vital to understand land surface composition impacts on flux measurements.

While model applications have indicated that the built environment impacts energy and water exchanges (e.g., Song and Wang, 2015; Wang *et al*., 2016), few studies have directly observed the effects of different urban land cover types on the surface energy balance or the partitioning of turbulent fluxes. In Chapter 2, meteorological fluxes were measured using the eddy covariance technique to obtain a detailed quantification of SEB processes and relate them to the urban land cover distributions within the sampled footprints of three short-term deployments and a stationary reference site in Phoenix. Comparisons of standard weather variables, meteorological fluxes and normalized SEB quantities between the mobile and reference sites were carried out to account for the effect of time-varying (seasonal) conditions during the short-term deployments. Results from the observational comparisons across sites, seasons and urban land cover types indicated that meteorological conditions were similar between the sites, but had small biases attributed to variations in vegetated land cover, with a higher *TA* at the REF site as compared to the XL and ML sites. Despite these similarities, large biases were noted in

the time-averaged Q^*, with the REF site having values of 7 to 43 W/m^2 less than the other sites, attributed to the larger radiometer footprint and its differences in impervious surfaces and undeveloped land cover. Also, individual radiation components provided insight into the large differences in Q^* among sites by isolating the effects of albedo on $K_{\uparrow}$ and of shallow soil temperature on $L_{\uparrow}$. Lower Q^* at the REF site was found to be either due to a higher albedo (relative to xeric landscaping at XL), a higher soil temperature (relative to mesic landscaping at ML) or a combination of both factors (relative to the parking lot at PL). The surface energy balance revealed sharp differences in the partitioning between sensible and latent heat flux among the sites based upon normalized quantities. For instance, *EF* was found to be much larger in the irrigated turf grass at ML, where a higher $(Q_H+Q_E)/Q_{\downarrow}$ was also measured. Sensible heat flux, on the other hand, was the dominant flux and exhibited lower variations among the other sites, suggesting less frequent or extensive outdoor water use. Lastly, the sensitivity of SEB processes to precipitation events varied considerably among the sites in accordance with the soil moisture conditions established through outdoor water use. While different urban land covers support similar sensible heat flux under different weather conditions, the latent heat flux varies significantly at those locations that are water-limited, whereas frequent sprinkler irrigation at ML renders the *EF* insensitive to additional water input.

Based upon these comparisons, key differences in the surface energy balance among the sites can be attributed to the urban land cover contained in the measurement footprints, including the frequency and amount of outdoor water use. These results could be especially beneficial to urban planners and help with the design of city spaces. The

eddy covariance measurements provide a needed insight to flux measurements over specific urban patches. An urban area will encompass different urban patches set in a unique pattern, which with the additional understanding obtained from this work, can help optimize urban conditions for improved thermal comfort or water conservation.

A different type of land cover change in the southwestern United States is evaluated in Chapters 3 and 4. Grasslands and savannas are particularly susceptible to woody plant encroachment. These semiarid systems can represent different scales of heterogeneity, due to vegetation changes such as woody plant encroachment, or other disturbances that impact vegetation distribution. Woody plant encroached landscapes and subsequent brush management lead to changes in ecosystem services that are not well understood.

In Chapter 3, observations are compared from two eddy covariance towers in the Sonoran Desert which represent landscapes that have undergone the encroachment of velvet mesquite (*Prosopis velutina* Woot.). While the sites are nearby, they have experienced different disturbance histories, which is well documented through the SRER data archives (McClaran, 2003). The ARS ECT has remained relatively untouched, while areas close by the ASU ECT have undergone mesquite treatment in the 1970s and a fire in 1994. Comparisons between the two sites reveal that mesquite, grass, and bare cover vary between the two sites, where the ARS ECT has a greater amount of mesquite (30% vs. 15%) and the ARS ECT has a greater amount of grass (25% vs. 18%). Mesquite canopies are taller at the ARS ECT compared to the ASU ECT. Differences in vegetation cover are likely due to historical disturbance differences and soil differences.

Precipitation measured at four different rain gauges varies depending on the year, with a significant difference in 2015. Spatial variability due to NAM type storms causes differences in precipitation totals. The different types of rain gauges used (weighing vs. tipping bucket) also needs to be considered. Net radiation is higher at the ARS ECT site from April to September, and lower from October to March. Net radiation is likely higher due to the differences in mesquite cover, where the mesquite begins to leaf out in April, which could lower surface temperature. Net radiation is higher at the ASU ECT site from October to March, possibly because annual grasses fill in bare areas, reducing albedo and surface temperature. More grass cover is observed at ASU ECT, expected because of less mesquite cover at the site. Sensible heat flux (H) is greater at ARS ECT from October to February, likely due to less grass cover. ASU ECT has higher H values from March to September, which may be a result of less mesquite cover. Latent heat flux (LE) peaks in July at both sites, expected with the increase in precipitation, and remains high during the NAM. LE is greater at ASU ECT for all months with the exception of June. The difference in LE between the two sites may be indicative of the grass cover differences and the relatively strong influence of grass to latent heat. Cumulative evapotranspiration (ET) differences between the two sites is dependent on precipitation differences. Greater ET is measured at ASU ECT for 2011to 2014, which may be indicative of fewer, smaller mesquite trees, thus less shading. ARS has greater ET in 2015 and 2016, corresponding with larger precipitation measured. Cumulative net ecosystem exchange (NEE) differences varies from year to year between the two sites. There is greater carbon uptake at ARS ECT in 2011 (partial year), 2014, and 2016 (partial year), otherwise ASU ECT

site has greater carbon uptake. Cumulative respiration (R_{eco}) is greater at the ARS ECT for all study year periods. This is likely due to the greater mesquite coverage. Cumulative gross ecosystem production (GEP) follows trends similar to cumulative ET and precipitation. When there is more water available, there is generally more GEP. Daytime dominant wind directions at both sites is from the southwest, regardless of minimum wind speed. There is also a strong wind influence from the east-southeast and north-northwest directions, which is emphasized when wind speed is greater than 2 m/s. Mesquite coverage varies radially around each tower, with greater variability around ASU ECT, indicating greater heterogeneity. Grass and bare (soil) coverage also varies radially, and is greater at ASU ECT, however the differences between the two sites are more uniform. When evaluating fluxes radially, ASU ECT has more wind directions where H, LE, and carbon fluxes are greater, on average. Generally, both sites act as carbon sinks, however the ARS ECT site is moreso, which is a refelction of mesquite cover differences. By evaluating these two datasets, the effect of different vegetation cover and soil type on energy and carbon fluxes can be quantified, even though the sites are relatively close to one another and represent the same type of ecosystem. Quantifying the differences will provide knowledge of how the woody-plant encroached landscape's disturbance histories impact their current states.

The impact of brush management (BM) on water and carbon fluxes is not well understood, and could influence the management of rangelands. In Chapter 4, two eddy covariance towers are compared to evaluate the initial impacts of an aerially applied mesquite treatment. Water and carbon fluxes, specifically ET, NEE, R_{eco}, and GEP, are

evaluated between the two sites to determine if and what differences are caused from mesquite treatment in the water and carbon cycles. Comparing flux measurements allows for greater insight into the initial impact of mesquite treatment. Although 2015 and 2016 were relatively wet years at both sites, ARS ECT received substantially more rainfall in 2015. High precipitation values observed at ARS ECT during 2015 strongly influences the carbon fluxes measured in early 2016. ET values increased at both sites for 2016, indicative of increased precipitation, however the difference in ET between ARS ECT and ASU ECT increases post-treatment. This is likely due to the lack of mesquite trees to transpire water with the onset of the NAM. R_{eco} is greater at ARS ECT, regardless of the year, and is highest during 2016. R_{eco} observed at ASU ECT for 2016 is about average for all of the study years, thus its low value may be due to BM, but could also be influenced by less rainfall from 2015 compared to ARS ECT. GEP in 2016 is strongly influenced by the high rainfall during the previous year at ARS ECT. Winter and spring 2016 periods show the greatest difference between ARS ECT and ASU ECT in GEP. Water use efficiency, determined by GEP/ET ratio, is higher in summer 2016 for both sites compared to previous years, with the increase greater at ASU ECT compared to ARS ECT. No changes are detected during fall 2016, possibly indicating that BM was no longer impacting the ecosystem. Lastly, mean monthly diurnal flux comparisons reinforce the coupling between water availability (ET) and carbon fluxes (NEE). ARS ECT has greater ET fluxes and more negative NEE fluxes in July 2016, likely a direct consequence of BM. However the pattern shifts in August and October, where ASU ECT has higher ET fluxes and more carbon uptake. October differences are likely due to the

impact of greater grass cover at ASU ECT. Both the water use efficiency and diurnal analyses indicate that BM impact is seemingly minimized by fall 2016. Although the comparison period is short, it is apparent that BM will impact water, energy, and carbon fluxes, and may do so in unexpected ways. This analysis provides rangeland managers greater insight to the impact of BM, however unknown climate patterns (e.g. drought or increased rainfall) or land use decisions will also play a role into how the landscape reacts to BM. Chapters 3 and 4 rely on paired eddy covariance towers, which enables differentiation between climate related impacts and impacts related to BM on post-treatment fluxes.

FUTURE WORK

There are several different avenues to which this work may be expanded. Land cover is dynamic and understanding how it influences energy, water, and carbon cycles is vital, especially in semiarid ecosystems.

In Chapter 2, the mobile deployments only sampled individual seasons, however comparisons to the reference site provided an opportunity to draw the important conclusions listed above. Nevertheless, it would be desirable to conduct cross-site comparisons over a full year and to improve the correspondence in the footprint dimensions among deployments. Longer comparisons, for instance, could be used to evaluate if frequent or high outdoor water use effectively decouples turbulent flux partitioning from precipitation during other seasons. Furthermore, additional studies are needed to verify if the application of urban irrigation can be an effective proxy for quantifying the spatiotemporal variability of the surface energy balance in arid urban

areas. A fruitful avenue would be the validation of a numerical model that simulates urban energy and water fluxes (e.g., Grimmond and Oke, 1991; Järvi *et al.*, 2011; Wang *et al*., 2013) and its subsequent application to quantify the link between urban irrigation and SEB processes. Based on this approach, considerable improvements could be made in estimating the spatiotemporal variability of the urban surface energy budget in desert cities.

Chapter 3 emphasizes the heterogeneity within semiarid ecosystems and how two nearby sites can behave differently with respect to energy, water and carbon fluxes. Further insight into differences between the two sites could be obtained by inspecting event-scale responses to fluxes. It would also be fruitful to expand the comparison analysis over a longer time period, where differences can be established during wetter and drier years, or wetter and drier NAM periods. It may also be beneficial to look into additional remote sensing products, such as Landsat, where differences in vegetation phenology could become more apparent at a finer spatial resolution. Using photosynthetic active radiation (PAR) measurements from both sites can also help identify vegetation differences observed at each tower. To further analyze ecosystem respiration differences, night-time and day-time estimates can be compared to identify when the differences are occurring. Additionally, analyzing runoff measurements from nearby watersheds that lie on similar soils to ASU ECT and ARS ECT can offer a deeper analysis into the ET/P ratio differences, and possibly help explain why the higher grass and bare soil cover at ASU ECT supports higher ET compared to ARS ECT with greater mesquite coverage.

In Chapter 4, further comparisons can be made by identifying specific time periods that have similar climatic conditions pre-treatment and post-treatment. Additionally, the use of additional remote sensing products at a finer spatial resolution, such as Landsat, can help discern vegetation differences post-treatment. Finally, due to the ineffectiveness of the first mesquite treatment beyond the summer period, another aerial herbicide application will take place and the comparisons presented can guide future efforts. From evaluating initial impacts to water and carbon fluxes, it is evident that BM impacts several ecosystem services, and the extent of that impact is unknown, especially at long time scales.

REFERENCES

Abrahams, A.D., A.J. Parsons, and J. Wainwright, 2003: Disposition of rainwater under creosotebush, *Hydrol. Process.*, **17**(13), 2555 – 2566, doi:10.1002/hyp.1272.

Adams, D.K. and A.C. Comrie,1997: The North American Monsoon. *Bull. Am. Meteorol. Soc.*, **78**, 2197 – 2213.

Alfieri, J.G., and P.D. Blanken, 2012: How representative is a point? The spatial variability of surface energy fluxes across short distances in a sand-sagebrush ecosystem, *J. Arid Environ.*, **87**, 42 – 49.

Anderson, C.A., 2013: *Assessing Land-Atmosphere Interactions through Distributed Footprint Sampling at Two Eddy Covariance Towers in Semiarid Ecosystems of the Southwestern U.S.* Masters of Science in Civil, Environmental and Sustainable Engineering, Arizona State University, 243 pp.

Anderson C.A., and E.R. Vivoni, 2016: Impact of land surface states within the flux footprint on daytime land-atmosphere coupling in two semiarid ecosystems of the southwestern U.S. *Water Resour. Res.*, **52**, 4785 – 4800, doi:10.1002-2015WR018016.

Archer, S., D.S. Schimel, and E.A. Holland, 1995: Mechanisms of shrubland expansion: land use, climate or CO2, *Clim. Change*, **29**, 91 – 99.

Archer, S., T.W. Boutton, and K.A. Hibbard, 2001: Trees in grasslands: biogeochemical consequences of woody plant expansion, in *Global Biogeochemical Cycles in the Climate System*, edited by E.-D. Schulze et al., pp. 115 – 138, Academic, San Diego, Calif.

Archer, S., 2010: Rangeland conservation and shrub encroachment: new perspectives on an old problem, in *Wild Rangelands: conserving wildlife while maintaining livestock in semiarid ecosystems*, edited by J. du Toit R. Kock, and J. C. Deutsch, pp. 53-97, John Wiley & Sons, Ltd, Chichester, UK. doi: 10.1002/9781444317091.ch4.

Archer, S. and K.I. Predick, 2014: An ecosystem services perspective on brush management: research priorities for competing land-use objectives, *J. Ecol.*, **102**, 1394 – 1407, doi:10.1111/1365-2745.12314.

Arnfield A.J., 2003: Two decades of urban climate research: a review of turbulence, exchanges of energy and water, and the urban heat island. *Int. J. Climatol.*, **23**, 1 – 26.

Aubinet, M., 2000: Estimates of the annual net carbon and water exchange of forests: the EUROFLUX methodology, *Adv. Ecol. Res.*, **30**, 113 – 175.

Bailey, R.G., 1996: Ecosystem geography, Springer, New York, New York, USA, 251 pp.

Baldocchi D., B.B. Hicks, and T.P. Meyers, 1988: Measuring biosphere-atmosphere exchanges of biologically related gases with micrometeorological method, *Ecology*, **69**, 1331 – 1340.

Baldocchi, D., E. Falge, L. Gu, R. Olson, D. Hollinger, S. Running, P. Anthoni, C. Bernhofer, K. Davis, R. Evans, J. Fuentes, A. Goldstein, G. Katul, B. Law, X. Lee, Y. Malhi, T. Meyers, W. Munger, W. Oechel, U.K.T. Paw, K. Pilegaard, H.P. Schmid, R. Valentini, S. Verma, T. Vesala, K. Wilson, and S. Wofsy, 2001: FLUXNET: a new tool to study the temporal and spatial variability of ecosystem scale carbon dioxide, water vapor, and energy flux densities, *Bull. Am. Meteorol. Soc.*, **82**, 2415 – 2434.

Baldocchi, D.D., 2003: Assessing the eddy covariance technique for evaluating carbon dioxide exchange rates of ecosystems: past present and future, *Glob. Chang. Biol*. **9**, 479 – 792.

Bassett R., X. Cai, L. Chapman, C. Heaviside, J.E. Thornes, C.L. Muller, D.T. Young, and E.L. Warran, 2016: Observations of urban heat island advection from a high-density monitoring network, *Q. J. R. Meteorol. Soc*., **142**, 2434 – 2441.

Benson-Lira V., M. Georgescu, S. Kaplan, and E.R. Vivoni, 2016: Loss of a lake system in a megacity: The impact of urban expansion on seasonal meteorology in Mexico City, *J. Geophys. Res.,* **121**, 3079 – 3099.

Best M.J and C.S.B. Grimmond, 2016: Modelling the partitioning of turbulent fluxes at urban sites with varying vegetation cover, *J. Hydrometeorol*., **17**, 2537 – 2553.

Betts R.A., 2001: Biogeophysical impacts of land use on present-day climate: near-surface temperature change and radiative forcing, *Atmos. Sci. Lett.*, **2**, 39 – 51, doi:10.1006/asle.2001.0023.

Bounoua L., R. Defries, G.J. Collatz, P. Sellers, and H. Khan, 2002: Effects of land cover conversion on surface climate, *Clim. Chang.*, **52**, 29 – 64.

Breckenfeld, D.J. and D. Robinett, 2003: Soil and ecological sites of the Santa Rita Experimental Range, in: *A century of vegetation change on the Santa Rita Experimental Range, in Santa Rita Experimental Range: 100 years (1903 to 2003) of accomplishments and contributions*, pp. 157 – 165, U.S. Department of Agriculture, Forest Service, Rocky Mountain Research Station, Tucson, AZ.

Breshears, D.D., J.W. Nyhan, C.E. Heil, and B.P. Wilcox, 1998: Effects of woody plants on microclimate in a semiarid woodland: Soil temperature and evaporation in canopy and intercanopy patches, *Int. J. Plant Sci.*, **159**(6), 1010 – 1017, doi:10.1086/314083.

Browning, D. M., S.R. Archer, G.P. Asner, M.P. McClaran, and C.A. Wessman, 2008: Woody plants in grasslands: post-encroachment stand dynamics, *Ecol. Appl.*, **18**(4), 928 – 944, doi:10.1890/07-1559.1.

Burrows, W.H., J.O. Carter, J C. Scanlan, and E.R. Anderson, 1990: Management of savannas for livestock production in north-east Australia: contrasts across the tree grass continuum, *J. Biogeogr.*, **17**(4/5), 503 – 512.

Buyantuyev A. and J. Wu, 2010: Urban heat islands and landscape heterogeneity: linking spatiotemporal variations in surface temperatures to land-cover and socioeconomic patterns, *Landsc. Ecol.*, **25**, 17 – 33.

Buyantuyev A and J. Wu J, 2012: Urbanization diversifies land surface phenology in arid environments: Interactions among vegetation, climate variations and land use patterns in the Phoenix metropolitan region, USA. *Landsc. Urban Plan.*, **105**, 149 –159.

Cable, D.R., 1975: Influence of precipitation on perennial grass production in the semidesert southwest, *Ecology*, **56**, 981 – 986, doi:10.2307/1936309.

Cable, D.R., 1977: Seasonal use of soil water by mature velvet mesquite, *J. Range Manage.*, **30**, 4 – 11, doi:10.2307/3898220.

Campbell, B.D. and D.M. Stafford Smith, 2000: A synthesis of recent global change research on pasture and rangeland production: reduced uncertainties and their management implications, *Agr. Ecosys. & Environ.*, **82**, 39–55.

Christen A. and R. Vogt, 2004: Energy and radiation valance of a central European city, *Int. J. Climatol.*, **24**, 1395 – 1421.

Chow W.T.L., T.J. Volo, E.R. Vivoni, G.D. Jenerette, and B.L. Ruddell, 2014a: Seasonal dynamics of a suburban energy balance in Phoenix, Arizona, *Int. J. Climatol.*, **34,** 3863 – 3880.

Chow W.T.L., F. Salamanca, M. Georgescu, A. Mahalov, J.F. Milne, and B.L. Ruddell, 2014b: A multi-method and multi-scale approach for estimating city-wide anthropogenic heat fluxes, *Atmos. Environ.*, **99**, 64 – 76.

Clement R., 1999: *EdiRe Data Software* (Version 1.5.0.32), Sch. Of Geosci., Univ. of Edinburgh, Edinburgh, U.K, http://www.geos.ed.ac.uk/abs/research/micromet/EdiRe.

Cook E.M., S.J. Hall, and K.L. Larson, 2012: Residential landscapes as social-ecological systems: A synthesis of multi-scalar interactions between people and their home environment, *Urban Ecosyst.*, **15**, 19 – 52.

Coutts A.M., J. Beringer, and N.J. Tapper, 2007: Impact of increasing urban density on local climate: Spatial and temporal variations in the surface energy balance in Melbourne, Australia, *J. Appl. Meteorol. Climatol.,* **46**, 477 – 493.

Detto, M., N. Montaldo, J. D. Albertson, M. Mancini, and G. Katul, 2006: Soil moisture and vegetation controls on evapotranspiration in a heterogeneous Mediterranean ecosystem on Sardinia, Italy, *Water Resour. Res.*, **42**, W08419, doi:10.1029/2005WR004693.

D'Odorico, P., G.S. Okin, and B.T. Bestelmeyer, 2012: A synthetic review of feedbacks and drivers of shrub encroachment in arid grasslands, *Ecohydrol.*, **5**, 520 – 530.

Eldridge D.J., M.A. Bowker, F.T. Masetre. E. Roger, J.F. Reynolds, and W.G. Whitford, 2011: Impacts of shrub encroachment on ecosystem structure and functioning: towards a global synthesis, *Ecol. Lett.*, **14**, 709 – 722.

Fensham, R.J., 1998: The influence of cattle grazing on tree mortality after drought in savanna woodland in north Queensland, *Aust. J. Ecol.*, **23**(4), 414 – 428.

Field C.B., M.J. Behrenfeld, J.T. Randerson, and P. Falkowski, 1998: Primary production of the biosphere: integrating terrestrial and oceanic components. *Science*, **281**, 237 – 240.

Foken T., 2006: 50 Years of the Monin-Obukhov similarity theory. *Bound. Layer Meteorol.*, **119**, 431 – 447.

Georgescu M., G. Miguez-Macho, L.T. Steyaert, and C.P. Weaver, 2009. Climatic effects of 30 years of landscape change over the Greater Phoenix, Arizona, region: 1. surface energy budget changes, *J. Geophys. Res.,* **114**: D05110, DOI: 10.1029/2008JD010745.

Georgescu M., W.T.L. Chow, Z.H. Wang, A. Brazel, B. Trapido-Lurie, M. Roth, and V. Benson-Lira, 2015: Prioritizing urban sustainability solutions: coordinated approaches must incorporate scale-dependent built environment induced effects, *Environ. Res. Lett*., **10**, 079601.

Gober P., A. Brazel, R. Quay, S. Myint, S. Grossman-Clarke, A. Miller, and S. Rossi, 2010: Using watered landscapes to manipulate urban heat island effects: How much water will it take to cool Phoenix?, *J. Am. Plann. Assoc.*, **76**, 109 – 121.

Goldbach A. and W. Kuttler, 2013: Quantification of turbulent heat fluxes for adaptation strategies within urban planning, *Int. J. Climatol*., **33,** 143 – 159.

Goodrich, D.C., T.O. Keefer, C.L. Unkrich, M.H. Nichols, H.B. Osborn, J.J. Stone, and J.R. Smith, 2008: Long-term precipitation database, Walnut Gulch Experimental Watershed, Arizona, United States, *Water Resour. Res.*, **44**, W05S04, doi:10.1029/2006WR005782.

Grimm N.B., S.H. Faeth, N.E. Golubiewski, C.L. Redman, J. Wu, X. Bai, and J.M. Briggs, 2008: Global change and the ecology of cities, *Science*, **319**, 756 – 760.

Grimmond C.S.B. and T.R. Oke, 1991: An evapotranspiration-interception model for urban areas, *Water Resour. Res.*, **27**(7)**,** 1739 – 1755.

Grimmond C.S.B., 2006: Progress in measuring and observing the urban atmosphere, *Theor. Appl. Climatol.*, **84**, 3 – 22.

Grimmond C.S.B. and T.R. Oke, 2002: Turbulent heat fluxes in urban areas: local-scale observations and a local-scale urban meteorological parameterization scheme (LUMPS), *J. Appl. Meteorol.*, **41**, 792 – 810.

Grimmond C.S.B, M. Roth, T.R. Oke, Y.C. Au, M. Best, R. Betts, G. Carmichael, H. Cleugh, W. Dabberdt, R. Emmanuel, E. Freitas, K. Fortuniak, S. Hanna, P. Klein, L.S. Kalkstein, C.H. Liu, A. Nickson, D. Pearlmutter, D. Sailor, and J. Voogt, 2010: Climate and more sustainable cities: climate information for improved planning and management of cities (producers/capabilities perspective), *Proc. Environ. Sci.*, **1**, 247 – 274.

Grimmond C.S.B. and A. Christen A, 2012: Flux measurements in urban ecosystems, *Fluxl. Newsl. Fluxnet*, **5**(1), 1 – 8.

Gutiérrez-Jurado, H.A., E.R. Vivoni, J.B.J. Harrison, and H. Guan, 2006: Ecohydrology of root zone water fluxes and soil development in complex semiarid rangelands, *Hydrol. Process.*, **20**(15), 3289 – 3316, doi: 10.1002/hyp.6333.

Hirt P., A. Gustafson, and K.L. Larson, 2008: The mirage in the Valley of the Sun, *Environ. Hist.,*. **13**, 482 – 514.

Hong J-W and J. Hong, 2016: Changes in the Seoul metropolitan area urban heat environment with residential redevelopment, *J. Appl. Meteorol. Climatol*., **55**, 1091 – 1106.

Hope D., C. Gries, W.X. Zhu, W.F. Fagan, C.L. Redman, N.B. Grimm, A.L. Nelson, C. Martin, and A. Kinzig, 2003: Socioeconomics drive urban plant diversity, *Proc. Nat. Aca. Sci.*, **100**, 8788 – 8792.

Huang, C.Y., S.E. Marsh, M.P. McClaran, and S.R. Archer, 2007: Postfire stand structure in a semiarid savanna: Cross-scale challenges estimating biomass, *Ecol. Appl.*, **17**(7), 1899 – 1910.

Huete, A., K. Didan, T. Miura, E.P. Rodriguez, X. Gao, and L.G. Ferreira, 2002: Overview of the radiometrics and biophysical performance of the MODIS vegetation indices, *Remote Sens. Environ.*, **83**, 193 – 213, doi:10.1016/S0034-4257(02)00096-2.

Huxman, T.E., K.A. Snyder, D. Tissue, A.J. Leffler, K. Ogle, W.T. Pockman, D.R. Sandquist, D.L. Potts, and S. Schwinning, 2004: Precipitation pulses and carbon fluxes in semiarid and arid ecosystems, *Oecologia*, **141**, 254 – 268, doi:10.1007/s00442-004-1682-4.

Huxman, T.E., B.P. Wilcox, D.D. Breshears, R.L. Scott, K.A. Snyder, E.E. Small, K. Hultine, W.T. Pockman, and R.B. Jackson, 2005: Ecohydrological implications of woody plant encroachment, *Ecology*, **86**(2), 308 – 319, doi:10.1890/03-0583.

Järvi L., C.S.B. Grimmond, and A. Christen, 2011: The Surface Urban Energy and Water Balance Scheme (SUEWS): Evaluation in Los Angeles and Vancouver, *J. Hydrol.*, **411**(3-4), 219 – 237.

Jenerette G.D., S.L. Harlan, W.L. Stefanov, and C.A. Martin, 2011: Ecosystem services and urban heat riskscape moderation: water, green spaces, and social inequality in Phoenix, USA, *Ecol. Appl,*. **21**, 2637 – 2651.

Kormann R. and F.X. Meixner, 2001: An analytical footprint model for non-neutral stratification, *Bound.-Layer Meteorol*., **99**, 207 – 224.

Kotthaus S. and C.S.B. Grimmond, 2012: Identification of micro-scale anthropogenic CO_2 heat and moisture sources – processing eddy covariance fluxes for a dense urban environment, *Atmos. Environ.*, **57**, 301 – 316.

Kurc, S.A. and E.E. Small, 2004: Dynamics of evapotranspiration in a semiarid grassland and shrubland ecosystems during the summer-monsoon season, central New Mexico, *Water Resour. Res.*, **40**(9), W09305, doi:10.1029/2004WR003068.

Lambin, E.F., B.L. Turner, H.J. Geist, S.J. Agbola, A. Angelsen, J.W. Bruce, O.T. Coomes, R. Dirzo, G. Fischer, C. Folke, P.S. George, K. Homewood, J. Imbernon, R. Leemans, X. Li, E.F. Moran, M. Mortimore, P.S. Ramakrishnan, J.F. Richards, H. Skanes, W. Steffan, G.D. Stone, U. Svedin, T.A. Veldkamp, C. Vogel, and J. Xu, 2003: The causes of land-use and land-cover change: moving beyond the myths, *Global Env. Chang.*, **11**, 261 – 269.

Landsburg H, 1981: The urban climate, New York: Academic Press. 275 pp.

Lee T.W., J.Y. Lee, Z.H. Wang, 2012: Scaling of the urban heat island intensity using time-dependent energy balance, *Urban Clim.*, **2**, 16 – 24.

Lemberg, B., J.W. Mjelde, J.R. Conner, R.C. Griffin, W.D. Rosenthal, and J.W. Stuth 2002:, An interdisciplinary approach to valuing water from brush control, *J. Am. Water Resour. Assoc.*, **38**(2), 409 – 422, doi:10.1111/j.1752-1688.2002.tb04326.x.

Litvak E and D.E. Pataki, 2016: Evapotranspiration of urban lawns in a semiarid environment: An in-situ evaluation of microclimatic conditions and water recommendations, *J. Arid Environ*., **134**, 87 – 96.

Loridan T. and C.S.B. Grimmond, 2012: Characterization of energy flux partitioning in urban environments: links with surface seasonal properties, *J. Appl. Meteorol. Climatol.*, **51**, 219 – 241.

Ma Y., S. Fan, H. Ishikawa., O. Tsukamoto, T. Yao, T. Koike, H. Zuo, Z. Hu, and Z. Su, 2005: Diurnal and inter-monthly variation of land surface heat fluxes over the central Tibetan Plateau area, *Theor. Appl. Climatol.*, **80**, 259 – 273.

Martin C.A., K. Busse, and S. Yabiku, 2007: North Desert Village: the effect of landscape manipulation on microclimate and its relation to human landscape preferences, *HortScience,* **42**, 853.

Martin, S.C. and H.L. Morton, 1993: Mesquite control increases grass density and reduces soil loss in southern Arizona, *J. Range Manage.*, **46**(2), 170 – 175.

Mascaro, G, 2017: Multiscale spatial and temporal statistical properties of rainfall in central Arizona, *J. Hydrometeor*., **18**, 227 – 245.

Massman W.J., 2001: Reply to comment by Rannik on: "A simple method for estimating frequency response corrections for eddy covariance systems," *Agr. For. Meteorol*., **107**, 247 – 251.

McClaran, M.P., 2003: *A century of vegetation change on the Santa Rita Experimental Range, in Santa Rita Experimental Range: 100 years (1903 to 2003) of accomplishments and contributions*, pp. 16 – 33, U.S. Department of Agriculture, Forest Service, Rocky Mountain Research Station, Tucson, AZ.

Middel A., A.J. Brazel, P. Gober, S.W. Myint, H. Chang, and J-D. Duh, 2012: Land cover, climate, and the summer surface energy balance in Phoenix, AZ, and Portland, OR, *Int. J. Climatol.*, **32**(13), 2020 – 2032.

Middel A,, N. Chhetri, and R. Quay, 2015: Urban forestry and cool roofs: Assessment of heat mitigation strategies in Phoenix residential neighborhoods, *Urban For. Urban Green*ing, **14**, 178 – 186.

Mitchell V.G., H.A. Cleugh, C.S.B. Grimmond, and J. Xu, 2008: Linking urban water balance and energy balance models to analyze urban design options, *Hydrol. Process.*, **22**, 2891 – 2900.

Mueller, E,N., J. Wainwright, and A.J. Parsons, 2007: Impact of connectivity on the modeling of overland flow within semiarid shrubland environments, *Water Resour. Res.*, **43**, W09412, doi:10.1029/2006WR005006.

Myint S.W., P. Gober, A. Brazel, S. Grossman-Clarke, and Q. Weng, 2011: Per-pixel vs. object-based classification of urban land cover extraction using high spatial resolution imagery, *Remote Sens. Environ.*, **115**, 1145 – 1161.

Naito, A.T., S.R. Archer, G.A. Barron-Gafford, J.A. Biederman, P.Heilman, K.T. Predick, R.L. Scott, T.L. Swetnam, H.L. Throop, N.P. Templeton, and E.R. Vivoni, 2017:, Brush management: An ecosystem services perspective. Science on the Sonoita Plain Symposium, Elgin, AZ.

Newman, B.D., B.P. Wilcox, A.S. Archer, D.D. Breshears, C.N. Dahm, C.J. Duffy, N.G. McDowell, F.M. Phillips, B.R. Scanlon, and E.R. Vivoni, 2006:, The ecohydrology of arid and semiarid environments: A scientific vision, *Water Resour. Res.*, **42**, W06302, doi:10.1029/2005WR004141.

Norton B.A., A.M. Coutts, S.J. Livesley, R.J. Harris, A.M. Hunter, and N.S.G. Williams, 2015: Planning for cooler cities: A framework to priorities green infrastructure to mitigate high temperatures in urban landscapes, *Landsc. Urban Plan.*, **134**, 127 – 138.

Offerle B., C.S.B. Grimmond, K. Fortuniak, and W. Pawlak, 2006: Intraurban differences of surface energy fluxes in a central Eurpoean city, *J. Appl. Meteorol. Climatol.*, **45**(1), 125 – 136.

Oke T.R., 1982: The energetic basis of the urban heat island, *Q. J. R. Meteorol. Soc.*, **108**, 1 – 24.

Oke T.R., 1988: The urban energy balance, *Progr. Phys. Geogr.*, **12**, 471 – 508.

Paw U K.T., D.D Baldocchi, T.P. Meyers, and K.B. Wilson, 2000: Correction of eddy-covariance measurements incorporating both advective effects and density fluxes, *Bound.- Layer Meteorol,*. **97**, 487 – 511.

Pielke R.A. Sr, RonI. Avissar, M. Raupach, A.J. Dolman, X. Zeng, and A.S. Denning, 1998: Interactions between the atmosphere and terrestrial ecosystems: influence on weather and climate, *Glob. Chang. Biol.*, **4**, 461 – 475. doi:10.1046/j.1365-2486.1998.t01-1-00176.x

Pierini, N.A., E.R. Vivoni, A. Robles-Morua, R.L. Scott, and M.A. Nearing, 2014: Using observations and a distributed hydrologic model to explore runoff threshold processes linked with mesquite encroachment in the Sonoran desert, *Water Resour. Res.*, **50**(10), 8191 – 8215, doi: 10.1002/2014WR015781.

Pima Association of Governments, 2011: *LiDAR Campaign (Pima County, AZ) Report of Survey*, Sanborn Total Geospatial Solutions, 15 pp.

Polyakov, V.O., M.A. Nearing, M.H. Nichols, R.L. Scott, J.J. Stone, and M.P. McClaran, 2010: Long-term runoff and sediment yields from small semiarid watersheds in southern Arizona, *Water Resour. Res.*, **46**(9), W09512, doi:10.1029/2009WR009001.

Reichstein, M., E. Falge, D. Baldocchi, D. Papale, M. Aubinet, P. Berbigier, C. Bernhofer, N. Buchmann, T. Gilmanov, A. Granier, T. Grünwald, K. Havránková, H. Ilvesniemi, D. Janous, A. Knohl, T. Laurila, A. Lohila, D. Loustau, G. Matteucci, T. Meyers, F. Miglietta, J.-M. Ourcival, J. Pumpanen, S. Rambal, E. Rotenberg, M. Sanz, J. Tenhunen, G. Seufert, F. Vaccari, T. Vesala, D. Yakir, and R. Valentini, 2005: On the separation of net ecosystem exchange into assimilation and ecosystem respiration: review and improved algorithm, *Glob. Chang. Biol.*, **11**, 1424 – 1439. doi:10.1111/j.1365-2486.2005.001002.x

Roques, K.G., T.G. O'Connor, and A.R. Watkinson, 2001: Dynamics of shrub encroachment in an African savanna: relative influences of fire, herbivory, rainfall and density dependence, *J. Applied Ecol.*, **38**(2), 268 – 280.

Sailor D.J., 2011: A review of methods for estimating anthropogenic heat and moisture emissions in the urban environment, *Int. J. Climatol.*, **31**, 189 – 299.

Sala O.E., F.S. Chapin, J.J. Armesto, E. Berlow, J. Bloomfield, R. Dirzo, E. Huber-Sanwald, L.F. Huenneke, R.B. Jackson, A. Kinzig, R. Leemans, D.M. Lodge, H.A. Mooney, M. Oesterheld, N.L. Poff, M.T. Sykes, B.H. Walker, M. Walker, and D.H. Wall, 2000: Global biodiversity scenarios for the year 2100, *Science*, **287**, 1770 – 1774.

Salamanca F., M. Georgescu, A. Mahalov, M. Moustaoui, and M. Wang, 2014: Anthropogenic heating of the urban environment due to air conditioning, *J. Geophys. Res,*. **119**, 5949 – 5965.

Santa Rita Experimental Range Digital Database. Funding for the digitization of these data was provided by USDA Forest Service Rocky Mountain Research Station and the University of Arizona. [Available at https://cals.arizona.edu/srer/data.html].

Santillán-Soto N., R. García-Cueto, Z. Haro-Rincón, S. Ojeda-Benitez, M. Quintero-Núñez, N. Velázquez-Limón, 2015: Radiation balance of urban materials and their thermal impact in Semi-Desert region: Mexicali, México Study Case, *Atmosfera*, **6**, 1578 – 1589.

Schmid H.P., H.A. Cleugh, C.S.B. Grimmond, and T.R. Oke, 1991: Spatial variability of energy fluxes in suburban terrain, *Bound.-Layer Meteorol.*, **54**, 249 – 276.

Schmid H.P., 1994: Source areas for scalars and scalar fluxes, *Bound.-Layer Meteorol.*, **67**, 293 – 318.

Scholes, R.J. and S.R. Archer, 1997: Tree-grass interactions in savannas, *Annu. Rev. Ecol. Syst.*, **28**(1), 517 – 544, doi:10.1146/annurev.ecolsys.28.1.517.

Scott, R. L., T.E. Huxman, W.L. Cable, and W.E. Emmerich, 2006: Partitioning of evapotranspiration and its relation to carbon dioxide exchange in a Chihuahuan desert shrubland, *Hydrol. Process.*, **20**(15), 3227 – 3243, doi:10.1002/hyp.6329.

Scott, R. L., G.D. Jenerette, D.L. Potts, and T.E. Huxman, 2009: Effects of seasonal drought on net carbon dioxide exchange from a woody-plant-encroached semiarid grassland, *J. Geophys. Res.*, **114**, G04004, doi:10.1029/2008JG000900.

Scott R.L., 2010: Using watershed water balance to evaluate the accuracy of eddy covariance evaporation measurements for three semiarid ecosystems, *Agr. For. Meteorol.*, **150**(2), 219 – 225.

Shaffer S.R., W.T.L. Chow, M. Georgescu, P. Hyde, G.D. Jenerette, A. Mahalov, M. Moustaoui, and B.L. Ruddell, 2015: Multiscale modeling and evaluation of urban surface energy balance in the Phoenix metropolitan area. *J. Appl. Meteorol. Climatol.*, **54**, 322 – 338.

Silva J.F., A. Zambrano, and M. Farinas, 2001: Increase in the woody component of seasonal savannas under different fire regimes in Calabozo, Venezuela, *J. Biogeogr.*, **28**(8), 977 – 983.

Song J. and Z.H. Wang, 2015: Impacts of mesic and xeric urban vegetation on outdoor thermal comfort and microclimate in Phoenix, AZ, *Building Env.* **94**, 558 – 568.

Stull R.B., 1988: *An Introduction to Boundary Layer Meteorology*, Kluwer Academic Publishers, Dordrecht, The Netherlands, 670 pp.

Templeton R.C., E.R. Vivoni, L.A. Mendez-Barroso, N.A. Pierini, C.A. Anderson, A. Rango, A.S. Laliberte, and R.L. Scott, 2014: High-resolution characterization of a semiarid watershed: Implications on evapotranspiration estimates, *J. Hydrol*., **509**, 306 – 319.

United Nations, Department of Economic and Social Affairs, Population Division 2015: *World Urbanization Prospects: The 2014 Revision*, (ST/ESA/SER.A/366), United Nations, New York, USA, 517 pp.

US Census Bureau, 2010: 2010 Census Data, http://2010.census.gov/2010censusdata/data/.

Van Auken O.W., 2000: Shrub invasions of North American semiarid grasslands, *Annu. Rev. Ecol. Syst*., **31**(1), 197 – 215, doi:10.1146/annurev.ecolsys.31.1.197.

Van Auken O.W., 2009: Causes and consequences of woody plant encroachment into western North American grasslands, *J. Environ. Manage.*, **90**(10), 2931 – 2942.

Van de Boer A., A.F. Moene, D. Schuttemeyer, and A. Graf, 2013: Sensitivity and uncertainty of analytical footprint models according to a combined natural tracer and ensemble approach, *Agr. For. Meteorol.*, **169**, 1 – 11.

Vivoni E.R., H.A. Moreno, G. Mascaro, J.C. Rodriguez, C.J. Watts, J. Garatuza-Payan, and R.L. Scott, 2008: Observed relation between evapotranspiration and soil moisture in the North American monsoon region, *Geophys. Res. Lett*., **35**, L22403, doi:10.1029/2008GL036001.

Vivoni, E.R., J.C. Rodriguez, and C.J. Watts, 2010: On the spatiotemporal variability of soil moisture and evapotranspiration in a mountainous basin within the North American monsoon region, *Water Resour. Res.*, **46**, W02509, doi: 10.1029/2009WR008240.

Volo T.J., E.R. Vivoni, C.A. Martin, S. Earl, and B.L. Ruddell, 2014: Modelling soil moisture, water partitioning and plant water stress under irrigated conditions in desert urban areas, *Ecohydrol*., **7**, 1297 – 1313.

Volo T.J., E.R. Vivoni, and B.L. Ruddell, 2015: An ecohydrological approach to conserving urban water through optimized landscape irrigation schedules, *Landsc. Urban Plan*., **133**, 127 – 132.

Wang J. and Y. Mitsuta, 1992: Evaporation from the desert: Some preliminary results of HEIFE, *Bound.-Layer Meteorol.*, **59**, 413 – 418.

Wang Z.H., E. Bou-Zeid, and J.A. Smith, 2013: A coupled energy transport and hydrological model for urban canopies evaluated using a wireless sensor network, *Q. J. R. Meteorol. Soc.*, **139**, 1643 – 1657.

Wang Z.H., X. Zhao, J. Yang, and J. Song, 2016: Cooling and energy saving potentials of shade trees and urban lawns in a desert city, *Appl. Energy*, **161**, 437 – 444.

Webb E.K., G.I. Pearman, and R. Leuning, 1980: Correction of flux measurements for density effects due to heat and water vapor transfer, *Q. J. R. Meteorol. Soc.*, **106**, 85 – 106.

Wilcox, B.P. and T.L. Thurow, 2006: Emerging issues in rangeland ecohydrology: vegetation change and the water cycle, *Rangeland Ecol. Manage.*, **59**(2), 220 – 224.

Williams, C.A. and J.D. Albertson, 2004: Soil moisture controls on canopy-scale water and carbon fluxes in an African savanna, *Water Resour. Res.*, **40**, W09302, doi:10.1029/2004WR003208.

Wilczak J.M., S.P. Oncley, and S.A. Stage, 2001: Sonic anemometer tilt correction algorithms, *Bound.-Layer Meteorol.*, **99**, 127 – 150.

Wilson K., A. Goldstein, E. Falge, M. Aubinet, D. Baldocchi, P. Berbigier, C. Bernhofer, R. Ceulemans, H. Dolman, C. Fiel, A. Grelle, A. Ibrom, B.E. Law, A. Kowalski, T. Meyers, J. Moncrieff, R. Monson, W. Oechel, J. Tenhunen, R. Valentini, and S. Verma, 2002: Energy balance closure at FLUXNET sites, *Agr. For. Meteorol.*, **113**, 223 – 243.

Wu J., G.D. Jenerette, A. Buyantuyev, and C.L. Redman, 2011: Quantifying spatiotemporal patterns of urbanization: The case of the two fastest growing metropolitan areas in the United States, *Ecol. Complex.*, **8**, 1 –8.

Yang J. and Wang Z.H., 2015: Optimizing urban irrigation schemes for the trade-off between energy and water consumption, *Energ. Buildings*, **107**, 335 – 344.

Yang J., Z.H. Wang, M. Georgescu, F. Chen, and M. Tewari, 2016: Assessing the impact of enhanced hydrological processes on urban hydrometeorology with application to two cities in contrasting climates, *J. Hydrometeorol.*, **17**, 1031 – 1047.

Yepez, E.A., D.G. Williams, R.L. Scott, and G. Lin, 2003: Partitioning overstory and understory evapotranspiration in a semiarid savanna woodland from the isotopic composition of water vapor, *Agr. For. Meteorol.*, **119**, 53 – 68.

Zhao Q., S.W. Myint, E.A. Wentz, and C. Fan, 2015: Rooftop surface temperature analysis in an urban residential environment, *Remote Sens.*, **7**, 12135 – 12159.

APPENDIX A

FIELD DATALOGGER PROGRAMS

A.1 Mobile Eddy Covariance Tower Datalogger Program

```
'CR5000 Series Datalogger
'To create a different opening program template, type in new
'instructions and select Template | Save as Default Template
'date:January 5 2015
'program author:Nicole Pierini
'Declare Public Variables

Public Batt_Volt
Public VW 'soil moisture at 5 cm
Public PA_uS 'soil moisture at 75 cm
Public VW_2
Public PA_uS_2
'Public VW_3
'Public PA_uS_3
Public AirTC
Public RH
Public AirTC_2
Public RH_2
Public AirTC_3
Public RH_3
Dim I
Public SWin 'Apogee SP-110 Sensor
Public PPFin 'Apogee SQ-110 Sensor
Public SWout
Public PPFout
Public PAR_ratio
Public PYR_ratio
Public r_nir
Public ndvi_Jenkins
Public ndvi_Huemmrich
Public ndvi_Wilson
Public evi2
Public par_in
Public par_out
Public p_par
Public par_ref
Public p_oir
Public VIS_in
Public VIS_out
Public NIR_in
Public NIR_out
Public p_nir
```

```
Public Rain_mm
Public PTemp_C
Public Temp_C
Public Temp_C_2
Public shf
Public shf_cal
Public BP_mbar
'CNR4 Net Radiometer
Public cnr4(4)
Alias cnr4(1) = short_up
Alias cnr4(2) = short_dn
Alias cnr4(3) = long_up
Alias cnr4(4) = long_dn
Public cnr4_T_C
Public cnr4_T_K
Public long_up_corr 'downwelling long-wave radiation with temperature correction
Public long_dn_corr 'upwelling long-wave radiation with temperature correction
Public Rs_net 'short-wave net radiation
Public Rl_net 'long-wave net radiation
Public albedo 'Albedo
Public Rn 'total net radiation
'===Soil heatflux calibration variables
Public shf_mV
Public shf_mV_run
Public shf_mV_0
Public shf_mV_180
Public shf_mV_360
Public V_Rf
Public V_Rf_run
Public V_Rf_180
Public V_Rf_360
Public shf_cal_on        'HFP01SC calibration flag.
Public wind(5)           'Wind, sonic temperature, and diagnostic data from
CSAT3.
Alias wind(1) = Ux
Alias wind(2) = Uy
Alias wind(3) = Uz
Alias wind(4) = Ts
Alias wind(5) = diag_csat
Units wind = m/s
Units Ts = degC
Units diag_csat = unitless

'Declare variables for the Apogee surface temperature probe
```

```
Dim TT_K_6
Dim SBT_K_7
Dim m_8
Dim b_9
Public BattV
Public TT_C
Public SBT_C
Public TTmV


Public diag_bits(9)                'Warning flags.
Alias diag_bits(1) = del_T_f         'Delta temperature warning flag.
Alias diag_bits(2) = track_f         'Tracking (signal lock) warning flag.
Alias diag_bits(3) = amp_h_f          'Amplitude warning high flag.
Alias diag_bits(4) = amp_l_f          'Amplitude low warning flag.
Alias diag_bits(5) = chopper_f                'Chopper warning flag.
Alias diag_bits(6) = detector_f               'Detector warning flag.
Alias diag_bits(7) = pll_f           'PLL warning flag.
Alias diag_bits(8) = sync_f           'Synchronization warning flag.
Alias diag_bits(9) = agc             'Automatic gain control.
Units diag_bits = unitless

'CS7500 has a fixed delay of 302.369 mSec (six scans at 20 Hz or three scans at 10 Hz).
Public irga(4)                                'Co2, h2o, and pressure from the CS7500
(LI-7500).
Alias irga(1) = co2
Alias irga(2) = h2o
Alias irga(3) = press
Alias irga(4) = diag_irga
Units co2 = mg/(m^3)
Units h2o = g/(m^3)
Units press = kPa

'Analog variables with three or six scan delay.
Public fw                                     'Fine wire thermocouple temperature.
Units fw = degC
Public tc_ref                                 'Thermocouple reference temperature.
Units tc_ref = degC

'Flux variables.
Public Fc                                     'CO2 flux.
Public LE                                     'Latent heat flux from CS7500 (LI-7500).
Public Hs                                     'Sensible heat flux using sonic temperature.
```

```
Public H                        'Sensible heat flux using finewire
thermocouple.
Public tau                      'Momentum flux.
Public u_star                   'Friction velocity.
Public cov_out_1(32)            'Covariances of wind and scalars + windspeed.
Units Fc = mg/(m^2 s)
Units LE = W/m^2
Units Hs = W/m^2
Units H = W/m^2
Units tau = kg*m/s^2
Units u_star = m/s

'Aliases for covariances.
Alias cov_out_1(1) = Uz_Uz_1
Alias cov_out_1(2) = Uz_Ux_1
Alias cov_out_1(3) = Uz_Uy_1
Alias cov_out_1(4) = Uz_co2_1
Alias cov_out_1(5) = Uz_h2o_1
Alias cov_out_1(6) = Uz_Ts_1
Alias cov_out_1(7) = Uz_fw_1
Alias cov_out_1(8) = Ux_Ux_1
Alias cov_out_1(9) = Ux_Uy_1
Alias cov_out_1(10) = Ux_co2_1
Alias cov_out_1(11) = Ux_h2o_1
Alias cov_out_1(12) = Ux_Ts_1
Alias cov_out_1(13) = Ux_fw_1
Alias cov_out_1(14) = Uy_Uy_1
Alias cov_out_1(15) = Uy_co2_1
Alias cov_out_1(16) = Uy_h2o_1
Alias cov_out_1(17) = Uy_Ts_1
Alias cov_out_1(18) = Uy_fw_1
Alias cov_out_1(19) = co2_co2_1
Alias cov_out_1(23) = h2o_h2o_1
Alias cov_out_1(26) = Ts_Ts_1
Alias cov_out_1(28) = fw_fw_1
Alias cov_out_1(31) = wnd_dir_compass
Units wnd_dir_compass = degrees

'Alternate Flux variables using running mean.
Public cov_out_2(22)
'Aliases for alternative covariances.
Alias cov_out_2(1) = Uz_Uz_2
Alias cov_out_2(2) = Uz_Ux_2
Alias cov_out_2(3) = Uz_Uy_2
```

```
Alias cov_out_2(4) = Uz_co2_2
Alias cov_out_2(5) = Uz_h2o_2
Alias cov_out_2(6) = Uz_Ts_2
Alias cov_out_2(7) = Uz_fw_2
Alias cov_out_2(8) = Ux_Ux_2
Alias cov_out_2(9) = Ux_Uy_2
Alias cov_out_2(10) = Ux_co2_2
Alias cov_out_2(11) = Ux_h2o_2
Alias cov_out_2(12) = Ux_Ts_2
Alias cov_out_2(13) = Ux_fw_2
Alias cov_out_2(14) = Uy_Uy_2
Alias cov_out_2(15) = Uy_co2_2
Alias cov_out_2(16) = Uy_h2o_2
Alias cov_out_2(17) = Uy_Ts_2
Alias cov_out_2(18) = Uy_fw_2
Alias cov_out_2(19) = co2_co2_2
Alias cov_out_2(20) = h2o_h2o_2
Alias cov_out_2(21) = Ts_Ts_2
Alias cov_out_2(22) = fw_fw_2
'moving average variables
Dim primes(7)                    'fluctuations from means, consistent with cov_in
Dim move_avg(7)                  'moving averages
Dim x_prod(22)                   'cross products...to compute covariance

'Diagnostic variables.
Public disable_flag_on(2)      'Intermediate processing disable.
    'disable_flag_on(1)      'Set high during site maintenance, flag(7) is set high.
    'disable_flag_on(2)      'Set high when CS7500 (LI-7500) failed to send data.
Public n(2)                    'Number of samples in the on-line covariances.
Public warnings(2)
Alias warnings(1) = csat_warnings      'Number of scans that at least one CSAT3
                                       ' warning flag was on.
Alias warnings(2) = irga_warnings      'Number of scans that the CS7500 (LI-7500)
Public flag(8)

'Measurement variables without delays.
Dim wind_in(5)                         'CSAT3 data, before adding delay.
Dim fw_in                              'TC signal, before adding delay.
Dim tc_ref_in                          'TC reference temperature, before adding
delay.

'Arrays to store delayed data.
Dim analog_data(3)                     'Three or six scan old data from the Data
Table 3_6_scan.
```

```
Dim csat_data(5)                    'One or four scan old data from the Data
Table 1_4_scan.

Dim cov_in(7)                       'Array used in the covariance instruction.
Dim j                               'Counter variable.
Dim rTime(9)                        'Real time from CR5000 clock.
Dim scan_count                          'Counts the number scans that have
been executed.
Dim hex_number                          'Used to break down the diagnostic
bits from the CSAT3.
Dim wind_east                           'Uy wind in compass coordinate
system.
Dim wind_north                          'Ux wind in compass coordinate
system.
Dim delays_loaded                   'A flag that gets set after three or six scans
have been executed.
                                        ' This flag is used to ensure that the

Data Table 1_4_scan                     ' and 3_6_scan are loaded with data.

'Declare Units
Units Batt_Volt=Volts
Units PA_uS=uSec
Units PA_uS_2=uSec
'Units PA_uS_3=uSec
Units AirTC=Deg C
Units RH=%
Units AirTC_2=Deg C
Units RH_2=%
Units AirTC_3=Deg C
Units RH_3=%
Units SWin=W/m²
Units PPFin=umol/m²s
Units SWout=W/m²
Units PPFout=umol/m²s
Units Rain_mm=mm
Units PTemp_C=Deg C
Units Temp_C=Deg C
Units Temp_C_2=Deg C
Units shf = W/m^2
Units BP_mbar=mbar
Units short_up=W/m²
Units short_dn=W/m²
Units long_up=W/m²
```

```
Units long_dn=W/m^2
Units cnr4_T_C = deg_C
Units cnr4_T_K = deg_C
Units long_up_corr=W/m^2
Units long_dn_corr=W/m^2
Units Rs_net=W/m^2
Units Rl_net=W/m^2
Units albedo=W/m^2
Units Rn=W/m^2
Units TT_C=Deg C
Units SBT_C=Deg C

Dim Rs, Vs_Vx

'Declare Constants
Const SCAN_INTERVAL = 50            '100 (mSec)                 50 (mSec)
Const CSAT_OPT = 20                         '10 (Hz)
        20 (Hz)
Const ANALOG_DELAY = 4                      '4 (3 scan delay)           7 (6
scan delay)
Const CSAT_DELAY = 2                '2 (1 scan delay)           5 (4 scan
delay)
Const GAMMA = 400                           'time constant in seconds

Const ANGLE_FROM_NORTH = 21                 'Negative when West of North,
positive when East of North. NEED TO ADJUST THIS VALUE!
Const CP = 1003                     'Estimate of heat capacity of air [J/(kg K)].
Const LV = 2440                     'Estimate of the latent heat of vaporization
[J/g].
Const RHO = 1.2                     'Estimate for air density at sea level
[kg/m^3].
Const SDM_PER = 30                          'Default SDM clock speed, 30 uSec
bit period.

Const A_0 = 6.107799961             'Coefficients for the sixth order
approximating
Const A_1 = 4.436518521e-1          ' saturation vapor pressure polynomial (Lowe,
Const A_2 = 1.428945805e-2          ' Paul R., 1976.:  An approximating polynomial for
Const A_3 = 2.650648471e-4          ' computation of saturation vapor pressure, J. Appl.
Const A_4 = 3.031240396e-6          ' Meteor., 16, 100-103).
Const A_5 = 2.034080948e-8
Const A_6 = 6.136820929e-11

'constants to convert voltage to ppm of  co2.
```

```
'Const Crange = 1000
'Const Vrange = 5

'constants to convert voltage to ppt of  h20.
'Const Hrange = 80
Const HFP01SC_CAL = 1000/47.83 'Unique multiplier for HFP01SC 1
(1000/sensitivity).
'Const HFP01SC_CAL_2 = 1000/63.5 'Unique multiplier for HFP01SC 2
(1000/sensitivity).
Const CAL_INTERVAL = 180                'HFP01SC insitu calibration interval
(minutes).

'CNR4 sensitivites: refer to certificate of calibration from Kipp & Zonene for sensitivity
values
Const pyra_up_sensitiv  = 12.52
Const pyra_dn_sensitiv  = 11.24
Const pyrg_up_sensitiv  = 12.12
Const pyrg_dn_sensitiv  = 12.96

Public cnr4_mult(4)
Const pyra_up_mult = 1000/pyra_up_sensitiv
Const pyra_dn_mult = 1000/pyra_dn_sensitiv
Const pyrg_up_mult = 1000/pyrg_up_sensitiv
Const pyrg_dn_mult = 1000/pyrg_dn_sensitiv

'Define Data Tables
DataTable(Met,True,1344)
  CardOut (0,1344)
        DataInterval(0,30,Min,10)
        Average(1,VW,FP2,False)
        Average(1,VW_2,FP2,False)
        'Average(1,VW_3,FP2,False)
        Average(1,AirTC,FP2,False)
        Average(1,RH,FP2,False)
        Average(1,AirTC_2,FP2,False)
        Average(1,RH_2,FP2,False)
        Average(1,AirTC_3,FP2,False)
        Average(1,RH_3,FP2,False)
        Average(1,PPFin,IEEE4,False)
        Average(1,ndvi_Jenkins,FP2,False)
        Average(1,ndvi_Huemmrich,FP2,False)
        Average(1,ndvi_Wilson,FP2,False)
        Average(1,evi2,FP2,False)
        Totalize(1,Rain_mm,FP2,False)
```

```
        Average(1,Temp_C,FP2,False)
        Average(1,Temp_C_2,FP2,False)
'       Average(1,Temp_C_3,FP2,False)
'       Average(1,Temp_C_4,FP2,False)
        Average(1,PTemp_C,FP2,False)
        Average (1,shf,IEEE4,shf_cal_on)
        Average(1,BP_mbar,FP2,False)
        Minimum(1,Batt_Volt,FP2,False,False)
        Average(1,PA_uS,FP2,False)
        Average(1,PA_uS_2,FP2,False)
        'Average(1,PA_uS_3,FP2,False)
        Average(4,cnr4(1),IEEE4,False)
        'Average(1,cnr4_T_C,IEEE4,False)
        'Average(1,long_up_corr,IEEE4,False)
        'Average(1,long_dn_corr,IEEE4,False)
        Average(1,Rs_net,IEEE4,False)
        Average(1,Rl_net,IEEE4,False)
        Average(1,albedo,IEEE4,False)
        Average(1,Rn,IEEE4,False)
        Sample(1,TT_C,FP2)
        Sample(1,SBT_C,FP2)
        Average(1,wnd_dir_compass,IEEE4,False)
EndTable

DataTable(Tips,True,1000)
  DataEvent (0,Rain_mm>0,Rain_mm=0,0)
  Sample (1,Rain_mm,FP2)
EndTable

DataTable (raw_in,TRUE,1)
  Sample (5,wind_in(1),IEEE4)
  Sample (3,irga(1),IEEE4)
  Sample (1,fw_in,IEEE4)
  Sample (1,tc_ref_in,IEEE4)
EndTable

'Delay the analog measurements by three or six scans.
DataTable (scan_3_6,TRUE,ANALOG_DELAY)
  Sample (1,tc_ref_in,IEEE4)
  Sample (1,fw_in,IEEE4)
EndTable

'Delay the CSAT3 measurements by one or four scans.
DataTable (scan_1_4,TRUE,CSAT_DELAY)
```

```
  Sample (5,wind_in(1),IEEE4)
EndTable

'Set flag(8) high to save time series data.  Set flag(5) also
'to break up the time series data file into one hour periods.
DataTable (ts_data,flag(8),-1)
  DataInterval (0,SCAN_INTERVAL,mSec,50)
  CardOut (0,-1)
  Sample (3,wind(1),IEEE4)
  Sample (2,irga(1),IEEE4)
  Sample (1,Ts,IEEE4)
  Sample (1,press,IEEE4)
  Sample (1,diag_csat,IEEE4)
'  Sample (1,diag_irga,IEEE4)
EndTable

'Compute the covariances of vertical wind, co2, h2o, natural log of
' the krypton voltage, sonic temperature, and finewire thermocouple
' temperature, as well as the other cross products, required to rotate
' the data into natural wind coordinates.  This data is output every
' 30 minutes.
DataTable (comp_cov,TRUE,1)
  DataInterval (0,30,min,1)
  Covariance (7,cov_in(1),IEEE4,(disable_flag_on(1) OR disable_flag_on(2) OR NOT
(flag(7))),28)
  WindVector (1,wind_east,wind_north,IEEE4,(disable_flag_on(1) OR NOT
(flag(7))),0,1,2)
EndTable

'Alternative covariance calculation for 21 days
DataTable (alt_cov,TRUE,1)
  DataInterval (0,30,min,1)
  Average (22,x_prod(1),IEEE4,(disable_flag_on(1) OR disable_flag_on(2) OR NOT
(flag(7))))
EndTable

'This table will hold 28 days of flux data.  This data is
'output every 30 minutes.
DataTable (flux,TRUE,1344)
  DataInterval (0,30,Min,10)
  CardOut (0,1344)
  Sample (1,Fc,IEEE4)
  Sample (1,LE,IEEE4)
  Sample (1,Hs,IEEE4)
```

```
  Sample (1,H,IEEE4)
  Sample (1,u_star,IEEE4)
  Sample (19,cov_out_1(1),IEEE4)
  Sample (1,cov_out_1(23),IEEE4)
  Sample (1,cov_out_1(26),IEEE4)
  Sample (1,cov_out_1(28),IEEE4)

  Average (3,wind(1),IEEE4,(disable_flag_on(1) OR NOT (flag(7)))
  Average (2,irga(1),IEEE4,(disable_flag_on(2) OR NOT (flag(7)))
  Average (1,fw_in,IEEE4,(disable_flag_on(1) OR NOT (flag(7))))
  Average (1,Ts,IEEE4,(disable_flag_on(1) OR NOT (flag(7)))

  Average (1,press,IEEE4,disable_flag_on(2))
  Average (1,tc_ref,FP2,FALSE)

  Sample (1,wnd_dir_compass,FP2)
  WindVector (1,Uy,Ux,FP2,(disable_flag_on(1) OR NOT (flag(7))),0,1,2)
  Average (1,Batt_volt,FP2,FALSE)



  Totalize (1,n(1),IEEE4,FALSE)
  Totalize (2,warnings(1),IEEE4,FALSE)
  Sample (22,cov_out_2(1),IEEE4)
EndTable

'Define subroutines
'Sub hfp01sc_cal 'Begin HFP01SC calibration one minute into every CAL_INTERVAL
minutes.
  'If ( IfTime (1,CAL_INTERVAL,Min) ) Then
    'shf_cal_on = TRUE
    'Move (shf_mV_0,1,shf_mV_run,1)
    'SW12=TRUE
  'EndIf

  'If ( IfTime (4,CAL_INTERVAL,Min) ) Then
    'Move (shf_mV_180,1,shf_mV_run,1)
    'Move (V_Rf_180,1,V_Rf_run,1)
    'SW12=FALSE
  'EndIf

  'If ( IfTime (19,CAL_INTERVAL,Min) ) Then
    'Move (shf_mV_360,1,shf_mV_run,1)
   'Compute new HFP01SC calibration factors.
```

```
     'shf_cal = V_Rf_180*V_Rf_180*128.7/ ABS(((shf_mV_0+shf_mV_360)/2)-
shf_mV_180)
   'Stop filtering data
   'shf_cal_on = FALSE
    'EndIf
'EndSub 'End HFP01SC calibration sequence.

'Sub hfp01sc_cal_2  'Begin HFP01SC PLATE 2 calibration one minute into every
CAL_INTERVAL minutes.
  'If ( IfTime (1,CAL_INTERVAL,Min) ) Then
    'shf_cal_2_on = TRUE
    'Move (shf_2_mV_0,1,shf_2_mV_run,1)
    'SW12=TRUE
  'EndIf

  'If ( IfTime (4,CAL_INTERVAL,Min) ) Then
    'Move (shf_2_mV_180,1,shf_2_mV_run,1)
    'Move (V_Rf_2_180,1,V_Rf_2_run,1)
    'SW12=FALSE
  'EndIf

  'If ( IfTime (19,CAL_INTERVAL,Min) ) Then
    'Move (shf_2_mV_360,1,shf_2_mV_run,1)
   'Compute new HFP01SC calibration factors.
      'shf_cal_2 = V_Rf_180*V_Rf_180*128.7/ ABS(((shf_mV_0+shf_mV_360)/2)-
shf_mV_180)
   'Stop filtering data
   'shf_cal_2_on = FALSE
    'EndIf
'EndSub 'End HFP01SC calibration sequence.

'Main Program
BeginProg
flag(1) = TRUE
  flag(7) = TRUE
  flag(8) = TRUE

'initiate moving average
  For j = 1 To 7
    move_avg(j) = 0
  Next j

 'Set all CSAT3 variables to NaN.
  For j = 1 To 5
```

```
  wind_in(j) = NaN
 Next j

'Set all CS7500 (LI-7500) variables to NaN.
 For j = 1 To 4
    irga(j) = NaN
 Next j

'Set the SDM clock speed.
 SDMSpeed (SDM_PER)

Scan(SCAN_INTERVAL,mSec,10,0)

  'Get CSAT3 wind and sonic temperature data.
   CSAT3 (wind_in(1),1,3,91,CSAT_OPT)

  'Get CS7500 (LI-7500) data.
   CS7500 (irga(1),1,7,6)

  'Convert CS7500 (LI-7500) data from molar density [mmol/m^3] to mass density.
  ' 44 [g/mol] - molecular weight of carbon dioxide
  ' 0.018 [g/mmol] - molecular weight of water vapor
   If (NOT (co2 = -99999)) Then (co2 = co2 * 44)
   h2o = h2o * 0.018

                'Get the battery voltage from the Status Table.
   Batt_Volt = Status.Battery(1,1)

        'If Batt_volt is < 11 Turn OFF IRGA
        If Batt_Volt < 11 Then
                WriteIO (&B10,&B00)
                flag(1) = TRUE
        EndIf
        If (flag(1) = TRUE AND Batt_Volt > 11.5) Then 'Turning IRGA back ON
                WriteIO (&B10,&B10)
                flag(1) = FALSE
        EndIf


 'Call humedad table.
   'CallTable moisture

 'Display the raw, unshifted turbulence data.
   CallTable raw_in
```

```
  'Delay the analog measurements by three or six scans.
   CallTable scan_3_6

  'Delay the CSAT3 measurements by one or four scans.
   CallTable scan_1_4

   If (NOT delays_loaded) Then (scan_count = scan_count + 1)
   If (scan_count = ANALOG_DELAY) Then (delays_loaded = TRUE)

  'Load in analog measurements that have been delayed by three or six scans.
   GetRecord (analog_data(1),scan_3_6,ANALOG_DELAY)
   tc_ref = analog_data(1)
   fw = analog_data(2)

  'Load in CSAT3 measurements that have been delayed by one or four scans.
   GetRecord (csat_data(1),scan_1_4,CSAT_DELAY)
   Ux = csat_data(1)
   Uy = csat_data(2)
   Uz = csat_data(3)
   Ts = csat_data(4)
   diag_csat = csat_data(5)
   wind_east = -1 * csat_data(2)
   wind_north = csat_data(1)

  'Turn on the intermediate processing disable flag when the CSAT3 is reporting NaN, a
   'Lost Trigger (&hf000), No Data (&hf03f), or an SDM error (&hf001).
   If ( (diag_csat = NaN) OR (diag_csat = &hf000) OR (diag_csat = &hf03f) OR
(diag_csat = &hf001))
     disable_flag_on(1) = TRUE
   Else
    'Check for any warning flags in CSAT3 data.  Filter all measurements associated
    ' with the CSAT3, when the warning flags are set.
     If (diag_csat AND &hf000)
       csat_warnings = 1
       disable_flag_on(1) = TRUE
     Else
       csat_warnings = 0
       disable_flag_on(1) = FALSE
     EndIf
   EndIf

'Keep the four most significant bits of the diagnostic word.
   diag_csat = INT ((diag_csat AND &hf000)/&h1000 + 0.5)
```

```
  'Break down the four most significant bits of the diagnostic word
  ' into a delta temperature flag, poor signal lock (tracking flag),
  ' amplitude high flag, and amplitude low flag.
   hex_number = &h0008
   For j = 1 To 4
     If ( ((diag_csat AND hex_number) = hex_number) AND NOT (diag_csat = &h000f)
)
       diag_bits(j) = 1
     Else
       diag_bits(j) = 0
     EndIf

     If ( diag_csat = NaN ) Then ( diag_bits(j) = NaN )

     hex_number = INT ((hex_number/&h0002) + 0.5)
   Next j

  'Compute the AGC.
   agc = INT ((diag_irga AND &h000f) * 6.25 + 0.5)

  'Keep the four most significant bits of the CS750 (LI-7500) diagnostic word
  ' and swap bits.
   diag_irga = (NOT (INT ((diag_irga AND &h00f0)/&h0010 + 0.5)) AND &h000f)

  'Turn on the intermediate processing disable flag when the CS7500 (LI-7500) has
  ' failed to send data to the CR5000 via SDM.
'    If ( (ABS (co2) >= 99990) OR (co2 = NaN) )
     If ( (co2 >=2000) OR (co2<=0) OR (co2 = NaN) OR (h2o <=0) OR (h2o >=50) )
      disable_flag_on(2) = TRUE
        irga_warnings = 1
     Else
      'Check for any warning flags in CS7500 (LI-7500) data.  Filter all measurements
      ' associated with the CS7500 (LI-7500), when the warning flags are set.
      If (diag_irga AND &h000f)
        irga_warnings = 1
        disable_flag_on(2) = TRUE
      Else
        irga_warnings = 0
        disable_flag_on(2) = FALSE
      EndIf
     EndIf

  'Decompose the warning flags.  Li-Cor uses reverse logic, e.g. bit set is okay.
```

```
  'The program changes the logic, e.g. bit not set is okay.
   hex_number = &h0008
   For j = 1 To 4
     If ( (diag_irga AND hex_number) = hex_number)
       diag_bits(j+4) = 1
     Else
       diag_bits(j+4) = 0
     EndIf

     If ( (ABS (co2) >= 99990) OR (co2 = NaN) ) Then ( diag_bits(j+4) = NaN )
     hex_number = INT ((hex_number/&h2) + 0.5)
   Next j


  'Perform time series and flux processing only after the Table 3_6_scan is loaded with
data.
   If (delays_loaded)

    'Write a file mark to the time series table every day.  The file mark is written only to
    ' to the PC Card if flag(5) is set high by the station operator and time series data are
being
    ' stored [flag(8) is high].  Both flag(8) and flag(5) must be set high by the station
operator
    ' using PC9000 or the CR5000 keyboard.

     If (flag(5) AND flag(8) AND IfTime (0,1440,Min) ) Then (FileMark (ts_data))
     CallTable ts_data

    'Load cov_in() array for the covariance computation.
     cov_in(1) = Uz
     cov_in(2) = Ux
     cov_in(3) = Uy
     cov_in(4) = co2
     cov_in(5) = h2o
     cov_in(6) = Ts
     cov_in(7) = fw

     CallTable comp_cov

'compute deviations from moving average
        For j = 1 To 7
                If (NOT disable_flag_on(1) AND NOT disable_flag_on(2) AND flag(7)
AND NOT (cov_in(j) = NaN) )
```

```
                    move_avg(j)=move_avg(j)*EXP(-1/(CSAT_OPT*GAMMA)) +
cov_in(j)*(1-EXP(-1/(CSAT_OPT*GAMMA)))
                    primes(j)=cov_in(j)-move_avg(j)
                EndIf
        Next j
        If (NOT disable_flag_on(1) AND NOT disable_flag_on(2) AND flag(7))
                x_prod(1)=primes(1)*primes(1)
                x_prod(2)=primes(1)*primes(2)
                x_prod(3)=primes(1)*primes(3)
                x_prod(4)=primes(1)*primes(4)
                x_prod(5)=primes(1)*primes(5)
                x_prod(6)=primes(1)*primes(6)
                x_prod(7)=primes(1)*primes(7)
                x_prod(8)=primes(2)*primes(2)
                x_prod(9)=primes(2)*primes(3)
                x_prod(10)=primes(2)*primes(4)
                x_prod(11)=primes(2)*primes(5)
                x_prod(12)=primes(2)*primes(6)
                x_prod(13)=primes(2)*primes(7)
                x_prod(14)=primes(3)*primes(3)
                x_prod(15)=primes(3)*primes(4)
                x_prod(16)=primes(3)*primes(5)
                x_prod(17)=primes(3)*primes(6)
                x_prod(18)=primes(3)*primes(7)
                x_prod(19)=primes(4)*primes(4)
                x_prod(20)=primes(5)*primes(5)
                x_prod(21)=primes(6)*primes(6)
                x_prod(22)=primes(7)*primes(7)
        EndIf

        CallTable alt_cov

    'Keep track of the number of samples in the covariances.
     If (NOT disable_flag_on(1) AND NOT disable_flag_on(2) AND flag(7))
       n(1) = 1
     Else
       n(1) = 0
     EndIf


     If (comp_cov.Output(1,1))

       GetRecord (cov_out_1(1),comp_cov,1)
```

```
    wnd_dir_compass = wnd_dir_compass + ANGLE_FROM_NORTH
        wnd_dir_compass = wnd_dir_compass MOD 360

   'Compute on-line fluxes.
    Fc = Uz_co2_1
    LE = LV * Uz_h2o_1
    Hs = RHO * CP * Uz_Ts_1
    H = RHO * CP * Uz_fw_1
    tau = SQR ((Uz_Ux_1)^2 + (Uz_Uy_1)^2)
    u_star = SQR (tau)
    tau = RHO * tau

  EndIf

     If (alt_cov.Output(1,1))
          GetRecord (cov_out_2(1),alt_cov,1)
     EndIf

  CallTable flux

EndIf

          'Default Datalogger Battery Voltage measurement Batt_Volt:
          Battery(Batt_Volt)

          'TE525/TE525WS Rain Gauge measurement Rain_mm:
          PulseCount(Rain_mm,1,1,2,0,0.254,0)
          CallTable(Tips)

     NextScan
     SlowSequence
     shf_cal = HFP01SC_CAL
     Scan(10,Sec,1,0)
       'CS616 Water Content Reflectometer measurements VW and PA_uS:
          PortSet(1,1)
          PeriodAvg(PA_uS,1,mV5000,1,0,0,100,10,1,0)
          PortSet(1,0)
          VW=-0.0663+(-0.0063*PA_uS)+(0.0007*PA_uS^2)
          'CS616 Water Content Reflectometer measurements VW_2 and PA_uS_2:
          PortSet(2,1)
          PeriodAvg(PA_uS_2,1,mV5000,2,0,0,100,10,1,0)
          PortSet(2,0)
          VW_2=-0.0663+(-0.0063*PA_uS_2)+(0.0007*PA_uS_2^2)
'         'CS616 Water Content Reflectometer measurements VW_3 and PA_uS_3:
```

```
'                PortSet(3,1)
'                PeriodAvg(PA_uS_3,1,mV5000,3,0,0,100,10,1,0)
'                PortSet(3,0)
'                VW_3=-0.0663+(-0.0063*PA_uS_3)+(0.0007*PA_uS_3^2)
                 'HMP155A (6-wire) Temperature & Relative Humidity Sensor
measurements AirTC and RH: HMP1 = 10 ft.
                 VoltSe(AirTC,1,mV1000,7,0,0,250,0.14,-80)
                 VoltSe(RH,1,mV1000,8,0,0,250,0.1,0)
                 If RH>100 AND RH<108 Then RH=100
                 'HMP155A (6-wire) Temperature & Relative Humidity Sensor
measurements AirTC_2 and RH_2: HMP2 = 20 ft
                 VoltSe(AirTC_2,1,mV1000,5,0,0,250,0.14,-80)
                 VoltSe(RH_2,1,mV1000,6,0,0,250,0.1,0)
                 If RH>100 AND RH<108 Then RH=100
                 'HMP155A (6-wire) Temperature & Relative Humidity Sensor
measurements AirTC_2 and RH_2: HMP = ground
                 VoltSe(AirTC_3,1,mV1000,9,0,0,250,0.14,-80)
                 VoltSe(RH_3,1,mV1000,10,0,0,250,0.1,0)
                 If RH>100 AND RH<108 Then RH=100


                 fw=AirTC_2*1.0  'Need to evaluate this measurement!
                 fw_in=AirTC_2*1.0
                 If (fw_in = NaN) Then fw_in = 0

   'CNR4 Measurements
   cnr4_mult(1)=pyra_up_mult
   cnr4_mult(2)=pyra_dn_mult
   cnr4_mult(3)=pyrg_up_mult
   cnr4_mult(4)=pyrg_dn_mult
   VoltSE(cnr4(),4,mv20C,29,True,0,_60Hz,cnr4_mult(),0)
   BrHalf(Vs_Vx,1,mv5000,27,Vx3,1,2500,True,0,250,1.0,0)
    Rs=1000*(Vs_Vx/(1-Vs_Vx))
      cnr4_T_C=1/(1.0295e-3+2.391e-4*LN(Rs)+1.568e-7*(LN(Rs))^3)-273.15
   'correct the long-wave radiation values from pyrgeometers
    long_up_corr=long_up+5.67e-8*(cnr4_T_C+273.15)^4
    long_dn_corr=long_dn+5.67e-8*(cnr4_T_C+273.15)^4
   'compute short-wave net radiation
     Rs_net=short_up-short_dn
    'compute long-wave net radiation
      Rl_net=long_up-long_dn
     'compute albedo
       albedo=short_dn/short_up
       'compute net radiation
```

```
        Rn=Rs_net+Rl_net

                'CS100 Barometric Pressure Sensor measurement BP_mbar:
                PortSet(4,1)
                VoltSe(BP_mbar,1,mV5000,11,1,0,250,0.2,600.0)
                BP_mbar=BP_mbar*1.0

                'Wiring Panel Temperature measurement PTemp_C:
                PanelTemp(PTemp_C,250)
                tc_ref=PTemp_C*1.0
                tc_ref_in=PTemp_C*1.0
                'Type E (chromel-constantan) Thermocouple measurements Temp_C:
                TCDiff(Temp_C,1,mV20C,2,TypeE,PTemp_C,True,0,250,1,0)
                'Type E (chromel-constantan) Thermocouple measurements Temp_C_2:
                TCDiff(Temp_C_2,1,mV20C,7,TypeE,PTemp_C,True,0,250,1,0)

  'For TE525MM Rain Gage, use multiplier of 0.1 in PulseCount instruction
    VoltDiff(SWin,1,AutoRange,8,True,0,_60Hz,5,0)  'sp_up
    VoltDiff(PPFin,1,AutoRange,9,True,0,_60Hz,5,0)  'sq_up
    VoltDiff(SWout,1,AutoRange,10,True,0,_60Hz,5,0)  'sp_down
    VoltDiff(PPFout,1,AutoRange,20,True,0,_60Hz,5,0) 'sq_down

'    VoltSe(SWout,1,mV1000,35,True,0,_60Hz,5,0)
'    VoltSe(PPFout,1,mV5000,36,True,0,_60Hz,5,0)
"Multiplexer call:
'    PortSet(6,1)
'    SubScan(0,sec,4)
'      PortSet(5,1)
'      Delay(0,2,mSec)
'      PortSet(5,0)
'      Delay(0,2,mSec)
'    '  VoltDiff(SWin,1,AutoRange,1,True,0,_60Hz,5,0)
'      VoltDiff(PPFin,1,AutoRange,2,True,0,_60Hz,5,0)
'      VoltDiff(SWout,1,AutoRange,3,True,0,_60Hz,5,0)
'      VoltDiff(PPFout,1,AutoRange,4,True,0,_60Hz,5,0)
'
'      NextSubScan
'      PortSet(6,0)

    PAR_ratio = PPFout/PPFin  'par_reflected/par_incoming
    PYR_ratio = SWout/SWin    'pyr_reflected/pyr_incoming

    'Jenkins NDVI:
    r_nir = (2 * PYR_ratio) - PAR_ratio
```

```
  ndvi_Jenkins = (r_nir - PAR_ratio) / (r_nir + PAR_ratio)

  'Huemmrich NDVI:
  par_in = PPFin * 0.25
  par_ref = PPFout * 0.25
  p_par = (par_ref / par_in)
  p_oir = (SWout - par_ref) / (SWin - par_in)
  ndvi_Huemmrich = (p_oir - p_par) / (p_oir + p_par)

  'Wilson NDVI:
  VIS_in = 0.45 * SWin
  NIR_in = 0.55 * SWin
  VIS_out = PAR_ratio * VIS_in
  NIR_out = SWout - VIS_out
  R_nir = NIR_out / NIR_in
  ndvi_Wilson = (R_nir - PAR_ratio) / (R_nir + PAR_ratio)

  'EVI2:
  p_nir = (SWout - (0.45 * SWin * PAR_ratio) )/ (0.55 * SWin)
  evi2 = 2.5 * ( (p_nir - PAR_ratio) / (p_nir + (2.4 * PAR_ratio) + 1) )

                'Measure the HFP01SC soil heat flux plate 1.
  VoltDiff(shf_mV,1,mV50,11,FALSE,200,200,1,0)
  shf = shf_mV * shf_cal
 'Measure voltage across the heater (Rf_V).
  VoltDiff(V_Rf, 1, mV5000, 12, FALSE, 200, 200, 0.001, 0)
 'Maintain filtered values for calibration.
  AvgRun (shf_mV_run,1,shf_mV,100)
  AvgRun (V_Rf_run,1,V_Rf,100)
  'Call hfp01sc_cal

  'Run the Apogee program to calculate the target temperature
        'Measure IRR-P sensor body thermistor temperature
              BrHalf(SBT_C,1,mV5000,35,2,1,5000,True,0,250,1,0)
              SBT_C=24900*(1/SBT_C-1)
              SBT_C=LOG(SBT_C)
              SBT_C=1/(1.129241e-3+2.341077e-4*SBT_C+8.775468e-
8*(SBT_C^3))-273.15
              'Measure IRR-P mV output of thermopile
              VoltDiff(TTmV,1,mV20,17,True,0,250,1,0)
              'Calculate slope (m) and offset (b) coefficients for target temperature
calculation
              m_8=1391950000+(7291020*SBT_C)+(77719.3*SBT_C^2)
              b_9=-10738300+(119484*SBT_C)+(2091.61*SBT_C^2)
```

```
            'Calculate target temperature using calculated slope (m) and offset (b)
            SBT_K_7=SBT_C+273.15
            TT_K_6=SBT_K_7^4+TTmV*m_8+b_9
            TT_K_6=SQR(SQR(TT_K_6))
            'Convert target temperature into desired units
            TT_C=TT_K_6-273.15
  'Call Output Tables
            CallTable (Met)
      NextScan
EndProg
```

A.2 Santa Rita Eddy Covariance Tower Datalogger Program

```
'CR5000 Series Datalogger
'To create a different opening program template, type in new
'instructions and select Template | Save as Default Template
'date:June 23 2008
'program author:Luis Mendez-Barroso
'edited: Nicole Templeton, last edit 9/1/2016
'Declare Public Variables

Public Batt_Volt
Public VW
Public PA_uS
Public VW_2
Public PA_uS_2
Public VW_3
Public PA_uS_3
Public VW_4
Public PA_uS_4
Public VW_5
Public PA_uS_5
Public VW_6
Public PA_uS_6
Public AirTC
Public RH
Public Rain_mm
Public PTemp_C
Public Temp_C
Public Temp_C_2
Public Temp_C_3
Public Temp_C_4
Public Solar_Wm2
Public Solar_kJ
Public shf
Public shf_cal
Public shf_2
Public shf_cal_2
Public BP_mbar
Public Net_shortwave
Public Net_longwave
'===Soil heatflux calibration variables
Public shf_mV
Public shf_mV_run
Public shf_mV_0
```

```
Public shf_mV_180
Public shf_mV_360
Public V_Rf
Public V_Rf_run
Public V_Rf_180
Public V_Rf_360
Public shf_cal_on               'HFP01SC calibration flag.
Public shf_2_mV
Public shf_2_mV_run
Public shf_2_mV_0
Public shf_2_mV_180
Public shf_2_mV_360
Public V_Rf_2
Public V_Rf_2_run
Public V_Rf_2_180
Public V_Rf_2_360
Public shf_cal_2_on 'HFP01SC calibration flag.
Public wind(5)                  'Wind, sonic temperature, and diagnostic data from
CSAT3.
Alias wind(1) = Ux
Alias wind(2) = Uy
Alias wind(3) = Uz
Alias wind(4) = Ts
Alias wind(5) = diag_csat
Units wind = m/s
Units Ts = degC
Units diag_csat = unitless

'Declare variables for the Apogee surface temperature probe
Dim TT_K_6
Dim SBT_K_7
Dim m_8
Dim b_9
Public BattV
Public TT_C
Public SBT_C
Public TTmV


Public diag_bits(9)               'Warning flags.
Alias diag_bits(1) = del_T_f        'Delta temperature warning flag.
Alias diag_bits(2) = track_f       'Tracking (signal lock) warning flag.
Alias diag_bits(3) = amp_h_f        'Amplitude warning high flag.
Alias diag_bits(4) = amp_l_f        'Amplitude low warning flag.
```

```
Alias diag_bits(5) = chopper_f              'Chopper warning flag.
Alias diag_bits(6) = detector_f             'Detector warning flag.
Alias diag_bits(7) = pll_f          'PLL warning flag.
Alias diag_bits(8) = sync_f          'Synchronization warning flag.
Alias diag_bits(9) = agc            'Automatic gain control.
Units diag_bits = unitless

'CS7500 has a fixed delay of 302.369 mSec (six scans at 20 Hz or three scans at 10 Hz).
Public irga(4)                              'Co2, h2o, and pressure from the CS7500
(LI-7500).
Alias irga(1) = co2
Alias irga(2) = h2o
Alias irga(3) = press
Alias irga(4) = diag_irga
Units co2 = mg/(m^3)
Units h2o = g/(m^3)
Units press = kPa

'Analog variables with three or six  delay.
Public fw                                   'Fine wire thermocouple temperature.
Units fw = degC
Public tc_ref                               'Thermocouple reference temperature.
Units tc_ref = degC

'Flux variables.
Public Fc                                   'CO2 flux.
Public LE                                   'Latent heat flux from CS7500 (LI-7500).
Public Hs                                   'Sensible heat flux using sonic temperature.
Public H                                    'Sensible heat flux using finewire
thermocouple.
Public tau                          'Momentum flux.
Public u_star                       'Friction velocity.
Public cov_out_1(32)          'Covariances of wind and scalars + windspeed.
Units Fc = mg/(m^2 s)
Units LE = W/m^2
Units Hs = W/m^2
Units H = W/m^2
Units tau = kg*m/s^2
Units u_star = m/s

'Aliases for covariances.
Alias cov_out_1(1) = Uz_Uz_1
Alias cov_out_1(2) = Uz_Ux_1
Alias cov_out_1(3) = Uz_Uy_1
```

```
Alias cov_out_1(4) = Uz_co2_1
Alias cov_out_1(5) = Uz_h2o_1
Alias cov_out_1(6) = Uz_Ts_1
Alias cov_out_1(7) = Uz_fw_1
Alias cov_out_1(8) = Ux_Ux_1
Alias cov_out_1(9) = Ux_Uy_1
Alias cov_out_1(10) = Ux_co2_1
Alias cov_out_1(11) = Ux_h2o_1
Alias cov_out_1(12) = Ux_Ts_1
Alias cov_out_1(13) = Ux_fw_1
Alias cov_out_1(14) = Uy_Uy_1
Alias cov_out_1(15) = Uy_co2_1
Alias cov_out_1(16) = Uy_h2o_1
Alias cov_out_1(17) = Uy_Ts_1
Alias cov_out_1(18) = Uy_fw_1
Alias cov_out_1(19) = co2_co2_1
Alias cov_out_1(23) = h2o_h2o_1
Alias cov_out_1(26) = Ts_Ts_1
Alias cov_out_1(28) = fw_fw_1
Alias cov_out_1(31) = wnd_dir_compass
Units wnd_dir_compass = degrees

'Alternate Flux variables using running mean.
Public cov_out_2(22)
'Aliases for alternative covariances.
Alias cov_out_2(1) = Uz_Uz_2
Alias cov_out_2(2) = Uz_Ux_2
Alias cov_out_2(3) = Uz_Uy_2
Alias cov_out_2(4) = Uz_co2_2
Alias cov_out_2(5) = Uz_h2o_2
Alias cov_out_2(6) = Uz_Ts_2
Alias cov_out_2(7) = Uz_fw_2
Alias cov_out_2(8) = Ux_Ux_2
Alias cov_out_2(9) = Ux_Uy_2
Alias cov_out_2(10) = Ux_co2_2
Alias cov_out_2(11) = Ux_h2o_2
Alias cov_out_2(12) = Ux_Ts_2
Alias cov_out_2(13) = Ux_fw_2
Alias cov_out_2(14) = Uy_Uy_2
Alias cov_out_2(15) = Uy_co2_2
Alias cov_out_2(16) = Uy_h2o_2
Alias cov_out_2(17) = Uy_Ts_2
Alias cov_out_2(18) = Uy_fw_2
Alias cov_out_2(19) = co2_co2_2
```

```
Alias cov_out_2(20) = h2o_h2o_2
Alias cov_out_2(21) = Ts_Ts_2
Alias cov_out_2(22) = fw_fw_2
'moving average variables
Dim primes(7)                    'fluctuations from means, consistent with cov_in
Dim move_avg(7)                  'moving averages
Dim x_prod(22)                   'cross products...to compute covariance

'Diagnostic variables.
Public disable_flag_on(2)      'Intermediate processing disable.
    'disable_flag_on(1)      'Set high during site maintenance, flag(7) is set high.
    'disable_flag_on(2)      'Set high when CS7500 (LI-7500) failed to send data.
Public n(2)                    'Number of samples in the on-line covariances.
Public warnings(2)
Alias warnings(1) = csat_warnings      'Number of scans that at least one CSAT3
                                       ' warning flag was on.
Alias warnings(2) = irga_warnings      'Number of scans that the CS7500 (LI-7500)
Public flag(8)

'Measurement variables without delays.
Dim wind_in(5)                         'CSAT3 data, before adding delay.
Dim fw_in                              'TC signal, before adding delay.
Dim tc_ref_in                    'TC reference temperature, before adding
delay.

'Arrays to store delayed data.
Dim analog_data(3)               'Three or six scan old data from the Data
Table 3_6_scan.
Dim csat_data(5)                 'One or four scan old data from the Data
Table 1_4_scan.

Dim cov_in(7)                    'Array used in the covariance instruction.
Dim j                            'Counter variable.
Dim rTime(9)                     'Real time from CR5000 clock.
Dim scan_count                         'Counts the number scans that have
been executed.
Dim hex_number                         'Used to break down the diagnostic
bits from the CSAT3.
Dim wind_east                          'Uy wind in compass coordinate
system.
Dim wind_north                         'Ux wind in compass coordinate
system.
Dim delays_loaded                'A flag that gets set after three or six scans
have been executed.
```

```
                                                    ' This flag is used to ensure that the
Data Table 1_4_scan
                                                    ' and 3_6_scan are loaded with data.

'Declare Units
Units Batt_Volt=Volts
Units PA_uS=uSec
Units PA_uS_2=uSec
Units PA_uS_3=uSec
Units PA_uS_4=uSec
Units PA_uS_5=uSec
Units PA_uS_6=uSec
Units AirTC=Deg C
Units RH=%
Units Rain_mm=mm
Units PTemp_C=Deg C
Units Temp_C=Deg C
Units Temp_C_2=Deg C
Units Temp_C_3=Deg C
Units Temp_C_4=Deg C
Units Solar_Wm2=W/m²
Units Solar_kJ=kJ/m²
Units shf = W/m^2
Units shf_2 = W/m^2
Units BP_mbar=mbar
Units Net_shortwave=W/m²
Units Net_longwave=W/m²
Units TT_C=Deg C
Units SBT_C=Deg C


'Declare Constants
Const SCAN_INTERVAL = 50            '100 (mSec)             50 (mSec)
Const CSAT_OPT = 10                 '10 (Hz)
        20 (Hz)
Const ANALOG_DELAY = 4              '4 (3 scan delay)       7 (6
scan delay)
Const CSAT_DELAY = 2                '2 (1 scan delay)       5 (4 scan
delay)
Const GAMMA = 400                   'time constant in seconds

Const ANGLE_FROM_NORTH = 240        'Negative when West of North,
positive when East of North.
Const CP = 1003                     'Estimate of heat capacity of air [J/(kg K)].
```

```
Const LV = 2440                         'Estimate of the latent heat of vaporization
[J/g].
Const RHO = 1.2                         'Estimate for air density at sea level
[kg/m^3].
Const SDM_PER = 30                              'Default SDM clock speed, 30 uSec
bit period.

Const A_0 = 6.107799961                 'Coefficients for the sixth order
approximating
Const A_1 = 4.436518521e-1          ' saturation vapor pressure polynomial (Lowe,
Const A_2 = 1.428945805e-2          ' Paul R., 1976.:  An approximating polynomial for
Const A_3 = 2.650648471e-4          ' computation of saturation vapor pressure, J. Appl.
Const A_4 = 3.031240396e-6          ' Meteor., 16, 100-103).
Const A_5 = 2.034080948e-8
Const A_6 = 6.136820929e-11

'constants to convert voltage to ppm of  co2.
'Const Crange = 1000
'Const Vrange = 5

'constants to convert voltage to ppt of  h20.
'Const Hrange = 80
Const HFP01SC_CAL = 1000/61.7   'Unique multiplier for HFP01SC 1
(1000/sensitivity).
Const HFP01SC_CAL_2 = 1000/62.5 'Unique multiplier for HFP01SC 2
(1000/sensitivity).
Const CAL_INTERVAL = 180                'HFP01SC insitu calibration interval
(minutes).


'Define Data Tables
DataTable(Met,True,1344)
  CardOut (0,1344)
        DataInterval(0,30,Min,10)
        Average(1,VW,FP2,False)
        Average(1,VW_2,FP2,False)
        Average(1,VW_3,FP2,False)
        Average(1,VW_4,FP2,False)
        Average(1,VW_5,FP2,False)
        Average(1,VW_6,FP2,False)
        Average(1,AirTC,FP2,False)
        Average(1,RH,FP2,False)
  Totalize(1,Rain_mm,FP2,False)
        Average(1,Temp_C,FP2,False)
```

```
        Average(1,Temp_C_2,FP2,False)
        Average(1,Temp_C_3,FP2,False)
        Average(1,Temp_C_4,FP2,False)
        Average(1,PTemp_C,FP2,False)
        Average(1,Solar_Wm2,FP2,False)
        Totalize(1,Solar_kJ,IEEE4,False)
        Average (1,shf,IEEE4,shf_cal_on)
  Average (1,shf_2,IEEE4,shf_cal_2_on)
  Average(1,Net_shortwave,FP2,False)
        Average(1,Net_longwave,FP2,False)
        Average(1,BP_mbar,FP2,False)
        Minimum(1,Batt_Volt,FP2,False,False)
        Average(1,PA_uS,FP2,False)
        Average(1,PA_uS_2,FP2,False)
        Average(1,PA_uS_3,FP2,False)
        Average(1,PA_uS_4,FP2,False)
        Average(1,PA_uS_5,FP2,False)
        Average(1,PA_uS_6,FP2,False)
        Sample(1,TT_C,FP2)
        Sample(1,SBT_C,FP2)
EndTable

DataTable(Tips,True,1000)
  DataEvent (0,Rain_mm>0,Rain_mm=0,0)
  Sample (1,Rain_mm,FP2)
EndTable

DataTable (raw_in,TRUE,1)
  Sample (5,wind_in(1),IEEE4)
  Sample (3,irga(1),IEEE4)
  Sample (1,fw_in,IEEE4)
  Sample (1,tc_ref_in,IEEE4)
EndTable

'Delay the analog measurements by three or six scans.
DataTable (scan_3_6,TRUE,ANALOG_DELAY)
  Sample (1,tc_ref_in,IEEE4)
  Sample (1,fw_in,IEEE4)
EndTable

'Delay the CSAT3 measurements by one or four scans.
DataTable (scan_1_4,TRUE,CSAT_DELAY)
  Sample (5,wind_in(1),IEEE4)
EndTable
```

```
'Set flag(8) high to save time series data.  Set flag(5) also
'to break up the time series data file into one hour periods.
DataTable (ts_data,flag(8),-1)
  DataInterval (0,SCAN_INTERVAL,mSec,50)
  CardOut (0,-1)
  Sample (3,wind(1),IEEE4)
  Sample (2,irga(1),IEEE4)
  Sample (1,Ts,IEEE4)
  Sample (1,press,IEEE4)
  Sample (1,diag_csat,IEEE4)
'  Sample (1,diag_irga,IEEE4)
EndTable

'Compute the covariances of vertical wind, co2, h2o, natural log of
' the krypton voltage, sonic temperature, and finewire thermocouple
' temperature, as well as the other cross products, required to rotate
' the data into natural wind coordinates.  This data is output every
' 30 minutes.
DataTable (comp_cov,TRUE,1)
  DataInterval (0,30,min,1)
  Covariance (7,cov_in(1),IEEE4,(disable_flag_on(1) OR disable_flag_on(2) OR NOT
(flag(7))),28)
  WindVector (1,wind_east,wind_north,IEEE4,(disable_flag_on(1) OR NOT
(flag(7))),0,1,2)
EndTable

'Alternative covariance calculation for 21 days
DataTable (alt_cov,TRUE,1)
  DataInterval (0,30,min,1)
  Average (22,x_prod(1),IEEE4,(disable_flag_on(1) OR disable_flag_on(2) OR NOT
(flag(7))))
EndTable

'This table will hold 28 days of flux data.  This data is
'output every 30 minutes.
DataTable (flux,TRUE,1344)
  DataInterval (0,30,Min,10)
  CardOut (0,1344)
  Sample (1,Fc,IEEE4)
  Sample (1,LE,IEEE4)
  Sample (1,Hs,IEEE4)
  Sample (1,H,IEEE4)
  Sample (1,u_star,IEEE4)
```

```
  Sample (19,cov_out_1(1),IEEE4)
  Sample (1,cov_out_1(23),IEEE4)
  Sample (1,cov_out_1(26),IEEE4)
  Sample (1,cov_out_1(28),IEEE4)
  Average (3,wind(1),IEEE4,(disable_flag_on(1) OR NOT (flag(7)))
  Average (2,irga(1),IEEE4,(disable_flag_on(2) OR NOT (flag(7)))
  Average (1,fw_in,IEEE4,(disable_flag_on(1) OR NOT (flag(7))))
  Average (1,Ts,IEEE4,(disable_flag_on(1) OR NOT (flag(7)))
  Average (1,press,IEEE4,disable_flag_on(2))
  Average (1,tc_ref,FP2,FALSE)
  Sample (1,wnd_dir_compass,FP2)
  WindVector (1,Uy,Ux,FP2,(disable_flag_on(1) OR NOT (flag(7))),0,1,2)
  Average (1,Batt_Volt,FP2,FALSE)
  Totalize (1,n(1),IEEE4,FALSE)
  Totalize (2,warnings(1),IEEE4,FALSE)
  Sample (22,cov_out_2(1),IEEE4)
        Average(1,VW,FP2,False)
        Average(1,VW_2,FP2,False)
        Average(1,VW_3,FP2,False)
        Average(1,VW_4,FP2,False)
        Average(1,VW_5,FP2,False)
        Average(1,VW_6,FP2,False)
        Average(1,AirTC,FP2,False)
        Average(1,RH,FP2,False)
        Average(1,Temp_C,FP2,False)
        Average(1,Temp_C_2,FP2,False)
        Average(1,Temp_C_3,FP2,False)
        Average(1,Temp_C_4,FP2,False)
        Average(1,PTemp_C,FP2,False)
        Average(1,Solar_Wm2,FP2,False)
        Totalize(1,Solar_kJ,IEEE4,False)
        Average (1,shf,IEEE4,shf_cal_on)
  Average (1,shf_2,IEEE4,shf_cal_2_on)
  Average(1,Net_shortwave,FP2,False)
        Average(1,Net_longwave,FP2,False)
        Average(1,BP_mbar,FP2,False)
        Minimum(1,Batt_Volt,FP2,False,False)
        Sample(1,TT_C,FP2)
        Sample(1,SBT_C,FP2)
EndTable

'Define subroutines
'Sub hfp01sc_cal 'Begin HFP01SC calibration one minute into every CAL_INTERVAL
minutes.
```

```
  'If ( IfTime (4,CAL_INTERVAL,Min) ) Then
    'Move (shf_mV_180,1,shf_mV_run,1)
    'Move (V_Rf_180,1,V_Rf_run,1)
    'SW12=FALSE
  'EndIf

  'If ( IfTime (19,CAL_INTERVAL,Min) ) Then
    'Move (shf_mV_360,1,shf_mV_run,1)
   'Compute new HFP01SC calibration factors.
      'shf_cal = V_Rf_180*V_Rf_180*128.7/ ABS(((shf_mV_0+shf_mV_360)/2)-
shf_mV_180)
   'Stop filtering data
   'shf_cal_on = FALSE
    'EndIf
'EndSub 'End HFP01SC calibration sequence.

'Sub hfp01sc_cal_2  'Begin HFP01SC PLATE 2 calibration one minute into every
CAL_INTERVAL minutes.
  'If ( IfTime (1,CAL_INTERVAL,Min) ) Then
    'shf_cal_2_on = TRUE
    'Move (shf_2_mV_0,1,shf_2_mV_run,1)
    'SW12=TRUE
  'EndIf

  'If ( IfTime (4,CAL_INTERVAL,Min) ) Then
    'Move (shf_2_mV_180,1,shf_2_mV_run,1)
    'Move (V_Rf_2_180,1,V_Rf_2_run,1)
    'SW12=FALSE
  'EndIf

  'If ( IfTime (19,CAL_INTERVAL,Min) ) Then
    'Move (shf_2_mV_360,1,shf_2_mV_run,1)
   'Compute new HFP01SC calibration factors.
      'shf_cal_2 = V_Rf_180*V_Rf_180*128.7/ ABS(((shf_mV_0+shf_mV_360)/2)-
shf_mV_180)
   'Stop filtering data
   'shf_cal_2_on = FALSE
    'EndIf
'EndSub 'End HFP01SC calibration sequence.

'Main Program
BeginProg
flag(1) = TRUE
  flag(7) = TRUE
```

```
  flag(8) = TRUE

'initiate moving average
  For j = 1 To 7
    move_avg(j) = 0
  Next j

 'Set all CSAT3 variables to NaN.
  For j = 1 To 5
    wind_in(j) = NaN
  Next j

 'Set all CS7500 (LI-7500) variables to NaN.
  For j = 1 To 4
     irga(j) = NaN
  Next j

 'Set the SDM clock speed.
  SDMSpeed (SDM_PER)

Scan(SCAN_INTERVAL,mSec,10,0)

   'Get CSAT3 wind and sonic temperature data.
    CSAT3 (wind_in(1),1,3,91,CSAT_OPT)

   'Get CS7500 (LI-7500) data.
    CS7500 (irga(1),1,7,6)

   'Convert CS7500 (LI-7500) data from molar density [mmol/m^3] to mass density.
   ' 44 [g/mol] - molecular weight of carbon dioxide
   ' 0.018 [g/mmol] - molecular weight of water vapor
    If (NOT (co2 = -99999)) Then (co2 = co2 * 44)
    h2o = h2o * 0.018

                'Get the battery voltage from the Status Table.
    Batt_Volt = Status.Battery(1,1)

        'If Batt_volt is < 11 Turn OFF IRGA
        If Batt_Volt < 11 Then
                WriteIO (&B10,&B00)
                flag(1) = TRUE
        EndIf
        If (flag(1) = TRUE AND Batt_Volt > 11.5) Then 'Turning IRGA back ON
                WriteIO (&B10,&B10)
```

```
            flag(1) = FALSE
        EndIf


  'Call humedad table.
    'CallTable moisture

  'Display the raw, unshifted turbulence data.
    CallTable raw_in

   'Delay the analog measurements by three or six scans.
    CallTable scan_3_6

   'Delay the CSAT3 measurements by one or four scans.
    CallTable scan_1_4

    If (NOT delays_loaded) Then (scan_count = scan_count + 1)
    If (scan_count = ANALOG_DELAY) Then (delays_loaded = TRUE)

   'Load in analog measurements that have been delayed by three or six scans.
    GetRecord (analog_data(1),scan_3_6,ANALOG_DELAY)
    tc_ref = analog_data(1)
    fw = analog_data(2)

   'Load in CSAT3 measurements that have been delayed by one or four scans.
    GetRecord (csat_data(1),scan_1_4,CSAT_DELAY)
    Ux = csat_data(1)
    Uy = csat_data(2)
    Uz = csat_data(3)
    Ts = csat_data(4)
    diag_csat = csat_data(5)
    wind_east = -1 * csat_data(2)
    wind_north = csat_data(1)

  'Turn on the intermediate processing disable flag when the CSAT3 is reporting NaN, a
    'Lost Trigger (&hf000), No Data (&hf03f), or an SDM error (&hf001).
    If ( (diag_csat = NaN) OR (diag_csat = &hf000) OR (diag_csat = &hf03f) OR
(diag_csat = &hf001))
      disable_flag_on(1) = TRUE
    Else
     'Check for any warning flags in CSAT3 data.  Filter all measurements associated
     ' with the CSAT3, when the warning flags are set.
      If (diag_csat AND &hf000)
        csat_warnings = 1
```

```
        disable_flag_on(1) = TRUE
      Else
        csat_warnings = 0
        disable_flag_on(1) = FALSE
      EndIf
    EndIf

'Keep the four most significant bits of the diagnostic word.
    diag_csat = INT ((diag_csat AND &hf000)/&h1000 + 0.5)

   'Break down the four most significant bits of the diagnostic word
   ' into a delta temperature flag, poor signal lock (tracking flag),
   ' amplitude high flag, and amplitude low flag.
    hex_number = &h0008
    For j = 1 To 4
      If ( ((diag_csat AND hex_number) = hex_number) AND NOT (diag_csat = &h000f)
)
        diag_bits(j) = 1
      Else
        diag_bits(j) = 0
      EndIf

      If ( diag_csat = NaN ) Then ( diag_bits(j) = NaN )

      hex_number = INT ((hex_number/&h0002) + 0.5)
    Next j

   'Compute the AGC.
    agc = INT ((diag_irga AND &h000f) * 6.25 + 0.5)

   'Keep the four most significant bits of the CS750 (LI-7500) diagnostic word
   ' and swap bits.
    diag_irga = (NOT (INT ((diag_irga AND &h00f0)/&h0010 + 0.5)) AND &h000f)

   'Turn on the intermediate processing disable flag when the CS7500 (LI-7500) has
   ' failed to send data to the CR5000 via SDM.
'    If ( (ABS (co2) >= 99990) OR (co2 = NaN) )
     If ( (co2 >=2000) OR (co2<=0) OR (co2 = NaN) OR (h2o <=0) OR (h2o >=50) )
      disable_flag_on(2) = TRUE
        irga_warnings = 1
     Else
      'Check for any warning flags in CS7500 (LI-7500) data.  Filter all measurements
      ' associated with the CS7500 (LI-7500), when the warning flags are set.
      If (diag_irga AND &h000f)
```

```
      irga_warnings = 1
      disable_flag_on(2) = TRUE
    Else
      irga_warnings = 0
      disable_flag_on(2) = FALSE
    EndIf
  EndIf

  'Decompose the warning flags.  Li-Cor uses reverse logic, e.g. bit set is okay.
  'The program changes the logic, e.g. bit not set is okay.
   hex_number = &h0008
   For j = 1 To 4
    If ( (diag_irga AND hex_number) = hex_number)
      diag_bits(j+4) = 1
    Else
      diag_bits(j+4) = 0
    EndIf

    If ( (ABS (co2) >= 99990) OR (co2 = NaN) ) Then ( diag_bits(j+4) = NaN )
    hex_number = INT ((hex_number/&h2) + 0.5)
   Next j


  'Perform time series and flux processing only after the Table 3_6_scan is loaded with
data.
   If (delays_loaded)

    'Write a file mark to the time series table every day.  The file mark is written only to
    ' to the PC Card if flag(5) is set high by the station operator and time series data are
being
    ' stored [flag(8) is high].  Both flag(8) and flag(5) must be set high by the station
operator
    ' using PC9000 or the CR5000 keyboard.

     If (flag(5) AND flag(8) AND IfTime (0,1440,Min) ) Then (FileMark (ts_data))
     CallTable ts_data

    'Load cov_in() array for the covariance computation.
     cov_in(1) = Uz
     cov_in(2) = Ux
     cov_in(3) = Uy
     cov_in(4) = co2
     cov_in(5) = h2o
     cov_in(6) = Ts
```

```
    cov_in(7) = fw

    CallTable comp_cov

'compute deviations from moving average
        For j = 1 To 7
                If (NOT disable_flag_on(1) AND NOT disable_flag_on(2) AND flag(7)
AND NOT (cov_in(j) = NaN) )
                        move_avg(j)=move_avg(j)*EXP(-1/(CSAT_OPT*GAMMA)) +
cov_in(j)*(1-EXP(-1/(CSAT_OPT*GAMMA)))
                        primes(j)=cov_in(j)-move_avg(j)
                EndIf
        Next j
        If (NOT disable_flag_on(1) AND NOT disable_flag_on(2) AND flag(7))
                x_prod(1)=primes(1)*primes(1)
                x_prod(2)=primes(1)*primes(2)
                x_prod(3)=primes(1)*primes(3)
                x_prod(4)=primes(1)*primes(4)
                x_prod(5)=primes(1)*primes(5)
                x_prod(6)=primes(1)*primes(6)
                x_prod(7)=primes(1)*primes(7)
                x_prod(8)=primes(2)*primes(2)
                x_prod(9)=primes(2)*primes(3)
                x_prod(10)=primes(2)*primes(4)
                x_prod(11)=primes(2)*primes(5)
                x_prod(12)=primes(2)*primes(6)
                x_prod(13)=primes(2)*primes(7)
                x_prod(14)=primes(3)*primes(3)
                x_prod(15)=primes(3)*primes(4)
                x_prod(16)=primes(3)*primes(5)
                x_prod(17)=primes(3)*primes(6)
                x_prod(18)=primes(3)*primes(7)
                x_prod(19)=primes(4)*primes(4)
                x_prod(20)=primes(5)*primes(5)
                x_prod(21)=primes(6)*primes(6)
                x_prod(22)=primes(7)*primes(7)
        EndIf

        CallTable alt_cov

    'Keep track of the number of samples in the covariances.
     If (NOT disable_flag_on(1) AND NOT disable_flag_on(2) AND flag(7))
       n(1) = 1
     Else
```

```
    n(1) = 0
  EndIf


  If (comp_cov.Output(1,1))

    GetRecord (cov_out_1(1),comp_cov,1)

    wnd_dir_compass = wnd_dir_compass + ANGLE_FROM_NORTH
        wnd_dir_compass = wnd_dir_compass MOD 360

   'Compute on-line fluxes.
    Fc = Uz_co2_1
    LE = LV * Uz_h2o_1
    Hs = RHO * CP * Uz_Ts_1
    H = RHO * CP * Uz_fw_1
    tau = SQR ((Uz_Ux_1)^2 + (Uz_Uy_1)^2)
    u_star = SQR (tau)
    tau = RHO * tau

  EndIf

      If (alt_cov.Output(1,1))
            GetRecord (cov_out_2(1),alt_cov,1)
      EndIf

  CallTable flux

 EndIf

            'Default Datalogger Battery Voltage measurement Batt_Volt:
            Battery(Batt_Volt)
            'TE525/TE525WS Rain Gauge measurement Rain_mm:
            PulseCount(Rain_mm,1,1,2,0,0.254,0)
            'For TE525MM Rain Gage, use multiplier of 0.1 in PulseCount instruction
 CallTable(Tips)

      NextScan
      SlowSequence
      shf_cal = HFP01SC_CAL
shf_cal_2 = HFP01SC_CAL_2
      Scan(10,Sec,1,0)
            'CS616 Water Content Reflectometer measurements VW and PA_uS:
            PortSet(1,1)
```

```
                    'CS616 (PA_uS,1,1,1,1,1.0,0)
                PeriodAvg(PA_uS,1,mV5000,1,0,0,100,5,1,0)
                PortSet(1,0)
                VW=-0.0663+(-0.0063*PA_uS)+(0.0007*PA_uS^2)
                'CS616 Water Content Reflectometer measurements VW_2 AND
PA_uS_2:
                PortSet(2,1)
                PeriodAvg(PA_uS_2,1,mV5000,2,0,0,100,5,1,0)
                PortSet(2,0)
   VW_2=-0.0663+(-0.0063*PA_uS_2)+(0.0007*PA_uS_2^2)
                'CS616 Water Content Reflectometer measurements VW_3 and PA_uS_3:
                PortSet(3,1)
                PeriodAvg(PA_uS_3,1,mV5000,3,0,0,100,5,1,0)
                PortSet(3,0)
                VW_3=-0.0663+(-0.0063*PA_uS_3)+(0.0007*PA_uS_3^2)
                'CS616 Water Content Reflectometer measurements VW_4 and PA_uS_4:
                PortSet(4,1)
                PeriodAvg(PA_uS_4,1,mV5000,4,0,0,100,5,1,0)
                PortSet(4,0)
                VW_4=-0.0663+(-0.0063*PA_uS_4)+(0.0007*PA_uS_4^2)
                'CS616 Water Content Reflectometer measurements VW_5 and PA_uS_5:
                PortSet(5,1)
                PeriodAvg(PA_uS_5,1,mV5000,33,0,0,100,5,1,0)
                PortSet(5,0)
                VW_5=-0.0663+(-0.0063*PA_uS_5)+(0.0007*PA_uS_5^2)
                'CS616 Water Content Reflectometer measurements VW_6 and PA_uS_6:
                PortSet(1,1)
                PeriodAvg(PA_uS_6,1,mV5000,34,0,0,100,5,1,0)
                PortSet(1,0)
                VW_6=-0.0663+(-0.0063*PA_uS_6)+(0.0007*PA_uS_6^2)

                'CS100 Barometric Pressure Sensor measurement BP_mbar:
                PortSet(6,1)
                VoltSe(BP_mbar,1,mV5000,7,1,0,250,0.2,600.0)
                BP_mbar=BP_mbar*1.0
                'PortSet(6,0)

        'Wiring Panel Temperature measurement PTemp_C:
                PanelTemp(PTemp_C,250)
                tc_ref=PTemp_C*1.0
                tc_ref_in=PTemp_C*1.0
```

```
                'HMP45C (6-wire) Temperature & Relative Humidity Sensor
measurements AirTC and RH:
   VoltSe(AirTC,1,mV1000,5,0,0,250,0.1,-40.0)
                VoltSe(RH,1,mV1000,6,0,0,250,0.1,0)
                If RH>100 AND RH<108 Then RH=100
                fw=AirTC*1.0
                fw_in=AirTC*1.0
                If (fw_in = NaN) Then fw_in = 0

                'Type E (chromel-constantan) Thermocouple measurements Temp_C:
                TCDiff(Temp_C,1,mV20C,6,TypeE,PTemp_C,True,0,250,1,0)
                'Temp_C is uncovered 2 cm
                'Temp_c_2 is uncovered 4 cm
                'Temp_C_3 is covered 2 cm
                'Temp_c_4 is covered 4 cm
                'Type E (chromel-constantan) Thermocouple measurements Temp_C_2:
                TCDiff(Temp_C_2,1,mV20C,7,TypeE,PTemp_C,True,0,250,1,0)
                'Type E (chromel-constantan) Thermocouple measurements Temp_C_3:
                TCDiff(Temp_C_3,1,mV20C,8,TypeE,PTemp_C,True,0,250,1,0)
                'Type E (chromel-constantan) Thermocouple measurements Temp_C_4:
                TCDiff(Temp_C_4,1,mV20C,9,TypeE,PTemp_C,True,0,250,1,0)

        'CM3 Pyranometer measurements Solar_kJ and Solar_Wm2:
                VoltDiff(Solar_Wm2,1,mV50,5,True,0,250,76.9231,0)
                If Solar_Wm2<0 Then Solar_Wm2=0
                Solar_kJ=Solar_Wm2*0.2

        'CNR2 Net radiation measurements
                VoltDiff(Net_shortwave,1,mV20,20,True,200,250,63.6132,0.0)
                VoltDiff(Net_longwave,1,mV20,19,True,0,250,84.0336,0.0)

 'Measure the HFP01SC soil heat flux plate 1.
   VoltDiff(shf_mV,1,mV50,11,FALSE,200,200,1,0)
   shf = shf_mV * shf_cal
  'Measure voltage across the heater (Rf_V).
   VoltDiff(V_Rf, 1, mV5000, 12, FALSE, 200, 200, 0.001, 0)
  'Maintain filtered values for calibration.
   AvgRun (shf_mV_run,1,shf_mV,100)
   AvgRun (V_Rf_run,1,V_Rf,100)
   'Call hfp01sc_cal
        'Measure the HFP01SC soil heat flux plate 2.
   VoltDiff(shf_2_mV,1,mV50,13,FALSE,200,200,1,0)
   shf_2 = shf_2_mV * shf_cal_2
  'Measure voltage across the heater (Rf_V).
```

```
   VoltDiff(V_Rf_2, 1, mV5000, 14, FALSE, 200, 200, 0.001, 0)
  'Maintain filtered values for calibration.
   AvgRun (shf_2_mV_run,1,shf_2_mV,100)
   AvgRun (V_Rf_2_run,1,V_Rf_2,100)
   'Call hfp01sc_cal_2

 'Run the Apogee program to calculate the target temperature
          'Measure IRR-P sensor body thermistor temperature
                BrHalf(SBT_C,1,mV5000,31,1,1,5000,True,0,250,1,0)
                SBT_C=24900*(1/SBT_C-1)
                SBT_C=LOG(SBT_C)
                SBT_C=1/(1.129241e-3+2.341077e-4*SBT_C+8.775468e-
8*(SBT_C^3))-273.15
                'Measure IRR-P mV output of thermopile
                VoltDiff(TTmV,1,mV20,15,True,0,250,1,0)
                'Calculate slope (m) and offset (b) coefficients for target temperature
calculation
                m_8=1340820000+(7418550*SBT_C)+(72785*SBT_C^2)
                b_9=14841900+(118490*SBT_C)+(23378*SBT_C^2)
                'Calculate target temperature using calculated slope (m) and offset (b)
                SBT_K_7=SBT_C+273.15
                TT_K_6=SBT_K_7^4+TTmV*m_8+b_9
                TT_K_6=SQR(SQR(TT_K_6))
                'Convert target temperature into desired units
                TT_C=TT_K_6-273.15
   'Call Output Tables
                CallTable (Met)
         NextScan
EndProg
```

APPENDIX B

EDDY COVARIANCE DATA PROCESSING

B.1 EdiRE Processing Scripts for Mobile Eddy Covariance Tower Data

The eddy covariance tower data is measured using a three-dimensional sonic anemometer and an open-path gas analyzer at 20 Hz. Data processing is performed using the EdiRE data software tool, which is available through the University of Edinburgh. To use the tool, a processing file in necessary. The processing file includes details specifying variables within the raw data files, the numerous corrections necessary to apply to the data, converting the raw data into flux measurements after the appropriate corrections are made, and determining the tower footprint. There are three different scripts for the three different mobile tower deployments, which are included below:

Palo Verde (Xeric) Mobile Eddy Covariance Tower Processing File:

Location Output Files
    Output File Calculations = M:\Mobile_tower\PV_Data\daily\3-13.txt
Extract
    From Time =
    To Time =
    Channel = 1
    Label for Signal = SECONDS
Extract
    From Time =
    To Time =
    Channel = 2
    Label for Signal = NANOSECONDS
Extract
    From Time =
    To Time =
    Channel = 3
    Label for Signal = RECORD
Extract
    From Time =
    To Time =
    Channel = 4
    Label for Signal = Ux
Extract
    From Time =
    To Time =
    Channel = 5
    Label for Signal = Uy
Extract
    From Time =
    To Time =
    Channel = 6
    Label for Signal = Uz
Extract
    From Time =
    To Time =
    Channel = 7
    Label for Signal = co2
Extract
    From Time =
    To Time =
    Channel = 8
    Label for Signal = h2o
Extract
    From Time =
    To Time =
    Channel = 9
    Label for Signal = Ts
Extract
    From Time =
    To Time =
    Channel = 10
    Label for Signal = press
Extract
    From Time =
    To Time =
    Channel = 11
    Label for Signal = diag_csat

Despike
From Time =
To Time =
Signal = co2
Standard Deviations = 4
Spike width = 200
Spike % consistency = 50
Replace spikes =
Storage Label spike count = co2spike
Outlier Standard Deviations = 4
Despike
From Time =
To Time =
Signal = h2o
Standard Deviations = 4
Spike width = 200
Spike % consistency = 50
Replace spikes =
Storage Label spike count = h2ospike
Outlier Standard Deviations = 4
Remove Lag
From Time =
To Time =
Signal = co2
Min Lag (sec) = -1
Lag (sec) = 0.3
Max Lag (sec) = 1
Below Min default (sec) =
Above Max default (sec) =
Remove Lag
From Time =
To Time =
Signal = h2o
Min Lag (sec) = -1
Lag (sec) = 0.3
Max Lag (sec) = 1
Below Min default (sec) =
Above Max default (sec) =
Raw Subset
From Time =
To Time =
Subset start time(s) =
Subset length(s) =
Signal for condition = diag_csat
Condition operators = <
Condition (lower limit) = 4096
Condition upper limit =
Storage Label % removed = csat_error
Number of signals = 6
Signal Subset = Ux
Signal Subset = Uy
Signal Subset = Uz
Signal Subset = co2
Signal Subset = h2o
Signal Subset = Ts
1 chn statistics
From Time =
To Time =
Signal = Ux
Storage Label Mean = Ux_mean
Storage Label Std Dev =
Storage Label Skewness =
Storage Label Kurtosis =
Storage Label Maximum = Ux_max
Storage Label Minimum =
Storage Label Variance =
Storage Label Turbulent Intensity =
Alt Turbulent Intensity Denominator =
1 chn statistics
From Time =
To Time =
Signal = Uy
Storage Label Mean = Uy_mean
Storage Label Std Dev = sd_Uy
Storage Label Skewness =
Storage Label Kurtosis =
Storage Label Maximum = Uy_max
Storage Label Minimum =
Storage Label Variance =
Storage Label Turbulent Intensity =

Alt Turbulent Intensity
Denominator =
1 chn statistics
From Time =
To Time =
Signal = Uz
Storage Label Mean = Uz_mean
Storage Label Std Dev =
Storage Label Skewness =
Storage Label Kurtosis =
Storage Label Maximum =
Uz_max
Storage Label Minimum =
Storage Label Variance =
Storage Label Turbulent
Intensity =
Alt Turbulent Intensity
Denominator =
1 chn statistics
From Time =
To Time =
Signal = co2
Storage Label Mean = co2_mean
Storage Label Std Dev =
Storage Label Skewness =
Storage Label Kurtosis =
Storage Label Maximum =
co2_max
Storage Label Minimum =
Storage Label Variance =
Storage Label Turbulent
Intensity =
Alt Turbulent Intensity
Denominator =
1 chn statistics
From Time =
To Time =
Signal = h2o
Storage Label Mean =
H2O_mean
Storage Label Std Dev =
Storage Label Skewness =
Storage Label Kurtosis =
Storage Label Maximum =
h20_max
Storage Label Minimum =
Storage Label Variance =
Storage Label Turbulent
Intensity =
Alt Turbulent Intensity
Denominator =
1 chn statistics
From Time =
To Time =
Signal = press
Storage Label Mean =
press_mean
Storage Label Std Dev =
Storage Label Skewness =
Storage Label Kurtosis =
Storage Label Maximum =
Storage Label Minimum =
Storage Label Variance =
Storage Label Turbulent
Intensity =
Alt Turbulent Intensity
Denominator =
1 chn statistics
From Time =
To Time =
Signal = Ts
Storage Label Mean = Ts_mean
Storage Label Std Dev =
Storage Label Skewness =
Storage Label Kurtosis =
Storage Label Maximum =
Storage Label Minimum =
Storage Label Variance =
Storage Label Turbulent
Intensity =
Alt Turbulent Intensity
Denominator =
Wind direction
From Time =
To Time =
Signal (u) = Ux
Signal (v) = Uy

Orientation = 21
Wind Direction Components = U+N_V+E
Wind Direction Output = N_0_deg-E_90_deg
Storage Label Wind Direction = Wind_dir
Storage Label Wind Dir Std Dev =
Rotation coefficients
From Time =
To Time =
Signal (u) = Ux
Signal (v) = Uy
Signal (w) = Uz
Storage Label Alpha =
Storage Label Beta =
Storage Label Gamma =
Optional mean u = Ux_mean
Optional mean v = Uy_mean
Optional mean w = Uz_mean
Rotation
From Time =
To Time =
Signal (u) = Ux
Signal (v) = Uy
Signal (w) = Uz
Alpha =
Beta =
Gamma =
Do 1st Rot = x
Do 2nd Rot = x
Do 3rd Rot = x
Gas conversion
From Time =
To Time =
Storage Label = e
Apply to =
Apply by =
Measured variable = H2O_mean
Convert from = Absolute density g/m3
Convert to = Partial Pressure kPa
Temperature (C) = Ts_mean
Pressure (kPa) = press_mean
Water vapour = H2O_mean
Water vapour units = Partial pressure kPa
Molecular weight (g/mole) = 18
Sensible heat flux coefficient
From Time =
To Time =
Storage Label = rhoCp
Apply to =
Apply by =
Vapour pressure (KPa) = e
Min or QC =
Max or QC =
Temperature (C) = Ts_mean
Min or QC =
Max or QC =
Pressure (KPa) = press_mean
Min or QC =
Max or QC =
Alternate rhoCp = 1296.0243
Latent heat of evaporation
From Time =
To Time =
Storage Label = L
Apply to =
Apply by =
Temperature (C) = Ts_mean
Min or QC =
Max or QC =
Pressure (KPa) = press_mean
Min or QC =
Max or QC =
LE flux coef, L = 2440
Friction Velocity
From Time =
To Time =
Signal (u) = Ux
Signal (v) = Uy
Signal (w) = Uz
Storage Label U* (uw) =
Storage Label U* (uw vw) = ustar
2 chn statistics

From Time =
To Time =
Signal = h2o
Signal = Uz
Storage Label Covariance = h2o_cov
Storage Label Correlation =
Storage Label Flux = LE
Flux coefficient = L
2 chn statistics
From Time =
To Time =
Signal = Ts
Signal = Uz
Storage Label Covariance = Ts_cov
Storage Label Correlation =
Storage Label Flux = H
Flux coefficient = rhoCp
2 chn statistics
From Time =
To Time =
Signal = co2
Signal = Uz
Storage Label Covariance = co2_cov
Storage Label Correlation =
Storage Label Flux = FC
Flux coefficient = 1
User defined
From Time =
To Time =
Storage Label = Wind_sp
Apply to =
Apply by =
Equation = SQRT(Ux_mean^2+Uy_mean^2)
Variable = Ux_mean
Variable = Uy_mean
Stability - Monin Obhukov
From Time =
To Time =
Storage Label = Stability
Apply to =
Apply by =
Measurement height (m) = 7
Zero plane displacement (m) = 2.5
Virtual Temperature (C) = Ts_mean
Min or QC =
Max or QC =
H flux (W/m2) = H
Min or QC =
Max or QC =
H flux coef, RhoCp = rhoCp
Min or QC =
Max or QC =
Scaling velocity (m/s) = ustar
Min or QC =
Max or QC =
Frequency response
From Time =
To Time =
Storage Label = H_frqres
Apply to =
Apply by =
Correction type = WX
Measurement height (m) = 7
Zero plane displacement (m) = 2.5
Boundary layer height (m) = 1500
Stability Z/L = Stability
Wind speed (m/s) = Wind_sp
Sensor 1 Flow velocity (m/s) = Wind_sp
Sensor 1 Sampling frequency (Hz) = 20.0
Sensor 1 Low pass filter type =
Sensor 1 Low pass filter time constant =
Sensor 1 High pass filter type =
Sensor 1 High pass filter time constant =
Sensor 1 Path length (m) = 0.15
Sensor 1 Time constant (s) = 0
Sensor 1 Tube attenuation coef =

Sensor 2 Flow velocity (m/s) = Wind_sp
Sensor 2 Sampling frequency (Hz) = 20.0
Sensor 2 Low pass filter type =
Sensor 2 Low pass filter time constant =
Sensor 2 High pass filter type =
Sensor 2 High pass filter time constant =
Sensor 2 Path length (m) = 0.15
Sensor 2 Time constant (s) = 0
Sensor 2 Tube attenuation coef =
Path separation (m) =
Get spectral data type = Model
Get response function from = model
Reference Tag =
Reference response condition =
Sensor 1 subsampled =
Sensor 2 subsampled =
Apply velocity distribution adjustment =
Use calculated distribution =
Velocity distribution std dev=
Stability distribution std dev=
Frequency response
From Time =
To Time =
Storage Label = CLE_frqres
Apply to =
Apply by =
Correction type = WX
Measurement height (m) = 7
Zero plane displacement (m) = 2.5
Boundary layer height (m) = 1500
Stability Z/L = Stability
Wind speed (m/s) = Wind_sp
Sensor 1 Flow velocity (m/s) = Wind_sp
Sensor 1 Sampling frequency (Hz) = 20.0
Sensor 1 Low pass filter type =
Sensor 1 Low pass filter time constant =
Sensor 1 High pass filter type =
Sensor 1 High pass filter time constant =
Sensor 1 Path length (m) = 0.15
Sensor 1 Time constant (s) = 0
Sensor 1 Tube attenuation coef =
Sensor 2 Flow velocity (m/s) = Wind_sp
Sensor 2 Sampling frequency (Hz) = 20.0
Sensor 2 Low pass filter type =
Sensor 2 Low pass filter time constant =
Sensor 2 High pass filter type =
Sensor 2 High pass filter time constant =
Sensor 2 Path length (m) = 0.125
Sensor 2 Time constant (s) = 0.0
Sensor 2 Tube attenuation coef =
Path separation (m) = 0.05
Get spectral data type = Model
Get response function from = model
Reference Tag =
Reference response condition =
Sensor 1 subsampled =
Sensor 2 subsampled =
Apply velocity distribution adjustment =
Use calculated distribution =
Velocity distribution std dev=
Stability distribution std dev=
Mathematical operation
From Time =
To Time =
Storage Label = Hc
Apply to =
Apply by =
Measured variable A = H
Operation = *
Measured variable B = H_frqres

Mathematical operation
From Time =
To Time =
Storage Label = LEc
Apply to =
Apply by =
Measured variable A = LE
Operation = *
Measured variable B = CLE_frqres
Mathematical operation
From Time =
To Time =
Storage Label = FCc
Apply to =
Apply by =
Measured variable A = FC
Operation = *
Measured variable B = CLE_frqres
Webb correction
From Time =
To Time =
Storage Label = WPL_LE
Apply to =
Apply by =
Scalar value type = Partial Pressure (kPa)
Scalar value = e
Min or QC =
Max or QC =
Water vapour value type = Partial Pressure (kPa)
Water vapour value = e
Min or QC =
Max or QC =
Temperature (C) = Ts_mean
Min or QC =
Max or QC =
Pressure (KPa) = press_mean
Min or QC =
Max or QC =
H flux (W/m2) = Hc
Min or QC =
Max or QC =
LE flux (W/m2) = LEc
Min or QC =
Max or QC =
H flux coef, RhoCp = rhoCp
Min or QC =
Max or QC =
LE flux coef, L = L
Min or QC =
Max or QC =
Scalar molecular wt. = 18
Scalar flux type = LE (W/m2)
Scalar flux coefficient = L
Min or QC =
Max or QC =
Alternate water vapour pressure (kPa) =
Alternate temperature (C) =
Alternate pressure (kPa) =
Mathematical operation
From Time =
To Time =
Storage Label = LEcw
Apply to =
Apply by =
Measured variable A = LEc
Operation = +
Measured variable B = WPL_LE
Webb correction
From Time =
To Time =
Storage Label = WPL_FC
Apply to =
Apply by =
Scalar value type = Density (mg/m3)
Scalar value = co2_mean
Min or QC =
Max or QC =
Water vapour value type = Partial Pressure (kPa)
Water vapour value = e
Min or QC =
Max or QC =

Temperature (C) = Ts_mean
Min or QC =
Max or QC =
Pressure (KPa) = press_mean
Min or QC =
Max or QC =
H flux (W/m2) = Hc
Min or QC =
Max or QC =
LE flux (W/m2) = LEcw
Min or QC =
Max or QC =
H flux coef, RhoCp = rhoCp
Min or QC =
Max or QC =
LE flux coef, L = L
Min or QC =
Max or QC =
Scalar molecular wt. = 44
Scalar flux type = Fx (mg/m2/s)
Scalar flux coefficient = 1
Min or QC =
Max or QC =
Alternate water vapour pressure (kPa) =
Alternate temperature (C) =
Alternate pressure (kPa) =
Mathematical operation
From Time =
To Time =
Storage Label = FCcw
Apply to =
Apply by =
Measured variable A = FCc
Operation = +
Measured variable B = WPL_FC
Mathematical operation
From Time =
To Time =
Storage Label = ZoverL
Apply to =
Apply by =
Measured variable A = 7
Operation = /
Measured variable B = Stability
Plot Value
From Time =
To Time =
Left Axis Value = Stability
Right Axis Value =
Left Axis Minimum =
Left Axis Maximum =
Right Axis Minimum =
Right Axis Maximum =
Match Left/Right Axes =
Plot Value
From Time =
To Time =
Left Axis Value = ZoverL
Right Axis Value =
Left Axis Minimum =
Left Axis Maximum =
Right Axis Minimum =
Right Axis Maximum =
Match Left/Right Axes =
Solar elevation angle
From Time =
To Time =
Storage Label = Solar_Elev
Apply to =
Apply by =
Site lat. (dec deg) = 33.42
Site long. (dec deg) = -111.93
Time standard long. (dec deg) =
Solar azimuth angle
From Time =
To Time =
Storage Label = Solar_Azimuth
Apply to =
Apply by =
Site lat. (dec deg) = 33.42
Site long. (dec deg) = -111.93
Time standard long. (dec deg) =
Solar elev. angle (dec deg) = Solar_Elev
Footprint
From Time =
To Time =

Storage Label = footp
Apply to =
Apply by =
Fetch (m) = 300
Measurement height (m) = 7
Wind speed (m/s) = Wind_sp
Friction velocity (m/s) = ustar
Std dev of V velocity (m/s) = sd_Uy
Stability Z/L = Stability
Wind direction (deg) = Wind_dir
Wind speed limit = 0.1
Friction velocity limit = 0.01
Stability limit (+/-) = 30
Fetch calculation step, m = 1
Footprint average
From Time =
To Time =
Storage Label = Avg_FP
Apply to =
Apply by =
Unique footprint tag = tag_AVP
Variable footprint? =
Variable to average =
Conditional variable = H
Condition operators = >
Condition (lower limit) = 2
Condition upper limit =
Output File = M:\Mobile_tower\PV_Data\daily\fp3-13.txt

<u>Parking Lot Mobile Eddy Covariance Tower Processing File</u>:

Location Output Files
Output File Calculations = M:\Mobile_tower\Parking_MobileData\daily\6-30.txt
Extract
From Time =
To Time =
Channel = 1
Label for Signal = SECONDS
Extract
From Time =
To Time =
Channel = 2
Label for Signal = NANOSECONDS
Extract
From Time =
To Time =
Channel = 3
Label for Signal = RECORD
Extract
From Time =
To Time =
Channel = 4
Label for Signal = Ux
Extract
From Time =
To Time =
Channel = 5
Label for Signal = Uy
Extract
From Time =
To Time =
Channel = 6
Label for Signal = Uz
Extract
From Time =
To Time =
Channel = 7
Label for Signal = co2
Extract
From Time =
To Time =
Channel = 8
Label for Signal = h2o
Extract
From Time =
To Time =
Channel = 9
Label for Signal = Ts
Extract
From Time =

To Time =
Channel = 10
Label for Signal = press
Extract
From Time =
To Time =
Channel = 11
Label for Signal = diag_csat
Despike
From Time =
To Time =
Signal = co2
Standard Deviations = 4
Spike width = 200
Spike % consistency = 50
Replace spikes =
Storage Label spike count =
co2spike
Outlier Standard Deviations = 4
Despike
From Time =
To Time =
Signal = h2o
Standard Deviations = 4
Spike width = 200
Spike % consistency = 50
Replace spikes =
Storage Label spike count =
h2ospike
Outlier Standard Deviations = 4
Remove Lag
From Time =
To Time =
Signal = co2
Min Lag (sec) = -1
Lag (sec) = 0.3
Max Lag (sec) = 1
Below Min default (sec) =
Above Max default (sec) =
Remove Lag
From Time =
To Time =
Signal = h2o
Min Lag (sec) = -1
Lag (sec) = 0.3
Max Lag (sec) = 1
Below Min default (sec) =
Above Max default (sec) =
Raw Subset
From Time =
To Time =
Subset start time(s) =
Subset length(s) =
Signal for condition = diag_csat
Condition operators = <
Condition (lower limit) = 4096
Condition upper limit =
Storage Label % removed =
csat_error
Number of signals = 6
Signal Subset = Ux
Signal Subset = Uy
Signal Subset = Uz
Signal Subset = co2
Signal Subset = h2o
Signal Subset = Ts
1 chn statistics
From Time =
To Time =
Signal = Ux
Storage Label Mean = Ux_mean
Storage Label Std Dev =
Storage Label Skewness =
Storage Label Kurtosis =
Storage Label Maximum =
Ux_max
Storage Label Minimum =
Storage Label Variance =
Storage Label Turbulent
Intensity =
Alt Turbulent Intensity
Denominator =
1 chn statistics
From Time =
To Time =
Signal = Uy
Storage Label Mean = Uy_mean
Storage Label Std Dev = sd_Uy

Storage Label Skewness =
Storage Label Kurtosis =
Storage Label Maximum =
Uy_max
Storage Label Minimum =
Storage Label Variance =
Storage Label Turbulent
Intensity =
Alt Turbulent Intensity
Denominator =
1 chn statistics
From Time =
To Time =
Signal = Uz
Storage Label Mean = Uz_mean
Storage Label Std Dev =
Storage Label Skewness =
Storage Label Kurtosis =
Storage Label Maximum =
Uz_max
Storage Label Minimum =
Storage Label Variance =
Storage Label Turbulent
Intensity =
Alt Turbulent Intensity
Denominator =
1 chn statistics
From Time =
To Time =
Signal = co2
Storage Label Mean = co2_mean
Storage Label Std Dev =
Storage Label Skewness =
Storage Label Kurtosis =
Storage Label Maximum =
co2_max
Storage Label Minimum =
Storage Label Variance =
Storage Label Turbulent
Intensity =
Alt Turbulent Intensity
Denominator =
1 chn statistics
From Time =
To Time =
Signal = h2o
Storage Label Mean =
H2O_mean
Storage Label Std Dev =
Storage Label Skewness =
Storage Label Kurtosis =
Storage Label Maximum =
h20_max
Storage Label Minimum =
Storage Label Variance =
Storage Label Turbulent
Intensity =
Alt Turbulent Intensity
Denominator =
1 chn statistics
From Time =
To Time =
Signal = press
Storage Label Mean =
press_mean
Storage Label Std Dev =
Storage Label Skewness =
Storage Label Kurtosis =
Storage Label Maximum =
Storage Label Minimum =
Storage Label Variance =
Storage Label Turbulent
Intensity =
Alt Turbulent Intensity
Denominator =
1 chn statistics
From Time =
To Time =
Signal = Ts
Storage Label Mean = Ts_mean
Storage Label Std Dev =
Storage Label Skewness =
Storage Label Kurtosis =
Storage Label Maximum =
Storage Label Minimum =
Storage Label Variance =
Storage Label Turbulent
Intensity =

Alt Turbulent Intensity Denominator =
Wind direction
From Time =
To Time =
Signal (u) = Ux
Signal (v) = Uy
Orientation = 227
Wind Direction Components = U+N_V+E
Wind Direction Output = N_0_deg-E_90_deg
Storage Label Wind Direction = Wind_dir
Storage Label Wind Dir Std Dev =
Rotation coefficients
From Time =
To Time =
Signal (u) = Ux
Signal (v) = Uy
Signal (w) = Uz
Storage Label Alpha =
Storage Label Beta =
Storage Label Gamma =
Optional mean u = Ux_mean
Optional mean v = Uy_mean
Optional mean w = Uz_mean
Rotation
From Time =
To Time =
Signal (u) = Ux
Signal (v) = Uy
Signal (w) = Uz
Alpha =
Beta =
Gamma =
Do 1st Rot = x
Do 2nd Rot = x
Do 3rd Rot = x
Gas conversion
From Time =
To Time =
Storage Label = e
Apply to =
Apply by =
Measured variable = H2O_mean
Convert from = Absolute density g/m3
Convert to = Partial Pressure kPa
Temperature (C) = Ts_mean
Pressure (kPa) = press_mean
Water vapour = H2O_mean
Water vapour units = Partial pressure kPa
Molecular weight (g/mole) = 18
Sensible heat flux coefficient
From Time =
To Time =
Storage Label = rhoCp
Apply to =
Apply by =
Vapour pressure (KPa) = e
Min or QC =
Max or QC =
Temperature (C) = Ts_mean
Min or QC =
Max or QC =
Pressure (KPa) = press_mean
Min or QC =
Max or QC =
Alternate rhoCp = 1296.0243
Latent heat of evaporation
From Time =
To Time =
Storage Label = L
Apply to =
Apply by =
Temperature (C) = Ts_mean
Min or QC =
Max or QC =
Pressure (KPa) = press_mean
Min or QC =
Max or QC =
LE flux coef, L = 2440
Friction Velocity
From Time =
To Time =

Signal (u) = Ux
Signal (v) = Uy
Signal (w) = Uz
Storage Label U* (uw) =
Storage Label U* (uw vw) = ustar
2 chn statistics
From Time =
To Time =
Signal = h2o
Signal = Uz
Storage Label Covariance = h2o_cov
Storage Label Correlation =
Storage Label Flux = LE
Flux coefficient = L
2 chn statistics
From Time =
To Time =
Signal = Ts
Signal = Uz
Storage Label Covariance = Ts_cov
Storage Label Correlation =
Storage Label Flux = H
Flux coefficient = rhoCp
2 chn statistics
From Time =
To Time =
Signal = co2
Signal = Uz
Storage Label Covariance = co2_cov
Storage Label Correlation =
Storage Label Flux = FC
Flux coefficient = 1
User defined
From Time =
To Time =
Storage Label = Wind_sp
Apply to =
Apply by =
Equation = SQRT(Ux_mean^2+Uy_mean^2)
Variable = Ux_mean
Variable = Uy_mean
Stability - Monin Obhukov
From Time =
To Time =
Storage Label = Stability
Apply to =
Apply by =
Measurement height (m) = 9
Zero plane displacement (m) = 2.0
Virtual Temperature (C) = Ts_mean
Min or QC =
Max or QC =
H flux (W/m2) = H
Min or QC =
Max or QC =
H flux coef, RhoCp = rhoCp
Min or QC =
Max or QC =
Scaling velocity (m/s) = ustar
Min or QC =
Max or QC =
Frequency response
From Time =
To Time =
Storage Label = H_frqres
Apply to =
Apply by =
Correction type = WX
Measurement height (m) = 9
Zero plane displacement (m) = 2.0
Boundary layer height (m) = 1000
Stability Z/L = Stability
Wind speed (m/s) = Wind_sp
Sensor 1 Flow velocity (m/s) = Wind_sp
Sensor 1 Sampling frequency (Hz) = 10.0
Sensor 1 Low pass filter type =

Sensor 1 Low pass filter time constant =
Sensor 1 High pass filter type =
Sensor 1 High pass filter time constant =
Sensor 1 Path length (m) = 0.15
Sensor 1 Time constant (s) = 0
Sensor 1 Tube attenuation coef =
Sensor 2 Flow velocity (m/s) = Wind_sp
Sensor 2 Sampling frequency (Hz) = 10.0
Sensor 2 Low pass filter type =
Sensor 2 Low pass filter time constant =
Sensor 2 High pass filter type =
Sensor 2 High pass filter time constant =
Sensor 2 Path length (m) = 0.15
Sensor 2 Time constant (s) = 0
Sensor 2 Tube attenuation coef =
Path separation (m) =
Get spectral data type = Model
Get response function from = model
Reference Tag =
Reference response condition =
Sensor 1 subsampled =
Sensor 2 subsampled =
Apply velocity distribution adjustment =
Use calculated distribution =
Velocity distribution std dev=
Stability distribution std dev=
Frequency response
From Time =
To Time =
Storage Label = CLE_frqres
Apply to =
Apply by =
Correction type = WX
Measurement height (m) = 9
Zero plane displacement (m) = 2.0
Boundary layer height (m) = 1000
Stability Z/L = Stability
Wind speed (m/s) = Wind_sp
Sensor 1 Flow velocity (m/s) = Wind_sp
Sensor 1 Sampling frequency (Hz) = 10.0
Sensor 1 Low pass filter type =
Sensor 1 Low pass filter time constant =
Sensor 1 High pass filter type =
Sensor 1 High pass filter time constant =
Sensor 1 Path length (m) = 0.15
Sensor 1 Time constant (s) = 0
Sensor 1 Tube attenuation coef =
Sensor 2 Flow velocity (m/s) = Wind_sp
Sensor 2 Sampling frequency (Hz) = 10.0
Sensor 2 Low pass filter type =
Sensor 2 Low pass filter time constant =
Sensor 2 High pass filter type =
Sensor 2 High pass filter time constant =
Sensor 2 Path length (m) = 0.125
Sensor 2 Time constant (s) = 0.0
Sensor 2 Tube attenuation coef =
Path separation (m) = 0.05
Get spectral data type = Model
Get response function from = model
Reference Tag =
Reference response condition =
Sensor 1 subsampled =
Sensor 2 subsampled =
Apply velocity distribution adjustment =
Use calculated distribution =
Velocity distribution std dev=
Stability distribution std dev=
Mathematical operation

From Time =
To Time =
Storage Label = Hc
Apply to =
Apply by =
Measured variable A = H
Operation = *
Measured variable B = H_frqres
Mathematical operation
From Time =
To Time =
Storage Label = LEc
Apply to =
Apply by =
Measured variable A = LE
Operation = *
Measured variable B = CLE_frqres
Mathematical operation
From Time =
To Time =
Storage Label = FCc
Apply to =
Apply by =
Measured variable A = FC
Operation = *
Measured variable B = CLE_frqres
Webb correction
From Time =
To Time =
Storage Label = WPL_LE
Apply to =
Apply by =
Scalar value type = Partial Pressure (kPa)
Scalar value = e
Min or QC =
Max or QC =
Water vapour value type = Partial Pressure (kPa)
Water vapour value = e
Min or QC =
Max or QC =
Temperature (C) = Ts_mean
Min or QC =
Max or QC =
Pressure (KPa) = press_mean
Min or QC =
Max or QC =
H flux (W/m2) = Hc
Min or QC =
Max or QC =
LE flux (W/m2) = LEc
Min or QC =
Max or QC =
H flux coef, RhoCp = rhoCp
Min or QC =
Max or QC =
LE flux coef, L = L
Min or QC =
Max or QC =
Scalar molecular wt. = 18
Scalar flux type = LE (W/m2)
Scalar flux coefficient = L
Min or QC =
Max or QC =
Alternate water vapour pressure (kPa) =
Alternate temperature (C) =
Alternate pressure (kPa) =
Mathematical operation
From Time =
To Time =
Storage Label = LEcw
Apply to =
Apply by =
Measured variable A = LEc
Operation = +
Measured variable B = WPL_LE
Webb correction
From Time =
To Time =
Storage Label = WPL_FC
Apply to =
Apply by =
Scalar value type = Density (mg/m3)

Scalar value = co2_mean
Min or QC =
Max or QC =
Water vapour value type = Partial Pressure (kPa)
Water vapour value = e
Min or QC =
Max or QC =
Temperature (C) = Ts_mean
Min or QC =
Max or QC =
Pressure (KPa) = press_mean
Min or QC =
Max or QC =
H flux (W/m2) = Hc
Min or QC =
Max or QC =
LE flux (W/m2) = LEcw
Min or QC =
Max or QC =
H flux coef, RhoCp = rhoCp
Min or QC =
Max or QC =
LE flux coef, L = L
Min or QC =
Max or QC =
Scalar molecular wt. = 44
Scalar flux type = Fx (mg/m2/s)
Scalar flux coefficient = 1
Min or QC =
Max or QC =
Alternate water vapour pressure (kPa) =
Alternate temperature (C) =
Alternate pressure (kPa) =
Mathematical operation
From Time =
To Time =
Storage Label = FCcw
Apply to =
Apply by =
Measured variable A = FCc
Operation = +
Measured variable B = WPL_FC
Mathematical operation
From Time =
To Time =
Storage Label = ZoverL
Apply to =
Apply by =
Measured variable A = 7
Operation = /
Measured variable B = Stability
Plot Value
From Time =
To Time =
Left Axis Value = Stability
Right Axis Value =
Left Axis Minimum =
Left Axis Maximum =
Right Axis Minimum =
Right Axis Maximum =
Match Left/Right Axes =
Plot Value
From Time =
To Time =
Left Axis Value = ZoverL
Right Axis Value =
Left Axis Minimum =
Left Axis Maximum =
Right Axis Minimum =
Right Axis Maximum =
Match Left/Right Axes =
Solar elevation angle
From Time =
To Time =
Storage Label = Solar_Elev
Apply to =
Apply by =
Site lat. (dec deg) = 33.42
Site long. (dec deg) = -111.94
Time standard long. (dec deg) =
Solar azimuth angle
From Time =
To Time =
Storage Label = Solar_Azimuth
Apply to =
Apply by =

Site lat. (dec deg) = 33.42
Site long. (dec deg) = -111.94
Time standard long. (dec deg) =
Solar elev. angle (dec deg) = Solar_Elev
Footprint
From Time =
To Time =
Storage Label = footp
Apply to =
Apply by =
Fetch (m) = 300
Measurement height (m) = 9
Wind speed (m/s) = Wind_sp
Friction velocity (m/s) = ustar
Std dev of V velocity (m/s) = sd_Uy
Stability Z/L = Stability
Wind direction (deg) = Wind_dir
Wind speed limit = 0.3
Friction velocity limit = 0.03
Stability limit (+/-) = 30
Fetch calculation step, m = 1
Footprint average
From Time =
To Time =
Storage Label = Avg_FP
Apply to =
Apply by =
Unique footprint tag = tag_AVP
Variable footprint? =
Variable to average =
Conditional variable = H
Condition operators = >
Condition (lower limit) = 2
Condition upper limit =
Output File = M:\Mobile_tower\Parking_MobileData\daily\fp1-20.txt

<u>Turf Grass (Mesic) Mobile Eddy Covariance Tower Processing File</u>:

Location Output Files
Output File Calculations = M:\Mobile_tower\ASU_Poly\daily\7-9.txt
Extract
From Time =
To Time =
Channel = 1
Label for Signal = SECONDS
Extract
From Time =
To Time =
Channel = 2
Label for Signal = NANOSECONDS
Extract
From Time =
To Time =
Channel = 3
Label for Signal = RECORD
Extract
From Time =
To Time =
Channel = 4
Label for Signal = Ux
Extract
From Time =
To Time =
Channel = 5
Label for Signal = Uy
Extract
From Time =
To Time =
Channel = 6
Label for Signal = Uz
Extract
From Time =
To Time =
Channel = 7
Label for Signal = co2
Extract
From Time =
To Time =
Channel = 8

Label for Signal = h2o
Extract
From Time =
To Time =
Channel = 9
Label for Signal = Ts
Extract
From Time =
To Time =
Channel = 10
Label for Signal = press
Extract
From Time =
To Time =
Channel = 11
Label for Signal = diag_csat
Despike
From Time =
To Time =
Signal = co2
Standard Deviations = 4
Spike width = 200
Spike % consistency = 50
Replace spikes =
Storage Label spike count = co2spike
Outlier Standard Deviations = 4
Despike
From Time =
To Time =
Signal = h2o
Standard Deviations = 4
Spike width = 200
Spike % consistency = 50
Replace spikes =
Storage Label spike count = h2ospike
Outlier Standard Deviations = 4
Remove Lag
From Time =
To Time =
Signal = co2
Min Lag (sec) = -1
Lag (sec) = 0.3
Max Lag (sec) = 1
Below Min default (sec) =
Above Max default (sec) =
Remove Lag
From Time =
To Time =
Signal = h2o
Min Lag (sec) = -1
Lag (sec) = 0.3
Max Lag (sec) = 1
Below Min default (sec) =
Above Max default (sec) =
Raw Subset
From Time =
To Time =
Subset start time(s) =
Subset length(s) =
Signal for condition = diag_csat
Condition operators = <
Condition (lower limit) = 4096
Condition upper limit =
Storage Label % removed = csat_error
Number of signals = 6
Signal Subset = Ux
Signal Subset = Uy
Signal Subset = Uz
Signal Subset = co2
Signal Subset = h2o
Signal Subset = Ts
1 chn statistics
From Time =
To Time =
Signal = Ux
Storage Label Mean = Ux_mean
Storage Label Std Dev =
Storage Label Skewness =
Storage Label Kurtosis =
Storage Label Maximum =
Storage Label Minimum =
Storage Label Variance =
Storage Label Turbulent Intensity =

Alt Turbulent Intensity
Denominator =
1 chn statistics
From Time =
To Time =
Signal = Uy
Storage Label Mean = Uy_mean
Storage Label Std Dev =
Storage Label Skewness =
Storage Label Kurtosis =
Storage Label Maximum =
Storage Label Minimum =
Storage Label Variance =
Storage Label Turbulent Intensity =
Alt Turbulent Intensity
Denominator =
1 chn statistics
From Time =
To Time =
Signal = Uz
Storage Label Mean = Uz_mean
Storage Label Std Dev =
Storage Label Skewness =
Storage Label Kurtosis =
Storage Label Maximum =
Storage Label Minimum =
Storage Label Variance =
Storage Label Turbulent Intensity =
Alt Turbulent Intensity
Denominator =
1 chn statistics
From Time =
To Time =
Signal = co2
Storage Label Mean = co2_mean
Storage Label Std Dev =
Storage Label Skewness =
Storage Label Kurtosis =
Storage Label Maximum =
Storage Label Minimum =
Storage Label Variance =
Storage Label Turbulent Intensity =
Alt Turbulent Intensity
Denominator =
1 chn statistics
From Time =
To Time =
Signal = h2o
Storage Label Mean = H2O_mean
Storage Label Std Dev =
Storage Label Skewness =
Storage Label Kurtosis =
Storage Label Maximum =
Storage Label Minimum =
Storage Label Variance =
Storage Label Turbulent Intensity =
Alt Turbulent Intensity
Denominator =
1 chn statistics
From Time =
To Time =
Signal = press
Storage Label Mean = press_mean
Storage Label Std Dev =
Storage Label Skewness =
Storage Label Kurtosis =
Storage Label Maximum =
Storage Label Minimum =
Storage Label Variance =
Storage Label Turbulent Intensity =
Alt Turbulent Intensity
Denominator =
1 chn statistics
From Time =
To Time =
Signal = Ts
Storage Label Mean = Ts_mean
Storage Label Std Dev =
Storage Label Skewness =
Storage Label Kurtosis =

Storage Label Maximum =
Storage Label Minimum =
Storage Label Variance =
Storage Label Turbulent Intensity =
Alt Turbulent Intensity Denominator =
Wind direction
From Time =
To Time =
Signal (u) = Ux
Signal (v) = Uy
Orientation = 230
Wind Direction Components = U+N_V+E
Wind Direction Output = N_0_deg-E_90_deg
Storage Label Wind Direction = Wind_dir
Storage Label Wind Dir Std Dev =
Rotation coefficients
From Time =
To Time =
Signal (u) = Ux
Signal (v) = Uy
Signal (w) = Uz
Storage Label Alpha =
Storage Label Beta =
Storage Label Gamma =
Optional mean u = Ux_mean
Optional mean v = Uy_mean
Optional mean w = Uz_mean
Rotation
From Time =
To Time =
Signal (u) = Ux
Signal (v) = Uy
Signal (w) = Uz
Alpha =
Beta =
Gamma =
Do 1st Rot = x
Do 2nd Rot = x
Do 3rd Rot = x
Gas conversion
From Time =
To Time =
Storage Label = e
Apply to =
Apply by =
Measured variable = H2O_mean
Convert from = Absolute density g/m3
Convert to = Partial Pressure kPa
Temperature (C) = Ts_mean
Pressure (kPa) = press_mean
Water vapour = H2O_mean
Water vapour units = Partial pressure kPa
Molecular weight (g/mole) = 18
Sensible heat flux coefficient
From Time =
To Time =
Storage Label = rhoCp
Apply to =
Apply by =
Vapour pressure (KPa) = e
Min or QC =
Max or QC =
Temperature (C) = Ts_mean
Min or QC =
Max or QC =
Pressure (KPa) = press_mean
Min or QC =
Max or QC =
Alternate rhoCp = 1296.0243
Latent heat of evaporation
From Time =
To Time =
Storage Label = L
Apply to =
Apply by =
Temperature (C) = Ts_mean
Min or QC =
Max or QC =
Pressure (KPa) = press_mean
Min or QC =

Max or QC =
LE flux coef, L = 2440
Friction Velocity
From Time =
To Time =
Signal (u) = Ux
Signal (v) = Uy
Signal (w) = Uz
Storage Label U* (uw) =
Storage Label U* (uw vw) = ustar
2 chn statistics
From Time =
To Time =
Signal = h2o
Signal = Uz
Storage Label Covariance = h2o_cov
Storage Label Correlation =
Storage Label Flux = LE
Flux coefficient = L
2 chn statistics
From Time =
To Time =
Signal = Ts
Signal = Uz
Storage Label Covariance = Ts_cov
Storage Label Correlation =
Storage Label Flux = H
Flux coefficient = rhoCp
2 chn statistics
From Time =
To Time =
Signal = co2
Signal = Uz
Storage Label Covariance = co2_cov
Storage Label Correlation =
Storage Label Flux = FC
Flux coefficient = 1
User defined
From Time =
To Time =
Storage Label = Wind_sp
Apply to =
Apply by =
Equation = SQRT(Ux_mean^2+Uy_mean^2)
Variable = Ux_mean
Variable = Uy_mean
Stability - Monin Obhukov
From Time =
To Time =
Storage Label = Stability
Apply to =
Apply by =
Measurement height (m) = 8
Zero plane displacement (m) = 5.0
Virtual Temperature (C) = Ts_mean
Min or QC =
Max or QC =
H flux (W/m2) = H
Min or QC =
Max or QC =
H flux coef, RhoCp = rhoCp
Min or QC =
Max or QC =
Scaling velocity (m/s) = ustar
Min or QC =
Max or QC =
Frequency response
From Time =
To Time =
Storage Label = H_frqres
Apply to =
Apply by =
Correction type = WX
Measurement height (m) = 8
Zero plane displacement (m) = 5.0
Boundary layer height (m) = 1500
Stability Z/L = Stability
Wind speed (m/s) = Wind_sp

Sensor 1 Flow velocity (m/s) = Wind_sp
Sensor 1 Sampling frequency (Hz) = 10.0
Sensor 1 Low pass filter type =
Sensor 1 Low pass filter time constant =
Sensor 1 High pass filter type =
Sensor 1 High pass filter time constant =
Sensor 1 Path length (m) = 0.15
Sensor 1 Time constant (s) = 0
Sensor 1 Tube attenuation coef =
Sensor 2 Flow velocity (m/s) = Wind_sp
Sensor 2 Sampling frequency (Hz) = 10.0
Sensor 2 Low pass filter type =
Sensor 2 Low pass filter time constant =
Sensor 2 High pass filter type =
Sensor 2 High pass filter time constant =
Sensor 2 Path length (m) = 0.15
Sensor 2 Time constant (s) = 0
Sensor 2 Tube attenuation coef =
Path separation (m) =
Get spectral data type = Model
Get response function from = model
Reference Tag =
Reference response condition =
Sensor 1 subsampled =
Sensor 2 subsampled =
Apply velocity distribution adjustment =
Use calculated distribution =
Velocity distribution std dev=
Stability distribution std dev=
Frequency response
From Time =
To Time =
Storage Label = CLE_frqres
Apply to =
Apply by =
Correction type = WX
Measurement height (m) = 8
Zero plane displacement (m) = 5.0
Boundary layer height (m) = 1500
Stability Z/L = Stability
Wind speed (m/s) = Wind_sp
Sensor 1 Flow velocity (m/s) = Wind_sp
Sensor 1 Sampling frequency (Hz) = 10.0
Sensor 1 Low pass filter type =
Sensor 1 Low pass filter time constant =
Sensor 1 High pass filter type =
Sensor 1 High pass filter time constant =
Sensor 1 Path length (m) = 0.15
Sensor 1 Time constant (s) = 0
Sensor 1 Tube attenuation coef =
Sensor 2 Flow velocity (m/s) = Wind_sp
Sensor 2 Sampling frequency (Hz) = 10.0
Sensor 2 Low pass filter type =
Sensor 2 Low pass filter time constant =
Sensor 2 High pass filter type =
Sensor 2 High pass filter time constant =
Sensor 2 Path length (m) = 0.125
Sensor 2 Time constant (s) = 0.0
Sensor 2 Tube attenuation coef =
Path separation (m) = 0.05
Get spectral data type = Model
Get response function from = model
Reference Tag =
Reference response condition =
Sensor 1 subsampled =
Sensor 2 subsampled =

Apply velocity distribution adjustment =
Use calculated distribution =
Velocity distribution std dev=
Stability distribution std dev=
Mathematical operation
From Time =
To Time =
Storage Label = Hc
Apply to =
Apply by =
Measured variable A = H
Operation = *
Measured variable B = H_frqres
Mathematical operation
From Time =
To Time =
Storage Label = LEc
Apply to =
Apply by =
Measured variable A = LE
Operation = *
Measured variable B = CLE_frqres
Mathematical operation
From Time =
To Time =
Storage Label = FCc
Apply to =
Apply by =
Measured variable A = FC
Operation = *
Measured variable B = CLE_frqres
Webb correction
From Time =
To Time =
Storage Label = WPL_LE
Apply to =
Apply by =
Scalar value type = Partial Pressure (kPa)
Scalar value = e
Min or QC =
Max or QC =
Water vapour value type = Partial Pressure (kPa)
Water vapour value = e
Min or QC =
Max or QC =
Temperature (C) = Ts_mean
Min or QC =
Max or QC =
Pressure (KPa) = press_mean
Min or QC =
Max or QC =
H flux (W/m2) = Hc
Min or QC =
Max or QC =
LE flux (W/m2) = LEc
Min or QC =
Max or QC =
H flux coef, RhoCp = rhoCp
Min or QC =
Max or QC =
LE flux coef, L = L
Min or QC =
Max or QC =
Scalar molecular wt. = 18
Scalar flux type = LE (W/m2)
Scalar flux coefficient = L
Min or QC =
Max or QC =
Alternate water vapour pressure (kPa) =
Alternate temperature (C) =
Alternate pressure (kPa) =
Mathematical operation
From Time =
To Time =
Storage Label = LEcw
Apply to =
Apply by =
Measured variable A = LEc
Operation = +
Measured variable B = WPL_LE
Webb correction
From Time =

To Time =
Storage Label = WPL_FC
Apply to =
Apply by =
Scalar value type = Density (mg/m3)
Scalar value = co2_mean
Min or QC =
Max or QC =
Water vapour value type = Partial Pressure (kPa)
Water vapour value = e
Min or QC =
Max or QC =
Temperature (C) = Ts_mean
Min or QC =
Max or QC =
Pressure (KPa) = press_mean
Min or QC =
Max or QC =
H flux (W/m2) = Hc
Min or QC =
Max or QC =
LE flux (W/m2) = LEcw
Min or QC =
Max or QC =
H flux coef, RhoCp = rhoCp
Min or QC =
Max or QC =
LE flux coef, L = L
Min or QC =
Max or QC =
Scalar molecular wt. = 44
Scalar flux type = Fx (mg/m2/s)
Scalar flux coefficient = 1
Min or QC =
Max or QC =
Alternate water vapour pressure (kPa) =
Alternate temperature (C) =
Alternate pressure (kPa) =
Mathematical operation
From Time =
To Time =
Storage Label = FCcw
Apply to =
Apply by =
Measured variable A = FCc
Operation = +
Measured variable B = WPL_FC
Mathematical operation
From Time =
To Time =
Storage Label = ZoverL
Apply to =
Apply by =
Measured variable A = 8
Operation = /
Measured variable B = Stability
Plot Value
From Time =
To Time =
Left Axis Value = Hc
Right Axis Value = H
Left Axis Minimum =
Left Axis Maximum =
Right Axis Minimum =
Right Axis Maximum =
Match Left/Right Axes =
Plot Value
From Time =
To Time =
Left Axis Value = LEcw
Right Axis Value = LEc
Left Axis Minimum =
Left Axis Maximum =
Right Axis Minimum =
Right Axis Maximum =
Match Left/Right Axes =
Plot Value
From Time =
To Time =
Left Axis Value = LEc
Right Axis Value = LE
Left Axis Minimum =
Left Axis Maximum =
Right Axis Minimum =
Right Axis Maximum =

Match Left/Right Axes =
Plot Value
From Time =
To Time =
Left Axis Value = LEcw
Right Axis Value = Hc
Left Axis Minimum =
Left Axis Maximum =
Right Axis Minimum =
Right Axis Maximum =
Match Left/Right Axes =
Plot Value
From Time =
To Time =
Left Axis Value = FCcw
Right Axis Value = FCc
Left Axis Minimum =
Left Axis Maximum =
Right Axis Minimum =
Right Axis Maximum =
Match Left/Right Axes =
Solar elevation angle
From Time =
To Time =
Storage Label = Solar_Elev
Apply to =
Apply by =
Site lat. (dec deg) = 33.31
Site long. (dec deg) = -111.68
Time standard long. (dec deg) =
Solar azimuth angle
From Time =
To Time =
Storage Label = Solar_Azimuth
Apply to =
Apply by =
Site lat. (dec deg) = 33.31
Site long. (dec deg) = -111.68
Time standard long. (dec deg) =
Solar elev. angle (dec deg) =
Solar_Elev
Footprint
From Time =
To Time =
Storage Label = footp
Apply to =
Apply by =
Fetch (m) = 300
Measurement height (m) = 8
Wind speed (m/s) = Wind_sp
Friction velocity (m/s) = ustar
Std dev of V velocity (m/s) =
sd_Uy
Stability Z/L = Stability
Wind direction (deg) = Wind_dir
Wind speed limit = 0.1
Friction velocity limit = 0.01
Stability limit (+/-) = 30
Fetch calculation step, m = 1
Footprint average
From Time =
To Time =
Storage Label = Avg_FP
Apply to =
Apply by =
Unique footprint tag = tag_AVP
Variable footprint? =
Variable to average =
Conditional variable = H
Condition operators = >
Condition (lower limit) = 2
Condition upper limit =
Output File =
M:\Mobile_tower\ASU_Poly\daily\fp7-
9.txt

B.2 EdiRE Processing Script for Santa Rita Eddy Covariance Tower Data

The eddy covariance tower data is measured using a three-dimensional sonic anemometer and an open-path gas analyzer at 20 Hz. Data processing is performed using the EdiRE data software tool, which is available through the University of Edinburgh. To use the tool, a processing file in necessary. The processing file includes details specifying variables within the raw data files, the numerous corrections necessary to apply to the data, converting the raw data into flux measurements after the appropriate corrections are made, and determining the tower footprint. The processing file for the Santa Rita eddy covariance tower is included below:

```
Location Output Files
    Output File Calculations = E:\New_Data\2016_winter_fp.csv
Extract
    From Time =
    To Time =
    Channel = 1
    Label for Signal = SECONDS
Extract
    From Time =
    To Time =
    Channel = 2
    Label for Signal = NANOSECONDS
Extract
    From Time =
    To Time =
    Channel = 3
    Label for Signal = RECORD
Extract
    From Time =
    To Time =
    Channel = 4
    Label for Signal = Ux
Extract
    From Time =
    To Time =
    Channel = 5
    Label for Signal = Uy
Extract
    From Time =
    To Time =
    Channel = 6
    Label for Signal = Uz
Extract
```

```
From Time =
        To Time =
        Channel = 7
        Label for Signal = co2
Extract
        From Time =
        To Time =
        Channel = 8
        Label for Signal = h2o
Extract
        From Time =
        To Time =
        Channel = 9
        Label for Signal = Ts
Extract
        From Time =
        Replace spikes =
        Storage Label spike count =
co2spike
        Outlier Standard Deviations = 4
Despike
        From Time =
        To Time =
        Signal = h2o
        Standard Deviations = 4
        Spike width = 200
        Spike % consistency = 50
        Replace spikes =
        Storage Label spike count =
h2ospike
        Outlier Standard Deviations = 4
Remove Lag
        From Time =
        To Time =
        Signal = co2
        Min Lag (sec) = -1
        Lag (sec) = 0.3
        Max Lag (sec) = 1
        Below Min default (sec) =
        Above Max default (sec) =
Remove Lag
        From Time =
        To Time =
        Channel = 10
        Label for Signal = press
Extract
        From Time =
        To Time =
        Channel = 11
        Label for Signal = diag_csat
Despike
        From Time =
        To Time =
        Signal = co2
        Standard Deviations = 4
        Spike width = 200
        Spike % consistency = 50

        Signal = h2o
        Min Lag (sec) = -1
        Lag (sec) = 0.3
        Max Lag (sec) = 1
        Below Min default (sec) =
        Above Max default (sec) =
Raw Subset
        From Time =
        To Time =
        Subset start time(s) =
        Subset length(s) =
        Signal for condition = diag_csat
        Condition operators = <
        Condition (lower limit) = 4096
        Condition upper limit =
        Storage Label % removed =
csat_error
        Number of signals = 6
        Signal Subset = Ux
        Signal Subset = Uy
        Signal Subset = Uz
        Signal Subset = co2
        Signal Subset = h2o
        Signal Subset = Ts
1 chn statistics
        From Time =
        To Time =
```

Signal = Ux
Storage Label Mean = Ux_mean
Storage Label Std Dev =
Storage Label Skewness =
Storage Label Kurtosis =
Storage Label Maximum =
Storage Label Minimum =
Storage Label Variance =
Storage Label Turbulent
Intensity =
Alt Turbulent Intensity
Denominator =
1 chn statistics
From Time =
To Time =
Signal = Uy
Storage Label Mean = Uy_mean
Storage Label Std Dev =
Storage Label Skewness =
Storage Label Kurtosis =
Storage Label Maximum =
Storage Label Minimum =
Storage Label Variance =
Storage Label Turbulent
Intensity =
Alt Turbulent Intensity
Denominator =
1 chn statistics
From Time =
To Time =
Signal = Uz
Storage Label Mean = Uz_mean
Storage Label Std Dev =
Storage Label Skewness =
Storage Label Kurtosis =
Storage Label Maximum =
Storage Label Minimum =
Storage Label Variance =
Storage Label Turbulent
Intensity =
Alt Turbulent Intensity
Denominator =
1 chn statistics
From Time =
To Time =
Signal = co2
Storage Label Mean = co2_mean
Storage Label Std Dev =
Storage Label Skewness =
Storage Label Kurtosis =
Storage Label Maximum =
Storage Label Minimum =
Storage Label Variance =
Storage Label Turbulent
Intensity =
Alt Turbulent Intensity
Denominator =
1 chn statistics
From Time =
To Time =
Signal = h2o
Storage Label Mean =
H2O_mean
Storage Label Std Dev =
Storage Label Skewness =
Storage Label Kurtosis =
Storage Label Maximum =
Storage Label Minimum =
Storage Label Variance =
Storage Label Turbulent
Intensity =
Alt Turbulent Intensity
Denominator =
1 chn statistics
From Time =
To Time =
Signal = press
Storage Label Mean =
press_mean
Storage Label Std Dev =
Storage Label Skewness =
Storage Label Kurtosis =
Storage Label Maximum =
Storage Label Minimum =
Storage Label Variance =
Storage Label Turbulent
Intensity =

Alt Turbulent Intensity Denominator =
1 chn statistics
From Time =
To Time =
Signal = Ts
Storage Label Mean = Ts_mean
Storage Label Std Dev =
Storage Label Skewness =
Storage Label Kurtosis =
Storage Label Maximum =
Storage Label Minimum =
Storage Label Variance =
Storage Label Turbulent Intensity =
Alt Turbulent Intensity Denominator =
Wind direction
From Time =
To Time =
Signal (u) = Ux
Signal (v) = Uy
Orientation = 240
Wind Direction Components = U+N_V+E
Wind Direction Output = N_0_deg-E_90_deg
Storage Label Wind Direction = Wind_dir
Storage Label Wind Dir Std Dev =
Rotation coefficients
From Time =
To Time =
Signal (u) = Ux
Signal (v) = Uy
Signal (w) = Uz
Storage Label Alpha =
Storage Label Beta =
Storage Label Gamma =
Optional mean u = Ux_mean
Optional mean v = Uy_mean
Optional mean w = Uz_mean
Rotation
From Time =
To Time =
Signal (u) = Ux
Signal (v) = Uy
Signal (w) = Uz
Alpha =
Beta =
Gamma =
Do 1st Rot = x
Do 2nd Rot = x
Do 3rd Rot = x
Gas conversion
From Time =
To Time =
Storage Label = e
Apply to =
Apply by =
Measured variable = H2O_mean
Convert from = Absolute density g/m3
Convert to = Partial Pressure kPa
Temperature (C) = Ts_mean
Pressure (kPa) = press_mean
Water vapour = H2O_mean
Water vapour units = Partial pressure kPa
Molecular weight (g/mole) = 18
Sensible heat flux coefficient
From Time =
To Time =
Storage Label = rhoCp
Apply to =
Apply by =
Vapour pressure (KPa) = e
Min or QC =
Max or QC =
Temperature (C) = Ts_mean
Min or QC =
Max or QC =
Pressure (KPa) = press_mean
Min or QC =
Max or QC =
Alternate rhoCp = 1296.0243
Latent heat of evaporation

From Time =
To Time =
Storage Label = L
Apply to =
Apply by =
Temperature (C) = Ts_mean
Min or QC =
Max or QC =
Pressure (KPa) = press_mean
Min or QC =
Max or QC =
LE flux coef, L = 2440
Friction Velocity
From Time =
To Time =
Signal (u) = Ux
Signal (v) = Uy
Signal (w) = Uz
Storage Label U* (uw) =
Storage Label U* (uw vw) = ustar
2 chn statistics
From Time =
To Time =
Signal = h2o
Signal = Uz
Storage Label Covariance = h2o_cov
Storage Label Correlation =
Storage Label Flux = LE
Flux coefficient = L
2 chn statistics
From Time =
To Time =
Signal = Ts
Signal = Uz
Storage Label Covariance = Ts_cov
Storage Label Correlation =
Storage Label Flux = H
Flux coefficient = rhoCp
2 chn statistics
From Time =
To Time =
Signal = co2
Signal = Uz
Storage Label Covariance = co2_cov
Storage Label Correlation =
Storage Label Flux = FC
Flux coefficient = 1
User defined
From Time =
To Time =
Storage Label = Wind_sp
Apply to =
Apply by =
Equation = SQRT(Ux_mean^2+Uy_mean^2)
Variable = Ux_mean
Variable = Uy_mean
Stability - Monin Obhukov
From Time =
To Time =
Storage Label = Stability
Apply to =
Apply by =
Measurement height (m) = 7
Zero plane displacement (m) = 2.0
Virtual Temperature (C) = Ts_mean
Min or QC =
Max or QC =
H flux (W/m2) = H
Min or QC =
Max or QC =
H flux coef, RhoCp = rhoCp
Min or QC =
Max or QC =
Scaling velocity (m/s) = ustar
Min or QC =
Max or QC =
Frequency response
From Time =
To Time =
Storage Label = H_frqres
Apply to =

Apply by =
Correction type = WX
Measurement height (m) = 7
Zero plane displacement (m) = 2.0
Boundary layer height (m) = 1000
Stability Z/L = Stability
Wind speed (m/s) = Wind_sp
Sensor 1 Flow velocity (m/s) = Wind_sp
Sensor 1 Sampling frequency (Hz) = 20.0
Sensor 1 Low pass filter type =
Sensor 1 Low pass filter time constant =
Sensor 1 High pass filter type =
Sensor 1 High pass filter time constant =
Sensor 1 Path length (m) = 0.15
Sensor 1 Time constant (s) = 0
Sensor 1 Tube attenuation coef =
Sensor 2 Flow velocity (m/s) = Wind_sp
Sensor 2 Sampling frequency (Hz) = 20.0
Sensor 2 Low pass filter type =
Sensor 2 Low pass filter time constant =
Sensor 2 High pass filter type =
Sensor 2 High pass filter time constant =
Sensor 2 Path length (m) = 0.15
Sensor 2 Time constant (s) = 0
Sensor 2 Tube attenuation coef =
Path separation (m) =
Get spectral data type = Model
Get response function from = model
Reference Tag =
Reference response condition =
Sensor 1 subsampled =
Sensor 2 subsampled =
Apply velocity distribution adjustment =
Use calculated distribution =
Velocity distribution std dev=
Stability distribution std dev=
Frequency response
From Time =
To Time =
Storage Label = CLE_frqres
Apply to =
Apply by =
Correction type = WX
Measurement height (m) = 7
Zero plane displacement (m) = 2.0
Boundary layer height (m) = 1000
Stability Z/L = Stability
Wind speed (m/s) = Wind_sp
Sensor 1 Flow velocity (m/s) = Wind_sp
Sensor 1 Sampling frequency (Hz) = 20.0
Sensor 1 Low pass filter type =
Sensor 1 Low pass filter time constant =
Sensor 1 High pass filter type =
Sensor 1 High pass filter time constant =
Sensor 1 Path length (m) = 0.15
Sensor 1 Time constant (s) = 0
Sensor 1 Tube attenuation coef =
Sensor 2 Flow velocity (m/s) = Wind_sp
Sensor 2 Sampling frequency (Hz) = 20.0
Sensor 2 Low pass filter type =
Sensor 2 Low pass filter time constant =
Sensor 2 High pass filter type =
Sensor 2 High pass filter time constant =
Sensor 2 Path length (m) = 0.125
Sensor 2 Time constant (s) = 0.0

Sensor 2 Tube attenuation coef =
Path separation (m) = 0.05
Get spectral data type = Model
Get response function from = model
Reference Tag =
Reference response condition =
Sensor 1 subsampled =
Sensor 2 subsampled =
Apply velocity distribution adjustment =
Use calculated distribution =
Velocity distribution std dev=
Stability distribution std dev=
Mathematical operation
From Time =
To Time =
Storage Label = Hc
Apply to =
Apply by =
Measured variable A = H
Operation = *
Measured variable B = H_frqres
Mathematical operation
From Time =
To Time =
Storage Label = LEc
Apply to =
Apply by =
Measured variable A = LE
Operation = *
Measured variable B = CLE_frqres
Mathematical operation
From Time =
To Time =
Storage Label = FCc
Apply to =
Apply by =
Measured variable A = FC
Operation = *
Measured variable B = CLE_frqres
Webb correction
From Time =
To Time =
Storage Label = WPL_LE
Apply to =
Apply by =
Scalar value type = Partial Pressure (kPa)
Scalar value = e
Min or QC =
Max or QC =
Water vapour value type = Partial Pressure (kPa)
Water vapour value = e
Min or QC =
Max or QC =
Temperature (C) = Ts_mean
Min or QC =
Max or QC =
Pressure (KPa) = press_mean
Min or QC =
Max or QC =
H flux (W/m2) = Hc
Min or QC =
Max or QC =
LE flux (W/m2) = LEc
Min or QC =
Max or QC =
H flux coef, RhoCp = rhoCp
Min or QC =
Max or QC =
LE flux coef, L = L
Min or QC =
Max or QC =
Scalar molecular wt. = 18
Scalar flux type = LE (W/m2)
Scalar flux coefficient = L
Min or QC =
Max or QC =
Alternate water vapour pressure (kPa) =
Alternate temperature (C) =
Alternate pressure (kPa) =
Mathematical operation
From Time =

To Time =
Storage Label = LEcw
Apply to =
Apply by =
Measured variable A = LEc
Operation = +
Measured variable B = WPL_LE
Webb correction
From Time =
To Time =
Storage Label = WPL_FC
Apply to =
Apply by =
Scalar value type = Density (mg/m3)
Scalar value = co2_mean
Min or QC =
Max or QC =
Water vapour value type = Partial Pressure (kPa)
Water vapour value = e
Min or QC =
Max or QC =
Temperature (C) = Ts_mean
Min or QC =
Max or QC =
Pressure (KPa) = press_mean
Min or QC =
Max or QC =
H flux (W/m2) = Hc
Min or QC =
Max or QC =
LE flux (W/m2) = LEcw
Min or QC =
Max or QC =
H flux coef, RhoCp = rhoCp
Min or QC =
Max or QC =
LE flux coef, L = L
Min or QC =
Max or QC =
Scalar molecular wt. = 44
Scalar flux type = Fx (mg/m2/s)
Scalar flux coefficient = 1
Min or QC =
Max or QC =
Alternate water vapour pressure (kPa) =
Alternate temperature (C) =
Alternate pressure (kPa) =
Mathematical operation
From Time =
To Time =
Storage Label = FCcw
Apply to =
Apply by =
Measured variable A = FCc
Operation = +
Measured variable B = WPL_FC
Plot Value
From Time =
To Time =
Left Axis Value = Hc
Right Axis Value = H
Left Axis Minimum =
Left Axis Maximum =
Right Axis Minimum =
Right Axis Maximum =
Match Left/Right Axes =
Plot Value
From Time =
To Time =
Left Axis Value = LEcw
Right Axis Value = LEc
Left Axis Minimum =
Left Axis Maximum =
Right Axis Minimum =
Right Axis Maximum =
Match Left/Right Axes =
Plot Value
From Time =
To Time =
Left Axis Value = LEc
Right Axis Value = LE
Left Axis Minimum =
Left Axis Maximum =
Right Axis Minimum =
Right Axis Maximum =

Match Left/Right Axes =
Plot Value
From Time =
To Time =
Left Axis Value = LEcw
Right Axis Value = Hc
Left Axis Minimum =
Left Axis Maximum =
Right Axis Minimum =
Right Axis Maximum =
Match Left/Right Axes =
Plot Value
From Time =
To Time =
Left Axis Value = FCcw
Right Axis Value = FCc
Left Axis Minimum =
Left Axis Maximum =
Right Axis Minimum =
Right Axis Maximum =
Match Left/Right Axes =
Solar elevation angle
From Time =
To Time =
Storage Label = Solar_Elev
Apply to =
Apply by =
Site lat. (dec deg) = 31.82
Site long. (dec deg) = -110.85
Time standard long. (dec deg) =
Solar azimuth angle
From Time =
To Time =
Storage Label = Solar_Azimuth
Apply to =
Apply by =
Site lat. (dec deg) = 31.82
Site long. (dec deg) = -110.85
Time standard long. (dec deg) =
Solar elev. angle (dec deg) =
Solar_Elev
Footprint
From Time =
To Time =
Storage Label = footp
Apply to =
Apply by =
Fetch (m) = 300
Measurement height (m) = 7
Wind speed (m/s) = Wind_sp
Friction velocity (m/s) = ustar
Std dev of V velocity (m/s) =
sd_Uy
Stability Z/L = Stability
Wind direction (deg) = Wind_dir
Wind speed limit = 0.3
Friction velocity limit = 0.03
Stability limit (+/-) = 30
Fetch calculation step, m = 1
Footprint average
From Time =
To Time =
Storage Label = Avg_FP
Apply to =
Apply by =
Unique footprint tag = tag_AVP
Variable footprint? =
Variable to average =
Conditional variable = H
Condition operators = >
Condition (lower limit) = 2
Condition upper limit =
Output File =
E:\New_Data\2016_winter.txt

APPENDIX C

GIS DATA REPOSITORY

This appendix describes a GIS data repository for the urban and rangeland sites, as stored in a digital format. The GIS repository includes sensor locations, remote sensing imagery (U.S.G.S. orthoimagery and LiDAR), land cover classifications, soil classifications, digital elevation models, canopy heights, and footprint derivations.

The urban GIS data is organized within the digital folder (:\NPT_Dissertation\Appendices\AppendixC\Urban\) as follows:

Folder Name	Description
SiteLocations	Coordinates of each mobile site deployment and reference site.
Orthoimagery	Orthoimage obtained for each mobile site deployment
LandCoverClass	Land cover classification based on orthoimage and supervised classification method in ArcGIS 10.4.

The rangeland GIS data is organized within the digital folder (:\NPT_Dissertation\Appendices\AppendixC\Rangeland\) as follows:

Folder Name	Description
SiteLocations	Coordinates of the two rangeland sites and four rain gauges.
Imagery	LiDAR data consisting of 0.3 m resolution orthoimagery over both sites
LandCoverClass	Land cover classification based on orthoimagery from LiDAR and supervised classification method in ArcGIS 10.4. for both sites
SoilClass	Soil classification shapefiles
Elevation	Digital elevation models (DEM) and canopy heights derived from LiDAR products for both sites.

Additional information and details can be found within the ReadMe file located in: :\NPT_Dissertation\Appendices\AppendixC\AppendixC_ReadMe.pdf

APPENDIX D

MOBILE EDDY COVARIANCE TOWER DATASETS

This appendix describes a repository for the urban tower datasets, as stored in a digital format. The urban data is organized within the digital folder (:\NPT_Dissertation\Appendices\AppendixD \) with three mobile tower folders and one reference tower folder, as follows:

Folder Name	Description
MobileTower_PL_Data	Data from the parking lot mobile deployment.
MobileTower_PV_Data	Data from the palo verde (xeric) mobile deployment.
MobileTower_PL_Data	Data from the turf grass (mesic) mobile deployment.
ReferenceTower_Maryvale_Data	Data from the reference site (suburban) tower.

The following folders are within each mobile tower folder:

Folder Name (\MobileTower_XX_Data\)	Description
Data_CardConvert	Contains raw data that has been card converted to daily intervals using Loggernet.
Data_Processed	Excel sheet(s) containing all meteorlogical and flux variables, post processing. Finalized table.
EdiRE_Output	Contains daily footprint output from EdiRE that is used to determine footprints at each tower.
Photos	All photographs of each deployment.
Raw_Data	Raw data collected from the datalogger.

The reference tower folder contains the following:

Folder Name (\ReferenceTower_Maryvale_Data\)	Description
CR1000_EC	Raw data and excel sheets summarizing eddy covariance measurments and metoerological measurements.
CR1000_Soil	Raw data and excel sheet summarizing soil measurements.
Photos	Photographs of reference tower site.

Additional information and details can be found within the ReadMe file located in: :\NPT_Dissertation\Appendices\AppendixD\AppendixD_ReadMe.pdf

APPENDIX E

SANTA RITA EDDY COVARIANCE TOWER DATASETS

This appendix describes a repository for the rangeland tower datasets, as stored in a digital format. The ARS ECT datasets are organized within the digital folder :\NPT_Dissertation\Appendices\AppendixE \ARS_ECT, and the ASU_ECT datasets are organized within the digital folder :\NPT_Dissertation\Appendices\AppendixE \ASU_ECT.

Within the ARS_ECT subfolder, the datasets are organized as follows:

Folder Name	Description
ARS_data_30min	30 minute meteorological and flux data for ARS ECT (2011 to 2016)
ARS_data_daily	Daily metoerological and flux data (gapfilled) for ARS ECT (2011 to 2016)

Within the ASU_ECT subfolder, the datasets are organized as follows:

Folder Name	Description
Raw_Data	All raw data collected from the datalogger (2011 to 2016)
Edire_Output	Processed fluxes using EdiRE
Processed_Data	Excel sheets summarizing meteorological and flux data (2011 to 2016)
Rainfall	Summary of rainfall at the four different rain gauges
TreatmentPhotos	Photos of the mesquite treatment at ASU ECT

APPENDIX F

VEGETATION AND LAND COVER CLASSIFICATION PROCESSING

This appendix describes the processing steps used to characterize the land cover/vegetation for each mobile tower deployment and the two rangeland sites. For the urban sites, the imagery to be used is contained in the folder, :\NPT_Dissertation\Appendices\AppendixC\Urban\Orthoimagery\. For the rangeland sites, the imagery to be used is contained in the folder, :\NPT_Dissertation\Appendices\AppendixC\Rangeland\Imagery\. Necessary software includes ArcMap, and steps below are based on ArcMap 10.4.1.

1. Load the aerial imagery (USGS orthoimage for urban sites or LiDAR image for rangdland sites) into ArcMap.
2. Enable the 'Image Classification' toolbar.
3. Within the toolbar, select 'Training Sample Manager.'
4. Next, select 'Draw Polygon.'
5. Determine which land cover class or vegetation class to focus on first.
6. Draw multiple polygons (at least 10) on the imagery that contain ONLY the specific land cover or vegetation class of interest. For example, to identify turf grass in the image, draw at least 10 different polygons that contain only turf grass on the image. The polygons may be as small or large as necessary. Also be careful to include class covers that may appear slightly different in the imagery. For example, bare soil at the rangeland sites has two distinct colors, due to different soil types, thus it is important to select an appropriate amount of training samples that represent both soil types, as they should both be classified as 'bare soil'.
7. Once a satisfactory number of polygons are drawn, revert to the 'Training Sample Manager' table.
8. Within the table, select all of the polygons that correspond to the specific land cover or vegetation class of interest, and select 'Merge Training Samples.' This will merge all the polygons into one unique ID number.
9. At this point, rename the 'Class Name' to the land cover class or vegetation class specified.
10. Repeat steps 6 to 9 for the remaining vegetation classifications. For the urban sites, there were 5 different ID values, representing the 5 land cover classes. For the rangeland sites, there were 3 different ID values representing the 3 vegetation classifications of interest.
11. Once all land cover/vegetation classes of interest have been identified, click on the icon on the right-hand side to create a signature file ('Create a signature file'), and save the signature file with an identifiable name.
12. On the Image Classification toolbar, under the 'Classification' menu option, select 'Maximum Likelihood Classification.'
13. For input raster bands, select the imagery (USGS orthoimage for urban sites or LiDAR image for rangdland sites).
14. For input signature file, load in the recently saved signature file containing the specified training samples.
15. Name output under Output classified raster.
16. Click OK, Maximum likelihood classification tool will run.

17. Once the tool runs, the output will be a vegetation classification map.
18. To verify the accuracy of the generated map, use Extraction in Spatial Analyst Tools to clip the map to an area of known vegetation classification. For the urban site, a visual inspection of the classification was deemed appropriate because of the familiarity of each mobile deployment. For the rangeland sites, a 60 meter radius circle was clipped around each tower site to compare the vegetation classification within the 60 meters to vegetation transect data.
19. Vegetation percentages can be determined using the pixel counts from the attribute table associated with the output raster.
20. If the vegetation classification does not match well, it is recommended to repeat the process with new polygons and generate a completely new signature file.

APPENDIX G

MATLAB SCRIPTS FOR DATA ANALYSIS

This appendix describes a repository for Matlab scripts used to analyze the datasets. The following table describes the folder name, script name, and a brief description of the script's use/purpose. The scripts are organized within the digital folder (:\NPT_Dissertation\Appendices\AppendixG \) corresponding to the dissertation chapter in which they were used (Chapter 2, or 3 and 4).

Folder Name	Script Name	Description
Ch2	Tower_timeseries	Plot and compare mobile tower datasets to reference tower
Ch2	Dirunal	Compute average diurnal cycles of meteorological or flux variables at the different urban sites
Ch2	DailyFluxes	Compute daily radiation and flux variables at urban sites
Ch3_4	Tower_compare_daily	Comparing ARS and ASU sites at 30 minute and daily time scale
Ch3_4	Tower_compare_month	Comparing ARS and ASU sites at monthly time scale
Ch3_4	Tower_compare_season	Comparing ARS and ASU sites at seasonal time scale
Ch3_4	Gapfill	ET, NEE gapfilling and Reco, GEP calculations
Ch3_4	Wind_Dir	Evalute fluxes with respect to wind direction (bins) and other criteria

APPENDIX H

DISSERTATION FIGURES

This appendix describes a repository containing the dissertation figures, in Matlab format (.fig) and TIFF format. Also included are Matlab or ArcMap files or scripts to generate each figure within this dissertation.

The dissertation figures, in Matlab and TIFF format, with associated scripts, are organized within the digital folder (:\NPT_Dissertation\Appendices\AppendixH\) as follows:

Folder Name	Description
Ch2_Figures	All figures from Chapter 2 (2.1 to 2.10)
Ch2_Scripts	Scripts to create figures from Chapter 2
Ch3_Figures	All figures from Chapter 3 (3.1 to 3.12)
Ch3_Scripts	Scripts to create figures from Chapter 3
Ch4_Figures	All figures from Chapter 4 (4.1 to 4.9)
Ch4_Scripts	Scripts to create figures from Chapter 4

Each figure and script are named to their corresponding number within the dissertation.

BIOGRAPHICAL SKETCH

Nicole (Nolie) Pierini Templeton grew up in South Lake Tahoe, CA, which strongly influenced her love for the environment. Nolie earned a B.S. in Environmental Engineering from the University of California, San Diego. Wanting to further explore her interest in water resources, Nolie (somewhat ironically) moved to the desert and pursued an M.S. degree in Civil, Environmental, and Sustainable Engineering from Arizona State University. Through her education, her interests in researching water resources issues, especially in the southwestern United States, only increased, and Nolie decided to pursue a Ph.D. in Civil, Environmental, and Sustainable Engineering. Although living in the desert had been an adjustment, she met her husband through their respective M.S. programs, and they are excitedly expecting a little girl in July 2017. In her spare time, Nolie loves to play soccer, hike, and enjoy the outdoors.